

A scanning electron micrograph (SEM) showing the microstructure of a glass-ceramic. The image displays a dense field of small, elongated, needle-like or plate-like crystalline phases embedded in a darker, amorphous glassy matrix. The crystals vary in size and orientation, with some appearing as long, thin needles and others as smaller, more equiaxed grains. The overall texture is granular and complex.

NUCLEATION AND CRYSTALLIZATION OF GLASSES AND GLASS-CERAMICS

EDITED BY : Wolfram Höland and Joachim Deubener
PUBLISHED IN : Frontiers in Materials



frontiers

Frontiers Copyright Statement

© Copyright 2007-2017 Frontiers Media SA. All rights reserved.

All content included on this site, such as text, graphics, logos, button icons, images, video/audio clips, downloads, data compilations and software, is the property of or is licensed to Frontiers Media SA ("Frontiers") or its licensees and/or subcontractors. The copyright in the text of individual articles is the property of their respective authors, subject to a license granted to Frontiers.

The compilation of articles constituting this e-book, wherever published, as well as the compilation of all other content on this site, is the exclusive property of Frontiers. For the conditions for downloading and copying of e-books from Frontiers' website, please see the Terms for Website Use. If purchasing Frontiers e-books from other websites or sources, the conditions of the website concerned apply.

Images and graphics not forming part of user-contributed materials may not be downloaded or copied without permission.

Individual articles may be downloaded and reproduced in accordance with the principles of the CC-BY licence subject to any copyright or other notices. They may not be re-sold as an e-book.

As author or other contributor you grant a CC-BY licence to others to reproduce your articles, including any graphics and third-party materials supplied by you, in accordance with the Conditions for Website Use and subject to any copyright notices which you include in connection with your articles and materials.

All copyright, and all rights therein, are protected by national and international copyright laws.

The above represents a summary only. For the full conditions see the Conditions for Authors and the Conditions for Website Use.

ISSN 1664-8714

ISBN 978-2-88945-224-8

DOI 10.3389/978-2-88945-224-8

About Frontiers

Frontiers is more than just an open-access publisher of scholarly articles: it is a pioneering approach to the world of academia, radically improving the way scholarly research is managed. The grand vision of Frontiers is a world where all people have an equal opportunity to seek, share and generate knowledge. Frontiers provides immediate and permanent online open access to all its publications, but this alone is not enough to realize our grand goals.

Frontiers Journal Series

The Frontiers Journal Series is a multi-tier and interdisciplinary set of open-access, online journals, promising a paradigm shift from the current review, selection and dissemination processes in academic publishing. All Frontiers journals are driven by researchers for researchers; therefore, they constitute a service to the scholarly community. At the same time, the Frontiers Journal Series operates on a revolutionary invention, the tiered publishing system, initially addressing specific communities of scholars, and gradually climbing up to broader public understanding, thus serving the interests of the lay society, too.

Dedication to quality

Each Frontiers article is a landmark of the highest quality, thanks to genuinely collaborative interactions between authors and review editors, who include some of the world's best academicians. Research must be certified by peers before entering a stream of knowledge that may eventually reach the public - and shape society; therefore, Frontiers only applies the most rigorous and unbiased reviews.

Frontiers revolutionizes research publishing by freely delivering the most outstanding research, evaluated with no bias from both the academic and social point of view.

By applying the most advanced information technologies, Frontiers is catapulting scholarly publishing into a new generation.

What are Frontiers Research Topics?

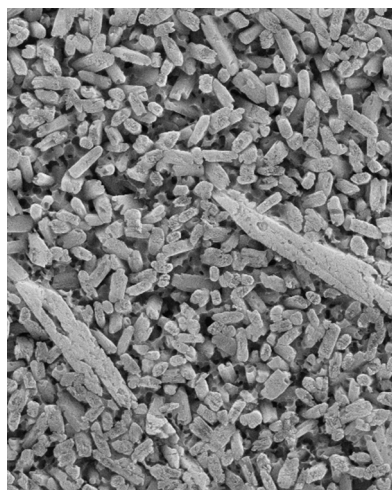
Frontiers Research Topics are very popular trademarks of the Frontiers Journals Series: they are collections of at least ten articles, all centered on a particular subject. With their unique mix of varied contributions from Original Research to Review Articles, Frontiers Research Topics unify the most influential researchers, the latest key findings and historical advances in a hot research area! Find out more on how to host your own Frontiers Research Topic or contribute to one as an author by contacting the Frontiers Editorial Office: researchtopics@frontiersin.org

NUCLEATION AND CRYSTALLIZATION OF GLASSES AND GLASS-CERAMICS

Topic Editors:

Wolfram Höland, Ivoclar Vivadent AG, Liechtenstein

Joachim Deubener, Clausthal University of Technology, Germany



Microstructure of lithium disilicate - diopside type glass-ceramic from Rampf et al. (this E-book).

The E-book “Nucleation and Crystallization of Glasses and Glass-Ceramics” highlights historic perspectives and current research in the field of glass-ceramic technology.

Glass-ceramic technology is promising to provide us with materials of high strength, high toughness, unique electrical/electronic or magnetic properties, exceptional optical or unusual thermal or chemical properties. The greater diversity of microstructure-property arrangements and processing routes over glasses and ceramics are responsible that glass-ceramics are the preferred choice of materials in many technical, consumer, optical, medical/dental, electrical/electronic, and architectural fields. This includes increasing uses of glass-ceramic materials for environment and energy applications in the last decades. The positive development of glass-ceramic technology has become true in particular due to the pioneering spirit, resourcefulness, and courage of researchers of the first generation. Extraordinary and, therefore, to be distinguished is the work of the glass-ceramic inventor S. Donald Stookey to whom this Research Topic is dedicated.

The authors, all experts in the field of glass-ceramics and based in industry, academia and governmental institutions, contributed to this E-book under the guidance of the Technical Committee 07 “Crystallization and Glass-Ceramics” of the International Commission on Glass (ICG).

Citation: Höland, W., Deubener, J., eds. (2017). Nucleation and Crystallization of Glasses and Glass-Ceramics. Lausanne: Frontiers Media. doi: 10.3389/978-2-88945-224-8

Table of Contents

- 04 Editorial: Nucleation and Crystallization of Glasses and Glass-Ceramics**
Joachim Deubener and Wolfram Höland
- 06 Dr. S. Donald (Don) Stookey (1915–2014): Pioneering Researcher and Adventurer**
George H. Beall
- 14 Coloration Mechanism of Fe Ions in β -Quartz s.s. Glass-Ceramics with TiO_2 and ZrO_2 as Nucleation Agents**
Shingo Nakane and Kosuke Kawamoto
- 20 Sintering and Foaming of Barium Silicate Glass Powder Compacts**
Boris Agea-Blanco, Stefan Reinsch and Ralf Müller
- 30 Controlled Parallel Crystallization of Lithium Disilicate and Diopside Using a Combination of Internal and Surface Nucleation**
Markus Rampf, Marc Dittmer, Christian Ritzberger and Wolfram Höland
- 39 The TTT Curves of the Heterogeneous and Homogeneous Crystallization of Lithium Disilicate – A Stochastic Approach to Crystal Nucleation**
Susanne Krüger and Joachim Deubener
- 48 Crystallization, Microstructure, and Viscosity Evolutions in Lithium Aluminosilicate Glass-Ceramics**
Qiang Fu, Bryan R. Wheaton, Karen L. Geisinger, Allen J. Credle and Jie Wang
- 56 Ion-Exchange in Glass-Ceramics**
George H. Beall, Monique Comte, Matthew J. Dejneka, Paulo Marques, Philippe Pradeau and Charlene Smith
- 67 Transparent Oxyfluoride Nano-Glass Ceramics Doped with Pr^{3+} and $\text{Pr}^{3+}\text{--Yb}^{3+}$ for NIR Emission**
Giulio Gorni, Alessandro Cosci, Stefano Pelli, Laura Pascual, Alicia Durán and M. J. Pascual
- 81 Nucleation and Crystal Growth in Laser-Patterned Lines in Glasses**
Takayuki Komatsu and Tsuyoshi Honma
- 89 Apatite Glass-Ceramics: A Review**
Tomas Duminis, Saroash Shahid and Robert Graham Hill



Editorial: Nucleation and Crystallization of Glasses and Glass-Ceramics

Joachim Deubener^{1*} and Wolfram Höland^{2*}

¹ Institute of Non-Metallic Materials, Clausthal University of Technology, Clausthal-Zellerfeld, Germany,

² Ivoclar Vivadent AG, Schaan, Liechtenstein

Keywords: glass-ceramic technology, heterogeneous and homogeneous nucleation, crystal growth, ceramming, sintering, nucleation agents, crystal patterning, non-linear optic crystals

The Editorial on the Research Topic

Nucleation and Crystallization of Glasses and Glass-Ceramics

Glass-ceramic technology, which is based on materials built from glasses *via* controlled nucleation and crystal growth, is promising to provide us with materials of high strength, high toughness, unique electrical/electronic or magnetic properties, exceptional optical or unusual thermal or chemical properties. Glass-ceramic technology has been used also to develop materials, which exhibit exceptional properties of hot and cold processing such as moldability and machinability, and it aims for better combining flexibility of these material and process characteristics in the future. The greater diversity of microstructure-property arrangements and processing routes over glasses and ceramics are responsible that glass-ceramics are the preferred choice of materials in many technical, consumer, optical, medical/dental, electrical/electronic, and architectural fields. This includes increasing uses of glass-ceramic materials for environment and energy applications in the last decades.

The positive development of glass-ceramic technology has become true in particular due to the pioneering spirit, resourcefulness, and courage of researchers of the first generation. Extraordinary and, therefore, to be distinguished is the work of the glass-ceramic inventor S. Donald Stookey (Beall) to whom this Research Topic is dedicated. He had realized, as early as at the mid of the last century, that glass-ceramic properties are mainly influenced by the controlling of the mechanisms of nucleation and crystal growth to achieve desired microstructures in the volume of these materials.

The last decades saw development of the downstream thermal treatment of formed glass parts (called “ceramming”) for a large variety of chemical systems, while nowadays, sintering of glass powders is available as a powerful route for glass-ceramic processing at lower fabrication temperatures and for complex shapes using powder compacts or slurry deposits on various substrates prepared by dipping, brushing, or spraying techniques or the emerging printing technologies (Höland and Beall, 2012; Müller and Reinsch, 2012). For both fabrication routes, crystal growth at or close to internal and external interfaces induced by heterogeneous nucleation is the key process transforming glass into glass-ceramic. Nucleation agents have been shown to trigger these processes in the volume of transparent glass-ceramics. Their coloration effects are subject of current developments (Nakane and Kawamoto). For sintered glass-ceramics, surface activation treatments by milling glass powders promote heterogeneous nucleation but these processes can cause gas release during the subsequent sintering step. To overcome limitations of sintered glass-ceramics for energy applications, such as SOFC sealants, measures to reduce the bubble formation are now being studied intensively (Agea-Blanco et al.). Further, activation of both heterogeneous surface and heterogeneous volume nucleation processes of sintered glass-ceramics is currently gaining importance for dental applications (Rampf et al.). To study the interplay of heterogeneous and homogeneous nucleation

OPEN ACCESS

Edited and Reviewed by:

John C. Mauro,
Corning Inc., USA

*Correspondence:

Joachim Deubener
joachim.deubener@tu-clausthal.de;
Wolfram Höland
wolfram.hoeland@ivoclarvivadent.com

Specialty section:

This article was submitted
to Glass Science,
a section of the journal
Frontiers in Materials

Received: 11 April 2017

Accepted: 05 May 2017

Published: 22 May 2017

Citation:

Deubener J and Höland W (2017)
Editorial: Nucleation and
Crystallization of Glasses and
Glass-Ceramics.
Front. Mater. 4:14.
doi: 10.3389/fmats.2017.00014

in glass-ceramic materials from a more fundamental point of view, current academic research is focusing on the underlying stochastic nature of the crystal nucleation process (Krüger and Deubener).

Cerammig is the core process in the case of consumer products and appliances. In order to achieve near-net shape fabrication, *in situ* analysis of changes in the thermomechanical behavior concurrent with the microstructure evolution is increasingly gaining attention (Fu et al.). For further performance improvements, additional, post-cerammig heat treatments with respect to ion-exchange and mechanical strength development have found renewed interest. The recent status of ion-exchanged glass-ceramics is reviewed in this topical issue (Beall et al.). The precipitation of optically active crystals can also be widely controlled by glass-ceramic technology. Efficient down-conversion processes in transparent glass-ceramics are one of the emerging fields where rare earth ions can be used to promote solar cell efficiency (Gorni et al.). Furthermore, laser-induced crystallization is shown to be attractive alternative to usual cerammig, which can provide novel functionalities to glass-ceramic materials by spatially selected patterning of non-linear optic crystals in glasses. Intensive R&D is now providing us with new insights on the mechanisms that control crystal growth directions (Komatsu and Honma). Glass-ceramic is also very attractive for hosting

apatite crystals. Current directions in the development of apatite glass-ceramics for orthopedics, dentistry, optoelectronics, and nuclear waste management are re-evaluated in this Research Topic (Duminis et al.).

AUTHOR CONTRIBUTIONS

This contribution is an editorial. As such, the topic editors equally contributed to this introduction.

ACKNOWLEDGMENTS

We would like to thank all the authors, reviewers, editors, publishers, and members of the Technical Committee 07 (Crystallization and Glass-ceramics) of the International Commission on Glass (ICG) who have supported this Research Topic.

FUNDING

The Topic Editors acknowledge the Coordinating Technical Committee (CTC) of the International Commission on Glass (ICG) for supporting the “11th International Symposium on Crystallization in Glasses and Liquids” October 11–14, 2015 in Nagaoka, Japan.

REFERENCES

- Höland, W., and Beall, G. H. (2012). *Glass-Ceramic Technology*. Hoboken, NJ: Wiley.
- Müller, R., and Reinsch, S. (2012). “Viscous phase silicate processing,” in *Processing Approaches for Ceramics and Composites*, eds N. Bansal and A. R. Boccaccini (Hoboken, NJ: John Wiley & Sons), 75–144.

Conflict of Interest Statement: The authors declare that the research was conducted in the absence of any commercial or financial relationships that could be construed as a potential conflict of interest.

Copyright © 2017 Deubener and Höland. This is an open-access article distributed under the terms of the Creative Commons Attribution License (CC BY). The use, distribution or reproduction in other forums is permitted, provided the original author(s) or licensor are credited and that the original publication in this journal is cited, in accordance with accepted academic practice. No use, distribution or reproduction is permitted which does not comply with these terms.



Dr. S. Donald (Don) Stookey (1915–2014): Pioneering Researcher and Adventurer

George H. Beall*

Corning Incorporated, Corning, NY, USA

OPEN ACCESS

Edited by:

Wolfram Höland,
Ivoclar Vivadent (Liechtenstein),
Liechtenstein

Reviewed by:

Mathieu Hubert,
CelSian Glass & Solar, Netherlands
Bruno Poletto Rodrigues,
Otto-Schott-Institute of Materials
Research, Germany
Ralf Mueller,
German Institute for Materials
Research and Testing, Germany

*Correspondence:

George H. Beall
beallgh@corning.com

Specialty section:

This article was submitted
to Glass Science,
a section of the journal
Frontiers in Materials

Received: 26 May 2016

Accepted: 20 July 2016

Published: 24 August 2016

Citation:

Beall GH (2016) Dr. S. Donald (Don)
Stookey (1915–2014): Pioneering
Researcher and Adventurer.
Front. Mater. 3:37.
doi: 10.3389/fmats.2016.00037

Don Stookey, the father of glass–ceramics, was a pioneer in inducing and understanding internal nucleation phenomena in glass. His early work on dense opal glasses and photosensitive precipitation of gold and silver in glass led to an amazing series of inventions: Fotalite®, a photosensitive opal, chemically machined Fotoform® and Fotoceram®, and TiO₂-nucleated Pyroceram™ products including missile nosecones and oven-proof cookware. He received a basic patent on glass–ceramics, which was contested and affirmed in court. Don was able to demonstrate a clear photochromic glass that showed reversible darkening for thousands of cycles. This material became a fixture in the ophthalmic industry. He went on to invent a full-color polychromatic glass, capable of yielding a permanent patterned and monolithic stained glass. In his life outside science, Don chaired an interfaith group that founded a home for the elderly in Corning. He was also a wilderness enthusiast, surviving a plane crash in the Arctic and two boat capsizings. Even in his later years, he continued fishing off the coast of Florida and on Lake Ontario and went solo on a trip to the Patagonian Andes. Don Stookey was a special person by any measure: an unassuming optimist, eminent scientist and inventor, adventurer, and a beloved family man.

Keywords: Stookey, career, invention, research, glass–ceramics, nucleation, photosensitive, photochromic

INTRODUCTION

Don Stookey (**Figure 1**) was a well-known and highly respected scientist at Corning Incorporated, formerly Corning Glass Works, for 50 years (1940–1990). He was responsible for developing an understanding of internal nucleation of crystallites in glass resulting in many products: photosensitive ruby glass, photosensitive opal glass, photochromic glass, polychromatic glass, and glass–ceramics, including Corningware® cookware and Pyroceram™ missile nosecones.

Don was born at Hay Springs, Nebraska on May 23, 1915. His family moved to Cedar Rapids Iowa in 1921. He graduated with a B.A. in Mathematics and Chemistry from Coe College in 1936. He then received a master's degree in Chemistry from Lafayette College in Easton, PA, USA, in 1938 and went on to earn a Ph.D. in Physical Chemistry from Massachusetts Institute of Technology in 1940. He married his Coe College sweetheart, Ruth Watterson, in the same year. He joined Corning Glass Works in 1940 and began working on dense and opal glasses of interest as the white background in glass thermometers as well as for decorative tableware and translucent lighting globes.

Don was fascinated by the effects of heat treating uncolored glass to yield a ruby glass in some cases and a white material in others. He understood that particles must be forming in the interior of such glasses and from the chemistry of the glass and previous research dating back in some cases to the middle ages, he realized that these particles were gold, silver, or copper in ruby glasses



FIGURE 1 | Don Stookey.

and crystals of titania or fluorides of sodium or calcium in opal glasses.

PHOTOSENSITIVE GLASSES

Don's first invention involved copper ruby glasses that required a heat treatment to bring out the copper particles. Don realized that the traditional added ingredients, such as the oxides of tin and antimony, must play a key role. He reasoned that reheating the glass must initiate a redox reaction where copper is reduced to the metallic state and tin and antimony are oxidized. He then systematically decreased the amount of these additives to the point where the glass remained colorless even after the heat treatment. He then exposed these glasses through a negative to ultraviolet light, and upon subsequent heating, only the exposed areas turned a ruby color. After producing a photosensitive copper ruby glass, Don felt he could do the same with the more beautiful gold ruby glass (**Figure 2**). The color mechanism here was already understood to be an effect of SnO_2 additions to the glass batch, yielding an oxidizing melt and allowing gold to be dissolved as ions. Subsequent reheating of the cold glass caused SnO to reoxidize to SnO_2 , thus reducing the gold ions allowing the precipitation of tiny gold particles. But, as Don decreased the tin level to the point of zero coloration on reheating, ultraviolet radiation had no effect in retrieving the ruby color through heat treatment. It was then that he tried additions of other multivalent oxides and found that only cerium oxide (CeO_2) additions allowed the ultraviolet exposed areas to create ruby patterns. Thereafter, the combination of ceria additions to both gold- and silver-containing glasses became the most important

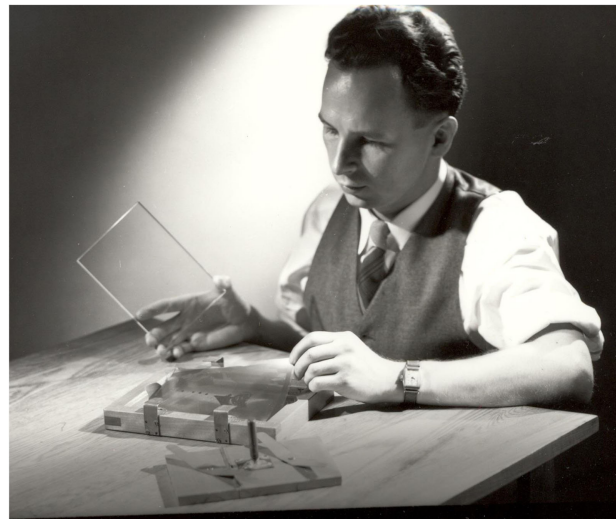


FIGURE 2 | Don Stookey at work on photosensitive gold ruby glass.



FIGURE 3 | Fotalite® dinner plate design.

feature in many new photosensitive materials, including photosensitive opal glasses. In this case, Don added silver and ceria and decreased the fluoride level to just below what was required to produce thermal opalization. The silver particles could be formed only in the exposed areas *via* the photochemical reaction: $\text{Ag}^{1+} + \text{Ce}^{4+} \rightarrow \text{Ag}^0 + \text{Ce}^{3+}$, and these nanocrystals were able to act as nuclei for sodium fluoride (NaF) crystals on reheating. Moreover, these NaF crystals grew large enough to scatter light. As a result, his first commercial success, Fotalite®, was produced (**Figure 3**). This material was used as sheets of white marbled glass that to this day cover the north face of the United Nations headquarters building in New York City.

FOTOFORM® AND FOTOCERAM®, THE FIRST GLASS-CERAMIC

After his discovery of controlled photosensitive precipitation of silver and its role in the nucleation of NaF , Don began to consider

whether other crystalline phases could also be internally nucleated in glass. He discovered that actual glass-forming silicate compounds such as barium disilicate and lithium metasilicate could be nucleated, albeit in small amounts. Then, at a meeting in 1947, Dr. J. T. Littleton, Corning's research director at that time, wondered if glass could somehow be used to make vital aperture masks guiding the electron beams in colored television (Corning already made the bulbs). Don left the meeting without any comment and went ahead testing the photo-precipitated compounds that he had made. To his delight, in one lithium-containing glass, the areas where lithium metasilicate was photo-precipitated could be easily etched with hydrofluoric acid, whereas the untreated glassy areas were resistant. This new photo-etchable material was called Fotoform®, and although it was never used for television apertures, 30 years later it developed into a significant business. It was used in a variety of complexly shaped structures for the electronic and communication industries as well as for decorative items (Figure 4).

The discovery of Fotoform® also led to an even more important albeit accidental discovery. One day, as Don was preparing to heat-treat a plate of pre-exposed Fotoform® glass, the temperature controller became stuck in the “on” position, and instead of remaining at 600°C, the furnace temperature increased to 900°C. Expecting to find a molten pool of glass, Don was amazed to see instead an undeformed opaque and solid plate. Snatching a pair of tongs, he pulled the plate out of the hot furnace, but it slipped from the tongs and fell onto the concrete floor, clanging like steel and remaining unbroken. He had, in fact, converted a glass article to a ceramic article. This first glass-ceramic, called Fotoceram®, was predominantly crystalline (lithium disilicate) and stronger than Fotoform® and could inherit a complex etched shape from Fotoform® through simple flood exposure and reheating (Figure 5).

EXPLOSION OF GLASS-CERAMIC COMPOSITIONS AND PROPERTIES

Don Stookey was not satisfied by producing Fotoceram® alone. He was convinced that this was just one example of a conversion

of glass to a ceramic and that other glasses of a wide variety of chemical composition would yield crystals of diverse and useful properties. Unfortunately, he found that silver and other metallic nucleating agents were ineffective in most glasses, especially in aluminosilicate formulations. Don knew of crystals of low coefficient of thermal expansion (CTE), such as cordierite ($\text{Mg}_2\text{Al}_4\text{Si}_5\text{O}_{18}$), used in thermal-shock-resistant ceramic kiln ware and lithium aluminosilicates that had been revealed in research at Pennsylvania State University (Penn State) to have low and even negative CTE values. He desperately needed to find an effective nucleating agent for aluminosilicate glasses, and from his knowledge of dense white opal glasses, particularly those based on rutile (TiO_2), he decided to add titania to these glass batches. Titania was amazingly effective, easily dissolving into the glasses and producing highly crystalline lithium and magnesium aluminosilicate glass-ceramics upon heat treatment. Surprisingly, little or no deformation was seen during the heating and crystallization process, and even delicate shapes of pressed and blown ware were faithfully retained. Two successful products resulted from this research in the late 1950s: radomes (nose cones for missiles) based on cordierite (Figure 6) and Corningware® (Figures 7 and 8) heat-resistant cookware based on the crystal β -spodumene ($\text{LiAlSi}_2\text{O}_6$ – $\text{LiAlSi}_5\text{O}_{12}$ solid solution). The first glass-ceramic electric cooktop was based on a similar material (Figure 9).

Don Stookey was also the first to produce transparent glass-ceramics. While experimenting in the late 1950s with various heat treatments of basic Li-aluminosilicate glasses doped with titania, he found that metastable silicate crystals preceded the development of β -spodumene. The X-ray diffraction pattern looked like that of β -eucryptite (LiAlSiO_4), a structural derivative of β -quartz, known for its negative CTE. This glass-ceramic was composed of nanocrystals about 50–100 nm in diameter, and because they were smaller than the wavelength of visible light, the glass-ceramic did not scatter light and was transparent. Later, it was found that these crystals were solid solutions of β -eucryptite and β -quartz, similar to the natural mineral: virgilitite. Glass-ceramics based on this crystal phase were to become

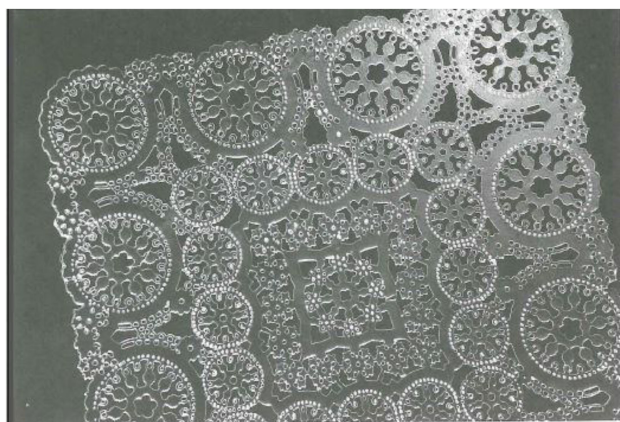


FIGURE 4 | Fotoform® glass lace.

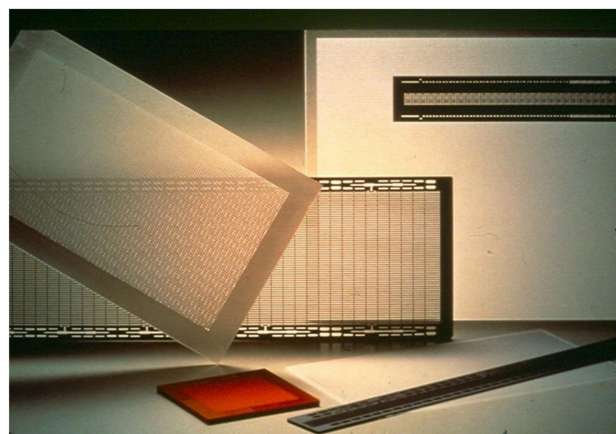


FIGURE 5 | Fotoform® and Fotoceram® (bottom) products.



FIGURE 6 | Don Stookey with Ben Allen (engineering manager), Jim Giffen (glass-forming expert), and Bill Armistead (R&D director) with first glass-ceramic radomes (c. 1957).



FIGURE 8 | Thermal shock resistance of Corningware® demonstrated.



FIGURE 7 | Don Stookey displays his invention as a successful product.



FIGURE 9 | First glass-ceramic cooktop: The Counter That Cooks™.

the basis of applications where dimensional stability over a wide spectrum of temperatures (near-zero CTE) is required. These include telescope mirrors (Schott Zerodur®), Visions® transparent cookware, and the largest current glass-ceramic business: dark electric range cooktops.

PHOTOCHROMIC GLASS

The development of a glass that darkens under sunlight and fades indoors was one of Don Stookey's finest inventions. It began when Dr. William Armistead (Bill), Corning's Director of Research and Development at this time, visited a customer who suggested the potential value of reversible sunglasses. Bill then asked Don if he could make such a glass. An accomplished researcher himself,

Bill remembered a yellow opal glass containing silver chloride (AgCl) that he had made. This glass appeared to darken under sunlight, so Bill suggested this as a starting point. Don jumped at the idea, and following the procedure that had been successful with photosensitive glasses, he decreased the level of the active agent, in this case AgCl, in the glass until it remained clear after cooling and annealing. Upon further heat treatment below the softening temperature, he was able to produce some opaque and translucent materials that showed some darkening under ultra-violet light, but very little fading. All of the samples that remained transparent were inactive. Remembering his success with ceria as a sensitizer in photosensitive glass, he tried this oxide as well as other multivalent oxide additions to the glass batch. Only

copper oxide was effective, not only in producing darkening in transparent samples but also fading as the light source was removed. Surprisingly, this action was reversible and unchanged after thousands of cycles. Transmission electron microscopy later revealed that spherical nanocrystals of Cu-doped AgCl were decorated with metallic silver patches (like continents on the earth) after darkening according to the reversible reaction: $\text{Ag}^{1+} + \text{Cu}^{1+} \leftrightarrow \text{Ag}^0 + \text{Cu}^{2+}$. The patches then disappeared upon removal of the light source, causing fading.

As a result of this work, Don had created the first truly reversible chemical reaction in a solid material. It was not long after this discovery that a multimillion dollar business in photochromic glass for both prescription lenses and sunglasses (Figure 10) became a reality.

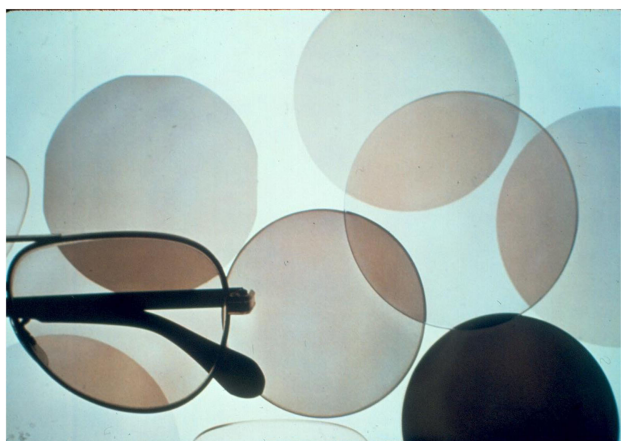


FIGURE 10 | Photochromic eye-glasses (1960s).

POLYCHROMATIC GLASS

The last of Don Stookey's major inventions was polychromatic glass, a photosensitive glass that could produce all colors in any patterned form (Figure 11). Don discovered that by including two halides, namely, sodium fluoride (NaF) and either sodium bromide (NaBr) or sodium chloride (NaCl), in the batch of certain compositions related to Fotalite®, a full-color spectrum could be developed in a single glass. To develop the colors, two exposures to ultraviolet light (~300 nm) followed in each case by special heat treatments were required. He found that the first exposure dose (time and/or ultraviolet intensity) controlled the final color, while the second exposure dose controlled the color intensity. The first heat treatment developed the silver nuclei near 475°C and produced both cubic crystals, presumed to be NaF, and crystallites of a peculiar pyramidal or comet-like shape around 525°C. The pyramidal crystals were thought to be mixed silver-doped complex sodium halide- Ag: Na(F,Cl,Br), because without a secondary halide, they could not be formed. The number and density of both silver nuclei and pyramidal halide crystallites increased as a function of the original radiation dose. The second exposure and heat treatment, which could be separated or done simultaneously on a hot plate at about 350°C, caused more silver to precipitate, this time at the tip of the pyramidal crystals. This silver was elongated to a degree dependent upon the density of crystals; the scattered crystals had more and longer silver at the tail, whereas crowded crystals had less and shorter silver tails. The color depended on the aspect ratio of these secondary silver particles at the crystallite tails, green with the longest going through blue, purple, red, orange, and yellow with the shortest.

Polychromatic glass was produced as both clear and opal glasses, depending upon the size of the halide crystals. To the

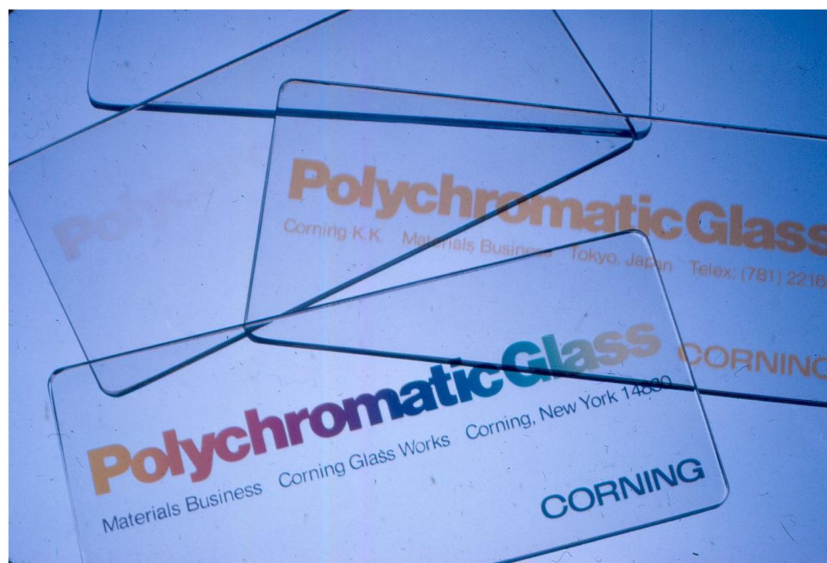


FIGURE 11 | Evolution of polychromatic glass as formed, after ultraviolet exposure and first heating, and after second ultraviolet exposure and heating.

disappointment of Don Stookey, no practical applications for this unique material have yet been found.

DON STOOKEY'S RESEARCH PHILOSOPHY

Don has described his research philosophy in a number of quotations which are listed below:

Be observant, diligent, and optimistic. Don was always an optimist, especially in research, but also in his outlook on the world in general.

Science can be fun, and the scientist-inventor need neither be mad, nor a genius, nor confined to an ivory tower. Don was a practical man and believed strongly in the value of useful research. He took a dim view of the idea that pure research was somehow superior to exploratory research and academic research is somehow contaminated by cooperation with industry.

The unique factor in promoting my career has been the proper mix of motivation and imagination, and the opportunity to exercise them. Don was especially grateful for the freedom he was given to do independent research at the Corning Glass Works and had great respect for the Houghton family and R&D director, Dr. William Armistead. He became a lifetime friend of former Corning Chief Executive Officer, Amory Houghton, Jr.

The increasingly popular use of research teams has its place, but original ideas come one at a time. Teamwork applies to later stages of innovation and should not displace the original inventor. Don was unhappy to see an apparent modern trend away from individual thought and accomplishment.

An embryo invention is a fragile flower, easily killed by the pessimism that seems to be a predominant characteristic of most adults. Don did not easily tolerate naysayers.

Meetings, fire calls to solve today's production problems, and assignments to improve on known inventions are general enemies to the birth of new inventions. Don understood the necessity of continual product development and crises problem-solving; indeed, he admired and gave full credit to those who made contributions in harnessing his inventions. He did, however, believe that those few who were enthusiastic and skilled in fundamental and exploratory research should be allowed to follow their instincts.

DON STOOKEY'S FISHING ADVENTURES

Don Stookey was an avid fisherman, and it was on fishing vacations that he had many unexpected adventures. One in the 1950s that nearly took his life took place above the Arctic Circle on Great Bear Lake in the Northwest Territories of Canada.

Don and his brother, Dave, were about to land in a float plane near their campsite when the pilot was evidently distracted by the wake of another float plane taking off. The lake was a glassy calm except for these developing waves, and the pilot had difficulty in gaging the distance between his plane and the lake. As a result, he failed to raise the nose of the plane as he hit a wave surface,

and the plane flipped over leaving the pilot and passengers upside down and quickly under ice-cold water. Don and the pilot were able to free themselves from their seat belts, and Don was able to open the passenger door against the pressure of the water and hold it open until his brother emerged from the back of the plane. They then hit the water surface and were able to crawl out and stand on the upside-down wing below the water surface, hanging on the floating pontoon on the surface of the lake. They had less than 10 min to survive in the freezing water, but fortunately they were within sight of the Innu (Eskimos) at the camp, and they were able to reach them by boat in time to save them.

Then there was the time in 1995, when a large group of fishermen including Don, his brother Dave, his two grandsons Dave and Steve, my two sons Doug and Tom, and I were on a fishing trip to Camp Minewan, a native Cree fishing camp about 100 miles east of James Bay in Northern Quebec. One day, we took a portage trail leading to the outlet of a lake where the fishing was so good that large northern pike about 2 ft in length attacked any lure thrown at them in almost every cast. Upon returning along the portage, Don was walking behind me at the end of the group, and I suddenly realized that I could no longer hear his footsteps. The terrain near this trail consisted of typical black spruce taiga with trees separated by a few yards, and it was the same for miles in any direction with no signs of anything beyond the occasional moose trail, one of which Don had evidently mistaken for the portage. Fortunately, my sons had good ears and heard a stick or branch breaking in the distance and off the trail. We were eventually able to find Don, who said he had just realized he was lost and alone when we found him.

Don was a lover of boats and bought a 36-ft Jinx cruiser on his way to Florida when he ran into Hurricane Agnes on Chesapeake Bay and became mired on a reef whose warning buoy had shifted in the storm. He did not know it at the time, but this same storm was to cause flooding in the Corning, NY, USA, area where Don's house was inundated nearly to the ceiling of the first floor.

Although by now, one might get the impression from these stories that Don was jinxed or prone to accidents, but in fact, he took many other fishing trips in exotic places without incident or apparent danger. He and his family and friends made many fishing trips to Lake Makokibatan on the Albany River in Northern Ontario. Famous for walleye, this lake was the home of an Ojibway Indian family, who supplied Don with an excellent guide who became a friend and companion. The guide returned his friendship by shooting a moose and presenting him with the meat and moccasins made from its hide.

Don also made many expeditions in Florida, one involving catching a 75-pound tarpon off Key West. He also fished in the Nile, catching a giant perch (**Figure 12**), and more recently took a solo trout-fishing trip in Patagonia when he was in his late 80s.

DON STOOKEY AND THE COMMUNITY

Don was active in community affairs beyond Corning Incorporated. He was a member of the First United Methodist Church, and in this capacity, he chaired an interfaith committee that was responsible for the development of Dayspring, a home for the elderly in the city of Corning.



FIGURE 12 | Don Stookey and Nile Perch (1997).

When asked to spend a year as guest professor at the Ceramic Centre of Alfred University, Don gave classes that were widely attended and that gave students a vivid perspective of the career of a respected scientist and inventor in industry.

Don treated everyone with respect, regardless of social status. He was always optimistic at work and elsewhere. The only thing that seemed to bother him was a negative or pessimistic attitude. He had a great professional relationship with Amory Houghton, Jr. former Chief Executive Officer of Corning Incorporated and multi-term Congressman, and they became lifelong friends. He also met regularly with his long-time technician and friend, Joe Pierson. Both men were present at Don's receiving of the Phoenix Award (Figure 13) and were regular visitors of Don during his retirement in Florida and in Rochester, NY, USA.

DON STOOKEY'S LEGACY

Don Stookey was a major positive force on the success of Corning Glass Works, now Corning Incorporated. The current Sullivan Park campus for research, product development, and engineering was built in the 1960s when Don's inventions, especially Corningware® and photochromic ophthalmic glass were impacting Corning's earnings. Management well appreciated the impact of Don's contributions as shown by a cartoon that they presented to him (Figure 14).



FIGURE 13 | Don Stookey with Phoenix Award (1975) and lifetime friends: technician Joe Pierson (left) and Corning Glass Works CEO and future U.S. Congressman Amory Houghton, Jr.

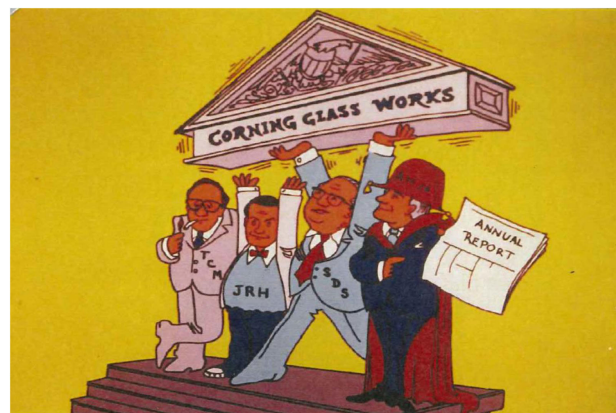


FIGURE 14 | Cartoon given to Don Stookey by Corning Senior Management.

Don mentored many younger scientists, including me, and his style was to lead and teach by example. He was certainly both a special friend to me and a masterly guide on how to conduct exploratory research.

Don earned many honors and awards during his distinguished career, including

1. John Price Wetherill Award to the Franklin Institute (1953 and 1962).
2. Coe College Alumni Award of Merit (1955).
3. Ross Coffin Purdy Award of the American Ceramic Society (1960).
4. Coe College Honorary D.Sc. (1963).
5. Toledo Glass and Science Award (1964).
6. Inventor of the Year Award, George Washington University (1970).

7. Award for Creative Invention of the American Chemical Society (1971).
8. Eugene Sullivan Award, Corning Section, American Chemical Society (1971).
9. Myers Achievement Award of Education Foundation in Ophthalmic Optics (1973).
10. Phoenix Award of the Glass Industry (1975).
11. Achievement Award of the Industrial Research Institute (1979).
12. Samuel Giejbeek Award of the American Ceramic Society.
13. Distinguished Inventor Award, Central New York Patent Law Association (1984).
14. Alfred University Honorary D.Sc. (1984).
15. National Medal of Technology presented by President Ronald Reagan (1986).
16. Distinguished Life Member, American Ceramic Society (1989).
17. Wilhelm Eitel Medallion for Excellence in Silicate Science (1993).
18. National Medal of Technology, White House Council (1994).
19. Inductee, National Inventors Hall of Fame (2010).

I believe that Don was most proud of the National Medal of Technology presented to him by President Reagan in 1986 (Figure 15).

Don maintained his interest in Corning Incorporated's research efforts during his retirement through frequent visits to Sullivan Park set up by Dr. David Morse, Corning's current executive vice president and chief technical officer. For these occasions, Don always brought a list of ideas for glass-related research. He was the ultimate example for younger scientists to follow, and he always reacted favorably to their ideas. He continued his optimism and good spirit even until his final days.

As David Morse described him: "Don Stookey was fearless; the unknown never daunted him. He was an unassuming and quiet but tough person with an extensive depth of knowledge."

ADDITIONAL READING

- Stookey, S. D. (1985). *Journey to the Center of the Crystal Ball*. Westerville, OH: The American Ceramic Society, 64.
- Stookey, S. D. (2000). *Explorations in Glass*. Westerville, OH: The American Ceramic Society, 74.
- Stookey, S. D., Beall, G. H., and Pierson, J. E. (1978). Full-color photosensitive glass. *J. Appl. Phys.* 10, 1978.
- Stookey, S. D. (1960). *Method of Making Ceramics and Product Thereof (Results of Litigation Described on p.53 of Reference Above)*. U.S. Patent 2,920,971.



FIGURE 15 | Dr. S. Donald Stookey receiving National Medal of Technology from President Ronald Reagan (1986).

I believe that these lines by Tennyson reflect Don's faith and optimism:

*Sunset and evening star,
And one clear call for me!
And may there be no moaning of the bar,
When I put out to sea,
For tho' from out our bourne of Time and Place
The flood may bear me far,
I hope to see my Pilot face to face
When I have crost the bar.*

AUTHOR CONTRIBUTIONS

The author confirms being the sole contributor of this work and approved it for publication. In composing this work, the author has relied upon his knowledge of the patents and publications of Dr. S. Donald Stookey, as well as 50 years experience as his colleague and friend.

Conflict of Interest Statement: The author declares that the research was conducted in the absence of any commercial or financial relationships that could be construed as a potential conflict of interest.

Copyright © 2016 Beall. This is an open-access article distributed under the terms of the Creative Commons Attribution License (CC BY). The use, distribution or reproduction in other forums is permitted, provided the original author(s) or licensor are credited and that the original publication in this journal is cited, in accordance with accepted academic practice. No use, distribution or reproduction is permitted which does not comply with these terms.



Coloration Mechanism of Fe Ions in β -Quartz s.s. Glass-Ceramics with TiO_2 and ZrO_2 as Nucleation Agents

Shingo Nakane* and Kosuke Kawamoto

Nippon Electric Glass Co., Ltd., Otsu, Japan

OPEN ACCESS

Edited by:

Wolfram Höland,
Ivoclar Vivadent, Liechtenstein

Reviewed by:

Robert Graham Hill,
Queen Mary University of
London, UK
Christian Ritzberger,
Ivoclar Vivadent, Liechtenstein

*Correspondence:

Shingo Nakane
snakane@neg.co.jp

Specialty section:

This article was submitted to
Glass Science,
a section of the journal
Frontiers in Materials

Received: 23 September 2016

Accepted: 08 March 2017

Published: 03 April 2017

Citation:

Nakane S and Kawamoto K (2017)
Coloration Mechanism of Fe Ions in
 β -Quartz s.s. Glass-Ceramics with
 TiO_2 and ZrO_2 as Nucleation Agents.
Front. Mater. 4:7.
doi: 10.3389/fmats.2017.00007

Transparent β -quartz s.s. glass-ceramics in $\text{Li}_2\text{O}-\text{Al}_2\text{O}_3-\text{SiO}_2$ system have an undesirable brown color owing to Fe ions as a contaminant, whereas the mother glass normally has a clear appearance. Elucidation of the coloration mechanism during crystallization is important for industry to develop highly transparent materials. In this study, the mother glass contained SiO_2 , Al_2O_3 , and Li_2O as its principal constituents and TiO_2 and ZrO_2 as nucleation agents. The amount of contaminant Fe ions in the form of Fe_2O_3 was 0.03 wt%. It was confirmed that the coloration was appeared by the coexistence of Fe and Ti ions in the glass matrix based on the experimental results using Ti-containing and Ti-free glasses with a composition identical to that of the glass matrix. The coordination and oxidation state of the Fe ions were not changed by the coexistence of Ti ion according to the results of X-ray absorption near-edge structure measurement. The coloration is considered to be due to the formation of Fe–O–Ti by the concentration of Fe and Ti ions in the glass matrix phase during the crystallization process.

Keywords: $\text{Li}_2\text{O}-\text{Al}_2\text{O}_3-\text{SiO}_2$ glass-ceramics, iron ion, coloration mechanism, glass matrix phase, coordination state, X-ray absorption near-edge structure

INTRODUCTION

Although $\text{Li}_2\text{O}-\text{Al}_2\text{O}_3-\text{SiO}_2$ low-expansion glass-ceramics having β -quartz s.s. or β -spodumene s.s. as main precipitated crystal were developed by Stookey more than 50 years ago, the research and development of the material is still active, particularly on their nucleation phenomena and improving their characteristics to apply them to various emerging applications (Bhattacharyya et al., 2010; Sakamoto and Yamamoto, 2010). The first developed $\text{Li}_2\text{O}-\text{Al}_2\text{O}_3-\text{SiO}_2$ glass-ceramics contained 2–20 mass% TiO_2 as a nucleation agent, and their appearance was white and opaque. The ceramics were used for heat-resistant tableware (Stookey, 1960). The glass was crystallized homogeneously by heat treatment to induce the nucleation of Al_2TiO_5 as a precipitate (Doherty, 1967). Shortly after the work of Stookey, Tashiro and Wada (1963) found that ZrO_2 is an effective nucleation agent, and transparent β -quartz s.s. glass-ceramics in $\text{Li}_2\text{O}-\text{Al}_2\text{O}_3-\text{SiO}_2$ system can be easily obtained by the addition of ZrO_2 and TiO_2 (Petzoldt, 1963; Beall, 1967; Müller, 1972; Tashiro et al., 1976). By improving the transparency and other characteristics by optimization of the composition and the conditions of the heat treatment for crystallization through many basic studies on nucleation and crystal growth (Nakagawa, 1972; Riello and Hopfe, 2001; Dymshits, 2005), the application of the transparent glass-ceramics has become widespread, such as in electronic and optical devices, production equipment, and home and cooking appliances.

However, the transparent glass-ceramics have an undesirable brown color owing to Fe ions as a contaminant, whereas the mother glass normally has a clear appearance. This coloration, which occurs through the crystallization process, causes two problems for industry. One is that it prevents further expansion of the market for fire-rated windows due to the mismatch in appearance with normal bluish windows of soda lime silicate glass. The other is that it is difficult to avoid the use of toxic arsenic oxide and/or antimony oxide as a fining agent because the non-toxic alternative of tin oxide cannot be used on account of its enhancement of the coloration (Nakane and Kawamoto, 2015). It is therefore necessary to determine the coloration mechanism to develop environmentally friendly glass-ceramics with high transparency.

Many investigations have been conducted on Fe coloration in various glass systems from the viewpoints of changes in the valence and coordination number and the formation of clusters (Traverse et al., 1992; Ehrt et al., 2001; Schutz et al., 2004). It is well known that optical absorption spectra of Fe ions can be changed and shifted easily by adjusting the composition and melting conditions because the d-d transition in the outermost electron orbital is sensitive to the surrounding environment. This means that there are various possible explanations for the coloration mechanism. Furthermore, in the case of glass-ceramics, the effects of changes in the phase and composition in the microstructure upon crystallization should be considered to elucidate the coloration-appearance phenomena through the crystallization process. Although many previous works have provided various insights, it is difficult to directly specify the coloration mechanism in glass-ceramics from the literature.

The objective of the present investigation is to elucidate the mechanism of the strong brown coloration caused by Fe ions in transparent β -quartz s.s. glass-ceramics in $\text{Li}_2\text{O}-\text{Al}_2\text{O}_3-\text{SiO}_2$ system. We determine the phase of the coloration and the key component responsible for the coloration. In addition, the relationship between the optical absorption and the valence and coordination state of Fe ions in the glass-ceramics is discussed on the basis of the results of Fe K-edge and Ti K-edge X-ray absorption near-edge structure (XANES) measurements and first-principles calculation.

EXPERIMENTAL

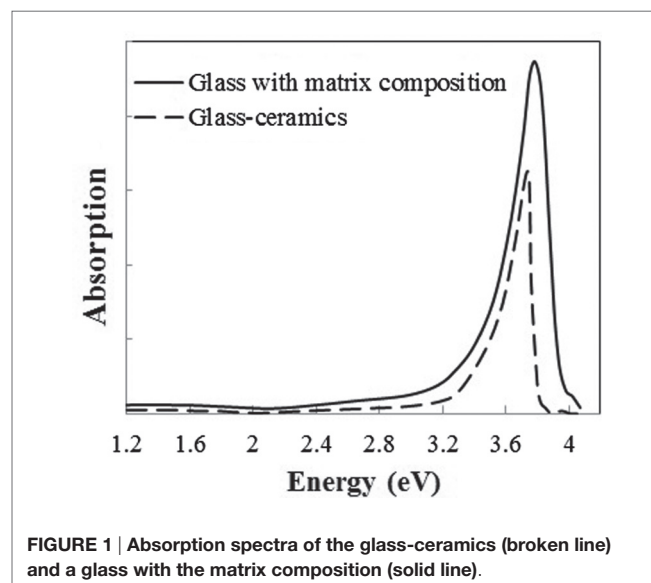
The specimens investigated in this study had a chemical composition (in mass percent) of 66 SiO_2 , 23 Al_2O_3 , 4 Li_2O , 2 TiO_2 , 2 ZrO_2 , and small amounts of Na_2O , K_2O , MgO , BaO , and P_2O_5 . Also, 0.03% of Fe_2O_3 was included as a contaminant. Mixture of raw materials was melted at 1,650°C for 20 h in air atmosphere, and then the melt were quenched with a metal roller. The obtained mother glass, which had a clear appearance, was crystallized in an electric furnace with a nucleation temperature of 780°C and a maximum temperature of 900°C. The heat-treatment times were 3 h at the nucleation stage and 1 h at the maximum temperature. After crystallization, the microstructure was observed using a scanning electron microscope to determine the crystallinity (SU8220, Hitachi). An X-ray diffractometer (RINT2000/PC, Rigaku) was used to analyze the crystalline phase. Optical

absorption was measured by a double-beam photospectrometer (UV-3100PC, Shimadzu). XANES measurement at the Fe K-edge (from 7,110 to 7,200 eV) and Ti K-edge (from 4,950 to 5,050 eV) was performed at beamline 24 of SPring8 in Hyogo Prefecture, Japan.

X-ray energy was monochromatized using a four-crystal of Si(111) and Si(400) in an anti-parallel setting (Galoisy et al., 2001).

RESULTS AND DISCUSSION

The broken line shown in **Figure 1** is the absorption spectrum for the sample after crystallization. A wide range of absorption from 2 to 3.5 eV, resulting in the brown color, and a strong peak at about 4 eV in the UV region were observed. According to the results of XRD, the sample mainly consisted of β -quartz s.s. (JCPDS 01-073-2336) and remained glass matrix phase. To specify which phase exhibits optical absorption, a glass with a composition identical to that of the glass matrix was prepared, and its optical absorption was measured. The glass matrix was assumed to have the following properties: the crystallinity was 75%, analyzed from the total area and the grain size of the precipitated crystal determined by SEM observation. The crystal composition was $\text{Li}_2\text{O}-\text{Al}_2\text{O}_3-6\text{SiO}_2$, estimated from the (406) peak position in the XRD pattern (Iwatsuki et al., 1974). The ratio of precipitated TiO_2 and ZrO_2 was 60%, quoted from the literature (Riello and Hopfe, 2001). All the Fe_2O_3 was assumed to remain in the glass phase. **Figure 1** shows the optical absorption spectrum of the glass with the matrix composition, which is almost identical to that of the glass-ceramics having a broad peak in the visible region and one sharp peak in the UV region, although there are slight differences in the peak position and shape, considered to be due to the deviation in the composition from the rough assumption. The absorption intensity in the visible region per Fe_2O_3 unit concentration was approximately 1.5 times larger than that of the glass-ceramics. This may indicate



that Fe content in the glass matrix phase was overestimated since some of the Fe ions precipitated to the crystal phase. However, no other absorption peak was observed in the spectrum of the glass-ceramics; therefore, it is concluded that most of the Fe ions remained in the glass matrix phase, resulting in the brown color of the glass-ceramics.

To determine which component in the glass matrix is responsible for the Fe ion coloration, the optical absorption spectra of various compositions, where the amount of only one component (Si, Al, Li, Ti, Zr, Na, K, or Ba) was changed from that in the above estimated matrix glass composition, were measured. Shown in **Figure 2** are the appearances of the Ti-containing and Ti-free glasses. In the case of the Ti-free glass, the coloration disappeared, while all the other glasses containing Ti had a brown color. **Figure 3** shows the optical absorption spectra of the Fe ions in the Ti-containing and Ti-free glasses, which were obtained by subtracting the Fe-free glass spectrum from the Fe-containing glass spectrum to eliminate the absorption from other components. The spectrum of the Ti-containing glass has a broad absorption

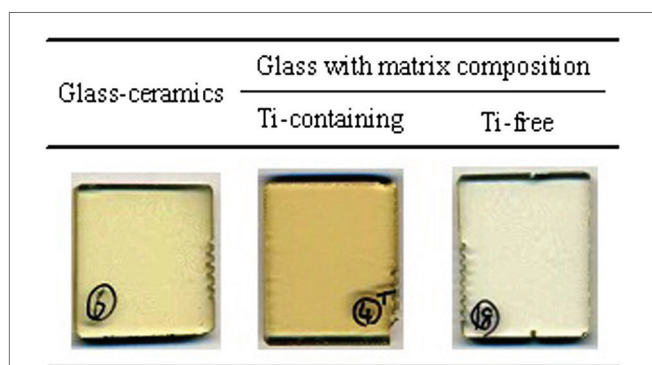


FIGURE 2 | Appearance of the glass-ceramics and Ti-containing and Ti-free glasses with the matrix glass composition.

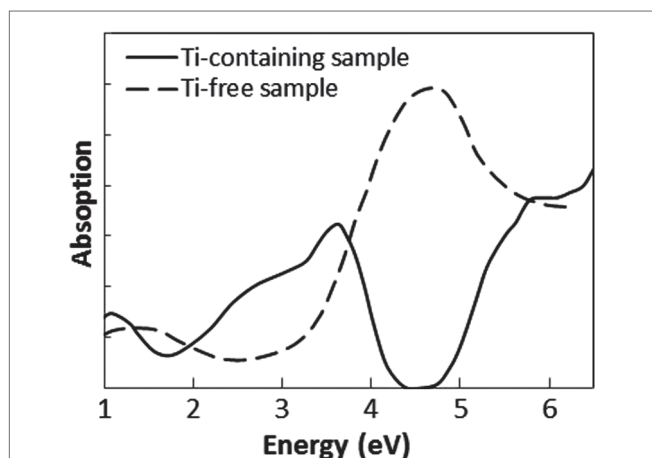


FIGURE 3 | Absorption spectra of Fe ion in Ti-containing and Ti-free glasses. These spectra were obtained by subtracting the spectrum of Fe-free glass from that of Fe-containing glass.

peak in the visible region from approximately 2 to 4 eV, whereas no peak in the visible region can be observed for the Ti-free glass. The amounts of Fe and Ti ions in the glass matrix were estimated to increase from 0.03 to 0.1% in the form of Fe_2O_3 and from 2 to 3% in the form of TiO_2 on the basis of the above. We speculate that the concentrations and the coexistence of Fe and Ti ions in the glass matrix phase may give the strong brown coloration in the glass-ceramics. Some previous works have mentioned a brown coloration due to the coexistence of Fe and Ti ions (Weyl, 1951). Weyl speculated that the coloration is caused by a change in the coordination number of Fe^{3+} from 6 to 4 due to the existence of Ti ions, but this was not sufficiently supported by experimental results. To determine the valence and coordination number in the Ti-containing and Ti-free glasses, XANES spectra at the Fe K-edge were measured. The other samples measured for reference were crystalline compounds of FeO and Fe_2O_3 . **Figure 4** shows the Fe-XANES spectra. The position of the XANES edge indicates the valence of the ions, in which the redox ratio is reflected in its position on the energy scale: 7,118 eV for Fe^{3+} in Fe_2O_3 and 7,114 eV for Fe^{2+} in FeO. The positions for both glasses were almost the same, 7,116 eV, which is almost halfway between those of the two minerals. The results clearly indicate that both Fe^{2+} and Fe^{3+} existed in the glasses, and that the ratio of the two ions did not change significantly with the existence or non-existence of Ti ions. **Figure 5** shows the pre-edge peak of Fe ions in the glasses around 7,110–7,120 eV. The pre-edge peak originated from a forbidden electron transition, which is partly allowed by making a hybrid orbital with p-electron, is affected by the coordination number. The pre-edge was extracted by fitting two Gaussian functions to the contribution of the main edge to the pre-edge feature. The peaks for both samples are made up of at least two peaks. Wilke et al. (2001) reported that four-coordinated Fe^{2+} and Fe^{3+} have two and one contributions, and six-coordinated Fe^{2+} and Fe^{3+} have two and three contributions, respectively. However, in this case, the coordination numbers of Fe^{2+} and Fe^{3+} in the samples could not be determined because of the insufficient S/N ratio to conduct peak separation owing to the small amount of Fe ions in the glass. Comparing the spectra of the two samples, no significant differences in the height and shape were detected.

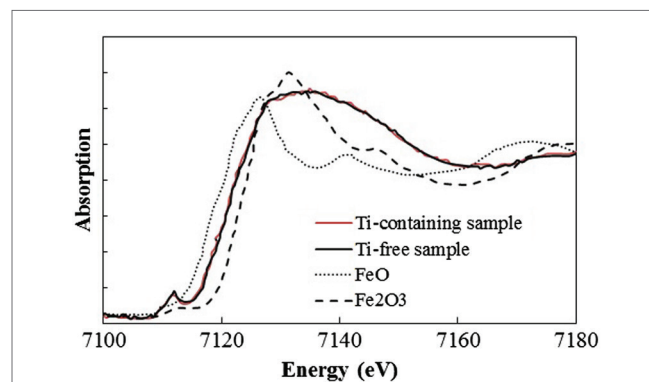


FIGURE 4 | Fe K-edge X-ray absorption near-edge structure spectra of Ti-containing and Ti-free glasses.

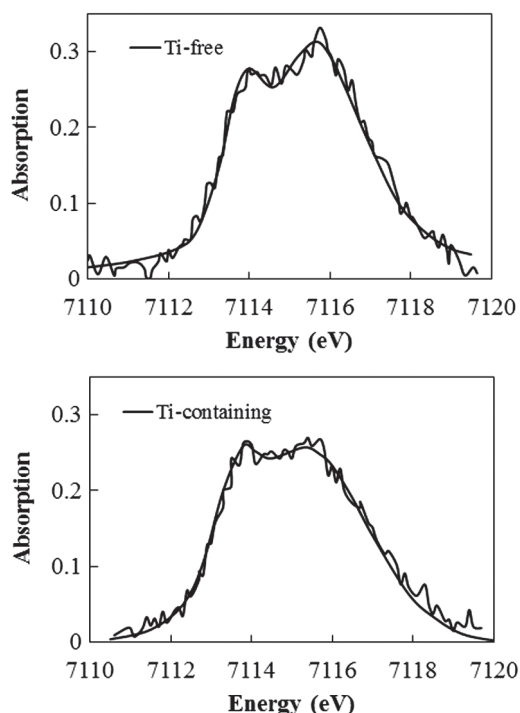


FIGURE 5 | Fe K-edge X-ray absorption near-edge structure spectrum in pre-edge region of Ti-containing and Ti-free glasses.

Wilke et al. (2005) suggested that the peak intensity significantly changes with the coordination number, with the peak intensity of a four-coordinated Fe ion being more than four times larger than that of a six-coordinated Fe ion. Their work indicates that the coordination number of the Fe ions in our samples is not changed by the coexistence of Ti ions. The peak position was shifted slightly to the lower-energy side by less than 0.3 eV with the coexistence of Ti ions. This shift may be a consequence of a very small decrease in the valence (Wilke et al., 2005).

In addition to the coloration from Fe ions, another past work showed that Ti^{3+} – Ti^{4+} mixed complexes cause a brown coloration (Bausa et al., 1991). To determine the valence of the Ti ions in our Ti-containing glass, the XANES spectra were measured at the Ti K-edge. The other samples measured for reference were crystalline Ti_2O_3 and TiO_2 . **Figure 6** shows the Ti–XANES spectra. The positions of the XANES edge indicating the valence are 4,972 eV for Ti^{3+} in Ti_2O_3 and 4,977 eV for Ti^{4+} in TiO_2 . The position in our glass is almost identical to that for Ti^{4+} in TiO_2 , where the existence of a certain amount of Ti^{3+} could not be confirmed. Similar results were reported for silicate glass systems prepared under normal melting conditions in a previous work (Schutz et al., 2004). In addition, we prepared Fe-free glass with the same composition to investigate the coloration by Ti ions, and it had a clear appearance without the strong brown coloration. These results indicate that Ti^{3+} – Ti^{4+} , which has an absorption band in the visible region, hardly exists in our glasses.

A first-principles calculation of the absorption of an Fe ion was conducted to clarify how Ti^{4+} ion affect the optical absorption of

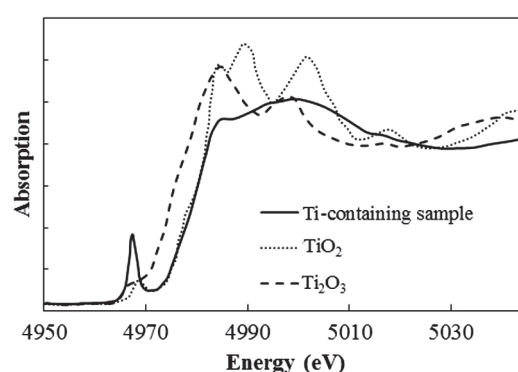


FIGURE 6 | Ti K-edge X-ray absorption near-edge structure spectra of Ti-containing glass.

Fe ions in the case of no changes in the valence and coordination conditions. The absorption spectra for Fe ions were obtained by the DV-ME method, which can be used to calculate absorption spectra while considering the d–d transition (Ogasawara et al., 1998). **Figure 7** shows the structure model used for the calculation, where a four-coordinated Fe^{3+} ion in the normal state in silicate glass (Schutz et al., 2004) is placed at the center of a SiO_4 tetrahedron, in which the bonding length of Si–O is 0.16 nm, obtained from CR912569 crystal code, and the Fe–O length is 0.18 nm from CR910311. To evaluate the effect of Ti, one Si^{4+} is substituted by Ti^{4+} at the second-nearest position from the Fe ion. **Figure 8** shows the calculated absorption spectra. Upon the substitution of the Ti ion, the absorption peak of the Fe ion from the d–d transition shifted to the lower-energy side that had qualitative agreement with the experimental results shown in **Figure 3**. This feature is caused by a change in the symmetry of the d-electron orbital in the Fe ion owing to the existence of a d-electron orbital in the Ti ion at the second-nearest position, even though the valence and coordination number are unchanged. Although this calculation does not have enough sufficient to give a definitive conclusion because of the oversimplified structure and components in the model, we tentatively conclude that the coloration is due to the formation of Fe–O–Ti in the glass matrix phase.

CONCLUSION

In this present work, the mechanism of the brown coloration of transparent β -quartz s.s. glass-ceramics in Li_2O – Al_2O_3 – SiO_2 system by Fe ions has been investigated. The preparation and evaluation of a glass with a composition identical to that of the glass matrix indicated that the concentration and coexistence of Fe and Ti ions in a glass matrix phase are the cause of the coloration. On the basis of this result, Nippon Electric Glass have developed and started to produce environmentally friendly glass-ceramics with high transparency (Nakane and Kawamoto, 2015). We hope that this finding will help understand the brown coloration in other glass-ceramics with TiO_2 in present applications including dental materials like lithium disilicate glass-ceramics where appearance is important. This study highlights the importance of the

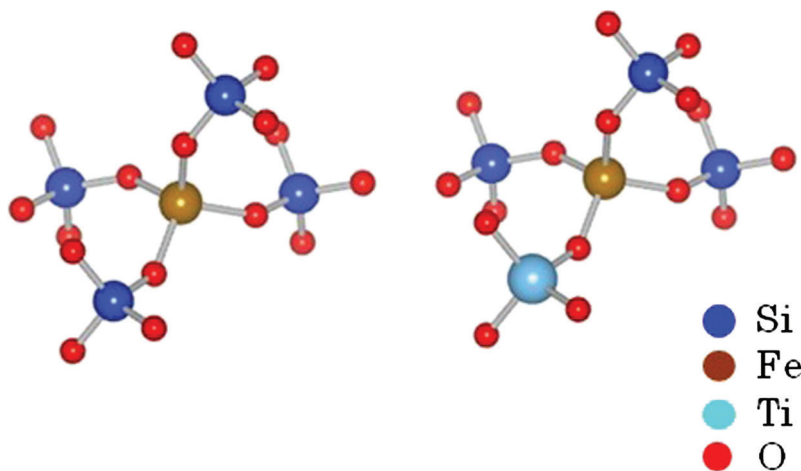


FIGURE 7 | Structure model for calculation of Fe ion absorption spectra.

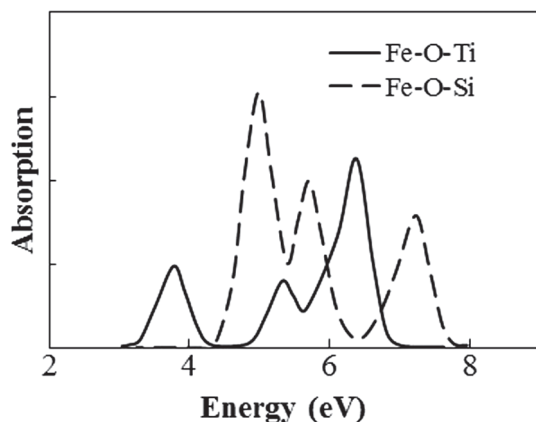


FIGURE 8 | Calculated absorption spectra of Fe ion with and without Ti at second-nearest ion position.

characteristics of the glass matrix phase in the development and improvement of various glass-ceramics for future applications.

AUTHOR CONTRIBUTIONS

SN: conception and design of the study, analysis and interpretation of data, collection and assembly of data, and drafting of the article. KK: conception and design of the study, analysis and interpretation of data, and collection and assembly of data.

ACKNOWLEDGMENTS

The authors thank Dr. Okajima of SAGA Light Source, Dr. Umesaki of Osaka University, and Dr. Matsui and Dr. Yokoyama of Hyogo Science and Technology Association for the measurement and analysis of the XANES spectra and for support in the first-principles calculation.

REFERENCES

- Bausa, L., Sole, J., Duran, A., and Navarro, J. (1991). Characterization of titanium induced optical absorption bands in phosphate glasses. *J. Non Cryst. Solids* 127, 267–272. doi:10.1016/0022-3093(91)90479-P
- Beall, G. (1967). Crystallization and chemical strength of stuffed β -quartz glass-ceramics. *J. Am. Ceram. Soc.* 50, 181–190. doi:10.1111/j.1151-2916.1967.tb15077.x
- Bhattacharyya, S., Höche, T., Jinschek, J. R., Avramov, I., Wurth, R., Müller, M., et al. (2010). Direct evidence of Al-rich layers around nanosized ZrTiO_4 in glass: putting the role of nucleation agents in perspective. *Cryst. Growth Des.* 10, 379–385. doi:10.1021/cg9009898
- Doherty, P. D. (1967). Direct observation of the crystallization of $\text{Li}_2\text{O}-\text{Al}_2\text{O}_3-\text{SiO}_2$ glasses containing TiO_2 . *J. Am. Ceram. Soc.* 50, 77–80. doi:10.1111/j.1151-2916.1967.tb15043.x
- Dymshits, O. (2005). Liquid phase separation and crystallization in CoO doped glasses of the $\text{Li}_2\text{O}-\text{Al}_2\text{O}_3-\text{SiO}_2-\text{TiO}_2$ system. *Phys. Chem. Glasses* 46, 227–231.
- Ehrt, D., Leister, M., and Matthai, A. (2001). Polyvalent elements iron, tin and titanium in silicate, phosphate and fluoride glasses and melts. *Phys. Chem. Glasses* 42, 231–239.
- Galoisy, L., Calas, G., and Arrio, M. A. (2001). High-resolution XANES spectra of iron in minerals and glasses: structural information from the pre-edge region. *Chem. Geol.* 174, 307–319. doi:10.1016/S0009-2541(00)00322-3
- Iwatsuki, M., Tanaka, M., and Fukasawa, T. (1974). Analysis of β -eucryptite solid solution in glass-ceramics by lattice constant method [in Japanese]. *Nippon Kagaku Kaishi* 1974, 505–510. doi:10.1246/nikkashi.1974.505
- Müller, G. (1972). Zur Wirkungsweise von Gemischen oxidischer Keimbildner in GlasKeramiken des Hochquarz-Mischkristalltyps glass-ceramics catalyzed with zirconia. *Glasstech. Ber.* 45, 189–194.
- Nakagawa, K. (1972). Metastable phase separation and crystallization of $\text{Li}_2\text{O}-\text{Al}_2\text{O}_3-\text{SiO}_2$ glasses. *J. Non Cryst. Solids* 7, 168–180. doi:10.1016/0022-3093(72)90287-6
- Nakane, S., and Kawamoto, K. (2015). *Li₂O-Al₂O₃-SiO₂ Glass-Ceramics*. U. S. patent 9126859.
- Ogasawara, K., Ishii, T., Ito, Y., Ida, H., Tanaka, I., and Adachi, H. (1998). Analysis of covalent effects on the multiplet structure of ruby based on first-principles cluster calculations. *Jpn. J. Appl. Phys.* 37, 4590–4594. doi:10.1143/JJAP.37.4590
- Petzoldt, J. (1963). Metastabile mischkristalle mit quarzstruktur im oxidsystem $\text{Li}_2\text{O}-\text{MgO}-\text{ZnO}-\text{Al}_2\text{O}_3-\text{SiO}_2$. *Glasstech. Ber.* 40, 385–396.

- Riello, P., and Hopfe, S. (2001). Nucleation and crystallization behavior of glass-ceramic materials in the $\text{Li}_2\text{O}-\text{Al}_2\text{O}_3-\text{SiO}_2$ system of interest for their transparency properties. *J. Non Cryst. Solids* 288, 127–139. doi:10.1016/S0022-3093(01)00518-X
- Sakamoto, S., and Yamamoto, S. (2010). Glass-ceramics: engineering principles and applications. *Int. J. Appl. Glass Sci.* 1, 237–247. doi:10.1111/j.2041-1294.2010.00027.x
- Schutz, A., Ehrt, D., Dubiel, M., Yang, X., Mosei, B., and Eckert, H. (2004). A multi-method characterization of borosilicate glasses doped with 1 up to 10 mol% of Fe, Ti and Sb. *Glass Sci. Technol.* 77, 295–305.
- Stookey, S. D. (1960). *Method of Making Ceramics and Product Thereof*. U. S. patent 2920971.
- Tashiro, M., Takagi, K., Wada, M., and Tanaka, K. (1976). *Glass-Ceramics*. Japanese patent 450729.
- Tashiro, M., and Wada, M. (1963). “Glass-ceramics catalyzed with zirconia,” in *Proceedings of the 6th International Congress on Glass* (Washington, DC), 18.
- Traverse, J. P., Toganidis, T., and Ades, C. (1992). Spectrophotometric analysis of ferrous, ferric and total iron content in soda-lime silica glass. *Glastech. Ber.* 65, 201–206.
- Weyl, W. (ed.). (1951). “The colours produced by titanium, tungsten and molybdenum,” in *Coloured Glasses* (Society of Glass Technology), 212–216.
- Wilke, M., Farges, F., Petit, P. E., Brown, G. E., and Martin, F. (2001). Oxidation state and coordination of Fe in minerals: an Fe K-XANES spectroscopic study. *Am. Mineral.* 86, 714–730. doi:10.2138/am-2001-5-612
- Wilke, M., Partzsch, M. G., Bernhardt, R., and Lattard, D. (2005). Determination of the iron oxidation state in basaltic glasses using XANES at the K-edge. *Chem. Geol.* 220, 143–161. doi:10.1016/j.chemgeo.2005.03.004

Conflict of Interest Statement: The authors declare that the research was conducted in the absence of any commercial or financial relationships that could be construed as a potential conflict of interest.

The reviewer CR and handling editor declared their shared affiliation, and the handling editor states that the process nevertheless met the standards of a fair and objective review.

Copyright © 2017 Nakane and Kawamoto. This is an open-access article distributed under the terms of the Creative Commons Attribution License (CC BY). The use, distribution or reproduction in other forums is permitted, provided the original author(s) or licensor are credited and that the original publication in this journal is cited, in accordance with accepted academic practice. No use, distribution or reproduction is permitted which does not comply with these terms.



Sintering and Foaming of Barium Silicate Glass Powder Compacts

Boris Agea-Blanco^{1,2}, Stefan Reinsch¹ and Ralf Müller^{1*}

¹ Division 5.6 "Glass", Federal Institute for Materials Research and Testing (BAM), Berlin, Germany, ² IQS School of Engineering, Barcelona, Spain

OPEN ACCESS

Edited by:

Wolfram Höland,
Ivoclar Vivadent, Liechtenstein

Reviewed by:

Sylwester Janusz Rzoska,
Institute of High Pressure Physics
(PAN), Poland
John Ballato,
Clemson University, USA

*Correspondence:

Ralf Müller
ralf.mueller@bam.de

Specialty section:

This article was submitted to
Glass Science,
a section of the journal
Frontiers in Materials

Received: 15 June 2016

Accepted: 22 September 2016

Published: 07 October 2016

Citation:

Agea-Blanco B, Reinsch S and
Müller R (2016) Sintering and
Foaming of Barium Silicate Glass
Powder Compacts.
Front. Mater. 3:45.
doi: 10.3389/fmats.2016.00045

The manufacture of sintered glasses and glass-ceramics, glass matrix composites, and glass-bonded ceramics or pastes is often affected by gas bubble formation. Against this background, we studied sintering and foaming of barium silicate glass powders used as SOFC sealants using different powder milling procedures. Sintering was measured by means of heating microscopy backed up by XPD, differential thermal analysis, vacuum hot extraction (VHE), and optical and electron microscopy. Foaming increased significantly as milling progressed. For moderately milled glass powders, subsequent storage in air could also promote foaming. Although the powder compacts were uniaxially pressed and sintered in air, the milling atmosphere significantly affected foaming. The strength of this effect increased in the order $\text{Ar} \approx \text{N}_2 < \text{air} < \text{CO}_2$. Conformingly, VHE studies revealed that the pores of foamed samples predominantly encapsulated CO_2 , even for powders milled in Ar and N_2 . Results of this study thus indicate that foaming is caused by carbonaceous species trapped on the glass powder surface. Foaming could be substantially reduced by milling in water and 10 wt% HCl.

Keywords: glass powder sintering, milling, foaming, degassing, SOFC

INTRODUCTION

Glass powders are widely used in fabricating sintered glass, sintered glass-ceramics, glass matrix composites, and glass-bonded ceramics or pastes when lower fabrication or processing temperatures, gas-tight seals, or complex shapes are required (Rabinovich, 1985; Schiller et al., 2008; Müller and Reinsch, 2012). One problem often addressed within this context is concurrent crystallization and sintering (Müller, 1994; German, 1996; Prado and Zanotto, 2002; Pascual and Duran, 2003; Prado et al., 2003a,b, 2008). This effect is most pronounced in sintered glass-ceramics, where a large crystal fraction is desired and rapid crystallization starts from the powder surface (Müller and Reinsch, 2012).

Many practical applications of sintered glass-ceramics, however, rely on slowly crystallizing glasses. Such glasses are, for instance, used for low temperature co-fired ceramics (Imanaka, 2005), paste glasses (Hwang et al., 2002), or SOFC sealants (Fergus, 2005; Gross et al., 2005). In the case of slow crystallization, however, another problem may arise. Due to the low glass viscosity required for joining and gas-tight sealing or obtaining a desired crystallinity, gas bubble formation, and related sample swelling ("foaming") often occur, even when organic aids are not used in powder processing.

Thus, Lucchini et al. (1983) observed an increased bubble formation with increasing glass volume fraction for sodium and calcium lead silicate glass-bonded barium hexaferrites and attributed this effect to glass volatilization. Pore formation was also observed in porcelain stoneware tiles (Leonelli et al., 2001) and lead borosilicate glass frits (Hwang et al., 2002). In the latter case, effusing oxygen

or water, physically or chemically adsorbed to the glass powder surface during manufacturing and storage, has been supposed to be potential foaming sources. However, neither dry quenching of the molten glass nor using vacuum-dried B_2O_3 for glass melting could reduce foaming. Lara et al. (2004) observed foaming during sintering and crystallization treatments of Ca, Mg, and Zn aluminosilicate glass powders for SOFC sealing to be most pronounced in Ca aluminosilicate glass powders (up to 30% silhouette area increase in heating microscopy experiments). The authors discussed the formation of crystals of lower density and/or gas evolution during crystallization for causing the observed foaming. More recently, foaming was mainly attributed to pore coalescence during over-firing (Lim et al., 2006), obviously assuming an encapsulated sintering atmosphere as the major foaming source. Due to the decreased sintering pressure of larger pores, less gas is forced to dissolve into the glass melt, and low viscosity allows easy bubble growth. An analogous explanation was given by Kim et al. (2007) for foaming of lead-free Bi_2O_3 – B_2O_3 – SiO_2 solder glass powders and by Müller et al. (2009) for LTCC model glass powders. Undesired porosity was also observed during sintering ashes for porcelain tile production, which was attributed to “some boiling and trapped gas effects” (Fernandes and Ferreira, 2007).

The aim of this paper was to study the effect of glass powder milling on foaming of barium disilicate glass powder compacts. The glass powders under study have been dry-milled for different times in different atmospheres, including argon, nitrogen, air, and carbon dioxide, or wet-milled in water and 10 wt% HCl, uniaxially pressed and sintered in air. Densification and foaming was studied by means of heating microscopy backed up by XRD, Differential thermal analysis (DTA), vacuum hot extraction (VHE), and microscopy.

EXPERIMENTAL

Materials

The present study was undertaken on a commercial barium disilicate glass with minor additions of B_2O_3 , Al_2O_3 , and ZnO used for SOFC sealing (Kerafol, 2010). The maximum particle size of the as-received commercial glass frit was limited to <2 mm by manual crushing in a metal mortar and sieving.

In order to reach an appropriate offset particle size for the milling experiments, *pre-milling* was performed in air using a planetary ball mill (Fritsch Pulverisette 5, Fritsch, Idar-Oberstein, Germany) loaded with two 500-ml corundum jars ($\varnothing_{in} \approx 102$ mm, $h = 78$ mm). Each jar was filled with six corundum balls ($\varnothing \approx 20$ mm) and about 250 g of the glass frit. Milling was done for 15 min at 320 rpm (maximum speed of supporting disk) (FRITSCH GmbH, 1987). No milling aids were used. Afterwards, a mechanical sieve (Analysette 3 PRO, Fritsch, Idar-Oberstein, Germany) was used to reduce the particle size distribution to 40–250 μ m (“p0” in Table 1).

Milling was performed in a planetary ball mill equipped with two 25-ml corundum grinding jars ($\varnothing_{in} \approx 33$ mm, $h = 45$ mm; Planetary micro mill Pulverisette 7, Fritsch, Idar-Oberstein, Germany) (FRITSCH GmbH, 1995). The jars were filled with four corundum balls ($\varnothing \approx 12$ mm) and ≈ 8 g of glass powder. In

TABLE 1 | Particle size of glass powders after different milling (p0: pre-milled).

Powder	Milling time (min)	Atmosphere	Milling aid	D_{10} (μ m)	D_{50} (μ m)	D_{90} (μ m)	D_{97} (μ m)
p0	–	Air	–	3	41	140	210
p1	5	Air	–	2	25	72	99
p2	10	Air	–	1	13	47	67
p3	15	Air	–	1	8	33	47
p4	2 × 15	Air	–	1	4	20	33
p5	3 × 15	Air	–	1	4	19	31
p6	4 × 15	Air	–	1	4	25	39
p7	15	Air	–	1	11	40	58
p8	15	CO ₂	–	1	12	37	53
p9	15	N ₂	–	2	14	42	61
p10	15	Ar	–	1	13	40	58
p11	15	Air	–	1	11	73	108
p12	4 × 15	CO ₂	–	1	7	25	37
p13	–	Air	–	18	223	538	688
p14	30	Air	–	1	6	32	62
p15	30	Air	H ₂ O	1	5	15	22
p16	30	Air	10 wt% HCl	1	9	22	30

order to provide a controlled milling atmosphere within these grinding jars, special ring seals were used. These rings were made of steel equipped with top and bottom silicone seals and a gas inlet capillary, which could be closed by a shuttle valve mounted on top of the rotating jar holder.

Milling progress was studied in air starting from glass powder p0 (Table 1). Glass powders were milled for 5–60 min at 766 rpm (maximum speed of supporting disk) (FRITSCH GmbH, 1995). Milling was temporarily stopped for 30 min after 15 min of milling to prevent overheating. Starting with a large decrease of D_{50} during the first milling stage, the decrease in particle size progressively slowed down to level out at ≈ 4 μ m. At 60-min dry-milling, slightly increased D_{90} and D_{97} values indicate progressive particle agglomeration (p1–p6).

Milling in controlled atmospheres (p7–p10) was carried out for 15 min also at 766 rpm (FRITSCH GmbH, 1995). In this case, the sealed milling jars were evacuated to <20 mbar and re-filled with CO₂, N₂, and Ar (99.99% purity, Air Liquide™, Germany) to 10⁵ Pa (1 bar). Evacuation and re-filling was repeated five times to minimize the amount of residual air. A liquid nitrogen trap was used to increase N₂ purity. For studying the effect of powder storage in air after milling, the glass frit was crushed to <1000 μ m (Jaw Crusher, Retsch BB51), sieved to 200–1000 μ m, and milled in air (p11) and CO₂ (p12) as described.

Wet-milling started from a glass frit crushed using the same jaw-crusher: about 400 g of starting glass frit was repeatedly crushed using a gap width decreasing from 1000 to 200 μ m in 200- μ m steps. The last crushing step (200 μ m gap width) was repeated three times (p13). Milling jars were filled with 8 g of this powder (p13) and milled for 30 min as for milling in controlled atmospheres. For powder p14, dry-milling was carried out in ambient air as a reference. Powders p15 and p16 were wet-milled in 8-g pure water and 10 wt% HCl (diluted from fuming HCl 37 wt%, Merck, Germany), respectively. Pure water was supplied by a MilliQ® device (Merck, Germany). Wet-milled powders were dried for 2 days at 120°C in air before sintering.

For the study of *sintering* and microstructural evolution, cylindrical powder compacts were uniaxially pressed in air at 60 MPa (green dimensions: $\varnothing \approx 5$ mm, $h \approx 2$ mm, and $m \approx 0.1$ g) without organic aids. After milling, the powder was stored in a closed HDPE box for between 2 and 4 days before uniaxial pressing. During that time, no significant effect on sintering and foaming could be observed.

For the study of *gas release* from the powder surface and foamed porosity, powder compacts of cylindrical shape were uniaxially pressed at 105 MPa ($\varnothing \approx 5$ mm, $h \approx 1$ mm, and $m \approx 0.050$ g) without binders or other aids and then cut down using a scalpel to pieces of ≈ 9 –10 mg. These pieces had been stored in a HDPE container before being studied by VHE.

Methods

Glass viscosity, η_G , was measured by means of rotational concentric cylinder viscometry (VT550, Haake, Erlangen, Germany) for $\eta < 10^5$ Pa s. The glass transition temperature $T_g = 649 \pm 3^\circ\text{C}$ and the coefficient of thermal expansion $CTE_{25-400^\circ\text{C}} = 7.6 \times 10^{-6} \text{ K}^{-1}$ were determined with a horizontal dilatometer (402 E, Netzsch, Selb, Germany; bulk glass bars, 25 mm \times 5 mm \times 5 mm). The viscosity data obtained in pascal second and degree Celsius could be approximated with $\log \eta = -2.77 + 2644/(T - 480)$ within $\Delta \log \eta \approx \pm 0.02$ accuracy.

Glass density, $\rho_G = 3.61 \text{ g/cm}^3$, was measured from glass bars by means of Archimedes' principle. A Mastersizer 2000 (Malvern Instruments, Worcestershire, U.K.) was used for *particle size* measurement. Particle agglomeration was minimized by dispersing ≈ 10 mg of glass powder in a 0.003M $\text{Na}_4\text{P}_2\text{O}_7$ solution and subsequent ultra-sonic treatments (1–5 min). The *bulk density* of green and sintered specimens was obtained from their sample geometry (heating microscope) and weight.

The *microstructure* of powder compacts heated to selected temperatures and quenched in air was studied from polished cross-sections by means of environmental scanning electron microscopy (ESEM-FEG, Philips-XL30, Eindhoven, Netherlands) or by an optical microscope (JENAPOL, Carl Zeiss Jena, Jena, Germany). Green powder compacts were embedded in synthetic resin for preparing cross-sections. Porosity was measured by image analysis of optical micrographs using the software Image C (Aqinto AG, Berlin, Germany).

Crystallization was studied by means of X-ray diffraction (Philips PW 1710, Eindhoven, Netherlands) using copper K_α with $\lambda = 1.5418 \text{ \AA}$, in Bragg–Brentano symmetry. Data were collected for $2\theta = 5$ – 80° in steps of $0.02^\circ/\text{s}$. Diffraction patterns were analyzed using EVA 15.1 software (Bruker-AXS, Karlsruhe, Germany) and compared to the JCPDS database (JCPDS, 2009, International Center for Diffraction Data). DTA–MS runs were performed in air at 5 K/min (15 K/min below 500°C) using ≈ 25 -mg pieces of powder compacts and Pt crucibles (TAG 24, Setaram, Caluire, France). The DTA device was coupled with a mass spectrometer (Balzers Quadstar 421, Balzers, Liechtenstein) by a heated (180°C) quartz glass capillary. In this way, evolved gases were simultaneously recorded in multiple ion detection (MID) modus.

Gas release from green and sintered powder compacts was studied by means of VHE with mass spectrometer evolved

gas detection (QMA4005, Balzers Instruments, Balzers, Liechtenstein). VHE analysis was performed in vacuum (10^{-4} – 10^{-5} mbar) during heating at 20 K/min using the MID mode (Müller et al., 2005).

Shrinkage of cylinder-shaped powder compacts during heating at 5 K/min ($< 500^\circ\text{C}$, 15 K/min) was examined using a heating microscope (Leitz, Wetzlar, Germany) with optical data acquisition (Hesse Prüftechnik, Osterode, Germany). Shrinkage and foaming are presented in terms of the silhouette area change, $s_A = \Delta A/A_0$, where A_0 is the initial sample silhouette area of the green compact.

RESULTS

Shrinkage and Foaming

Figure 1 shows the silhouette area change, s_A , for powders milled in air for different milling times (p1–p6). Sintering of the pre-milled powder (p0) starts at $\approx 710^\circ\text{C}$, and final densification is attained at $\approx 800^\circ\text{C}$. With increasing milling time, i.e., with decreasing particle size, the onset and saturation stage of sintering shift to a lower temperature by ≈ 20 and ≈ 30 K, respectively, while the attainable maximum densification tends to increase. Beyond maximum densification, progressive foaming is evident, which is strongly promoted by prolonged milling.

Figure 2 illustrates the shrinkage and foaming behavior of glass powders milled for 15 min in controlled atmospheres (p7–p10). Sintering starts at $\approx 700^\circ\text{C}$ for all powders and undergoes an initial deceleration at $\approx 760^\circ\text{C}$. The weak shrinkage between 760 and 800°C , best visible for the N_2 milled powder, might be caused by viscous settling of the sample to the substrate under the effect of gravity. Except for milling in CO_2 , the shrinkage maximum occurs at 800°C beyond which a progressive increase of s_A due to foaming occurs. This foaming is most pronounced for milling in CO_2 , where it already starts at $\approx 770^\circ\text{C}$. This finding gives clear evidence that foaming can be affected by the milling atmosphere and that CO_2 is most efficient in this context.

Figure 3 shows shrinkage and foaming of glass powders milled for 15 min in air (p11) and stored for different exposure

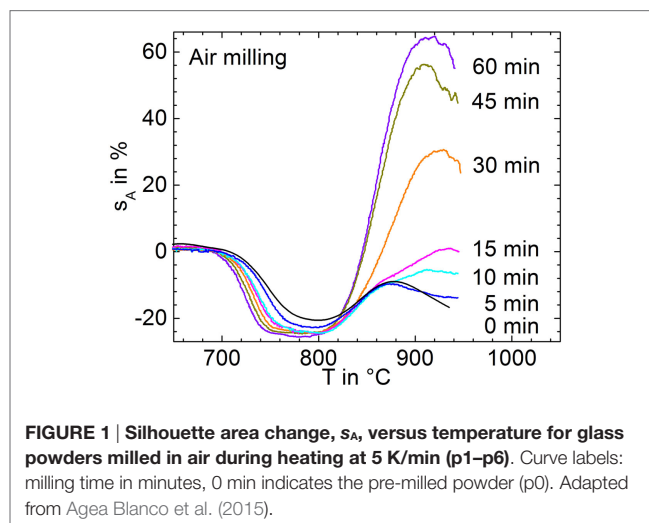


FIGURE 1 | Silhouette area change, s_A , versus temperature for glass powders milled in air during heating at 5 K/min (p1–p6). Curve labels: milling time in minutes, 0 min indicates the pre-milled powder (p0). Adapted from Agea Blanco et al. (2015).

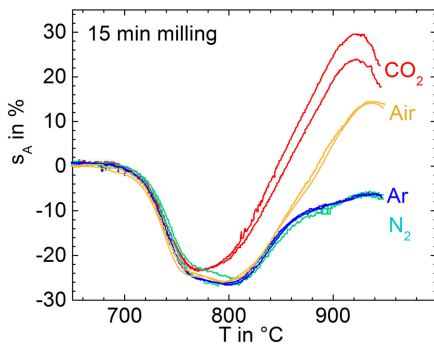


FIGURE 2 | Silhouette area change, s_A , versus temperature for glass powders milled for 15 min in different atmospheres (p7–p10) during heating at 5 K/min. Two experiments are shown for each condition in order to illustrate reproducibility. Adapted from Agea Blanco et al. (2015).

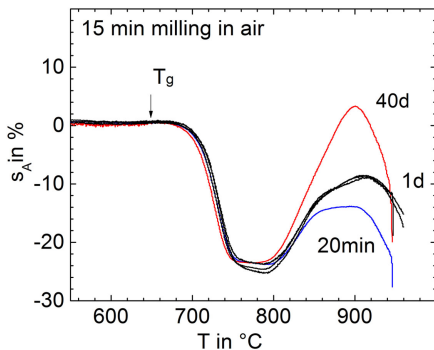


FIGURE 3 | Silhouette area change, s_A , versus temperature for glass powders milled for 15 min in air (p11) and subsequently stored in air for different times (curve labels) before sintering at 5 K/min. Arrow: $T_g = 649^\circ\text{C}$. Adapted from Agea Blanco et al. (2015).

time in air before uniaxial pressing and sintering. It is clearly seen that even short storage (1 day) substantially promoted foaming. This result indicates that gas uptake during storage in the ambient atmosphere can promote foaming.

Figure 4 illustrates the evolution of porosity during sintering for the powder milled for 15 min in N_2 . The minimum porosity occurs at 795°C , corresponding to a maximum densification stage in **Figure 2**. At 875°C , foaming is clearly detectable. The foaming maximum in **Figure 2** occurred at $\approx 940^\circ\text{C}$. Conformingly, the largest porosity in **Figure 4** is seen for the cross-section of the sample heated to 950 and 1000°C . No crystals could be observed even for the sample heated to 1000°C . Conformingly, X-ray diffraction patterns of the powder milled for 15 min in N_2 (p9), heated to 940°C , and quenched in air did not reveal the presence of crystalline phases (not shown).

Figure 5 illustrates the VHE–MS degassing behavior of green powder compacts milled for 15 min in different atmospheres. Below the onset of gas bubble bursting ($<800^\circ\text{C}$), water ($m/e = 18$) is the most prominent degassing species. Degassing of surface-adsorbed water occurs between 50 and 350°C , as previously seen for other silicate glass powders (Müller et al., 2005). This effect

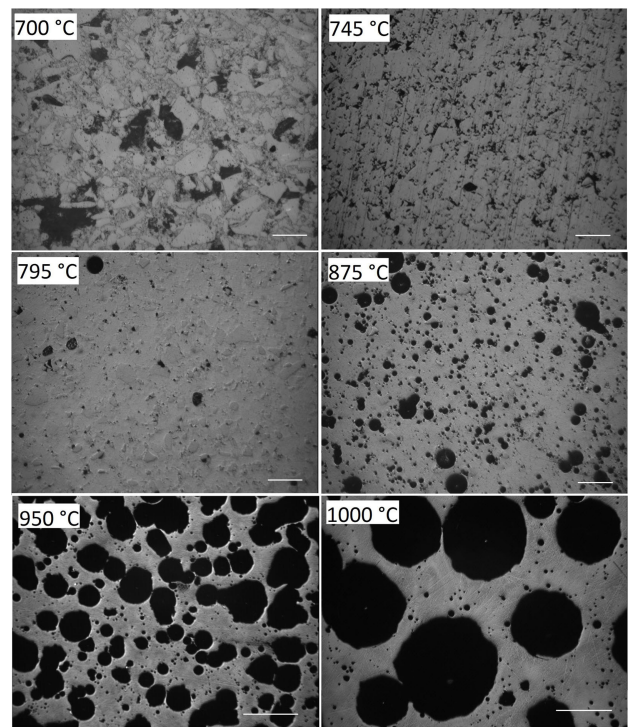


FIGURE 4 | Optical micrographs of powder compacts (15 min milling in N_2 , p9) heated at 5 K/min to the temperatures indicated and quenched in air. Diamond polished cross-sections. Bars = 100 μm (700– 875°C) and 500 μm (950, 1000°C). Porosity: 48% (700°C), 12% (745°C), 4% (795°C), 20% (875°C), 52% (950°C), and 53% (1000°C).

causes a broad weakly structured degassing peak, which is similar for all powders. The flat degassing curve between 400 and 600°C mainly reflects the VHE blank value of water. Water degassing is newly accelerated when the temperature approaches T_g (649°C , arrows) and then decreases due to sintering $>700^\circ\text{C}$, indicating that the water degassing mechanism is not exhausted but delayed by sintering. The second most intensive degassing below the onset of bubble bursting is that of CO_2 ($m/e = 44$) followed by CO ($m/e = 28$). The related mass number is probably not caused by N_2 because of the quite different degassing characteristics of N ($m/e = 14$).

During bubble bursting (spikes $>800^\circ\text{C}$), CO_2 is the dominant species followed by C ($m/e = 12$), which is expected to occur as a fragment of CO_2 . This finding indicates that CO_2 degassing is less exhausted below sintering than that of other volatiles. In contrast to CO_2 , Ar ($m/e = 40$) and N_2 ($m/e = 14$) did not significantly contribute to bubble bursting even for the powders milled in these atmospheres. The CO_2 -milled powder shows the most intensive CO_2 degassing during bubble bursting confirming the observed ordering of foaming activity in **Figure 2**. Conformingly, integrating the CO_2 ion currents ($m/e = 44$) for each of the 9-mg samples over the temperature range of foaming (800 – 1000°C) yields 6.0, 3.8, 3.1, 2.9, and $0.2 \mu\text{A min g}^{-1}$ for milling in CO_2 , Air, Ar, N_2 , and the pre-milled powder, respectively. Furthermore, bubble bursting starts at $\approx 800^\circ\text{C}$ ($\log \eta/\text{Pas} = 5.4$) when milled

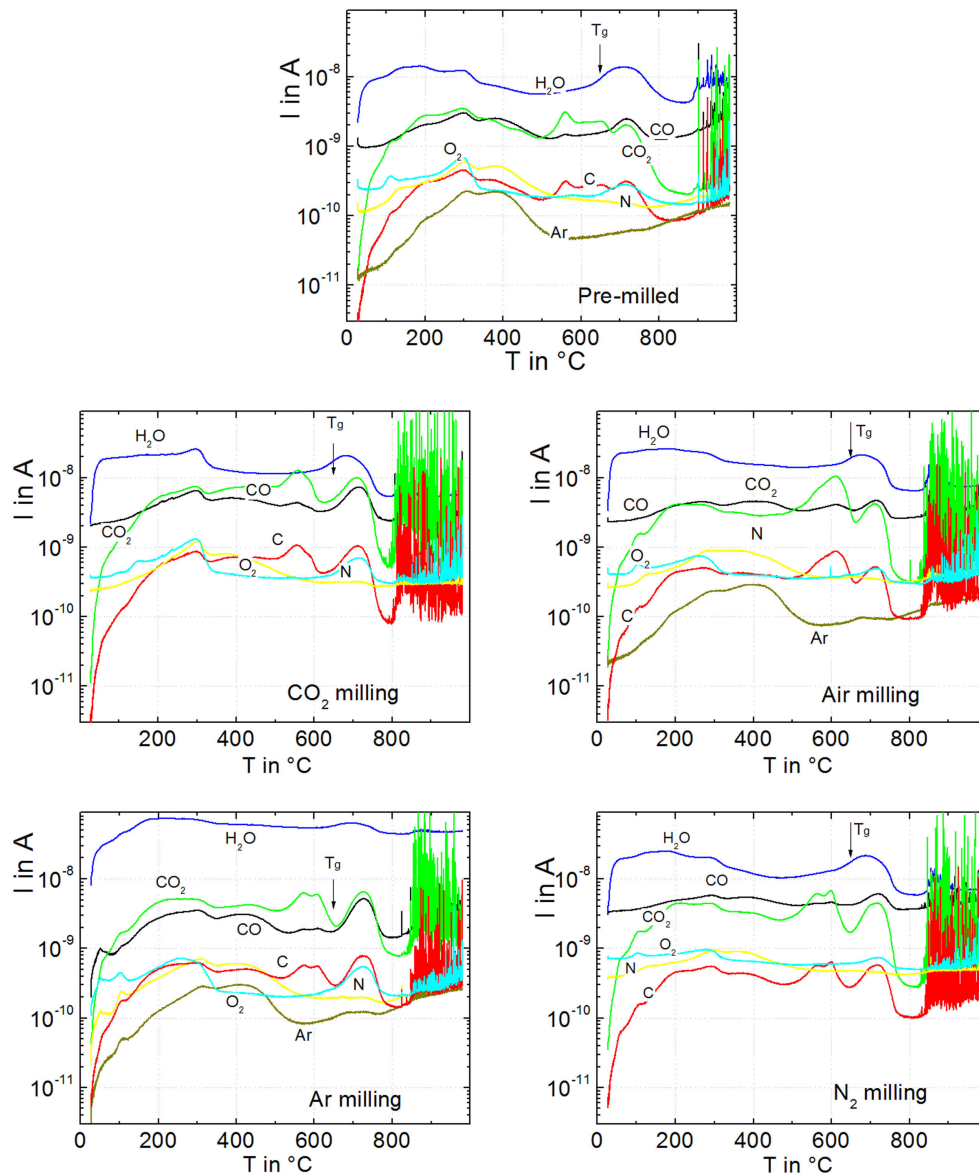


FIGURE 5 | Degassing of green powder compacts during heating at 20 K/min for pre-milling (p0), milling in air (p7), in CO₂ (p8), in N₂ (p9), and in Ar (p10). Degassing activity is presented in terms of respective ion currents, I , versus temperature, T . Sample mass: ≈ 9 mg. Arrows: $T_g = 649^\circ\text{C}$. Adapted from Agea Blanco et al. (2015).

in CO₂, while for milling in Ar, N₂, and air, bubble bursting starts at $\approx 840^\circ\text{C}$ ($\log \eta / \text{Pas} = 4.6$). This effect resembles the similar trend in onset temperatures of foaming in **Figure 2**. The onset temperature of bubble bursting is controlled by viscosity and bubble pressure. The almost identical sintering observed among all samples in **Figure 2** indicates that the milling atmosphere has a negligible effect on glass viscosity. The early onset of foaming for milling in CO₂ should, therefore, mainly reflect increased bubble pressure.

Enhanced CO₂, CO, and C degassing is evident around 300°C , at ≈ 500 – 650°C , and at ≈ 650 – 800°C below the onset of foaming. Since it is obviously delayed by sintering, the latter peak at ≈ 650 – 800°C is the most likely source of foaming. It is worth

noting that the onset of this degassing peak nicely correlates with the glass transition temperature (arrows in **Figure 5**). Similar degassing patterns were observed for the diffusion-limited release of water dissolved during glass melting at ambient pressure (Müller et al., 2005). However, it is seen from the much less intensive bubble bursting of pre-milled powders that this effect should have minor impact on the extensive bubble bursting of milled powders. Instead, because of the large effect of particle size on foaming (**Figure 1**), this observation might indicate diffusive degassing from the near-surface region of the powder.

Figure 6 compares CO₂ degassing, silhouette area change, and DTA curves of a glass powder milled for 1 h in CO₂ (p12). The prolonged milling time was required in order to overcome

the lower gas detection limit of the DTA-MS device used here. Besides CO_2 , no other volatiles were detectable. **Figure 6** gives clear evidence that CO_2 is the dominant foaming source even during heating in air and ambient pressure. The broad structureless degassing peak (T_{max} at $\approx 300^\circ\text{C}$) further indicates a pronounced continuous release of CO_2 during heating and that sintering only traps a rather small fraction of its initial amount. Nevertheless, this small amount obviously causes substantial foaming until the foamed sample starts to collapse at $>880^\circ\text{C}$ via gas bubble bursting (spikes). In contrast to **Figure 5**, no pronounced increase of degassing activity is seen just above T_g . The DTA curve reveals a weak endothermic shoulder at T_g , a distinct endothermic shoulder within the temperature range of shrinkage and a broad pronounced peak nicely correlating with foaming.

Figure 7 compares sintering and foaming when milled for 30 min in air (p13), water (p14), and 10 wt% HCl (p15). Sintering starts at $\approx 700^\circ\text{C}$ in all cases. Wet-milled powders exhibit slightly increased area shrinkage, which may at least partially reflect different powder compact green densities due to possibly altered glass surface properties ($\rho_0 = 62, 55$, and 55% for p14, p15, and

p16, respectively). Furthermore, shrinkage was slightly decelerated for the powder milled in HCl, although its particle size does not significantly differ from powders p14 and p15 (**Table 1**). This effect is accompanied by a shift of the foaming onset by 30 K to 820°C . Both observations hint of a possible increase of viscosity. The latter effect could be caused by increased glass viscosity (e.g., related to aqueous Ba dissolution from the glass surface), the presence of rigid inclusions (e.g., BaCl_2 precipitates), or by both phenomena.

Most notably, however, **Figure 7** gives clear evidence that foaming has been substantially reduced by means of wet-milling. Thus, foaming caused a silhouette area increase of $\Delta s_A = 35\%$ for the 30 min dry-milled powder (p14), whereas $\Delta s_A = 7\%$ and even 4% were evident for the powders milled in water (p15) and HCl (p16), respectively. **Table 1** indicates that this effect is not just feigned by a deviating particle size distribution as D_{10} and D_{50} values are quite similar. Decreased D_{90} and D_{97} data for water milling may reflect a reduced agglomeration tendency.

Water- versus dry-milling experiments, similar to that presented in **Figure 7**, have also been conducted repeatedly using various milling materials including Cr-Ni steel, Si_3N_4 , and WC. In all cases, a substantial reduction of foaming was observed. The use of steel milling jars in wet-milling could reduce foaming from $\Delta s_A = 48\%$ (dry-milling) to $\Delta s_A = 9\%$. Similar ratios ($\Delta s_A = 52\text{--}34\%$ versus $\Delta s_A = 5\text{--}8\%$) occurred for Al_2O_3 , Si_3N_4 , and WC. Furthermore, it was found that for milling in corundum jars and 10 wt% HCl, prolonged storage up to 12 days did not significantly influence Δs_A , which scattered between 5 and 6% for all applied storage times.

DISCUSSION

As discussed in previous literature, different sources may contribute to foaming: *gases encapsulated* within the closed pore volume of the powder compact (Lim et al., 2006; Kim et al., 2007; Müller et al., 2009), *gases adsorbed* onto the glass powder surface (Hwang et al., 2002), *glass volatilization* (Lucchini et al., 1983), or effusing *oxygen* from the glass bulk (Hwang et al., 2002). Due to the strong effect of particle size on foaming activity (**Figures 1 and 5**), the latter two mechanisms should not dominate foaming in the present study.

Gas Trapped in the Foaming Sample

In order to reveal to what extent encapsulated and adsorbed gases may contribute to foaming in the present study, the amount of gas trapped in the maximal foamed sample, n_{Max} , was estimated first. The 15-min N_2 -milled powder was used for this estimation as an optimum between detectable foaming and minor bubble bursting activity below the foaming maximum. Nevertheless, n_{Max} can only provide a lower limit of this amount.

- (i) As an initial approach for estimating n_{Max} , the porosity, P , of foamed samples was measured from cross-section micrographs of powder compacts heated to different temperatures and quenched in air, by means of image analysis. Respective

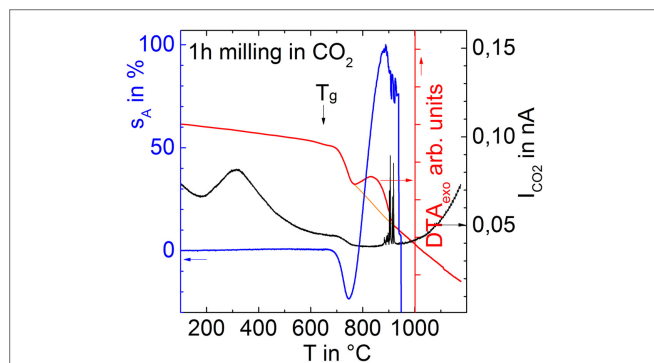


FIGURE 6 | Silhouette area change (s_A), MS degassing current for CO_2 (I_{CO_2}), and DTA of a glass powder milled for 1 h in CO_2 (p12) during heating in ambient air at 5 K/min.

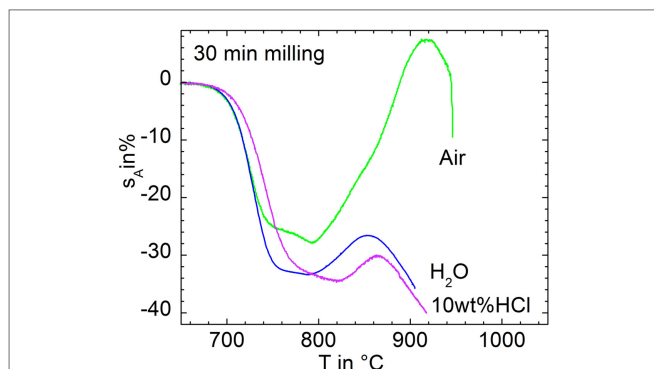


FIGURE 7 | Silhouette area change, s_A , versus temperature for 30 min milled in air (p14), water (p15), and 10 wt% HCl (p16) during heating at 5 K/min.

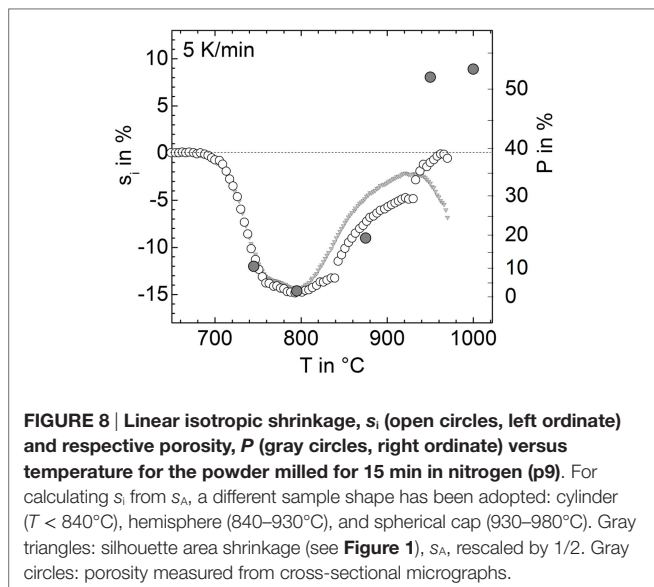


FIGURE 8 | Linear isotropic shrinkage, s_i (open circles, left ordinate) and respective porosity, P (gray circles, right ordinate) versus temperature for the powder milled for 15 min in nitrogen (p9). For calculating s_i from s_A , a different sample shape has been adopted: cylinder ($T < 840^\circ\text{C}$), hemisphere ($840\text{--}930^\circ\text{C}$), and spherical cap ($930\text{--}980^\circ\text{C}$). Gray triangles: silhouette area shrinkage (see **Figure 1**), s_A , rescaled by $1/2$. Gray circles: porosity measured from cross-sectional micrographs.

values are shown in **Figure 8** (right ordinate, gray circles). Maximal porosity scatters around 52% (0.52). n_{Max} can be estimated from this value with Eq. 1, where P is the porosity, V the sample volume, $P \cdot V$ the pore volume, R the ideal gas constant, T the temperature, and p the internal pressure:

$$p(V \cdot P) = n_{\text{Max}} RT \quad (1)$$

p was assumed to be $\approx 10^5$ Pa (1 bar) due to the low viscosity expected at the foaming maximum and because the majority of pore radii, r , were much greater than $50 \mu\text{m}$. For such condition and a surface energy of $\gamma \approx 0.3 \text{ J m}^{-2}$ (estimated with SciGlass 6.5 software), the Laplace pressure $P_L \approx 2\gamma/r$ (German, 1996) should be small ($< 0.12 \times 10^5$ Pa) and was therefore neglected. Based on $P \approx 0.52$, $n_{\text{Max}} \approx 16 \times 10^{-8}$ mol was found.

- (ii) A more average value of P can be calculated from the linear isotropic shrinkage, $s_i = (\Delta V/V_0)^{-3}$, where V_0 is the initial sample volume. s_i is related to P according to Eq. 2 (Winkel et al., 2012)

$$P = 1 - \rho = 1 - \frac{\rho_0}{(1 - s_i)^3} \quad (2)$$

where ρ and ρ_0 denote the relative density and the relative green density, respectively. In order to calculate s_i from the measured silhouette area change data, s_A , the current sample volume, V , has to be inferred from the sample silhouette area, A . In that case, a regular sample shape must be adopted. Up to 800°C , the sample shape could be reasonably approximated as a cylinder. Its volume is given by Eq. 3 as follows (Sieber, 1980):

$$V_C = \frac{\pi}{4} d^2 h = \frac{\pi}{4h} A^2 \quad (3)$$

where d , h , and A (where $A = d \cdot h$) represents the diameter and the height of the cylinder and its silhouette area, respectively. Above 850°C , heating microscopy data showed that samples

underwent substantial rounding resembling more a hemisphere (not shown). The volume of a hemisphere can be related to its sample silhouette according to Eq. 4 (Sieber, 1980)

$$V_H = \frac{4\pi}{6} \left(\frac{d}{2} \right)^3 = \frac{4\pi}{6} \left(\frac{2A}{\pi} \right)^{\frac{3}{2}} \quad (4)$$

where d refers to the diameter of the hemisphere and $A = (1/8)\pi d^2$ to its silhouette. Above 920°C , the sample shape rather resembles a spherical cap. Its volume is given by Eq. 5 as follows (Sieber, 1980):

$$V_P = \frac{\pi h}{6} \left(\frac{3d^2}{4} + h^2 \right) \quad (5)$$

In this case, d denotes the base radius of the cap.

The linear isotropic shrinkage calculated in this way is shown in **Figure 8** (open circles) in terms of s_i (left ordinate) and P (right ordinate). Below 840°C , s_i clearly resembles the measured silhouette area shrinkage rescaled by $1/2$. Above 800°C , silhouette area shrinkage significantly deviates from s_i . The discontinuities in s_i at 840 and 930°C represent a rough measure of the calculation errors caused by the incorrect, sample-shape assumptions. Among the large variety of error sources, the loss of rotational symmetry of the sample during foaming seems to be most important. Nevertheless, estimating n_{Max} from shrinkage data indicates similar volumes of the maximal foamed sample and the green powder compact, i.e., similarity of the respective porosity $P \approx 0.39$. Thus, as a rough measure, $n_{\text{Max}} \approx 12 \times 10^{-8}$ mol could be estimated from Eq. 1.

Encapsulated Gas

The amount of gas encapsulated within the closing porosity during sintering, n_{Enc} , was roughly estimated assuming that porosity suddenly closes at $\rho = 0.8$ (German, 1996). The number of gas moles encapsulated therein was approximated from Eq. 1, estimating V from the measured sample weight (94 mg), the relative compact density ($\rho = 0.8$) and the glass density ($\rho_G = 3.61 \text{ g/cm}^3$). This estimation results in $n_{\text{Enc}} \approx 8 \times 10^{-8}$ mol.

Comparing $n_{\text{Enc}} \approx 8 \times 10^{-8}$ mol with $n_{\text{Max}} \approx 12\text{--}16 \times 10^{-8}$ mol suggests that gases physically encapsulated within the porosity of sintered compacts may actually contribute to foaming. However, since mainly CO_2 is released during bubble bursting and only traces of N_2 and Ar were detected even for the powders milled in these atmospheres (**Figure 5**), the powder atmosphere must have changed after milling.

Moreover, this estimation was done for the sample milled for 15 min in N_2 . As seen from **Figure 1**, prolonged milling significantly increases foaming activity. Since the amount of encapsulated gas, i.e., the volume of 20% porosity, should not be affected by particle size and keeping in mind that n_{Max} provides only a lower limit, this observation gives clear evidence that the encapsulated sintering atmosphere does not significantly contribute to foaming in this case. Instead, foaming seems to be clearly caused by species located at the glass powder surface.

Adsorbed Gases

In order to check the potential effect of adsorbed gases on foaming, the respective amount of adsorbed gas, n_A , was roughly estimated assuming a mono-atomic layer of nitrogen molecules remaining stable until sintering. The specific powder surface area, $a_s = 0.42 \text{ m}^2/\text{g}$, was taken from PSD analysis as the average from all 15 min milling experiments. The diameter of the nitrogen molecule, d_{N_2} , was set at 0.34 nm (Doremus, 1973). The total powder surface area, $S = 3.7 \times 10^{-2} \text{ m}^2$ was then obtained from the measured sample mass, $m \approx 9.4 \times 10^{-2} \text{ g}$. Assuming that one nitrogen molecule occupies an area of $\approx \pi(d_{N_2}/2)^2 \approx 0.11 \text{ nm}^2$, $n_A \approx 70 \times 10^{-8} \text{ mol}$ of nitrogen molecules can be adsorbed onto the total sample surface area. It is interesting to note that n_A is about 10 times larger than n_{Max} emphasizing the potentially strong effect of surface desorption on foaming. Taking into account that multiple physisorbed layers or multilayers grown from chemisorption and reorganization or chemical reaction processes can occur (Bhushan, 2013), this conclusion seems even more reasonable.

For *physically adsorbed gases*, as is expected for N_2 and Ar, this conclusion however, is questionable because of low thermal stability (Bhushan, 2013). Thus, **Figure 5** shows that N_2 and Ar do not significantly contribute to foaming even for milling in these atmospheres and that the respective broad degassing peak is exhausted at around 500°C. Low desorption temperatures are also known for CO_2 . Thus, complete degassing of physically adsorbed CO_2 was found <250°C for silica surfaces (Antonini and Hochstra, 1972) and <120°C for $\eta\text{-Al}_2\text{O}_3$ (Morterra et al., 1977).

Much higher desorption temperatures can be expected for *chemisorbed gases*. Water is known to strongly interact with silicate glass surfaces. Thus, a significant concentration of 1.2 OH groups per square nanometer was found even after high vacuum annealing at 700°C (5.2 OH/nm² at 23°C) (Dunken, 1981). Conformingly, **Figure 5** shows that water is the dominant degassing species below the onset temperature of foaming at $\approx 800^\circ\text{C}$.

Nevertheless, bubble bursting, i.e., foaming, is dominated by CO_2 . This gives clear evidence that CO_2 adsorption results in carbonaceous species being thermally stable at least up to the temperature at which the open porosity of sintering powder compacts is closed ($\approx 750^\circ\text{C}$). It is reasonable to assume that the carbonaceous species, most likely carbonates, may provide sufficient thermal stability. Thus, the decomposition temperature of $BaCO_3$ in air is found at $\approx 900^\circ\text{C}$ (Liptay, 1976), $BaCO_3$ species at Pt/ $BaO/\gamma\text{-Al}_2\text{O}_3$ surfaces remain stable up to 500°C in vacuum (Epling et al., 2008), and pronounced CO_2 degassing from silica glass-fiber surfaces between 500 and 700°C has been attributed to $\equiv\text{Si-O-C(O)-O-Si}\equiv$ (Eremenko et al., 1991). Further, Cerruti and Morterra (2004) reported carbonate species stable up to 800°C at the surface of bioactive glass powders. It is also known that intensive milling of alkaline earth metasilicates can yield remarkable CO_2 uptake (Kalinkin and Kalinkina, 2010) and that even grinding of $Na_2Si_2O_5$ glass in air can cause detectable amounts of $NaCO_3$ at the surface (Baker et al., 1995). Conclusions on the nature of the dominant carbonaceous species,

however, cannot be drawn from the present study. Due to the expected small concentration ($\approx 60 \text{ ppm } CO_2$ would result from $n_{\text{Max}} = 12 \times 10^{-8} \text{ mol}$, $m_{\text{Sample}} \approx 92 \text{ mg}$, and $\rho_{\text{Glass}} \approx 3.61 \text{ g/cm}^3$ as discussed above for **Figure 8**), XRD, DTA, and ATR-FTIR studies conducted so far have not yet revealed any reliable hint of the nature of the carbonaceous species responsible for foaming found in the present study.

Dissolved Gases

The detection of these carbonaceous species might be even more complicated as adsorbed carbonaceous species could partially diffuse into the glass forming a layer of *near-surface dissolved carbonates* during heating. Such an effect seems reasonable as **Figure 6** indicates a large amount of carbonaceous surface species even during progressive heating. In this way, desorption of these species can be accompanied by simultaneous inward diffusion. Once desorption is complete, the dissolved carbonaceous species may provide a further source of CO_2 degassing. Such a possibility might be indicated by **Figure 5** in as much as the onset of the degassing activity at $\approx 650\text{--}800^\circ\text{C}$ nicely correlates with glass transition temperature (T_g). This latter mechanism is most likely responsible for foaming as it is obviously retarded by sintering. Similar VHE degassing patterns could be attributed to the diffusive release of bulk water (Müller et al., 2005). CO_2 dissolution in oxide glasses was comprehensively studied by Brooker et al. (2001) who detected CO_3^{2-} like species in different local environments, albeit at higher pressure and temperature (0.2–2.7 GPa, 1175–1700°C) and not for boron-containing glasses. CO_2 solubility of 0.11 and 0.28 wt% was reported for natural rhyolitic melts at 1100°C for 200 and 500 MPa, respectively (Tamir et al., 2001). Although much lower solubility should be expected for 1 bar, increased local pressure can be expected during sintering and healing of the mechanically damaged near-surface region of milled glass powders.

Foaming Mitigation Strategies

As shown above, *encapsulated gas* can contribute to the foaming of coarse glass powders. In this case, vacuum sintering seems to be the only foaming mitigation strategy. On the other hand, gases with better mobility could help to enhance diffusive degassing from closed porosity below the onset of foaming.

As clearly shown in the present study and known from common experience, *gases trapped on the powder surface* can essentially contribute to foaming. Hence, the use of coarser glass particles is the most obvious and probably the most frequently applied strategy in reducing sinter foaming.

Beyond this, however, the present study (sintering at $\approx 700\text{--}800^\circ\text{C}$) indicates that foaming is dominated by carbon gases, even when organic aids have not been used in powder processing, and that foaming can be affected by the milling atmosphere, milling aids, and powder storage. These observations can be reasonably explained assuming that gas uptake occurs at the freshly fractured and highly damaged glass powder surface as a relaxation mechanism and that carbonaceous species are preferentially adsorbed as a result of adsorption–desorption phenomena during milling or later storage.

In this sense, further foaming mitigation strategies could be based on minimizing the possible uptake of ambient CO_2 during powder processing. Among these strategies, powder processing in a controlled atmosphere or vacuum seems to be the most obvious but probably most expensive method. Alternatively, less CO_2 uptake can be achieved by means of blocking active (i.e., the most basic) glass surface sites, which are most likely related to BaO .

The significant decrease of foaming activity attained by *water milling* presented in **Figure 7** indicates that this blocking can be made with water. **Figure 5** shows that water does not contribute much to foaming, although it is the most prominent degassing species below the onset of sintering. This advantage probably reflects its better diffusivity. It should be noted, however, that this strategy relies on sufficiently high sintering temperatures. For lower sintering temperatures, water and even less stable species could also contribute to foaming. Additional BaCO_3 formation during water milling as a result of aqueous dissolution of Ba from the glass surface and CO_2 from the ambient atmosphere does not seem very likely since a pH value >12 is required for BaCO_3 formation at 1 bar (Brookins, 1988) and pH <11 was measured for milling in water in the present study.

Alternatively, foaming was substantially reduced by milling in 10 wt% HCl (**Figure 7**). The decreased shrinkage rate and the simultaneously increased foaming onset temperature indicate increased glass viscosity, at least near to the powder surface. Such phenomenon could be caused by Ba dissolution from the glass surface. It is reasonable to assume that this effect would allow the formation of BaCl_2 , which is thermally stable up to 963°C (melting point) (Merck, 2015). In this sense, Ba dissolution from the glass surface and the formation of thermally stable Ba salts may provide another strategy for blocking active CO_2 adsorption sites. In acidic aqueous solutions, CO_2 solubility is also very limited (Acker et al., 1999).

Another foaming mitigation strategy could be utilizing increased sintering temperatures. This is due to the fact that foaming intensity is controlled by the temperature relationships between densification (T_s), decomposition of foaming species (T_D), and crystallization (T_C). Most pronounced foaming is expected for $T_s < T_D < T_C$. For $T_D \ll T_s$ surface-adsorbed foaming agents largely decompose and escape *via* open pores. For $T_D \approx T_s$, this degassing process is retarded by closing porosity, which later yields gas bubble formation and foaming. Due to this general relationship, foaming probability seems to increase with decreasing sintering temperature as even less stable surface-adsorbed species (e.g., water or less stable carbonaceous species as indicated by **Figure 5**) may contribute to foaming. On the other hand, a higher sintering temperature can, for example, affect redox equilibria of the glass melt, increase oxygen mobility, and could cause oxygen degassing as a new foaming source. For most practical cases, however, a substantial change of glass transition temperature does not seem to be an applicable foaming mitigation strategy.

For a given glass, however, foaming of coarse powders is expected to be less intense not only due to the fact that a less specific surface will adsorb less foaming species as discussed above but also due to the more complete degassing, which can occur until porosity is closed. On the other hand, sintering is controlled by the effective viscosity of powder compacts. Hence, dispersed

rigid particles can also decrease the shrinkage rate (Müller et al., 2007; Müller and Reinsch, 2012) and therefore provide more complete surface desorption. In a similar sense, glasses with a less temperature-dependent viscosity, causing a broader temperature range of sintering, should be less prone to foaming.

For $T_D > T_C$, foaming can be retarded by the presence of crystals, which hinder gas bubble coalescence and growth due to the increased effective viscosity of the crystal bearing melt. If full densification is not reached ($T_C \approx T_s$), the remaining open porosity will allow full degassing without foaming even when $T_s < T_D$.

However, our final conclusions on how to mitigate sinter foaming, beyond the rather speculative discussion presented here, require much deeper understanding of the potential foaming mechanism and may largely depend on given experimental or processing conditions.

CONCLUSION

Sintering and foaming of barium silicate glass powder compacts were studied for different milling times and atmospheres. Foaming was strongly promoted by progressive milling and was affected by the milling atmosphere where foaming activity increased in the order $\text{Ar} \approx \text{N}_2 < \text{air} < \text{CO}_2$. For moderately milled glass powders, subsequent storage in air could also promote foaming. Degassing studies revealed that foaming is mainly driven by CO_2 even for powders milled in Ar and N_2 . Only traces of these species were detected during bubble bursting of compacts for which glass powder milling was performed within these atmospheres. This observation, together with respective estimation of the possible amount of gas encapsulated within the closing porosity during densification, suggests that an encapsulated milling atmosphere does not dominate foaming. Instead, a potentially large effect on foaming of stable surface-adsorbed carbonaceous species was indicated by enhanced CO_2 degassing during foaming. In this sense, milling in water and weak HCl acid could substantially reduce foaming.

AUTHOR CONTRIBUTIONS

RM: acquisition and design of the work, data interpretation, literature review, partial manuscript draft and revising, and final approval. SR: conception of experimental work, thermo-analytical measurements and data interpretation, literature review, partial manuscript draft, and final approval. BA-B: conception of experimental work, other experimental work, data analysis, literature review, partial manuscript draft, and final approval. All authors agree to be accountable for all aspects of the work.

ACKNOWLEDGMENTS

We gratefully acknowledge experimental support by our colleagues M. Gaber (vacuum hot extraction), R. Sojref (glass powder preparation and characterization), I. Feldmann (SEM), and D. Nicolaides (XRD). We finally acknowledge financial support by Erasmus Lifelong Learning Programs for BA-B (MINISTERIO DE EDUCACIÓN, CULTURA Y DEPORTE # 11015347).

REFERENCES

- Acker, K., Barnes, I., Becker, K.-H., Crutzen, P. J., Hüttel, R., and Kalaß, D. (1999). *Atmospheric Environmental Research: Critical Decisions between Technological Progress and Preservation of Nature*, 1st Edn. Heidelberg, Germany: Springer, 186.
- Agea Blanco, B., Blaess, C., Reinsch, S., Brauer, D., and Müller, R. (2015). Sintering and foaming of barium and calcium silicate glass powders. *Addition. Conf.* 2015, 000031–000037. doi:10.4071/CICMT-TA21
- Antonini, J. F., and Hochstra, G. (1972). Surface states of pristine silica surfaces: II. UHV studies of the CO₂ adsorption-desorption phenomena. *Surf. Sci.* 32, 665–686. doi:10.1016/0039-6028(72)90193-8
- Baker, G. J., Greaves, G. N., Surman, M., and Oversluizen, M. (1995). An oxygen XAFS study of sodium disilicate glass surfaces. *Nucl. Instrum. Methods Phys. Res. Sect. B-Beam Interact. Mat. Atoms* 97, 375–382. doi:10.1016/0168-583X(95)00332-0
- Bhushan, B. (2013). *Solid Surface Characterization. Introduction to Tribology*, 2nd Edn. West Sussex: John Wiley & Sons.
- Brooker, R. A., Kohn, S. C., Holloway, J. R., and McMillan, P. F. (2001). Structural controls on the solubility of CO₂ in silicate melts: part II: IR characteristics of carbonate groups in silicate glasses. *Chem. Geol.* 174, 241–254. doi:10.1016/S0009-2541(00)00318-1
- Brookins, G. D. (1988). *Eh-pH Diagrams for Geochemistry*, 1st Edn. Berlin, Heidelberg: Springer-Verlag.
- Cerruti, M., and Morterra, C. (2004). Carbonate formation on bioactive glasses. *Langmuir* 20, 6382–6388. doi:10.1021/la049723c
- Doremus, R. H. (1973). *Glass Science*. New York, USA: John Wiley & Sons, 133.
- Dunken, H. H. (1981). “Chemische Reaktionen an Glasoberflächen,” in *Physikalische Chemie der Glasoberfläche* (Leipzig: VEB Deutscher Verlag für Grundstoffindustrie), 262–338.
- Epling, W. S., Peden, C. H. F., and Szanyi, J. (2008). Carbonate formation and stability on a Pt/BaO/γ-Al₂O₃ NOx storage/reduction catalyst. *J. Phys. Chem. C* 112, 10952–10959. doi:10.1021/jp712180q
- Eremenko, G. O., Larichev, M. N., and Leypunsky, I. O. (1991). “Thermal desorption mass-spectrometric (TDMS) analysis of the carbon dioxide desorption from the glass fiber surface,” in *MICC 90*, ed. I.N.e.a. Fridlyander (Moscow: Elsevier Science Publishers Ltd.).
- Fergus, J. W. (2005). Sealants for solid oxide fuel cells. *J. Power Sources* 147, 46–57. doi:10.1016/j.jpowsour.2005.05.002
- Fernandes, H. R., and Ferreira, J. M. F. (2007). Recycling of chromium-rich leather ashes in porcelain tiles production. *J. Eur. Ceram. Soc.* 27, 4657–4663. doi:10.1016/j.jeurceramsoc.2007.03.037
- FRITSCH GmbH. (1987). *Operator's Manual “pulverisette 5”*. Idar-Oberstein: Fritsch GmbH.
- FRITSCH GmbH. (1995). *Operator's Manual “pulverisette 7” Version 1*. Idar-Oberstein: Fritsch GmbH.
- German, R. M. (1996). *Sintering Theory and Practice*. New York, Chichester, Brisbane, Toronto, Singapore: John Wiley & Sons, Inc.
- Gross, S. M., Koppitz, T., Rimmel, J., and Reisgen, U. (2005). “Glass-ceramic materials of the system BaO-CaO-SiO₂ as sealants for SOFC applications,” in *International Conference on Advanced Ceramics and Composites Ceramic Engineering and Science Proceedings*, eds N. Bansal, D. Zhu, and W. M. Kriven (Cocoa Beach, FL), 239–245.
- Hwang, G. H., Jeon, H. J., and Kim, Y. S. (2002). Physical properties of barrier ribs of plasma display panels: I, formation of pores during sintering of lead borosilicate glass frits. *J. Am. Ceram. Soc.* 85, 2956–2960. doi:10.1111/j.1151-2916.2002.tb00562.x
- Imanaka, Y. (2005). *Multilayered Low Temperature Cofired Ceramics (LTCC) Technology*. New York: Springer.
- Kalinkin, A. M., and Kalinkina, E. V. (2010). The mechanosorption of carbon dioxide by magnesium, calcium, and strontium metasilicates. *Russ. J. Phys. Chem. A* 84, 1585–1591. doi:10.1134/S0036024410090256
- Kerafol. (2010). *Glass solder powder type K01 (Product-ID 6.FC0700.DL.00000) Supplied by Kerafol Keramische Folien GmbH Eschenbach Germany*.
- Kim, B.-S., Lim, E.-S., Lee, J.-H., and Kim, J.-J. (2007). Effect of Bi₂O₃ content on sintering and crystallization behavior of low-temperature firing Bi₂O₃-B₂O₃-SiO₂ glasses. *J. Eur. Ceram. Soc.* 27, 819–824. doi:10.1016/j.jeurceramsoc.2006.04.013
- Lara, C., Pascual, M. J., Prado, M. O., and Durán, A. (2004). Sintering of glasses in the system RO-Al₂O₃-BaO-SiO₂ (R=Ca, Mg, Zn) studied by hot-stage microscopy. *Solid State Ionics* 170, 201–208. doi:10.1016/j.ssi.2004.03.009
- Leonelli, C., Bondioli, F., Veronesi, P., Romagnoli, M., Manfredini, T., Pellacani, G. C., et al. (2001). Enhancing the mechanical properties of porcelain stoneware tiles: a microstructural approach. *J. Eur. Ceram. Soc.* 21, 785–793. doi:10.1016/S0955-2219(00)00266-1
- Lim, E. S., Kim, B.-S., Lee, J.-H., and Kim, J.-J. (2006). Effect of BaO content on the sintering and physical properties of BaO-B₂O₃-SiO₂ glasses. *J. Non-Cryst. Solids* 352, 821–826. doi:10.1016/j.jnoncrysol.2006.01.021
- Liptay, G. (1976). *Atlas of Thermoanalytical Curves*, Vol. 5. Budapest, Hungary: Akademiai Kiado.
- Lucchini, E., Meriani, S., and Slokar, G. (1983). Sintering of glass bonded ceramic barium hexaferrite magnetic powders. *J. Sci. Mater.* 18, 1331–1334. doi:10.1007/BF01111950
- Merck. (2015). *Sicherheitsdatenblatt Version 10.13 für Bariumchlorid 99.995 Suprapur®*, CAS-Nr. 10361-37-2. Available at: www.merckgroup.com
- Morterra, C., Zecchina, A., Coluccia, S., and Chiorino, A. (1977). I.R. spectroscopic study of CO₂ adsorption onto η-Al₂O₃. *J. Chem. Soc. Faraday Trans. 173*, 1544–1560. doi:10.1039/f19777301544
- Müller, R. (1994). On the kinetics of sintering and crystallization of glass powders. *Glastech. Ber-Glass Sci. Technol.* 67C, 93–98.
- Müller, R., Eberstein, M., Reinsch, S., Schiller, W. A., Deubener, J., and Thiel, A. (2007). Effect of rigid inclusions on sintering of low temperature co-fired ceramics. *Phys. Chem. Glass. Eur. J. Glass Sci. Technol. B* 48, 259–266.
- Müller, R., Meszaros, R., Peplinski, B., Reinsch, S., Eberstein, M., Schiller, W. A., et al. (2009). Dissolution of alumina, sintering, and crystallization in glass ceramic composites for LTCC. *J. Am. Ceram. Soc.* 92, 1703–1708. doi:10.1111/j.1551-2916.2009.03089.x
- Müller, R., Gottschling, P., and Gaber, M. (2005). Water concentration and diffusivity in silicates obtained by vacuum extraction. *Glass Sci. Technol.* 78, 76–89.
- Müller, R., and Reinsch, S. (2012). “Viscous phase silicate processing,” in *Processing Approaches for Ceramics and Composites*, eds N. Bansal and A. R. Boccaccini (Hoboken, New Jersey, USA: John Wiley & Sons), 75–144.
- Pascual, M. J., and Durán, A. (2003). Sintering with concurrent crystallization of a borosilicate glass. *Phys. Chem. Glasses* 44, 409–415.
- Prado, M. O., Fredericci, C., and Zanotto, E. D. (2003a). Non-isothermal sintering with concurrent crystallization of polydispersed soda-lime-silica glass beads. *J. Non-Cryst. Solids* 331, 157–167. doi:10.1016/j.jnoncrysol.2003.08.076
- Prado, M. O., Zanotto, E. D., and Fredericci, C. (2003b). Sintering polydispersed spherical glass particles. *J. Mater. Res.* 18, 1347–1354. doi:10.1557/JMR.2003.0185
- Prado, M. O., Nascimento, M. L. F., and Zanotto, E. D. (2008). On the sinterability of crystallizing glass powders. *J. Non-Cryst. Solids* 354, 4589–4597. doi:10.1016/j.jnoncrysol.2008.06.006
- Prado, M. O., and Zanotto, E. D. (2002). Glass sintering with concurrent crystallization. *Comptes Rendus Chimie* 5, 773–786. doi:10.1016/S1631-0748(02)01447-9
- Rabinovich, E. M. (1985). Preparation of glass by sintering. *J. Sci. Mater.* 20, 4259–4297. doi:10.1007/BF00559317
- Schiller, W. A., Müller, R., Eberstein, M., Reinsch, S., and Rabe, T. (2008). Sintering of LTCC. *cfi/Berichte der DKG* 85, 12–17.
- Sieber, H. (1980). *Mathematische Tafeln*, 2nd Edn. Stuttgart, Germany: Ernst Klett Verlag.
- Tamic, N., Behrens, H., and Holtz, F. (2001). The solubility of H₂O and CO₂ in rhyolitic melts in equilibrium with a mixed CO₂-H₂O fluid phase. *Chem. Geol.* 174, 333–347. doi:10.1016/S0009-2541(00)00324-7
- Winkel, A., Meszaros, R., Reinsch, S., Müller, R., Travitzsky, N., Frey, T., et al. (2012). Sintering of 3D-printed glass/hap composites. *J. Am. Ceram. Soc.* 95, 3387–3393. doi:10.1111/j.1551-2916.2012.05368.x

Conflict of Interest Statement: The authors declare that the research was conducted in the absence of any commercial or financial relationships that could be construed as a potential conflict of interest.

Copyright © 2016 Agea-Blanco, Reinsch and Müller. This is an open-access article distributed under the terms of the Creative Commons Attribution License (CC BY). The use, distribution or reproduction in other forums is permitted, provided the original author(s) or licensor are credited and that the original publication in this journal is cited, in accordance with accepted academic practice. No use, distribution or reproduction is permitted which does not comply with these terms.



Controlled Parallel Crystallization of Lithium Disilicate and Diopside Using a Combination of Internal and Surface Nucleation

Markus Rampf*, Marc Dittmer, Christian Ritzberger and Wolfram Höland

Ivoclar Vivadent AG, Schaan, Liechtenstein

OPEN ACCESS

Edited by:

John C. Mauro,
Corning Incorporated, USA

Reviewed by:

Takayuki Komatsu,
Nagaoka University
of Technology, Japan
Lina Ma,
Corning Incorporated, USA

*Correspondence:

Markus Rampf
markus.rampf@ivoclarvivadent.com

Specialty section:

This article was submitted
to Glass Science,
a section of the journal
Frontiers in Materials

Received: 29 July 2016

Accepted: 26 September 2016

Published: 17 October 2016

Citation:

Rampf M, Dittmer M, Ritzberger C
and Höland W (2016)
Controlled Parallel Crystallization
of Lithium Disilicate and
Diopside Using a Combination of
Internal and Surface Nucleation.
Front. Mater. 3:47.
doi: 10.3389/fmats.2016.00047

In the mid-twentieth century, Dr. Donald Stookey identified the importance and usability of nucleating agents and mechanisms for the development of glass-ceramic materials. Today, a number of various internal and surface mechanisms as well as combinations thereof have been established in the production of glass-ceramic materials. In order to create new innovative material properties, the present study focuses on the precipitation of $\text{CaMgSi}_2\text{O}_6$ as a minor phase in $\text{Li}_2\text{Si}_2\text{O}_5$ -based glass-ceramics. In the base glass of the SiO_2 - Li_2O - P_2O_5 - Al_2O_3 - K_2O - MgO - CaO system, P_2O_5 serves as nucleating agent for the internal precipitation of $\text{Li}_2\text{Si}_2\text{O}_5$ crystals, while a mechanical activation of the glass surface by means of ball milling is necessary to nucleate the minor $\text{CaMgSi}_2\text{O}_6$ crystal phase. For a successful precipitation of $\text{CaMgSi}_2\text{O}_6$, a minimum concentration of MgO and CaO in the range between 1.4 and 2.9 mol% in the base glasses was determined. The nucleation and crystallization of both crystal phases takes place during sintering a powder compact. Dependent on the quality of the sintering process, the dense $\text{Li}_2\text{Si}_2\text{O}_5$ - $\text{CaMgSi}_2\text{O}_6$ glass-ceramics show a mean biaxial strength of up to 392 ± 98 MPa. The microstructure of the glass-ceramics is formed by large (5–10 μm) bar-like $\text{CaMgSi}_2\text{O}_6$ crystals randomly embedded in a matrix of small (≤ 1 μm) plate-like $\text{Li}_2\text{Si}_2\text{O}_5$ crystals arranged in an interlocking manner. While there is no significant influence of the minor $\text{CaMgSi}_2\text{O}_6$ phase on the strength of the material, the translucency of the material decreases upon precipitation of the minor phase.

Keywords: glass-ceramics, lithium disilicate, diopside, twofold crystallization, nucleation, surface activation, sintering

INTRODUCTION

In the 1950s, Dr. Donald Stookey succeeded in the production of the first glass-ceramic of the lithium disilicate type worldwide (Stookey, 1959; Höland and Beall, 2012). His discovery and following research on this new class of materials paved the way for a number of innovative technical solutions affecting daily life, high-tech industry, and fundamental research in various fields. Stove tops and kitchenware belong to the most famous applications of glass-ceramics just as telescope mirrors, the nosecones of spaceships, and dental prostheses (Höland and Beall, 2012). In light of this wide field of applications for Donald Stookey's invention, the impact of his work on not only the technological progress of humankind becomes obvious but also has his research motivated and driven the mind and work of a huge number of scientists in various fields of research ever since.

In this spirit, the authors of the present publication want to recognize the outstanding activities of Dr. Donald Stookey.

To identify and use the nucleating effect of Ag clusters in the development of glass-ceramics in the SiO_2 – Li_2O system, as well as transferring the general principles of nucleation and crystallization to other glass systems, was a crucial part of his great achievement (Stookey, 1959). Besides enhancing the mechanical strength and machinability of glasses, the precipitation of certain crystal phases helped to control a number of different material properties including optical and electrical properties of glass matrix materials (Beall, 1971, 2014; Mauro et al., 2013).

Initiated after the development of the first lithium disilicate glass-ceramic by Donald Stookey, this system was the subject matter in a multitude of fundamental research topics. A molar ratio $\text{SiO}_2/\text{Li}_2\text{O}$ of 2, similar to the stoichiometric composition of lithium disilicate, was the basis for most of the compositions investigated (Höland and Beall, 2012). Moreover, glass-ceramics of the lithium disilicate type from multicomponent base glass systems were developed as well. There, the molar ratio of $\text{SiO}_2/\text{Li}_2\text{O}$ considerably deviated from the stoichiometric value of 2. Technical glass-ceramics as well as consumer applications were developed this way (Beall, 1992, 2014; Echeverría, 1992). Likewise, Höland et al. (1994, 2005, 2007, 2008, 2009) succeeded in the development of lithium disilicate glass-ceramics for dental applications using such multicomponent base glass systems.

Based on this research and development of lithium disilicate glass-ceramics for dental applications and driven by the quest for innovative combinations of material properties, the authors of the present publication pursued the objective of the parallel controlled nucleation and crystallization of lithium disilicate and diopside $\text{CaMgSi}_2\text{O}_6$ from a multicomponent base glass. The fundamental extension of the chemical composition of the lithium disilicate base glass system by adding MgO and CaO was mandatory just as the enhancement of nucleation and crystallization mechanisms. From a glass-ceramic engineering point of view, the authors assumed that controlling two separate nucleation mechanisms is mandatory to precipitate both a layer silicate and a chain silicate from a base glass. Only the development of a powder compact processing facilitated the crystallization of diopside according to the nucleation and crystallization mechanisms reported by Kokubo et al. (1989), Müller et al. (2000), and Reinsch et al. (2008) for different glass systems. The influence of the parallel precipitation of lithium disilicate and diopside on nucleation and crystallization principles as well as on properties crucial for dental applications, e.g., biaxial strength and translucency, were investigated.

MATERIALS AND METHODS

Glass Formation and Powder Production

Four glasses with different compositions in the SiO_2 – Li_2O – P_2O_5 – Al_2O_3 – K_2O – MgO – CaO system were melted from the raw materials quartz, lithium carbonate, aluminum metaphosphate, aluminum oxyhydroxyhydrate, potassium carbonate, alkaline magnesium carbonate, and calcium carbonate in batches of 100 g in an uncovered Pt–Rh crucible using an electric furnace. The melts were held for 2 h at 1500°C and subsequently casted into

water. The glass frit was dried in an oven preheated at 150°C for about 2 h. A chemical analysis of the glass frit was conducted by means of X-ray fluorescence (XRF S8 Tiger; Bruker, Karlsruhe, Germany). The dried glass granules were comminuted using a porcelain ball mill loaded with a mixture of steatite, Al_2O_3 , and porcelain milling beads measuring 10–30 mm in diameter. Milling was conducted until a mean grain size of $20 \pm 2 \mu\text{m}$ was reached. The grain size distribution was determined using a particle size analyzer (CILAS 1064, Quantachrome GmbH & Co. KG, Odelzhausen, Germany). Thermal analysis of the glass powder was conducted by means of differential scanning calorimetry (DSC) (STA 449 F3, Netzsch, Selb, Germany) using a heating rate of 10 K/min. Heating microscope analysis (HMA) was used to investigate the sintering characteristics of the glass powder. Therefore, cylinders of 3 mm height and a diameter of 2 mm were pressed and heated with a rate of 10 K/min simultaneously recording its silhouettes (EMI V 2.3, Hesse Instruments, Osterode, Germany). The crystallization behavior of the glass powders was investigated by means of high temperature X-ray diffraction (HT-XRD). The glass powder was heated to 400°C with a rate of 30 K/min. Subsequently, the powder was further heated to 1200°C in 20 K steps. Diffraction patterns were recorded from 10° to 60° 2θ and a step size of 0.014° with a D8-Advance diffractometer (Bruker, Karlsruhe, Germany) at each step. Therefore, the temperature was held for approximately 30 min at each step during recording the diffraction pattern. Qualitative analysis was carried out using the software Bruker Diffrac.Suite EVA. The PDF entries 70-4856 ($\text{Li}_2\text{Si}_2\text{O}_5$), 29-0828 (Li_2SiO_3), 15-0760 (Li_3PO_4), and 89-0830 ($\text{CaMgSi}_2\text{O}_6$) were used for phase identification.

To investigate the crystallization behavior of the bulk glass A and D, glass was casted into a graphite mold measuring 12 mm × 12 mm × 40 mm and immediately put in a muffle furnace preheated at 480°C for 20 min before slowly cooling the glass in the closed furnace. A disk of approximately 3 mm thickness was sawn from the glass, heated with a rate of 10 K/min to 860°C in a furnace of the Programat® type (Ivoclar Vivadent AG, Schaan, Liechtenstein). The temperature was held for 5 min before slowly opening the oven. One side of the crystallized glass-ceramic disk was ground using a 125 μm diamond grit grinding disk. The ground and the “as fired” surface were analyzed using room temperature XRD applying the parameters described above. Subsequently, the glass-ceramic disk was broken, and the fracture surface was investigated by means of scanning electron microscopy (SEM) after etching for 30 s with vapor of 40% hydrofluoric acid and coating with a 1 to 2 nm Au–Pd layer.

Production and Sintering of Powder Compacts

Very small amounts of water, acting as binder, were added to the glass powders before uniaxial pressing of specimen. In this way, powder compacts with different geometries were produced *via* uniaxial pressing using different press molds. Cubes with an edge length of 18 mm, bars measuring 36 mm × 4.8 mm × 6 mm, and disks with a diameter of 24 and 4 mm thickness were made. The powder compacts were sintered in vacuum to dense glass-ceramics using a furnace of the Programat® type (Ivoclar Vivadent AG, Schaan, Liechtenstein). The powder compacts were

heated to 480°C with a rate of 30 K/min and a subsequent dwell time of 20 min. Subsequently, the powder compact was further heated with 10 K/min to 860°C. This temperature was held for 5 min before slowly opening the furnace and thereby cooling the glass-ceramic to room temperature.

Characterization of the Glass-Ceramics

Sintered glass-ceramics were pulverized using a mortar grinder (Mortar Grinder RM 200, Retsch, Haan, Germany) and subsequently sieved <45 μm . In order to qualitatively investigate the crystal phases, diffraction patterns were recorded from 10° to 60° 2 θ applying a step size of 0.014°. Furthermore, a quantitative study of the crystal phase formation was conducted applying Rietveld refinement. Therefore, the pulverized glass-ceramic material was elutriated with approximately 20% of its mass of $\alpha\text{-Al}_2\text{O}_3$ (Alfa Aesar, 99.9%, 20–50 μm /ICSD number: 31548) as internal standard in acetone. The solvent was evaporated in an oven preheated at 80°C. After recording the powder XRD patterns from 10° to 100° 2 θ in 0.014° steps, the quantification of the crystal phases was done with the TOPAS software from Bruker.

The biaxial fracture strength was determined according to ISO 6872, including a surface finishing with a 15 μm diamond grit grinding disk. The specimen were milled from the sintered glass-ceramic cubes using a CEREC® InLab milling machine (Sirona, Bensheim, Germany). The biaxial strengths are given as mean values of 10 data sets \pm SD.

The thermal expansion of the glass ceramics was determined according to ISO 6872 by applying dilatometric analysis using a sapphire reference. The sintered glass-ceramic bars were ground to the required dimensions using a 40 μm diamond grit grinding disk. The error of the measurements is in the range of $\pm 0.5 \times 10^{-6} \text{ K}^{-1}$.

The contrast ratio (CR) of the glass-ceramic disks was determined using a spectrometer of the type CM-3700d (Konica-Minolta, Tokyo, Japan). The sintered disks were prepared according to BS5612. The translucency of a material decreases with increasing CR value.

Micrographs of the glass-ceramics were taken by means of SEM. The surface of the glass-ceramic samples was therefore polished using a 0.5 μm diamond grit grinding disk and subsequently etched with the vapor of 40% hydrofluoric acid for 30 s.

The porosity of the sintered glass-ceramics was estimated using the line intercept method. Therefore, three fragments of the samples broken within testing the biaxial strength of each glass-ceramic were polished using a 0.5 μm diamond grit grinding disk and examined by SEM. The linear ratio of pores is given as means of three data sets \pm SD.

RESULTS

Properties and Crystallization Behavior of the Base Glasses

The chemical composition of the base glasses calculated in mol% from the results obtained from XRF analysis is given in Table 1. The concentration of MgO and CaO in the base glasses increases from glasses A to D. The results of the thermal analysis of the

base glass powders are presented in Figure 1. The glass transition temperatures T_g as well as the exothermic and endothermic peak temperatures are summarized in Table 2. Base glass A shows a T_g , which is increased by approximately 10 K compared to the base glasses B–D. The first exothermic peak temperatures $T_{\text{exo}1}$ increase from base glasses A to D, while the opposite trend can be observed for the second exothermic peak temperatures $T_{\text{exo}2}$. The third exothermal process can only be detected for the base glasses B–D. Compared to the rather sharp first and second exothermal signals, the third exothermal reaction of the base glasses is characterized by a very wide peak in the temperature range between 780 and 840°C. The first endothermic heat flow could be detected at approximately 947°C for base glass A. Significantly lower endothermic peak temperatures $T_{\text{endo}1}$ between 887 and 899°C were determined for base glasses B–D. The second endothermic peak $T_{\text{endo}2}$ could be detected for base glasses B–D.

Figure 2 shows the data obtained by HMA. The area of the silhouette is plotted as a function of the temperature. The first

TABLE 1 | Chemical compositions of the base glasses in mol% calculated from the composition determined by XRF analysis.

	A	B	C	D
SiO_2	64.9	62.2	61.0	60.9
Li_2O	25.6	25.5	25.4	25.0
K_2O	2.2	2.1	2.1	2.1
MgO	1.4	2.9	3.6	3.8
CaO	1.6	3.1	3.7	4.0
Al_2O_3	2.2	2.1	2.1	2.1
P_2O_5	2.1	2.1	2.1	2.1

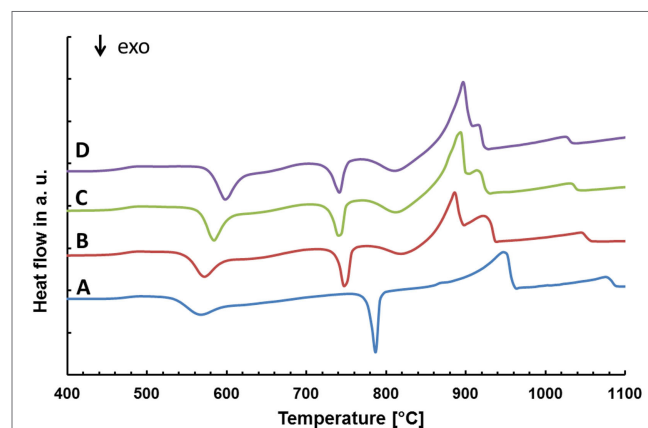


FIGURE 1 | Thermal analysis of the different base glasses.

TABLE 2 | Thermal analysis of the base glasses by means of DSC.

Base glass	A	B	C	D
T_g (°C)	462	456	456	453
$T_{\text{exo}1}$ (°C)	568	572	584	599
$T_{\text{exo}2}$ (°C)	787	750	742	741
$T_{\text{exo}3}$ (°C)	–	819	811	811
$T_{\text{endo}1}$ (°C)	947	887	893	898
$T_{\text{endo}2}$ (°C)	–	921	914	917

reduction of the silhouette area occurs for all base glasses in approximately the same temperature range between 500 and 550°C. After running through a plateau between 550 and 700°C, the area again decreases for all glasses within the same temperature range between 700 and 800°C. However, while glasses B–D

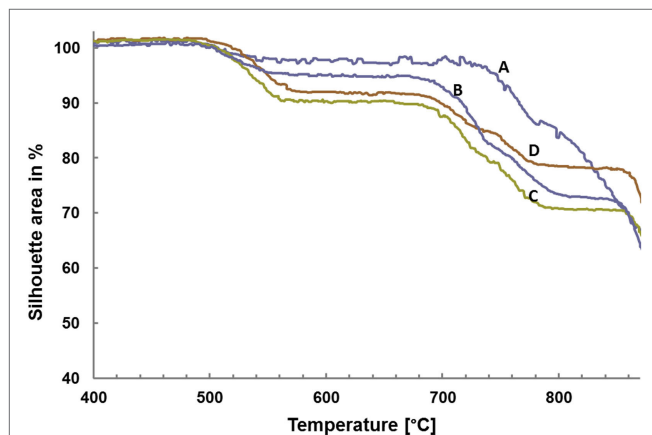


FIGURE 2 | Sintering behavior of the glass powders determined by high temperature microscopy.

again show a plateau between 800 and 850°C, no such second plateau can be found for glass A. A continuous reduction of the shadow area can be observed for all glasses at temperatures exceeding 860°C.

Diffractograms of glass D obtained by HT-XRD are presented in **Figure 3**. The diffraction patterns obtained at 29 and 500°C reveal no crystalline phases. First indications for the crystallization of Li_2SiO_3 could be observed at 540°C. Characteristic $\text{Li}_2\text{Si}_2\text{O}_5$ peaks could be analyzed in the diffractogram recorded at 680°C. At 700°C, no Li_2SiO_3 peaks were detected. However, the intensity of the $\text{Li}_2\text{Si}_2\text{O}_5$ peaks is strongly increased and Li_3PO_4 can be detected. Reflections characteristic for diopside occur at 760°C. The intensity of the diopside peaks increases until 860°C. A similar evaluation of the HT-XRD results obtained for glass-ceramics A–D is shown in **Table 3**, where those temperatures are summarized at which a first evidence for the crystallization of a certain crystal phase was found. No diopside formation was detected for glass A. Compared to B–D, glass A shows significantly increased crystallization temperatures for Li_2SiO_3 and $\text{Li}_2\text{Si}_2\text{O}_5$.

Investigating the crystallization behavior of the bulk base glass D by means of room temperature, XRD revealed $\text{Li}_2\text{Si}_2\text{O}_5$ and $\text{CaMgSi}_2\text{O}_6$ for the “as fired” sample surface. No diopside crystals were detected in the diffraction pattern recorded of the ground sample.

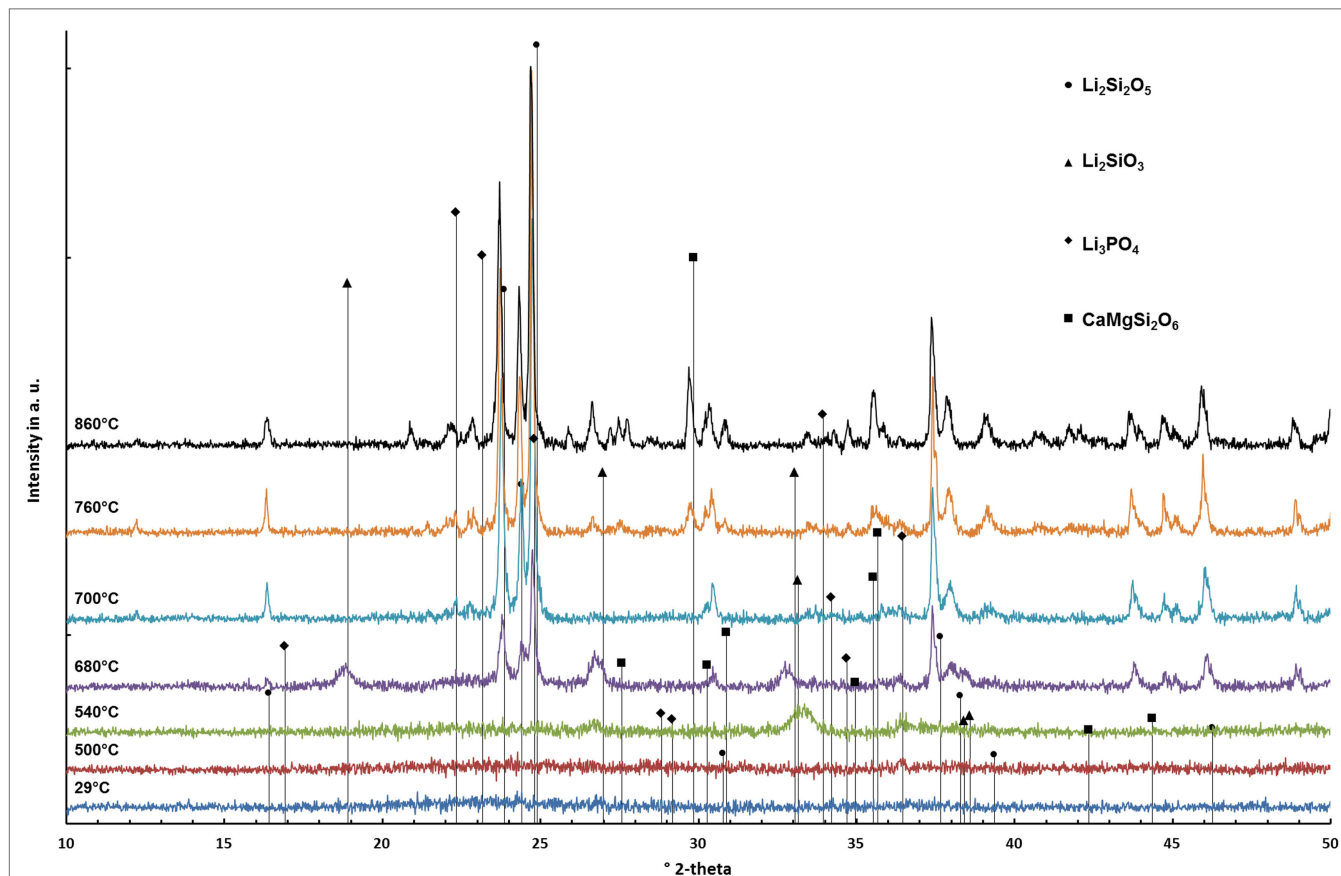


FIGURE 3 | Diffractograms of glass D surveyed at different temperatures.

TABLE 3 | Sequence of crystal phase formation as a function of temperature determined by HT-XRD.

	A	B	C	D
$\text{Li}_2\text{Si}_2\text{O}_5$ (°C)	520	520	520	540
$\text{Li}_2\text{Si}_2\text{O}_5$ (°C)	740	680	680	680
Li_3PO_4 (°C)	760	700	700	700
$\text{CaMgSi}_2\text{O}_6$ (°C)	–	740	740	760

The additional investigation of the micrograph of the fracture surface in **Figure 4** shows small ($\leq 1\ \mu\text{m}$) plate-like crystals in the bulk of the material and large bar-like crystals growing from the surface into the bulk of the material. The investigation of bulk base glass A revealed solely the formation of $\text{Li}_2\text{Si}_2\text{O}_5$, and no surface crystallization of diopside could be observed.

Characterization of the Glass-Ceramics

Diffraction patterns of the sintered glass-ceramics recorded at room temperature are shown in **Figure 5**. $\text{Li}_2\text{Si}_2\text{O}_5$ and Li_3PO_4 could be detected in all glass-ceramics. However, glass-ceramics B–D reveal the presence of diopside.

The results of the quantitative crystal phase analysis by means of Rietveld refinement are shown in **Table 4**. $\text{Li}_2\text{Si}_2\text{O}_5$ is the main crystal phase in the glass-ceramics. The content of $\text{Li}_2\text{Si}_2\text{O}_5$ decreases from A to D, while the content of diopside increases from B to C. With respect to the accuracy of measurement and refinement, there is no difference in the ratio of diopside in glass-ceramics C and D. Glass-ceramic A comprises a considerably higher ratio of amorphous residual glass phase than B–D.

Micrographs of the glass-ceramics A–D displayed in **Figure 6** reveal an interlocking microstructure of small ($\leq 1\ \mu\text{m}$) plate-like crystals. The microstructure of glass-ceramics B–D additionally comprises bar-like crystals with a length between 3 and $10\ \mu\text{m}$. The large bar-like crystals are randomly distributed within the microstructure. The analysis of the porosity revealed thoroughly dense glass-ceramics A and D, while B and C showed a linear ratio of pores of 4.5 ± 3.4 or $0.9 \pm 0.4\%$, respectively.

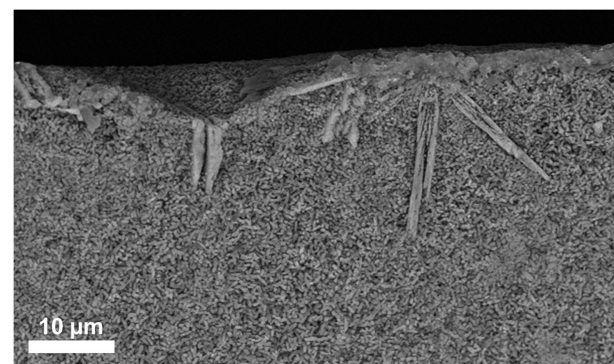
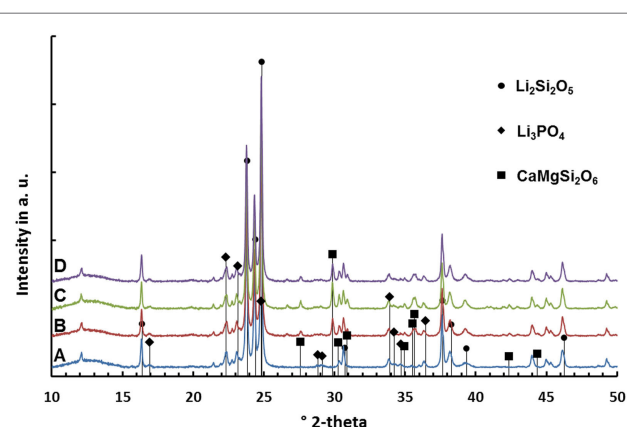
The biaxial strength of the glass-ceramics is presented in **Table 5**. Glass-ceramic D shows the highest mean biaxial strength. With respect to the SD of the measurement results, the biaxial strength of glass-ceramic D is significantly higher than that of glass-ceramics B and C. The strength of glass-ceramics A and D is in a similar range.

No significant difference in the thermal expansion properties of the different glass-ceramics could be analyzed. The results are presented in **Table 5**. $\text{CTE}_{25-500^\circ\text{C}}$ values in the range between $9.8 \times 10^{-6}\ \text{K}^{-1}$ and $10.2 \times 10^{-6}\ \text{K}^{-1}$ were determined.

All glass-ceramics show a low degree of translucency. Glass-ceramic A revealed a considerably lower opacity than glass-ceramics B–D, which are rather similar (**Table 5**).

DISCUSSION

The extension of the chemical composition of the base glass by certain amounts of MgO and CaO is the prerequisite for the precipitation of $\text{CaMgSi}_2\text{O}_6$ as a minor crystal phase in $\text{Li}_2\text{Si}_2\text{O}_5$ glass-ceramics. Increasing the content of MgO and CaO from

**FIGURE 4 | SEM micrograph taken from the fracture surface of a bulk base glass sample D crystallized at 860°C for 5 min.****FIGURE 5 | Diffractograms of glass-ceramics after sintering at 860°C for 5 min.****TABLE 4 | Quantitative composition of glass-ceramics after sintering and crystallization at 860°C for 5 min (ICSD number).**

	A	B	C	D
wt.% $\text{Li}_2\text{Si}_2\text{O}_5$ (280481)	47.8	45.7	45.2	43.2
wt.% $\text{CaMgSi}_2\text{O}_6$ (10222)	–	7.4	10.8	10.5
wt.% Li_3PO_4 (50058)	9.1	8.8	8.6	8.2
wt.% amorphous phase	43.1	38.2	35.4	38.1

approximately 1.4 to 2.9 mol% yielded the precipitation of diopside in the present study. However, no internal nucleation and crystallization of diopside was found in the present base glasses, but surface crystallization of diopside could be verified in the preliminary study of the crystallization behavior of the bulk base glass D (**Figure 4**). Hence, an activation of the glass surface was mandatory to nucleate the crystallization of diopside. In the present study, the activation of the glass surface was achieved by means of ball milling. It is important to note that the magnitude of activation of a glass surface is strongly dependent on the method and processing parameters used. There exist a lot of different milling techniques as well as there are various alternative ways to

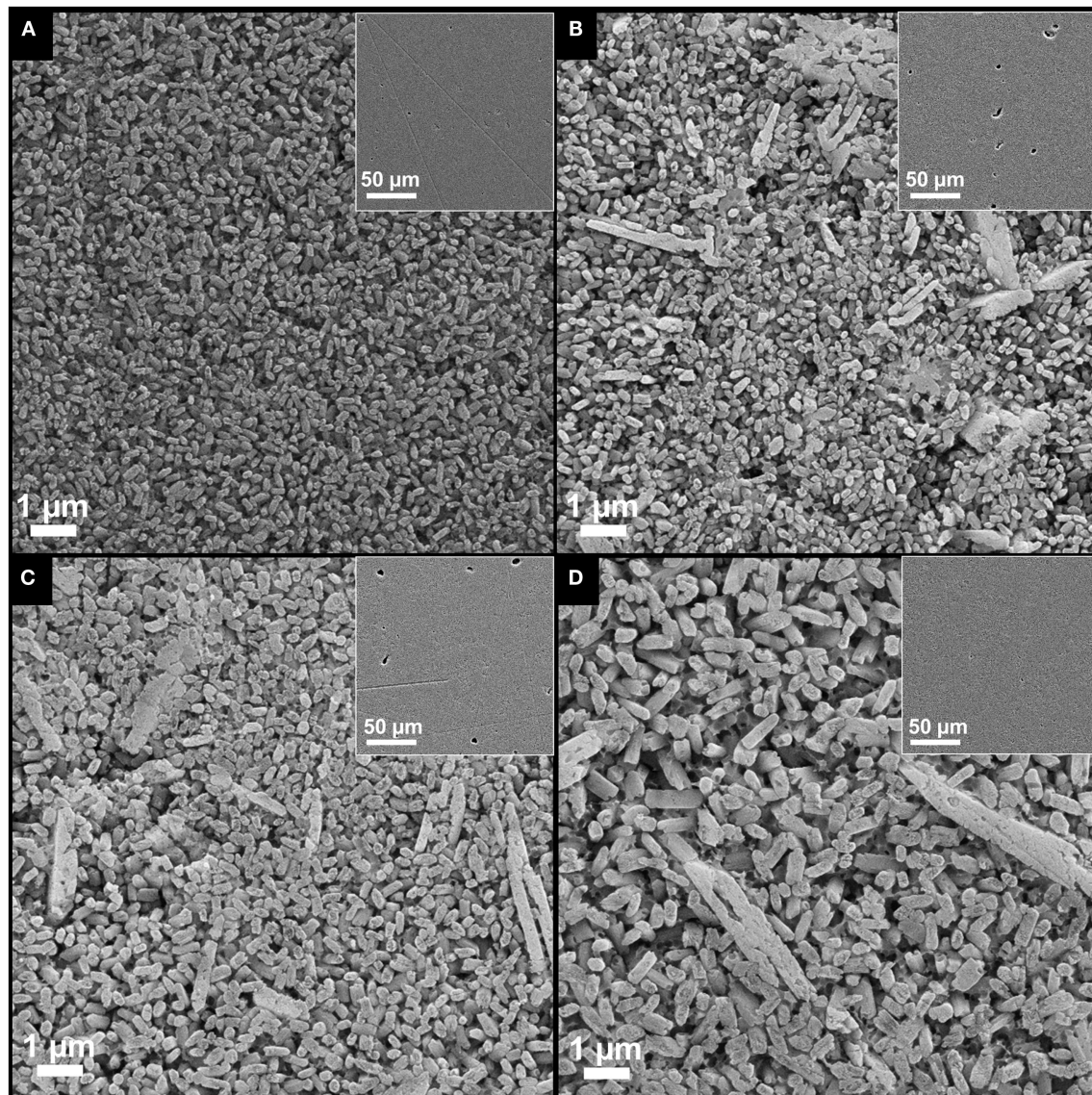


FIGURE 6 | Micrographs of the glass-ceramics (A–D) after sintering at 860°C for 5 min.

initiate surface nucleation and crystallization for different material systems, e.g., by means of tribochemistry (Henicke, 1984). Hence, the concentration of MgO and CaO that is mandatory for the crystallization of diopside can deviate dependent on the method used for the activation of the glass surface.

The analysis of the base glasses by means of DSC (**Figure 1; Table 2**) reveals two rather sharp exothermal peaks for all the base glasses. According to the data obtained by HT-XRD (**Table 3**), these peaks can be correlated to the crystallization of Li_2SiO_3 and $\text{Li}_2\text{Si}_2\text{O}_5$. The rather sharp characteristic of these peaks suggests that an internal nucleation and crystallization mechanism is dominant. The effect of P_2O_5 as internal nucleating agent for lithium silicates at a glassy amorphous interphase was previously reported in literature (Höland and Beall, 2012). HT-XRD studies in the present glass-ceramics reveal that crystalline Li_3PO_4 can

only be detected after heat treatments above 700°C, whereas the crystallization of Li_2SiO_3 already starts at $\geq 520^\circ\text{C}$ (**Table 3**). Hence, a mechanism reported by Höland and Beall (2012) describing the nucleation of lithium silicate at the interphase of a glassy amorphous or disordered nanocrystalline early phase of Li_3PO_4 seems most likely.

A rather wide exothermal signal in the DSC curves of glass B–D between 780 and 860°C are an indication for a surface nucleation and crystallization mechanism. The data obtained by HT-XRD show that diopside forms in exactly this temperature range. Hence, the authors conclude that diopside crystallizes on the activated surface of the glass grains. Furthermore, surface nucleation and crystallization display well-known mechanisms found in the investigations on diopside glass-ceramics (Kokubo et al., 1989; Zanotto, 1991; Müller et al., 2000).

TABLE 5 | Properties of the glass-ceramics.

	A	B	C	D
σ_{biax} (MPa)	329 ± 67	270 ± 60	262 ± 71	391 ± 98
CR (%)	77	88	92	92
$\text{CTE}_{25-500^\circ\text{C}} \times 10^{-6} \text{ K}^{-1}$	10.2	10.1	9.8	9.8

In summary, the precipitation of two different silica-based crystal phases from the present glass system requires the control of two essentially different nucleation mechanisms. On the one hand, the layer silicate $\text{Li}_2\text{Si}_2\text{O}_5$ is nucleated by an internal nucleation mechanism, and on the other hand, surface activation nucleates the crystallization of the chain silicate $\text{CaMgSi}_2\text{O}_6$.

To produce bulk glass-ceramics from internal and surface crystallizing base glasses, a powder compact process was developed. Crystallization of the glass powder and sintering of the powder compacts to achieve dense bulk glass-ceramics has to be controlled in parallel. Analyzing the sintering behavior of the glass powders by means of HMA (**Figure 2**), together with the results of the HT-XRD studies (**Table 3**), was the basis to develop an adequate firing cycle. According to the HMA curves, densification starts at approximately 500°C for all base glasses. Since the T_g of the base glass powders is between 450 and 460°C, the starting densification is clearly a result of the softening and beginning viscous flow of the glass. Crystallization of Li_2SiO_3 and $\text{Li}_2\text{Si}_2\text{O}_5$ between 540 and 700°C clearly increase the viscosity of the glasses and hence stop the densification as can be seen in the first plateau of the HMA curve. Base glasses B–D show a second plateau ending at approximately 855°C, which can be explained by the crystallization of diopside hindering the sintering process. Dissolution of crystal phases and melting of the glass-ceramics begins at temperatures >860°C.

Based on these results, the crystallization and sintering cycle of the powder compacts was developed. It starts with a fast heating to 480°C, where the temperature is kept for 20 min in order to internally nucleate lithium silicate at a glassy amorphous P_2O_5 -rich interface (Höland and Beall, 2012). After internal nucleation, the powder compacts were heated to 860°C with a reduced heating rate of 10 K/min. Crystallization and sintering takes place in this temperature range. To obtain a dense glass-ceramic with minimal crystal phase dissolution and viscous deformation of the specimen, the sintering cycle stops after a dwell time of 5 min at 860°C. The micrographs of the glass-ceramics in **Figure 6** reveal pores in the glass-ceramics B and C. Glass-ceramics A and D show a more homogeneous and dense microstructure than the other glass-ceramics. Based on the quantitative crystal phase analysis of the glass-ceramics (**Table 4**) and assuming that the entire ratio of amorphous P_2O_5 – Li_2O phase precipitates to Li_3PO_4 , one can roughly estimate the composition of the residual glass phases. The estimated composition of residual glass phase is shown in **Table 6**. According to this estimation, the residual glass phase of the glass-ceramic D comprises a considerably higher concentration of network modifiers such as Li_2O , MgO , and CaO . This would result in a reduced viscosity of the residual glass phases compared to glass-ceramics A–C and therefore displays an interesting point

TABLE 6 | Estimated chemical compositions of the residual glass phases in mol%.

	A	B	C	D
SiO_2	76.4	73.3	71.9	70.1
Li_2O	4.4	7.5	9.0	9.7
K_2O	5.7	6.2	6.6	6.1
MgO	3.7	3.0	2.7	3.4
CaO	4.1	3.7	3.1	4.2
Al_2O_3	5.7	6.3	6.7	6.2
P_2O_5	–	–	–	0.3

of discussion regarding the sintering properties of the glass-ceramics. Comparing the sintering properties of glass-ceramic A to B and C, the restraining influence of crystallization processes on the sintering process becomes obvious, since glass-ceramic A shows no diopside formation in contrast to B and C. A more dedicated investigation is necessary to resolve the different results of the sintering process. Furthermore, enhancing the powder processing, e.g., by granulation of the glass powder prior to uniaxial pressing, could improve the densification and sintering of the powder compacts.

The influence of the chemical composition of the base glasses on the quantitative crystal phase composition of the final glass-ceramics is shown in **Table 4**. Obviously, a concentration of ≤ 1.4 or 1.6 mol% of MgO and CaO in the base glasses is insufficient for the precipitation of $\text{CaMgSi}_2\text{O}_6$ in the present base glass system. However, as mentioned in the first paragraph of the discussion, this finding is only true for the activation of the glass powders surface by means of ball milling down to a mean grain size of about 20 μm . Increasing the concentration of MgO and CaO from 2.9 or 3.1 to 3.6 or 3.7 mol%, respectively, resulted in a considerable increase of the diopside content by 3.4 wt.%, while further increasing to 3.8 or 4 mol%, respectively, did not significantly change the concentration of diopside in the glass ceramic. The reduced content of SiO_2 together with the consumption of SiO_2 during the crystallization of $\text{Li}_2\text{Si}_2\text{O}_5$ could explain the stagnant precipitation of $\text{CaMgSi}_2\text{O}_6$, although higher concentrations of CaO and MgO are provided in the base glass.

Based on the preliminary study of crystallization (**Figure 4**) and comparing the micrographs B–D with the micrograph of the diopside-free glass-ceramic A (**Figure 6**), the crystals forming the microstructure of the glass-ceramics can be identified. Large (5–10 μm) bar-like diopside crystals are embedded in a matrix of rather small (<1 μm) plate-like $\text{Li}_2\text{Si}_2\text{O}_5$ crystals (**Figure 6**).

High concentrations of crystalline phases (>55 wt.%) (**Table 4**) as well as the arrangement of $\text{Li}_2\text{Si}_2\text{O}_5$ and $\text{CaMgSi}_2\text{O}_6$ crystals in an interlocking microstructure (**Figure 6**) contribute to the biaxial strength of the glass-ceramics (Dittmer et al., 2014). However, pores in the microstructure, as they were found particularly in glass-ceramics B and C (**Figure 6**), can decrease the biaxial strength of the materials. In a previous study on tailoring, the thermal expansion of $\text{Li}_2\text{Si}_2\text{O}_5$ glass-ceramics by precipitating a high CTE minor phase significant effects on the biaxial strength of the glass-ceramics due to the considerable mismatch in the CTEs of the involved crystal phases were reported (Rampf et al., 2015, 2016). However, in the glass-ceramic system investigated

in the present study, such effects are unlikely since there is no such huge difference in the thermal expansion of the involved crystal phases. The $\text{CTE}_{200-800^\circ\text{C}}$ of diopside crystals was investigated to be approximately $7.4 \times 10^{-6} \text{ K}^{-1}$ (Rigby and Green, 1942) and therefore very close to polycrystalline lithium disilicate ($\text{CTE}_{25-600^\circ\text{C}} = 11.4 \times 10^{-6} \text{ K}^{-1}$) compared to the investigations by Rampf et al. (2015, 2016).

The precipitation of diopside as a minor phase in $\text{Li}_2\text{Si}_2\text{O}_5$ glass-ceramics reduces the translucency of the glass-ceramic materials due to the introduction of a further interface where scattering of light occurs (Nassau, 2001). The influence of a minor crystal phase $\text{Ca}_5(\text{PO}_4)_3\text{F}$ on the optical properties of $\text{Li}_2\text{Si}_2\text{O}_5$ glass-ceramics was previously investigated by Rampf et al. (2015, 2016). They reported the optical properties, in particular the translucency, to be dominated by the $\text{Li}_2\text{Si}_2\text{O}_5$ crystals, which appeared to be significantly larger than the submicron sized apatite crystals. However, the apatite crystals having dimensions in the range of visible light did affect the opalescence of the materials. In the present system, the diopside crystals are significantly larger than the approximately $0.5\text{--}1 \mu\text{m}$ -sized $\text{Li}_2\text{Si}_2\text{O}_5$ crystals. Hence, the precipitation of diopside displays an effective tool to influence the translucency of $\text{Li}_2\text{Si}_2\text{O}_5$ glass-ceramics without affecting its opalescence properties.

Machining of the crystallized glass-ceramics using conventional CAD/CAM technology was feasible without problems. The minor diopside phase enhanced the machinability of the $\text{Li}_2\text{Si}_2\text{O}_5$ glass-ceramics probably by interfering with the high-strength interlocking $\text{Li}_2\text{Si}_2\text{O}_5$ microstructure.

CONCLUSION

Glass-ceramics comprising $\text{Li}_2\text{Si}_2\text{O}_5$ as main crystal phase and $\text{CaMgSi}_2\text{O}_6$ as minor crystal phase can be produced from base glasses in the $\text{SiO}_2\text{--Li}_2\text{O--P}_2\text{O}_5\text{--Al}_2\text{O}_3\text{--K}_2\text{O--MgO--CaO}$ system. The parallel precipitation of a layer silicate ($\text{Li}_2\text{Si}_2\text{O}_5$) on the one side and crystals of the chain silicate type ($\text{CaMgSi}_2\text{O}_6$) on

the other side require the control of two separate nucleation and crystallization mechanisms. $\text{Li}_2\text{Si}_2\text{O}_5$ can be nucleated internally at an amorphous glassy $\text{P}_2\text{O}_5\text{--Li}_2\text{O}$ -rich interphase. The activation of the glass surface, e.g., by means of ball milling, is mandatory to efficiently nucleate the crystallization of $\text{CaMgSi}_2\text{O}_6$.

The chemical composition, in particular a sufficient concentration of MgO and CaO, of the base glass is essential for the precipitation of the $\text{CaMgSi}_2\text{O}_6$ minor phase. However, the mandatory concentration of MgO and CaO can deviate with the extent or method applied for surface activation.

A reproducible powder compact process, including uniaxial pressing and sintering, was developed to produce dense $\text{Li}_2\text{Si}_2\text{O}_5\text{--CaMgSi}_2\text{O}_6$ glass ceramic materials.

$\text{Li}_2\text{Si}_2\text{O}_5\text{--CaMgSi}_2\text{O}_6$ glass-ceramics could be machined by means of conventional CAD/CAM technology and reach a biaxial strength of $391 \pm 98 \text{ MPa}$ based on the interlocking microstructure and possible additional compressive stress formation.

The large ($5\text{--}10 \mu\text{m}$) bar-like $\text{CaMgSi}_2\text{O}_6$ crystals embedded in a matrix of interlocking ($\leq 1 \mu\text{m}$) $\text{Li}_2\text{Si}_2\text{O}_5$ crystals reduce the translucency of the material and hence display a further potential tool to create new combinations of material properties within $\text{Li}_2\text{Si}_2\text{O}_5$ -based glass-ceramics.

AUTHOR CONTRIBUTIONS

MR: planning, organization, and execution of experiments; interpretation and discussion of results; and compilation of manuscript and artwork. MD: execution of Rietveld refinement; interpretation and discussion of results on XRD analysis; and assistance in compilation of the manuscript. CR: consulting in planning of experiments; interpretation and discussion of HMA and DSC; and assistance in compilation of the manuscript. WH: consulting regarding the state of the art literature on the topic; interpretation and discussion of results; and assistance in the compilation and proofreading of the manuscript.

REFERENCES

- Beall, G. H. (1971). "Structure, properties, and nucleation of glass-ceramics," in *Advances in Nucleation and Crystallization in Glasses*, 8 Edn, Vol. Special Publ. 5, eds L. L. Hench and S. S. Freiman (Columbus, OH: The Am. Ceram. Soc.), 251–261.
- Beall, G. H. (1992). Design and properties of glass-ceramics. *Annu. Rev. Mater. Sci.* 22, 91–119. doi:10.1146/annurev.ms.22.080192.000515
- Beall, G. H. (2014). Milestones in glass-ceramics – a personal perspective. *Int. J. Appl. Glass-Sci.* 5, 1–11. doi:10.1111/ijag.12063
- Dittmer, M., Ritzberger, C., Schweiger, M., Rheinberger, V., Wörle, M., and Höland, W. (2014). Phase and microstructure formation and their influence on the strength of two types of glass-ceramics. *J. Non-Cryst. Solids* 384, 55–60. doi:10.1016/j.jnoncrysol.2013.03.009
- Echeverría, L. M. (1992). New lithium disilicate glass-ceramic. *Bol. Soc. Ceram. Vid.* 5, 183–188.
- Henicke, G. (1984). *Tribochemistry*. München, Wien: Carl Hanser Verlag.
- Höland, W., and Beall, G. H. (2012). *Glass-Ceramic Technology*. Hoboken, NJ: Wiley.
- Höland, W., Frank, M., Schweiger, M., and Rheinberger, V. (1994). "Development of translucent glass-ceramics for dental applications," in *Proceedings of the 5th International Otto Schott Colloquium*, ed. C. Rüsel (Frankfurt: Verlag der Deutschen Glastechnischen Gesellschaft), 117–121.
- Höland, W., Rheinberger, V., Apel, E., and van't Hoen, C. (2007). Principles and phenomena of bioengineering with glass-ceramics for dental restorations. *J. Eur. Ceram. Soc.* 27, 1521–1526. doi:10.1016/j.jeurceramsoc.2006.04.101
- Höland, W., Rheinberger, V., van't Hoen, C., and Apel, E. (2005). P_2O_5 as an effective nucleating agent of lithium disilicate glass-ceramics. *Phosphorus Res. Bull.* 19, 36–41. doi:10.3363/prb1992.19.0_36
- Höland, W., Schweiger, M., Rheinberger, V. M., and Kappert, H. (2009). Bioceramics and their application for dental restoration. *Adv. Appl. Ceram.* 108, 373–380. doi:10.1179/174367609X414099
- Höland, W., Schweiger, M., Watzke, R., Peschke, A., and Kappert, H. (2008). Ceramics as biomaterials for dental restoration. *Expert Rev. Med. Devices* 5, 729–745. doi:10.1586/17434440.5.6.729
- Kokubo, T., Sakka, S., Sako, W., and Ikejiri, S. (1989). Preparation of glass-ceramic containing crystalline apatite and magnesium titanate for dental crown. *J. Ceram. Soc. Jpn. Ed.* 97, 236–240.
- Mauro, J. C., Ellison, A. J., and Pye, L. D. (2013). Glass: the nanotechnology connection. *Int. J. Appl. Glass-Sci.* 4, 64–75. doi:10.1111/ijag.12030
- Müller, R., Zanotto, E. D., and Fokin, V. M. (2000). Surface crystallization of silicate glasses: nucleation sites and kinetics. *J. Non-Cryst. Solids* 274, 208–213. doi:10.1016/S0022-3093(00)00214-3
- Nassau, K. (2001). *The Physics and Chemistry of Color*. Hoboken, NJ: Wiley.
- Rampf, M., Dittmer, M., Ritzberger, C., Schweiger, M., and Höland, W. (2015). Properties and crystallization phenomena in $\text{Li}_2\text{Si}_2\text{O}_5\text{--Ca}_5(\text{PO}_4)_3\text{F}$ and

- $\text{Li}_2\text{Si}_2\text{O}_5$ – $\text{Sr}_5(\text{PO}_4)_3\text{F}$ glass–ceramics via twofold internal crystallization. *Front. Bioeng. Biotechnol.* 3:122. doi:10.3389/fbioe.2015.00122
- Rampf, M., Fisch, M., Dittmer, M., Ritzberger, C., and Höland, W. (2016). Tailoring the thermal expansion of glass-ceramics by controlled twofold crystallization of $\text{Li}_2\text{Si}_2\text{O}_5$ and $\text{CsAlSi}_5\text{O}_{12}$. *Int. J. Appl. Glass Sci.* 7, 285–294. doi:10.1111/ijag.12180
- Reinsch, S., Nascimento, M. L. F., Müller, R., and Zanotto, E. D. (2008). Crystal growth kinetics in cordierite and diopside glasses in wide temperature ranges. *J. Non-Cryst. Solids* 354, 5386–5394. doi:10.1016/j.jnoncrysol.2008.09.007
- Rigby, G. R., and Green, A. T. (1942). The thermal expansion characteristics of some calcareous and magnesium minerals. *Trans. Br. Ceram. Soc.* 41, 123–143.
- Stookey, S. D. (1959). Catalyzed crystallization of glass in theory and practice. *Ind. Eng. Chem.* 51, 805–808. doi:10.1021/ie50595a022
- Zanotto, E. D. (1991). Surface nucleation of diopside glass. *J. Non-Cryst. Solids* 130, 217–219. doi:10.1016/0022-3093(91)90458-I

Conflict of Interest Statement: The authors are employees of the company Ivoclar Vivadent AG. A patent was filed on the present subject.

The reviewer LM and handling Editor declared their shared affiliation, and the handling Editor states that the process nevertheless met the standards of a fair and objective review.

Copyright © 2016 Rampf, Dittmer, Ritzberger and Höland. This is an open-access article distributed under the terms of the Creative Commons Attribution License (CC BY). The use, distribution or reproduction in other forums is permitted, provided the original author(s) or licensor are credited and that the original publication in this journal is cited, in accordance with accepted academic practice. No use, distribution or reproduction is permitted which does not comply with these terms.



The TTT Curves of the Heterogeneous and Homogeneous Crystallization of Lithium Disilicate – A Stochastic Approach to Crystal Nucleation

Susanne Krüger and Joachim Deubener*

Institute of Non-Metallic Materials, Clausthal University of Technology, Clausthal-Zellerfeld, Germany

OPEN ACCESS

Edited by:

Ashutosh Goel,
Rutgers University, USA

Reviewed by:

John Stuart McCloy,
Washington State University, USA

Qiang Fu,

Corning Inc., USA

Daniel Roberto Cassar,
Federal University of Sao Carlos,

Brazil

Anuraag Gaddam,
University of Aveiro, Portugal

*Correspondence:

Joachim Deubener
joachim.deubener@tu-clausthal.de

Specialty section:

This article was submitted to
Glass Science, a section of the
journal *Frontiers in Materials*

Received: 09 July 2016

Accepted: 12 August 2016

Published: 31 August 2016

Citation:

Krüger S and Deubener J (2016) The
TTT Curves of the Heterogeneous
and Homogeneous Crystallization of
Lithium Disilicate – A Stochastic
Approach to Crystal Nucleation.
Front. Mater. 3:42.
doi: 10.3389/fmats.2016.00042

The present study explores the temperature and time dependence of heterogeneous (HET) crystal nucleation in a lithium disilicate glass using the stochastic approach. In particular, a single lithium disilicate sample was repeatedly (284 runs) undercooled to 1173 K in a PtRh-crucible and the crystallization onset time during an isothermal hold was detected in each run. The statistical distribution of the times elapsed before crystallization is described by a first-order reaction with a HET crystal nucleation rate of $(9.19 \pm 0.04) \times 10^{-4} \text{ s}^{-1}$ while individually shaped crystallization exotherms of each run were recorded, which indicate growth of a single or only few crystals during crystallization of the entire volume. The data were used together with results of previous stochastic experiments and those of double-stage heat treatments to calculate the crystallization time of a fraction of 10^{-4} percent for all temperatures between glass transition and melting. The derived TTT diagram shows a double-nose of crystallization in the volume at large undercoolings ($0.53\text{--}0.61 T_m$) and crystallization at the surface at small undercoolings ($0.62\text{--}0.92 T_m$) initiated by homogeneous and HET crystal nucleation, respectively. The critical cooling rate at the HET nose is approximately 73 K s^{-1} .

Keywords: lithium disilicate glass, time of formation of the first supercritical nucleus, stochastic nature of crystal nucleation, effective nucleation rate, TTT representation, coast-island microstructure

INTRODUCTION

In the last 40 years, crystal nucleation in silicate glasses has been addressed by counting crystal number densities in the volume of glass specimens subjected to double-stage heat treatments (Fokin et al., 2006). The technique bears the advantage of direct determination of the crystal nucleation rate from calculating the first time derivative of the number density curve but has the drawback that it is limited to a narrow temperature range near the glass transformation temperature ($T_g \leq T \leq 1.2 T_g$) where driving forces are high and crystal nucleation is occurring frequently in the volume. Another drawback is the dissolution of nuclei that are critical at the first stage but subcritical at the second stage. In the case of surface crystallization, the accessible temperature range becomes broader but the time period of crystal nucleation is mostly limited due to fast saturation of active sites. A short nucleation period merely allows for an indirect determination of the crystal nucleation rate. Thus, birth- (from crystal size distribution) (Müller et al., 2000) and impingement-times (Krüger and Deubener, 2015a) of crystals at the surface have been analyzed to deduce

their rates of nucleation. In each of these methods (and also for analyzing high-temperature X-ray diffraction data (Dressler et al., 2011, 2014), an ensemble of crystals is analyzed in order to derive nucleation parameters. The criterion applies for large undercoolings but becomes ineffective at higher temperatures where crystal growth rates are generally high and the entire liquid volume is shortly consumed by the first nucleated crystal. In consequence, nucleation data for temperatures $T > 1.2 T_g$ are lacking for both binary/ternary model glasses and for technical multi-component glass systems. The occurrence of a substantial gap in the reported nucleation data is surprising and unexpected if one recalls the large number of glasses produced in industrial practice by forming during quench. Furthermore, the analysis of a crystal ensemble does not allow to prove randomness in the nucleation events, a necessary condition in the framework of CNT. By contrast, the observation of single crystal events helps in discriminating partition of long-range diffusion fluxes (Kelton, 2000).

In the light of the above, this study aims at establishing nucleation kinetics by its time average of repeated single crystal nucleation events rather than using the ensemble average of crystals of double-stage heat treatments. The so-called stochastic approach to crystal nucleation has been introduced for undercooled low viscous (mPa s) liquids, such as metals and hydrous suspensions (Toshev and Markov, 1967; Toshev and Gutzow, 1972; Toshev et al., 1972; Toshev, 1973; Morton et al., 1994; Barlow and Haymet, 1995; Uttormark et al., 1997; Heneghan et al., 2001, 2002; Heneghan and Haymet, 2002; Wilson et al., 2005; Wilde et al., 2006, 2009; Yang et al., 2009, 2011, 2013). Our results show that it is applicable to high viscous (kPa s) silicate melts and it results in heterogeneous (HET) crystal nucleation rates from which TTT representations and critical cooling rates can be derived.

The formation of supercritical nuclei is a stochastic process. Nucleation events occur randomly and independent from each other. Already in the 1960s, Toshev and Markov (1967) showed that the electrolytic deposition of cadmium on platinum single crystal electrodes follows a Poisson distribution. Thereby, both the number of nuclei in a given time interval and the time necessary to form a certain number of nuclei are linked to probability distributions (Toshev and Gutzow, 1972; Toshev et al., 1972; Toshev, 1973).

Later probability distribution functions in the formation of the first supercritical nucleus have been studied for other liquid metals, such as niobium and zirconium (Morton et al., 1994), aluminum (Uttormark et al., 1997), gold and copper (Wilde et al., 2006, 2009), and tin (Yang et al., 2009, 2011, 2013) but also in water (pure and seeded) (Barlow and Haymet, 1995; Heneghan et al., 2001, 2002; Heneghan and Haymet, 2002; Wilson et al., 2005) and in gas hydrates (Maeda et al., 2011, 2012). In all these experiments, a single sample was repeatedly undercooled from above the melting temperature, while either the time (at an isothermal hold) or the temperature (at an isochronal cooling) of crystallization was detected. These experiments provided primary information on the average lag time and the mean undercooling, from which the crystal nucleation rate and the critical cooling rate can be derived. Secondary information include the activity of seeds and the purification of the liquid upon thermal cycling. Especially the ALTA (“automated lag time apparatus”) concept

developed for studying the freezing behavior of water (Barlow and Haymet, 1995) is acknowledged since it has been designed to permit time-saving through a feed-back control that heats the sample immediately upon freezing.

In the past years, non-adiabatic fast scanning calorimetry has been developed to *in situ* measure the response of single metallic drops to temperature changes in a large range of cooling rate spanning four orders of magnitude (Yang et al., 2009, 2011, 2013). In these experiments, a small drop (volume $\approx 10^{-6} \text{ mm}^3$) is repeatedly heated and cooled on a thin film sensor with rates up to 10^4 K s^{-1} . Unfortunately, current technology of the so-called flash- or chip-calorimeters is limited to a maximum sensor temperature of about 700 K, which is much lower than the liquidus temperature of lithium disilicate glass [1306 K (Kracek, 1930)].

Glasses in the binary $\text{Li}_2\text{O}-\text{SiO}_2$ system, such as lithium disilicate ($\text{Li}_2\text{Si}_2\text{O}_5$) have been the object of extensive research (see, for example, Tomozawa, 1972, 1973; Matusita and Tashiro, 1973; James, 1974, 1985; Fokin et al., 1981; Weinberg and Neilson, 1985; Barker et al., 1988; Deubener et al., 1993; Ota et al., 1997; Burgner and Weinberg, 2001; Nascimento et al., 2011) since their crystal nucleation and growth rates are relatively low at high undercoolings ($T < 1.2 T_g$) and thus conveniently measurable from crystal number densities and crystal sizes of optical microscopy images (James, 1974, 1989; Rowlands and James, 1979). Furthermore, detailed thermodynamic data are available for this system (Takahashi and Yoshio, 1973) which allow to test the validity of basic nucleation models from comparisons of predicted rates with measured data (Neilson and Weinberg, 1979; Rowlands and James, 1979; Zanutto and James, 1985; Weinberg and Zanutto, 1989; Fokin et al., 2010a).

$\text{Li}_2\text{Si}_2\text{O}_5$ crystals nucleate homogeneously in the volume (James et al., 1978; James, 1985; Zanutto and James, 1985; Zanutto, 1987; Barker et al., 1988) disregarding the controversy of metastable phase formation prior to the crystallization of stable $\text{Li}_2\text{Si}_2\text{O}_5$ crystals (Hench et al., 1971; Tomozawa, 1972; Barker et al., 1988; Deubener et al., 1993; Zanutto, 1997; Burgner et al., 1999; Iqbal et al., 1999) but also heterogeneously at suspended particles, such as platinum (Cronin and Pye, 1986; Narayan et al., 1996; Ray and Day, 1996; Ray et al., 1996; Mishima et al., 2006; Ranasinghe et al., 2007) and at the surfaces with the surrounding gas atmosphere (James, 1989; Ray and Day, 1996; Ray et al., 1996; Ranasinghe et al., 2007; Fokin et al., 2010b). Ranasinghe et al. (2007) performed heat treatments on pure and platinum doped $\text{Li}_2\text{Si}_2\text{O}_5$ glasses and found that the critical cooling rate increases and the activation energy of crystallization decreases when $\text{Li}_2\text{Si}_2\text{O}_5$ glass is heated in a container as compared to containerless processing (levitation) and that in both cases platinum promotes the crystallization of lithium disilicate glasses. However, the temperature dependence of preferred HET crystal nucleation leading to observable “coast-island” microstructures [see Fig. 1C in Krüger and Deubener (2015a) and Fig. 14 in Fokin et al. (2010b)] is not well understood with respect to isothermal heat treatments and for ramping at constant rates from above melting temperature and below glass transformation temperature, respectively.

The present paper reports on novel experiments of HET crystal nucleation, which have been performed by the stochastic approach under isothermal conditions at small undercooling ($1.6 T_g$). In

particular, the time elapsed before the formation of the first supercritical nucleus is detected from repeated measurements in a PtRh-crucible and the HET steady-state nucleation rate is derived from the first-order kinetics of the probability distribution function. Using previous data (Krüger and Deubener, 2014, 2015a), a TTT diagram is produced from which the HET and homogeneous (HOM) crystallization can be clearly distinguished. The TTT curves of lithium disilicate help in understanding the development of coast-island microstructures observed in practice during cooling from above the liquidus temperature. We assume that the here established method is able to clarify also the crystallization mechanisms in other glass-forming systems.

EXPERIMENTAL

A glass of nominal composition $\text{Li}_2\text{Si}_2\text{O}_5$ was prepared by melting a batch of the raw materials SiO_2 and Li_2CO_3 (both of analytical grade). The batch was mixed and melted three times in a platinum crucible at 1673 K for 1 h under ambient conditions. The melt was subsequently quenched between two steel plates, which resulted in cooling rates of $\sim 150\text{--}250\text{ K min}^{-1}$. The glass was analyzed by X-ray fluorescence (S4 Pioneer; Bruker AXS, Karlsruhe, Germany) while the Li_2O content was determined by atomic emission spectroscopy (ICP-OES Vista MPX; Varian). The analyzed chemical composition was 77.4 SiO_2 , 21.0 Li_2O , and 1.6

impurities (all in percent by weight), which slightly deviates from the nominal stoichiometry of $\text{Li}_2\text{Si}_2\text{O}_5$.

A chip ($= 21.4\text{ mg}$) of the glass was inserted in a lidded PtRh-crucible and subjected to high-temperature differential scanning calorimetry (DSC 404 F3 Pegasus; Netzsch, Selb, Germany) under nitrogen atmosphere. A scheme of the operating mode of the DSC with the characteristic repeatedly performed heating-dwelling-cooling-dwelling cycles (red dashed-dotted line) is shown in **Figure 1**. In particular, the glass chip was heated at 0.167 K s^{-1} to a temperature of 1353 K, which is 47 K above T_m [$T_m = 1306\text{ K}$ (Kracek, 1930)], dwelled for 300 s to ensure fully melting of the sample, cooled by $\sim 1.25\text{ K s}^{-1}$ to the dwell temperature of 1173 K (undercooling $\Delta T = 133\text{ K}$) and dwelled for 3360 s [the dwell time was set to ca. 1 h, a reasonable time in accordance with the results of Krüger and Deubener (2014)]. After dwelling the sample was immediately heated again to start the next run. In total 284 ($= N_0$) runs were performed. In each run, the time elapsed before the first supercritical nucleus is formed (δ_N and δ_{N+1}) was calculated by subtracting the beginning of the isothermal hold ($t_{b(N)}$ and $t_{b(N+1)}$) from the crystallization onset time (t_N and t_{N+1}) of the isothermal exothermal DSC signal (blue solid line in **Figure 1**). We assume that the recorded crystallization onset times follow the same distribution as δ_N and δ_{N+1} since the time for crystal growth is negligible at this high temperature.

RESULTS

The basic result of our experiment is a histogram of the time of the formation of the first supercritical nucleus for each run δ_N in dependence of the run number N (**Figure 2**). This histogram provides the following information: first, 26 runs were crystallized before the dwell temperature at $\Delta T = 133\text{ K}$ was reached ($\delta_N < 0\text{ s}$,

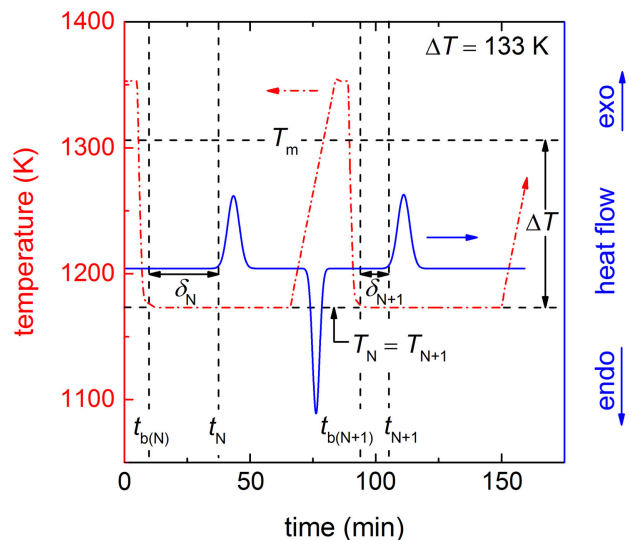


FIGURE 1 | Scheme of the DSC protocol for two subsequent cooling-dwelling runs (N and $N + 1$) in the isothermal operating mode ($\Delta T = 133\text{ K}$). The red dashed-dotted line shows the progression of the temperature of the heating-dwelling-cooling-dwelling cycles. The black horizontal dashed lines are T_m and the nucleation temperature of the runs N and $N + 1$ with $T_N = T_{N+1} = 1173\text{ K}$, thus $\Delta T = 133\text{ K}$ (black double arrow). The black vertical dashed lines show the times of the beginning of the isothermal hold of the runs N and $N + 1$ with $t_{b(N)}$ and $t_{b(N+1)}$, respectively and the times of the start of the crystallization of both runs with t_N and t_{N+1} . Herein, the beginning of the crystallization equals the onset of the exothermal peak in the DSC signal (blue solid line). The time of the formation of the first supercritical nucleus in each run (black horizontal double arrows) δ_N (for run N) and δ_{N+1} (for run $N + 1$) is calculated by $t_N - t_{b(N)}$ and $t_{N+1} - t_{b(N+1)}$, respectively.

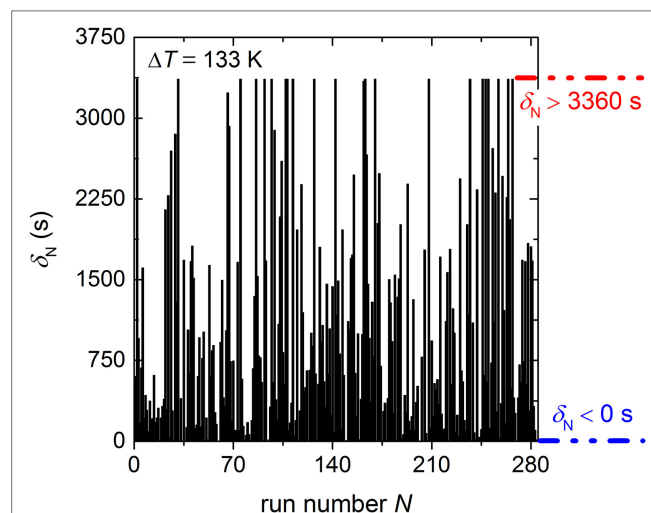


FIGURE 2 | Time of formation of the first supercritical nucleus δ_N in dependence of the run number for the undercooling of 133 K. It has to be noted that 26 runs crystallized during cooling to the dwell temperature ($\delta_N < 0\text{ s}$; blue dashed-dotted line) and 21 runs were not crystallizing within the dwell time 3360 s ($\delta_N > 3360\text{ s}$; red dashed-dotted line).

blue dashed-dotted line of **Figure 2**) and 21 runs remained uncrystallized due to the programmed maximum dwell time of 3360 s ($\delta_N > 3360$ s, red dashed-dotted line of **Figure 2**). Second, the histogram shows a random distribution of δ_N which indicates that the preferred HET nucleation site is continuously active during the entire experiment. A fast Fourier transformation (not shown) proved absence of any diurnal or other periodic behavior. One may assume that the crystal nucleates at the three-phase boundary between the silicate melt, the crucible wall, and the nitrogen atmosphere, but this is not known. Furthermore, the silhouette of **Figure 2** (black outline of the time elapsed before the first supercritical nucleus is formed) seems to be horizontal, which indicates that compositional changes of the melt due to possible nitrogen dissolution and lithium evaporation at the surface are negligible. Furthermore, no shift in the integrated signal values was observed (not shown) which confirms the absence of any traceable mass loss during the entire period of the experiment.

In order to determine the HET steady-state nucleation rate $I_0(\text{HET})$ from this isothermal experiment, the relative frequencies of the number of runs remained unfrozen after a certain time are calculated. The procedure is similar to the calculation of the survival curve in Barlow and Haymet (1995) and Krüger and Deubener (2014). The δ_N data of **Figure 2** are first arranged according to their length. At the shortest δ_N ($=0$ s), there are 258 runs uncrystallized (26 runs crystallized during cooling to the dwell temperature). In all other runs, crystallization occurred at larger δ_N . For $\delta_N = 0$, the uncrystallized fraction is $N(\delta_N = 0)/N_0 = 258/284 = 0.908$. For the second shortest δ_N , the fraction uncrystallized is $257/284 = 0.905$ and so on. The last $N(\delta_N)/N_0$ fraction calculated in that way is $21/284 = 0.074$ at $\delta_N = 3342$ s since 21 runs were still uncrystallized at the end of the programmed isothermal hold. This fraction is set to 0. The calculated fractions $N(\delta_N)/N_0$ are plotted as a function of δ_N (**Figure 3**). The distribution curve shows a simple exponential decay that illustrates an increase in the nucleation probability with longer δ_N . The nucleation probability can be described by a simple first-order rate equation

$$\frac{N(\delta_N)}{N_0} = A \exp(-I_0(\text{HET})\delta_N) \quad (1)$$

and its logarithmic form

$$\ln\left(\frac{N(\delta_N)}{N_0}\right) = \ln(A) - I_0(\text{HET})\delta_N \quad (2)$$

where the constant A accounts for the initially crystallized fraction at $\delta_N = 0$. Equation 2 is shown by the insert of **Figure 3**. The apparently linear dependence of the data on δ_N confirmed first-order reaction kinetics, and fitting the data (green solid line in **Figure 3**) results in a HET crystal nucleation rate of $I_0(\text{HET}) = (9.19 \pm 0.04) \times 10^{-4} \text{ s}^{-1}$. We note that exclusion of the 26 runs crystallized before the isothermal hold is reached results in the same value of $I_0(\text{HET})$ but the parameter A of Eq. 1 will become unity. However, we think that the consideration of all data points in the probability distribution as shown in **Figure 3** is the most appropriate linking to the stochastic experiment.

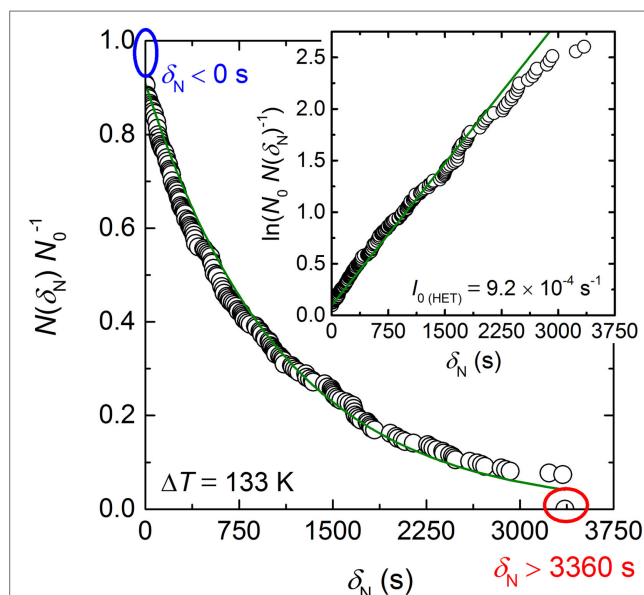


FIGURE 3 | Probability distribution of the fraction of runs uncrystallized ($N(\delta_N)/N_0$) in dependence of δ_N . The ovals (blue and red) correspond to the dashed-dotted lines of **Figure 2**. The insert shows the logarithmic Eq. 2. $I_0(\text{HET})$ is given as the slope of the linear dependence. The green solid line is the best linear fit through the data with a regression coefficient $R^2 = 0.995$.

DISCUSSION

The most striking feature of the results is that the found exponential decay of **Figure 3** is similar to those reported for seeded water (Barlow and Haymet, 1995; Heneghan et al., 2001, 2002). This underlines the fundamental character of crystal nucleation as a stochastic process obeying first-order reaction kinetics. However, one should note that due to the experimental constraints, such as the limited cooling rate to reach the dwell temperature and the restricted dwell time of 3360 s, 47 of the 248 runs are not captured by the probability distribution. Thus, a second crystal nucleation mechanism might be active with characteristic time scales $t_N < t_{b(N)}$ and $t_N > \delta_N$ (3360 s). This assumption is supported by the fact that the long time fractions of **Figure 3** show a negative deviation from the proposed linearity. On the other hand, the negative deviation can also arise from an insufficient number of cooling runs preventing good statistics and, therefore, underestimating $N(\delta_N)/N_0$ at long times.

In order to exclude memory effects between adjacent runs of the histogram (**Figure 2**), a Pearson correlation test (Barlow and Haymet, 1995; Heneghan et al., 2001) was performed (not shown). A Pearson correlation coefficient $r = 0.01$ was obtained, which confirms that the probability of having correlation between adjacent runs is close to 0. The exclusion of memory effects is illustrated by different onset times of adjacent runs (**Figure 4**). Herein, the runs 6 and 7 exhibit significantly different crystallization onset times. Moreover, the individual evolution of the heat release of each run of **Figure 4** reveals growth of one or only few crystals (Krüger and Deubener, 2014). A larger ensemble of growing crystals would lead to an averaged signal shape (Gaussian) as it is typical for heating lithium disilicate glasses in DTA/DSC experiments

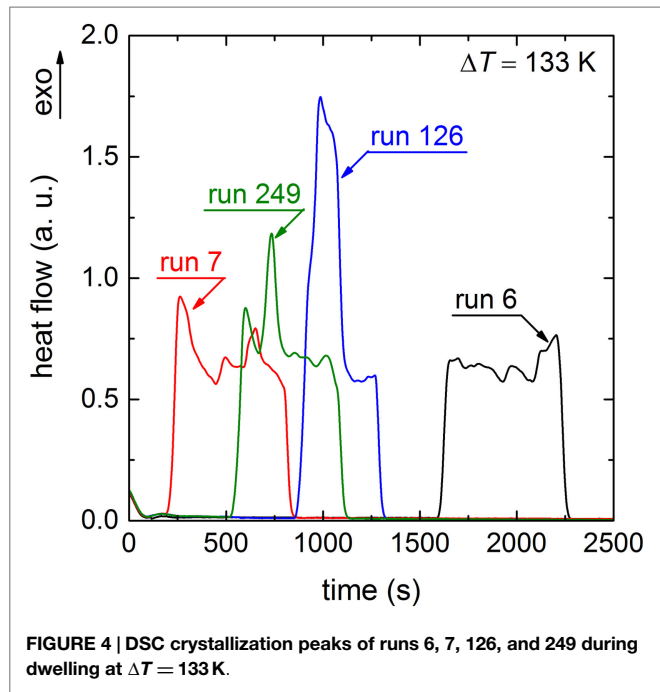


FIGURE 4 | DSC crystallization peaks of runs 6, 7, 126, and 249 during dwelling at $\Delta T = 133$ K.

from temperatures below glass transformation (Krüger et al., 2013).

Additionally to the visual inspection of the signal's shape the broadness is analyzed. As an example, the signal of run 249 exhibits a broadness of 600 s (Figure 4). Assuming only one growing crystal and a crystal size that corresponds to the circumference of the crucible (the final geometry of the crystal after 284 runs is ring-shaped due to wetting of the crucible walls by the $\text{Li}_2\text{Si}_2\text{O}_5$ melt) leads to a crystal growth rate of $3.4 \times 10^{-5} \text{ m s}^{-1}$. The approximated growth rate from the signal's length is very close to the reported value ($5.1 \times 10^{-5} \text{ m s}^{-1}$) of Burgner and Weinberg (2001) for the same temperature that supports the assumption that the entire liquid volume is consumed by only one or few crystals. Few crystals would result in a somewhat smaller broadness (see, e.g., run 126 of Figure 4). A low number of crystals growing simultaneously at the surface are further supported by the observations of Ranasinghe et al. (2007). They found that only up to two crystals were simultaneously growing at the surface of levitated $\text{Li}_2\text{Si}_2\text{O}_5$ drops. Thus, in accordance with our DSC protocol (Figure 1), assigning the onset time of the crystallization peak to the time of the formation of the first supercritical nucleus seems to be reasonable.

In order to link $I_{0(\text{HET})}$ to our previous stochastic experiment (Krüger and Deubener, 2014), which was run under constant cooling conditions (cooling rate = 0.083 K s^{-1}), nucleation rate data have to be derived from the undercooling-dependent $N(\Delta T)/N_0$ vs. ΔT distribution curve (Figure 5). In this case, the probability curve with the fractions of runs remaining unfrozen $N(\Delta T)/N_0$ at a certain undercooling is deconvoluted considering the temperature-dependent $I_{0(\text{HET})}$:

$$I_{0(\text{HET})} = \frac{C_1}{\eta} \exp\left(-\frac{C_2}{T\Delta T^2}\right) \quad (3)$$

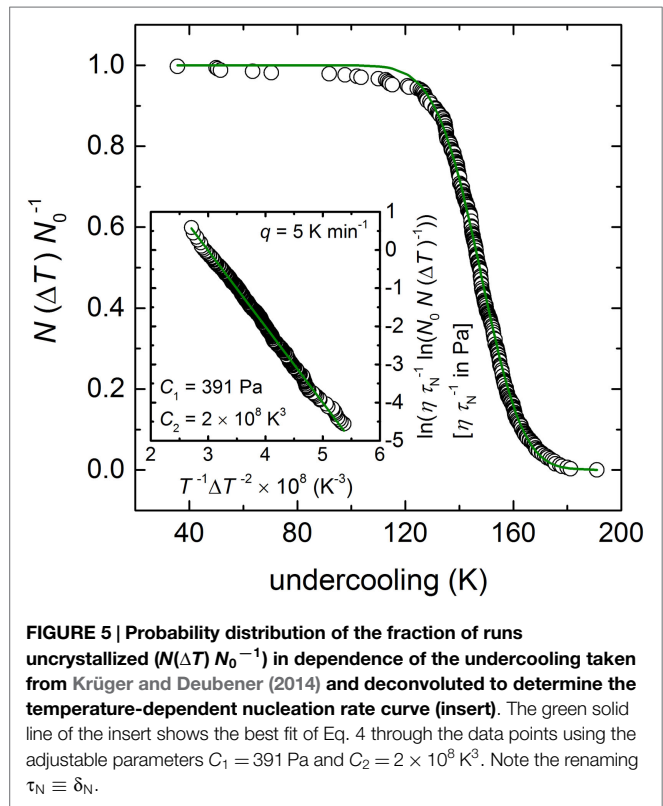


FIGURE 5 | Probability distribution of the fraction of runs uncrystallized ($N(\Delta T) N_0^{-1}$) in dependence of the undercooling taken from Krüger and Deubener (2014) and deconvoluted to determine the temperature-dependent nucleation rate curve (insert). The green solid line of the insert shows the best fit of Eq. 4 through the data points using the adjustable parameters $C_1 = 391$ Pa and $C_2 = 2 \times 10^8 \text{ K}^3$. Note the renaming $\tau_N \equiv \delta_N$.

where C_1 and C_2 are temperature-independent constants and η is the viscosity of the $\text{Li}_2\text{Si}_2\text{O}_5$ melt. In order to determine C_1 and C_2 from the isochronal experiment, Eq. 3 is inserted in Eq. 1 and the parameter A is set to unity. By doing so, we assume that the crystal nucleation process is independent on the cooling rate. Rearranging the equation and taking the logarithm results in:

$$\ln\left[\frac{\eta}{\delta_N} \ln\left(\frac{N_0}{N(\Delta T)}\right)\right] = \ln(C_1) - \frac{C_2}{T\Delta T^2}. \quad (4)$$

By applying Eq. 4 to the already published data of Krüger and Deubener (2014) and the temperature-dependent viscosity of Krüger and Deubener (2015b), the adjustable parameter $C_1 = 391$ Pa and $C_2 = 2 \times 10^8 \text{ K}^3$ were determined (green solid line in the insert of Figure 5). We note the small deviation from the fitted trend of the runs of $\Delta T < 120$ K that is either an artifact of an insufficient number of cooling runs or an indication of a second crystal nucleation mechanism as already discussed in case of the isothermal experiment.

Plotting together the HET nucleation rate curve of the above calculation in the range 0.62 – $0.92 T_m$ (red solid line), $I_{0(\text{HET})}$ of the isothermal experiment at $T = 0.898 T_m$ (red circle), $I_{0(\text{HET})}$ of single-stage experiments in the range 0.64 – $0.68 T_m$ (Krüger and Deubener, 2015a) (red squares), and the HOM nucleation rates of double-stage experiments in the range 0.53 – $0.61 T_m$ (James, 1974; Zanutto and James, 1985; Barker et al., 1988; Deubener et al., 1993) (blue circles) on the reduced temperature scale T/T_m reveals that the HET nucleation rate curve is well separated from the HOM one. Maximum nucleation rates are found at $T_{\text{max (HOM)}} = 0.55 T_m$ and $T_{\text{max (HET)}} = 0.82 T_m$ for the HOM and

the HET crystal nucleation, respectively (Figure 6). The equations of the classical nucleation theory and the material-specific input parameters listed in Tables 1 and 2 were used to fit these experimental data (OriginPro 9.0.0G; OriginLab Corp.). In order

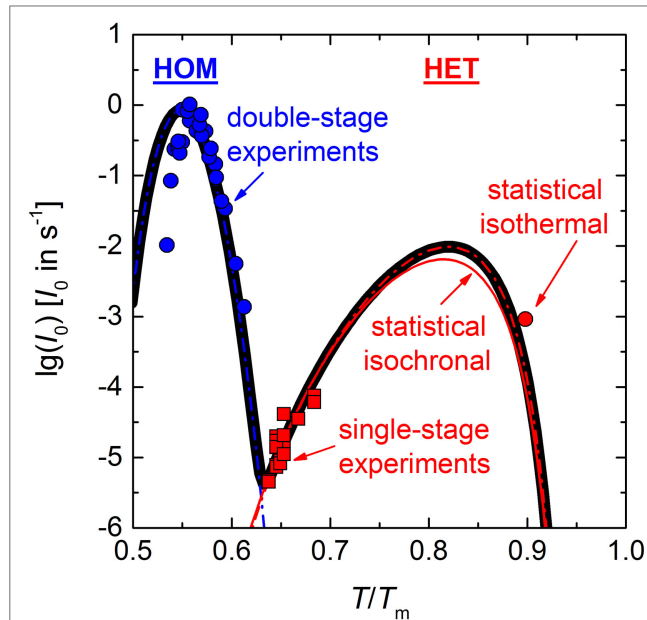


FIGURE 6 | Temperature-dependent homogeneous (HOM) and heterogeneous (HET) nucleation rate curves (blue and red dashed-dotted lines, respectively) and the effective nucleation rate curve (black solid line). Data: surface nucleation rate calculated by Eq. 3 and using the constants C_1 and C_2 as determined in Figure 5 (red solid line), I_0 (HET) of the isothermal experiment of Figure 3 (red circle), I_0 (HET) as determined from impingement times of single-stage experiments (Krüger and Deubener, 2015a) (red squares). Homogeneous nucleation rates of double-stage experiments (James, 1974; Zanotto and James, 1985; Barker et al., 1988; Deubener et al., 1993) (blue circles).

to calculate crystal nucleation rates (blue and red dashed-dotted lines in Figure 6) in the dimension of a frequency, HOM and HET nucleation rates were multiplied by the sample volume and the surface area, respectively. The liquid–crystal interfacial energy was treated as an adjustable parameter for which a linear temperature dependence in accordance with James (1985) was anticipated (Tables 1 and 2). The coordination number of the moving particle ($CN = 2$) and the number of atoms in a structural unit ($n = 9$) both entering the Eyring equation to adopt diffusivity to viscous flow where utilized from a previous study (Krüger and Deubener, 2015b). In case of the HET nucleation rate curve, additionally the number of active nucleation sites $n_s = (0.023 \pm 0.001) \text{ m}^{-2}$ and the wetting angle $\theta = (26.4 \pm 0.1)^\circ$ were adjusted to fit the data best. The resulting curves emphasize that at T_{\max} the HET crystal nucleation rate is about two orders of magnitude smaller than the HOM one. The sum of both rates is the effective crystal nucleation rate that is highlighted by the black solid line in Figure 6. We note that possible sources of the small deviation between I_0 (HET) of the isothermal and the isochronal statistical experiment are differences in the glass composition and changes in the quality of the crucible used in the two studies.

With regard to the large difference in T_{\max} between surface and volume crystal nucleation in lithium disilicate, it is interesting to compute a TTT diagram for the crystalline fraction $\alpha = 10^{-6}$ (Uhlmann, 1972) using the following two equations (Zanotto, 1996):

$$t_V = \left(-\frac{3 \ln(1 - \alpha)}{\pi I_{0(\text{HOM})} U^3} \right)^{\frac{1}{4}} \quad (5)$$

and

$$t_S = \left(-\frac{\ln(1 - \alpha)}{I_{0(\text{HET})} U^2} \right)^{\frac{1}{3}}. \quad (6)$$

In Equations 5 and 6, t_V and t_S are the times necessary to crystallize 10^{-4} percent of the glass in the volume and at the surface, respectively. U is the crystal growth rate that is utilized from

TABLE 1 | Parameters of the calculation of the homogeneous (HOM) and heterogeneous (HET) nucleation rate of $\text{Li}_2\text{Si}_2\text{O}_5$ crystals in lithium disilicate melt.

Parameter	HOM	HET	Reference
Number of formula units per unit volume n_V (m^{-3})	9.43×10^{27}	–	Neilson and Weinberg (1979)
Density of the supercooled liquid ρ_{liquid} (g cm^{-3}) ^b		2.350	Schmelzer et al. (2004)
Molar mass M (g mol^{-1})		150.05	
Number of active nucleation sites per unit surface area n_s (m^{-2})	–	0.023 ± 0.001^a	
Interfacial energy parameter a (J m^{-2})		$(2885 \pm 8) \times 10^{-5a,c}$	
Interfacial energy parameter b ($\text{J m}^{-2} \text{K}^{-1}$)		$(1655 \pm 8) \times 10^{-7a,c}$	
Molar volume V_M ($\text{m}^3 \text{mol}^{-1}$)		6.15×10^{-5}	Krüger and Deubener (2015b)
Crystal density ρ_{crystal} (g cm^{-3})		2.438	Deubener et al. (1993)
Molar enthalpy of melting ΔH_m (J mol^{-1})		61090	Takahashi and Yoshio (1973)
Thermodynamic ratio ω		0.34	Takahashi and Yoshio (1973)
Contact angle θ ($^\circ$)	180	26.4 ± 0.1^a	
Atomic jump distance λ (m)		4.68×10^{-10}	Krüger and Deubener (2015b)
VFT parameter A_{VFT}		–2.37	Krüger and Deubener (2015b)
VFT parameter B_{VFT} (K)		3248.62	Krüger and Deubener (2015b)
VFT parameter T_0 (K)		500.24	Krüger and Deubener (2015b)
Coordination number CN		2	Krüger and Deubener (2015b)
Number of atoms per formula unit n		9	

^aAdjustable parameter.

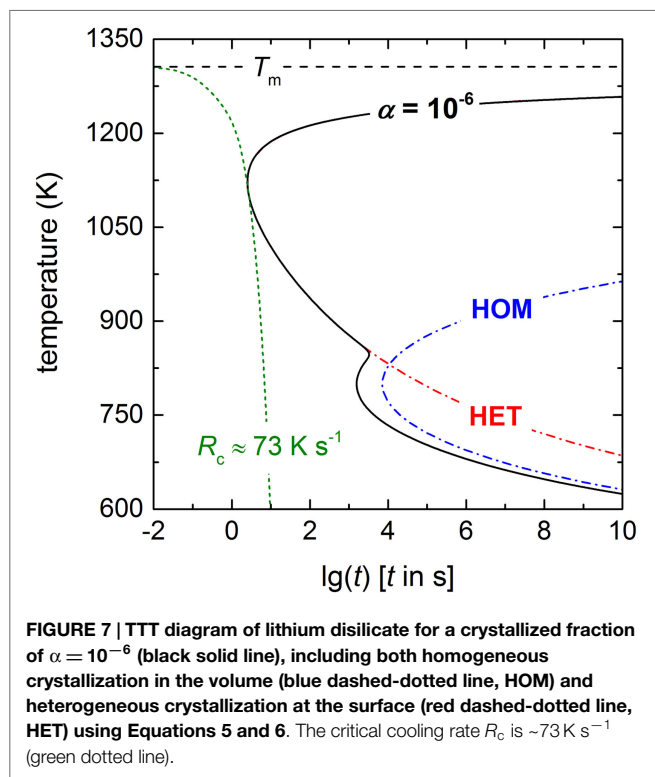
^bGlass density at room temperature. Thermal expansion of the liquid volume is neglected.

^cInterfacial energy parameters of James (1985): $a = 2911 \times 10^{-5} \text{ J m}^{-2}$, $b = 1617 \times 10^{-7} \text{ J m}^{-2} \text{K}^{-1}$ were used as initial values for the fitting.

TABLE 2 | Equations of the calculation of the homogeneous (HOM) and heterogeneous (HET) crystal nucleation rate.

Equation	HOM	HET	Reference
Number of formula units per volume $n_V =$		$p_{\text{liquid}} N_A/M$	James (1985, 1989)
Molar volume $V_m =$		M/ρ_{crystal}	James (1985, 1989)
Liquid–crystal interfacial energy $\sigma =$		$a + bT$	James (1985, 1989)
Atomic jump distance $\lambda =$		$\left(\frac{V_m}{N_A}\right)^{1/3}$	James (1985, 1989)
Viscosity $\lg(\eta) =$		$A_{\text{VFT}} + \frac{B_{\text{VFT}}}{T - T_0}$	Vogel (1921), Fulcher (1925), and Tammann and Hesse (1926)
Gibbs energy of crystallization $\Delta G =$	$\Delta H_m \left(1 - \frac{T}{T_m}\right) \left[1 - \frac{\omega}{2} \left(1 - \frac{T}{T_m}\right)\right]$	with $\omega = \frac{\Delta C_p(T_m)}{\Delta S_m}$	Gutzow and Schmelzer (1995)
Diffusion coefficient $D =$		$\frac{kT}{\eta} \frac{1}{CN} \left(\frac{nN_A}{V_m}\right)^{1/3}$	Eyring et al. (1982)
Kinetic barrier $\frac{\Delta G_D}{kT} =$		$\ln \left(\frac{kT\lambda^2}{hD}\right)$	James (1985, 1989)
Thermodynamic barrier $\frac{W}{kT} =$		$\frac{16\pi\sigma^3 V_m^2}{3\Delta G^2} \frac{2 - 3 \cos(\theta) + \cos^3(\theta)}{4}$	Gutzow and Schmelzer (1995)
Prefactor $A_i =$	$\frac{kT}{h} n_V$	$\frac{kT}{h} n_s$	James (1985, 1989)
Nucleation rate $I_0 =$		$A_i \exp \left(-\frac{W + \Delta G_D}{kT}\right)$	Turnbull (1956)

Constants: Avogadro $N_A = 6.0221 \times 10^{23} \text{ mol}^{-1}$, Boltzmann $k = 1.3806 \times 10^{-23} \text{ JK}^{-1}$ and Planck $h = 6.626 \times 10^{-34} \text{ Js}$. Parameters: ΔS_m = molar entropy of melting, $\Delta C_p(T_m)$ = difference in the molar heat capacity between the liquid and crystalline state at the melting point.



the data compilation of Burgner and Weinberg (2001). **Figure 7** shows that crystallization initiated by HET surface nucleation (red dashed-dotted line) and HOM volume nucleation (blue dashed-dotted line) overlap only partially. In order to calculate the overall crystallization time, Eq. 6 was used, while $I_0(\text{HOM})$ was converted to a surface nucleation rate $[I_0(\text{HOM}, s) = I_0(\text{HOM}, v)^{2/3} \times t_V^{-1/3}]$ (Krüger and Deubener, 2015a), the uncertainty of the conversion is less than 1% and added to the HET nucleation rate. The shape of

the overall time with a “double-nose” (black solid line) resembles those of an aqueous lithium chloride solution (MacFarlane et al., 1983) and of polybutylene terephthalate (Androsch et al., 2015). The double-nose diagram helps to explain the formation of a coast-island microstructure if lithium disilicate glass is heated at low rates from below T_g in practice. In agreement with the microstructures shown for different heating rates in Krüger and Deubener (2015a), larger heating rates suppress HOM volume nucleation of crystals and allow for surface crystallization only. By contrast, if a lithium disilicate glass sample is subjected at the first stage of the double-stage heat treatment to a temperature in the HOM nucleation range dwelling will form initially crystal nuclei in the volume (James, 1974). Additionally, the distinct HET nose of the TTT diagram emphasizes that cooling a lithium disilicate melt from above T_m always leads to a crystallized surface and dictates the critical cooling rate in this system. The latter is estimated by the so-called nose method using the simple calculus $R_c = (T_n - T_m)/t_n$ (Uhlmann, 1972). With the coordinates of the nose $T_n = 1122 \text{ K}$ and $t_n = 2.51 \text{ s}$, the critical cooling rate is ca. 73 K s^{-1} (green dotted line in **Figure 7**).

We are fully aware that R_c is overestimated by the TTT representation (Xu et al., 2013). A TTT diagram has to be converted to a CCT diagram to calculate the critical cooling rate more exactly (Grange and Kiefer, 1941; Zhu et al., 2006). However, it was shown by Davies (1976), Ramachandrarao et al. (1977), Uhlmann and Yinnon (1983), and Scherer (1991) that R_c calculated from a TTT diagram meets the experimental result within one order of magnitude. A first attempt to determine TTT and CCT diagrams in lithium disilicate was performed by Zhu et al. (2006) 10 years ago. They spotted a small glass volume on the tip of a Pt-thermocouple and measured the onset temperature and time of the crystallization peak in isochronal and isothermal mode of operation. By comparison to **Figure 7**, their single nose can be clearly identified as the HET part of the overall crystallization leading to exclusively surface crystallization.

CONCLUSION

The most striking outcome of the present study is the “double-nose” TTT diagram of lithium disilicate due to a decoupling of the nucleation mechanisms of HOM volume nucleation of crystals at large undercoolings (0.53–0.61 T_m) and HET surface nucleation of crystals at smaller undercoolings (0.62–0.92 T_m). This behavior is the origin for the evolution of coast-island microstructures of lithium disilicate in practice. Due to the stochastic experiments at small undercoolings HET nucleation is measurable and the corresponding rate with a maximum at 1071 K is quantified for the first time. Based on the calculated TTT diagram the critical cooling rate is about 73 K s⁻¹.

The results emphasize that exploring the time average of nucleation events by thermal cycling is a novel and highly attractive

route to study HET crystal nucleation in silicate glasses. In particular, they point out that the rare data on HET nucleation rates and critical cooling rates that are based on one-time cooling experiments have to be reconsidered to include statistical certainty.

AUTHOR CONTRIBUTIONS

SK performed experiments. SK and JD prepared manuscript.

ACKNOWLEDGMENTS

We acknowledge support by Open Access Publishing Fund of Clausthal University of Technology.

REFERENCES

- Androsch, R., Rhoades, A. M., Stolte, I., and Schick, C. (2015). Density of heterogeneous and homogeneous crystal nuclei in poly (butylene terephthalate). *Eur. Polym. J.* 66, 180–189. doi:10.1016/j.eurpolymj.2015.02.013
- Barker, M. F., Wang, T.-H., and James, P. F. (1988). Nucleation and growth kinetics of lithium disilicate and lithium metasilicate in lithia-silica glasses. *Phys. Chem. Glasses* 29, 240–248.
- Barlow, T. W., and Haymet, A. D. J. (1995). ALTA: an automated lag-time apparatus for studying the nucleation of supercooled liquids. *Rev. Sci. Instrum.* 66, 2996–3007. doi:10.1063/1.1145586
- Burgner, L. L., and Weinberg, M. C. (2001). An assessment of crystal growth behavior in lithium disilicate glass. *J. Non-Cryst. Solids* 279, 28–43. doi:10.1016/S0022-3093(00)00325-2
- Burgner, L. L., Weinberg, M. C., Lucas, P., Soares, P. C. Jr., and Zanolto, E. D. (1999). XRD investigation of metastable phase formation in Li₂O-2SiO₂ glass. *J. Non-Cryst. Solids* 255, 264–268. doi:10.1016/S0022-3093(99)00376-2
- Cronin, D., and Pye, L. D. (1986). Platinum catalyzed crystallization of Li₂O-2SiO₂ glass. *J. Non-Cryst. Solids* 84, 196–205. doi:10.1016/0022-3093(86)90778-7
- Davies, H. A. (1976). Formation of metallic glasses. *Phys. Chem. Glasses* 17, 159–173.
- Deubener, J., Brückner, R., and Sternitzke, M. (1993). Induction time analysis of nucleation and crystal growth in di- and metasilicate glasses. *J. Non-Cryst. Solids* 163, 1–12. doi:10.1016/0022-3093(93)90638-E
- Dressler, M., Rüdinger, B., and Deubener, J. (2011). An in situ high-temperature X-ray diffraction study of early-stage crystallization in lithium aluminosilicate glass-ceramics. *J. Am. Ceram. Soc.* 94, 1421–1426. doi:10.1111/j.1551-2916.2010.04252.x
- Dressler, M., Rüdinger, B., and Deubener, J. (2014). Crystallization kinetics in a lithium aluminosilicate glass using SnO₂ and ZrO₂ additives. *J. Non-Cryst. Solids* 389, 60–65. doi:10.1016/j.jnoncrysol.2014.02.008
- Eyring, H., Henderson, D., Stover, B. J., and Eyring, E. M. (1982). *Statistical Mechanics and Dynamics*, 2nd Edn. New York, NY: Wiley.
- Fokin, V. M., Kalinina, A. M., and Filipovich, V. N. (1981). Nucleation in silicate glasses and effect of preliminary heat treatment on it. *J. Cryst. Growth* 52, 115–121. doi:10.1016/0022-0248(81)90178-0
- Fokin, V. M., Zanolto, E. D., and Schmelzer, J. W. P. (2010a). On the thermodynamic driving force for interpretation of nucleation experiments. *J. Non-Cryst. Solids* 356, 2185–2191. doi:10.1016/j.jnoncrysol.2010.07.040
- Fokin, V. M., Cabral, A. A., Reis, R. M. C. V., Nascimento, M. L. F., and Zanolto, E. D. (2010b). Critical assessment of DTA-DSC methods for the study of nucleation kinetics in glasses. *J. Non-Cryst. Solids* 356, 358–367. doi:10.1016/j.jnoncrysol.2009.11.038
- Fokin, V. M., Zanolto, E. D., Yuritsyn, N. S., and Schmelzer, J. W. P. (2006). Homogeneous crystal nucleation in silicate glasses: a 40 years perspective. *J. Non-Cryst. Solids* 352, 2681–2714. doi:10.1016/j.jnoncrysol.2006.02.074
- Fulcher, G. S. (1925). Analysis of recent measurements of the viscosity of glasses. *J. Am. Ceram. Soc.* 8, 789–794. doi:10.1111/j.1151-2916.1925.tb16731.x
- Grange, R. A., and Kiefer, J. M. (1941). Transformation of austenite on continuous cooling and its relation to transformation at constant temperature. *Trans. ASM* 29, 85.
- Gutzow, I., and Schmelzer, J. (1995). *Nucleation in Glass-Forming Systems, The Vitreous State*. Berlin: Springer, 218–281.
- Hench, L. L., Frieman, S. W., and Kinser, D. L. (1971). Early stages of crystallisation in a Li₂O-2SiO₂ Glass. *Phys. Chem. Glasses* 12, 58–63.
- Heneghan, A. F., and Haymet, A. D. J. (2002). Liquid-to-crystal nucleation: a new generation lag-time apparatus. *J. Chem. Phys.* 117, 5319–5327. doi:10.1063/1.1497635
- Heneghan, A. F., Wilson, P. W., and Haymet, A. D. J. (2002). Heterogeneous nucleation of supercooled water, and the effect of an added catalyst. *Proc. Nat. Acad. Sci. U.S.A.* 99, 9631–9634. doi:10.1073/pnas.152253399
- Heneghan, A. F., Wilson, P. W., Wang, G., and Haymet, A. D. J. (2001). Liquid-to-crystal nucleation: automated lag-time apparatus to study supercooled liquids. *J. Chem. Phys.* 115, 7599–7608. doi:10.1063/1.1407290
- Iqbal, Y., Lee, W. E., Holland, D., and James, P. F. (1999). Crystal nucleation in P₂O₅-doped lithium disilicate glasses. *J. Mater. Sci.* 34, 4399–4411. doi:10.1023/A:1004668701163
- James, P. F. (1974). Kinetics of crystal nucleation in lithium silicate-glasses. *Phys. Chem. Glasses* 15, 95–105.
- James, P. F. (1985). Kinetics of crystal nucleation in silicate glasses. *J. Non-Cryst. Solids* 73, 517–540. doi:10.1016/0022-3093(85)90372-2
- James, P. F. (1989). “Volume nucleation in silicate glasses,” in *Glasses and Glass-Ceramics*, ed. M. H. Lewis (New York: Chapman and Hall), 59–105.
- James, P. F., Scott, B., and Armstrong, P. (1978). Kinetics of crystal nucleation in lithium disilicate glass. A comparison between melts prepared in platinum and silica crucibles and between melts prepared from ordinary and high purity starting materials. *Phys. Chem. Glasses* 19, 24–27.
- Kelton, K. F. (2000). Kinetic model for nucleation in partitioning systems. *J. Non-Cryst. Solids* 274, 147–154. doi:10.1016/S0022-3093(00)00185-X
- Kracek, F. C. (1930). The binary system Li₂O-SiO₂. *J. Phys. Chem.* 34, 2641–2650. doi:10.1021/j150318a001
- Krüger, S., and Deubener, J. (2014). Stochastic nature of the liquid-to-crystal heterogeneous nucleation of supercooled lithium disilicate liquid. *J. Non-Cryst. Solids* 388, 6–9. doi:10.1016/j.jnoncrysol.2014.01.036
- Krüger, S., and Deubener, J. (2015a). Heterogeneous surface nucleation of lithium disilicate glass: an isothermal DSC study. *J. Non-Cryst. Solids* 417, 45–51. doi:10.1016/j.jnoncrysol.2015.03.013
- Krüger, S., and Deubener, J. (2015b). Lag time to crystal nucleation of supercooled lithium disilicate melts: a test of the classical nucleation theory. *J. Non-Cryst. Solids* 426, 1–6. doi:10.1016/j.jnoncrysol.2015.06.023
- Krüger, S., Deubener, J., Ritzberger, C., and Höland, W. (2013). Nucleation kinetics of lithium metasilicate in ZrO₂-bearing lithium disilicate glasses for dental application. *Int. J. Appl. Glass Sci.* 4, 9–19. doi:10.1111/ijag.12011
- MacFarlane, D. R., Kadiyala, R. K., and Angell, C. A. (1983). Homogeneous nucleation and growth of ice from solutions. TTT curves, the nucleation rate, and the stable glass criterion. *J. Chem. Phys.* 79, 3921–3927. doi:10.1063/1.446260
- Maeda, N., Wells, D., Becker, N. C., Hartley, P. G., Wilson, P. W., Haymet, A. D. J., et al. (2011). Development of a high pressure automated lag time apparatus for experimental studies and statistical analyses of nucleation and growth of gas hydrates. *Rev. Sci. Instrum.* 82, 065109. doi:10.1063/1.3602926

- Maeda, N., Wells, D., Hartley, P. G., and Kozielski, K. A. (2012). Statistical analysis of supercooling in fuel gas hydrate systems. *Energy Fuels* 26, 1820–1827. doi:10.1021/ef201965z
- Matusita, K., and Tashiro, M. (1973). Rate of homogeneous nucleation in alkali disilicate glasses. *J. Non-Cryst. Solids* 11, 471–484. doi:10.1016/0022-3093(73)90092-6
- Mishima, N., Wakasugi, T., and Ota, R. (2006). Bulk crystallisation in mixed alkali disilicate glasses doped with a nucleating agent. *Phys. Chem. Glasses* 47, 259–265.
- Morton, C. W., Hofmeister, W. H., Bayuzick, R. J., and Robinson, M. B. (1994). A statistical approach to understanding nucleation phenomena. *Mater. Sci. Eng. A* 178, 209–215. doi:10.1016/0921-5093(94)90545-2
- Müller, R., Zanotto, E. D., and Fokin, V. M. (2000). Surface crystallization of silicate glasses: nucleation sites and kinetics. *J. Non-Cryst. Solids* 274, 208–231. doi:10.1016/S0022-3093(00)00214-3
- Narayan, K. L., Kelton, K. F., and Ray, C. S. (1996). Effect of Pt doping on nucleation and crystallization in Li_2O - 2SiO_2 glass: experimental measurements and computer modeling. *J. Non-Cryst. Solids* 195, 148–157. doi:10.1016/0022-3093(95)00526-9
- Nascimento, M. L. F., Fokin, V. M., Zanotto, E. D., and Abyzov, A. S. (2011). Dynamic processes in a silicate liquid from above melting to below the glass transition. *J. Chem. Phys.* 135, 194703. doi:10.1063/1.3656696
- Neilson, G. F., and Weinberg, M. C. (1979). A test of classical nucleation theory: crystal nucleation of lithium disilicate glass. *J. Non-Cryst. Solids* 34, 137–147. doi:10.1016/0022-3093(79)90013-9
- Ota, R., Mishima, N., Wakasugi, T., and Fukunaga, J. (1997). Nucleation of Li_2O - SiO_2 glass and its interpretation based on a new liquid model. *J. Non-Cryst. Solids* 219, 70–74. doi:10.1016/S0022-3093(97)00253-6
- Ramachandrarao, P., Cantor, B., and Cahn, R. W. (1977). Viscous behaviour of undercooled metallic melts. *J. Non-Cryst. Solids* 24, 109–120. doi:10.1016/0022-3093(77)90065-5
- Ranasinghe, K. S., Ray, C. S., Day, D. E., Rogers, J. R., Hyers, R. W., and Rathz, T. (2007). Containerless processing of a lithium disilicate glass. *J. Mater. Sci.* 42, 4291–4297. doi:10.1007/s10853-006-1232-z
- Ray, C. S., and Day, D. E. (1996). Identifying internal and surface crystallization by differential thermal analysis for the glass-to-crystal transformations. *Thermochim. Acta* 280/281, 163–174. doi:10.1016/0040-6031(95)02640-1
- Ray, C. S., Day, D. E., Huang, W., Narayan, K. L., Cull, T. S., and Kelton, K. F. (1996). Non-isothermal calorimetric studies of the crystallization of lithium disilicate glass. *J. Non-Cryst. Solids* 204, 1–12. doi:10.1016/0022-3093(96)00401-2
- Rowlands, E. G., and James, P. F. (1979). Analysis of steady state crystal nucleation rates in glasses. Part 1. Methods of analysis and application to lithium disilicate glass. Part 2. Further comparison between theory and experiment for lithium disilicate glass. *Phys. Chem. Glasses* 20, 9–14.
- Scherer, G. W. (1991). “Glass formation and relaxation,” in *Materials Science and Technology – A Comprehensive Treatment, Vol. 9: Glasses and Amorphous Materials*, eds R. W. Cahn, P. Haasen, E. J. Kramer, and J. Zarzycki (Weinheim: VCH Verlagsgesellschaft mbH), 119–173.
- Schmelzer, J. W. P., Potapov, O. V., Fokin, V. M., Müller, R., and Reinsch, S. (2004). The effect of elastic stress and relaxation on crystal nucleation in lithium disilicate glass. *J. Non-Cryst. Solids* 333, 150–160. doi:10.1016/j.jnoncrysol.2003.10.002
- Takahashi, K., and Yoshio, T. (1973). Thermodynamic quantities of alkali silicates in the temperature range from 25°C to melting point. *Yogyo Kyokai Shi* 81, 524–533. doi:10.2109/jcersj1950.81.940_524
- Tammann, G., and Hesse, W. (1926). Die Abhängigkeit der Viscosität von der Temperatur bei unterkühlten Flüssigkeiten. *Z. Anorg. Allg. Chem.* 156, 245–257. doi:10.1002/zaac.19261560121
- Tomozawa, M. (1972). Liquid phase separation and crystal nucleation in Li_2O - SiO_2 glasses. *Phys. Chem. Glasses* 13, 161–166.
- Tomozawa, M. (1973). Liquid phase separation and crystal growth in Li_2O - SiO_2 glass. *Phys. Chem. Glasses* 14, 112–115.
- Toschev, S. (1973). “Homogeneous nucleation,” in *Crystal Growth: An Introduction*, ed. P. Hartman (Amsterdam: North-Holland Publishing Co.), 1–49.
- Toschev, S., and Gutzow, I. (1972). Nichtstationäre Keimbildung: Theorie und Experiment. *Krist. Tech.* 7, 43–73. doi:10.1002/crat.19720070108
- Toschev, S., and Markov, I. (1967). Electrolytic nucleation of cadmium. *Electrochim. Acta* 12, 281–286. doi:10.1016/0013-4686(67)80006-9
- Toschev, S., Milchev, A., and Stoyanov, S. (1972). On some probabilistic aspects of the nucleation process. *J. Cryst. Growth* 1, 123–127. doi:10.1016/0022-0248(72)90073-5
- Turnbull, D. (1956). “Phase changes,” in *Solid State Physics*, Vol. 3, eds F. Seitz and D. Turnbull (New York: Academic Press), 225–306.
- Uhlmann, D. R. (1972). A kinetic treatment of glass formation. *J. Non-Cryst. Solids* 7, 337–348. doi:10.1016/0022-3093(72)90269-4
- Uhlmann, D. R., and Yinnon, H. (1983). “The formation of glasses,” in *Glass: Science and Technology, Vol. 1: Glass-Forming Systems*, eds D. R. Uhlmann and N. J. Kreidl (New York, London, Paris, San Diego, San Francisco, Sao Paulo, Sydney, Tokyo, Toronto: Academic Press, Inc.), 1–47.
- Uttomark, M. J., Zanter, J. W., and Perepezko, J. H. (1997). Repeated nucleation in an undercooled aluminum droplet. *J. Cryst. Growth* 177, 258–264. doi:10.1016/S0022-0248(96)01121-9
- Vogel, H. (1921). The law of the relation between the viscosity of liquids and the temperature. *Phys. Z.* 22, 645–646.
- Weinberg, M. C., and Neilson, G. F. (1985). On the possibility of critical radius measurements in the homogeneous crystal nucleation of glass. *J. Non-Cryst. Solids* 74, 177–179. doi:10.1016/0022-3093(85)90412-0
- Weinberg, M. C., and Zanotto, E. D. (1989). Re-examination of the temperature dependence of the classical nucleation rate: homogeneous crystal nucleation in glass. *J. Non-Cryst. Solids* 108, 99–108. doi:10.1016/0022-3093(89)90337-2
- Wilde, G., Santhaweesuk, C., Sebright, J. L., Bokeloh, J., and Perepezko, J. H. (2009). Kinetics of heterogeneous nucleation on intrinsic nucleants in pure fcc transition metals. *J. Phys. Condens. Matter* 21, 464113. doi:10.1088/0953-8984/21/46/464113
- Wilde, G., Sebright, J. L., and Perepezko, J. H. (2006). Bulk liquid undercooling and nucleation in gold. *Acta Mater.* 54, 4759–4769. doi:10.1016/j.actamat.2006.06.007
- Wilson, P. W., Lester, D., and Haymet, A. D. J. (2005). Heterogeneous nucleation of clathrates from supercooled tetrahydrofuran (THF)/water mixtures, and the effect of an added catalyst. *Chem. Eng. Sci.* 60, 2937–2941. doi:10.1016/j.ces.2004.12.047
- Xu, K., Wang, Y., Li, J., and Li, Q. (2013). Critical cooling rate for the glass formation of ferromagnetic Fe80P13C7 alloy. *Acta Metall. Sin. (Engl. Lett.)* 26, 56–62. doi:10.1007/s40195-012-0117-1
- Yang, B., Abyzov, A. S., Zhuravlev, E., Gao, Y., Schmelzer, J. W. P., and Schick, C. (2013). Size and rate dependence of crystal nucleation in single tin drops by fast scanning calorimetry. *J. Chem. Phys.* 138, 054501. doi:10.1063/1.4789447
- Yang, B., Gao, Y., Zou, C., Zhai, Q., Abyzov, A. S., Zhuravlev, E., et al. (2011). Cooling rate dependence of undercooling of pure Sn single drop by fast scanning calorimetry. *Appl. Phys. A* 104, 189–196. doi:10.1007/s00339-010-6100-7
- Yang, B., Gao, Y. L., Zou, C. D., Zhai, Q. J., Zhuravlev, E., and Schick, C. (2009). Repeated nucleation in an undercooled tin droplet by fast scanning calorimetry. *Mater. Lett.* 63, 2476–2478. doi:10.1016/j.matlet.2009.08.041
- Zanotto, E. D. (1987). Isothermal and adiabatic nucleation in glass. *J. Non-Cryst. Solids* 89, 361–370. doi:10.1016/S0022-3093(87)80278-8
- Zanotto, E. D. (1996). The applicability of the general theory of phase transformations to glass crystallization. *Thermochim. Acta* 28, 73–82. doi:10.1016/0040-6031(95)02636-3
- Zanotto, E. D. (1997). Metastable phases in lithium disilicate glasses. *J. Non-Cryst. Solids* 219, 42–48. doi:10.1016/S0022-3093(97)00249-4
- Zanotto, E. D., and James, P. F. (1985). Experimental tests of the classical nucleation theory for glasses. *J. Non-Cryst. Solids* 74, 373–394. doi:10.1016/0022-3093(85)90080-8
- Zhu, D., Zhou, W., Ray, C. S., and Day, D. E. (2006). Method for estimating continuous cooling transformation curves of glasses. *Phys. Chem. Glasses* 47, 271–277.

Conflict of Interest Statement: The authors declare that the research was conducted in the absence of any commercial or financial relationships that could be construed as a potential conflict of interest.

Copyright © 2016 Krüger and Deubener. This is an open-access article distributed under the terms of the Creative Commons Attribution License (CC BY). The use, distribution or reproduction in other forums is permitted, provided the original author(s) or licensor are credited and that the original publication in this journal is cited, in accordance with accepted academic practice. No use, distribution or reproduction is permitted which does not comply with these terms.



Crystallization, Microstructure, and Viscosity Evolutions in Lithium Aluminosilicate Glass-Ceramics

Qiang Fu^{1*}, Bryan R. Wheaton¹, Karen L. Geisinger¹, Allen J. Credle¹ and Jie Wang²

¹ Science and Technology Division, Corning Incorporated, Corning, NY, USA, ² Argonne National Laboratory, Center for Nanoscale Materials, Lemont, IL, USA

OPEN ACCESS

Edited by:

Wolfram Höland,
Ivoclar Vivadent, Liechtenstein

Reviewed by:

William LaCourse,
Alfred University, USA
Daqin Chen,
Hangzhou Dianzi University, China
Christian Rüssel,
Jena University, Germany

*Correspondence:

Qiang Fu
fuq2@corning.com

Specialty section:

This article was submitted
to Glass Science,
a section of the journal
Frontiers in Materials

Received: 23 July 2016

Accepted: 17 October 2016

Published: 08 November 2016

Citation:

Fu Q, Wheaton BR, Geisinger KL,
Credle AJ and Wang J (2016)
Crystallization, Microstructure, and
Viscosity Evolutions in Lithium
Aluminosilicate Glass-Ceramics.
Front. Mater. 3:49.
doi: 10.3389/fmats.2016.00049

Lithium aluminosilicate glass-ceramics have found widespread commercial success in areas such as consumer products, telescope mirrors, fireplace windows, etc. However, there is still much to learn regarding the fundamental mechanisms of crystallization, especially related to the evolution of viscosity as a function of the crystallization (ceramming) process. In this study, the impact of phase assemblage and microstructure on the viscosity was investigated using high-temperature X-ray diffraction (HTXRD), beam bending viscometry (BBV), and transmission electron microscopy (TEM). Results from this study provide a first direct observation of viscosity evolution as a function of ceramming time and temperature. Sharp viscosity increases due to phase separation, nucleation, and phase transformation are noticed through BBV measurement. A near-net shape ceramming can be achieved in TiO₂-containing compositions by keeping the glass at a high viscosity ($>10^9$ Pa s) throughout the whole thermal treatment.

Keywords: lithium aluminosilicate glass-ceramics, crystallization, viscosity, microstructure, phase assemblage

INTRODUCTION

There have been increasing uses of glass-ceramics in areas such as consumer, biomedical, and construction markets since their discovery by Stookey in 1950s (Stookey, 1960a,b; Holand and Beall, 2002; Zanutto, 2010). Lithium aluminosilicate glass-ceramics have gained considerable commercial success due to the combination of low thermal expansion [coefficient of thermal expansion (CTE), close to $0 \times 10^{-7}/^{\circ}\text{C}$] and high mechanical strength attributed to its two main crystalline phases, β -quartz and β -spodumene (keatite) solid solutions (ss) (Ostertag et al., 1968; Holand and Beall, 2002; Dressler et al., 2011a). Both ZrO₂ and TiO₂ are commonly used as nucleation agents to produce controlled bulk crystallization in the precursor glass (Henderson, 1979; Holand and Beall, 2002; Zanutto, 2010). Although small in concentration, nucleation agents lead to the formation of nuclei for crystal growth (Holand and Beall, 2002). Fine-grained microstructures composed of small crystals (0.1–1.0 μm) uniformly distributed in a residual glassy phase are usually observed in lithium aluminosilicate glass-ceramics, which is important to achieve a desired mechanical strength (Beall and Doman, 1987; Beall and Pinckney, 1999; Guedes et al., 2001; Holand and Beall, 2002).

The crystallization process and its associated microstructural evolution are generally studied by differential scanning calorimetry (DSC), X-ray diffraction (XRD), scanning electron microscopy (SEM), or transmission electron microscopy (TEM). Thermal analysis serves as a rapid and convenient technique for the study of the kinetics of chemical reactions and crystallization of glass (Matusita and Sakka, 1980). It has been used to study the crystallization kinetics of various glass systems including the lithium aluminosilicate (Ray and Day, 1990; Barbieri et al.,

1997a; Kim et al., 2004; Fernandes et al., 2008; Wang et al., 2010; Lilensten et al., 2014). Recently, high-temperature X-ray diffraction (HTXRD) and anomalous small-angle X-ray scattering (ASAXS) have been utilized for the *in situ* observation of the phase transition and structural changes during high-temperature heat treatment (Misture, 2003; Holand et al., 2006; Sinton et al., 2008; Dressler et al., 2011b; Bocker et al., 2013; Lilensten et al., 2014; Raghuwanshi et al., 2014; Kleebusch et al., 2016). Despite the comprehensive understanding of the crystallization mechanism and microstructural changes, the viscosity evolution during the crystallization process remained unclear. However, the control of glass viscosity is critical to achieve a near-net-shape ceramming in the manufacturing of glass-ceramic products (Holand and Beall, 2011).

The objective of this work is to investigate the crystallization, microstructure, and viscosity evolutions in lithium aluminosilicate glass. Both HTXRD and TEM were used to characterize structural evolution in the glass-ceramics during ceramming, while beam bending viscometry (BBV) was used to measure the changes in glass viscosity.

EXPERIMENTAL

Base glass composition (wt%) of 67 SiO₂, 25 Al₂O₃, 5.0 Li₂O, 1.5 MgO, and 1.5 ZnO was prepared by melting a mixture of analytical grade raw materials in platinum crucibles at 1600°C. TiO₂ (0–10 wt%) was added on top of the base glass composition to investigate the glass stability with different nucleation agent levels. **Table 1** listed the glass compositions for this work. Glasses were poured onto a steel plate to form into patties and then annealed at 600°C to remove thermal stress.

Crystalline phases formed in the annealed glasses were detected using XRD. Data were collected from 5° to 80° (2θ) using a Bruker D4 Endeavor equipped with a LynxEye™ (Bruker Corporation, Billerica, MA, USA) silicon strip detector. The XRD pattern was analyzed using the PDF-4 database and Jade.

Differential scanning calorimetry was used to determine the non-isothermal kinetic parameters for crystallization. About 40 mg of fine glass powders (1–10 μm) was used for the DSC analysis, which was performed with a Netzsch DSC 404 F1 Pegasus. The powders were contained in a platinum cup and heated at 10°C/min.

High-temperature XRD was used as an isothermal technique to determine the kinetic parameters for crystallization. *In situ* HTXRD study was carried out on a PANalytical MPD XRD system equipped with an Anton Paar HTK1200N high-temperature furnace and an X'Celerator multiple strip

detector. A polished glass disk (15 mm in diameter × 1 mm thick) was used for the analysis. A rapid heating rate, 20°C/min, from RT to crystallization temperature was followed by continuous data collection at an isothermal hold temperature. XRD diffraction traces in the 2θ range of 10–70° were collected every 10 min.

The viscosity–temperature behavior of glass was analyzed to investigate the viscosity evolution during ceramming. Glass viscosity below the softening point, in the range of 10⁸–10¹³ Pa s, was measured using BBV using a three-point bend, BBV-1000 beam bending viscometer (Orton Ceramics, Westerville, OH, USA) according to the American Society for Testing and Materials (ASTM) standard (ASTM International, 2013). Briefly, a load was applied on a glass beam (2.5 mm × 2.5 mm × 55 mm) in a three-point beam bending. To avoid over deformation due

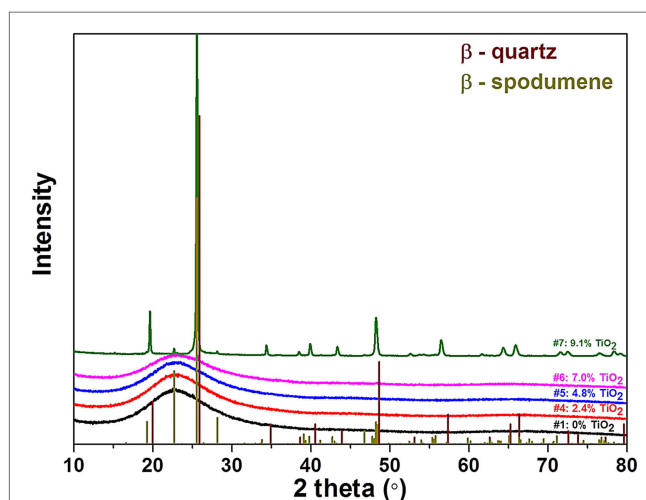


FIGURE 1 | X-ray diffraction patterns of annealed glasses (compositions #1, 4–7).

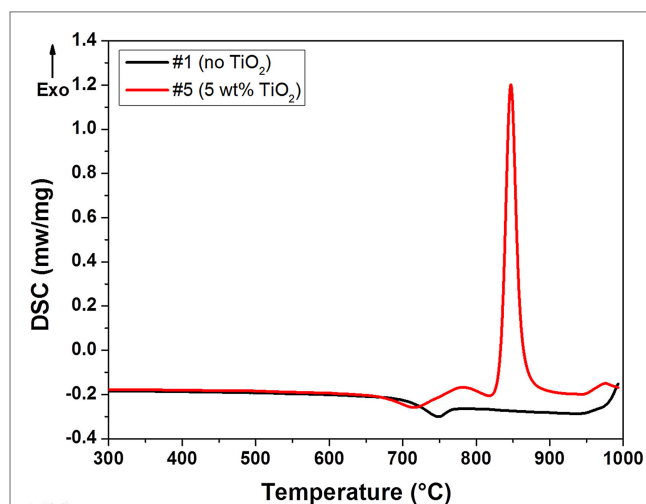


FIGURE 2 | Differential scanning calorimetry of glass compositions #1 and 5.

TABLE 1 | Glass compositions (wt%) used for the current study.

Oxide (wt%)	1	2	3	4	5	6	7
SiO ₂	67.0	66.6	66.3	65.3	63.8	62.3	60.9
Al ₂ O ₃	25.0	24.9	24.7	24.4	23.8	23.3	22.7
Li ₂ O	5.0	5.0	5.0	4.9	4.8	4.7	4.5
MgO	1.5	1.5	1.5	1.5	1.4	1.4	1.4
ZnO	1.5	1.5	1.5	1.5	1.4	1.4	1.4
TiO ₂	0	0.5	1.0	2.4	4.8	7.0	9.1

to low viscosity in the nucleation stage, the measurement of glass viscosity in the crystal growth stage was conducted on beams pre-nucleated at 750°C for 2 h.

High-resolution scanning transmission electron microscopy (HRSTEM) was used to observe the detailed crystal morphology and to determine the elemental partitioning in the cerammed samples using energy dispersive X-ray (EDX) elemental mapping. Electron-transparent thin sections of less than 100 nm were prepared using focused ion beam (FIB) and observed under TEM with 200-kV accelerating voltage.

RESULTS

Green (Non-Cerammed) Glass

The addition of TiO₂ has a substantial impact on the glass stability. When TiO₂ concentrations were below 7.0 wt%, no phase separation or devitrification was observed in glass. However, when more TiO₂ (7.0 wt% or above) was added to the base glass,

phase separation (composition #6) and significant devitrification (composition #7) were observed in the annealed glasses. XRD analysis in **Figure 1** confirmed the amorphous nature of compositions #1–5. In contrast, a small amount of β -quartz ss was detected in composition #6, while a completely devitrified sample was obtained in #7. Compositions #1 (no TiO₂) and #5 (5.0 wt% TiO₂) with no phase separation or devitrification were selected for further studies in this work.

Thermal Analysis

Figure 2 shows the DSC analysis of the two compositions (#1 and 5) of interest. The addition of TiO₂ to the lithium aluminosilicate glass results in pronounced exothermal reactions in DSC while none in TiO₂-free glass. No detectable exothermal peaks were observed in TiO₂-free glass (#1) below 950°C, while three exothermal peaks were observed in TiO₂-containing glass (#5), indicative of the marked crystallization due to addition of a nucleation agent.

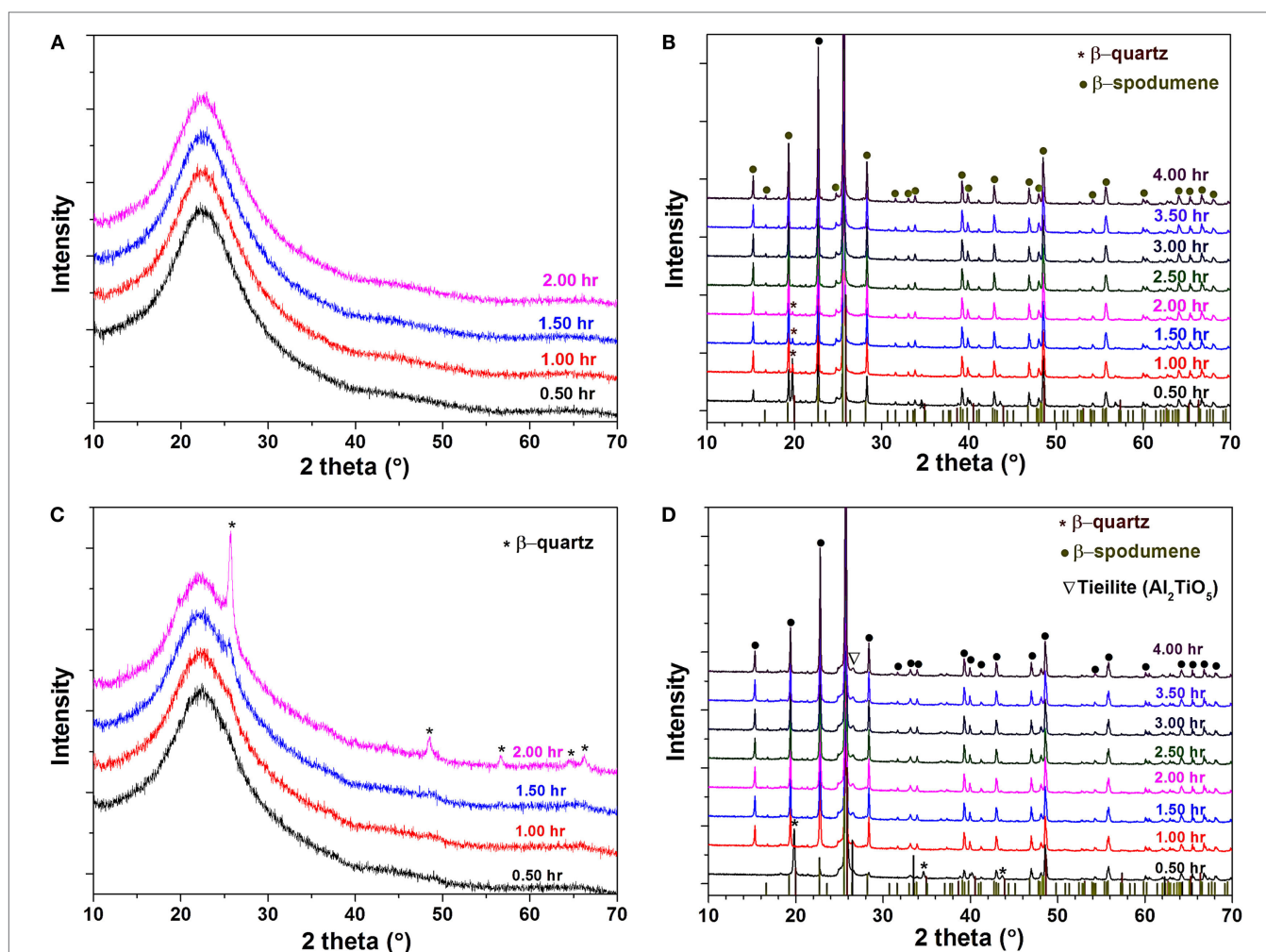


FIGURE 3 | High-temperature X-ray diffraction patterns of glass composition #1: (A) after nucleation at 750°C for 0.5–2.0 h and (B) after crystal growth at 1050°C for 0.5–4.0 h; and of composition #5: (C) after nucleation at 750°C for 0.5–2.0 h and (D) after crystal growth at 1050°C for 0.5–4.0 h.

Phase Assemblage

Figure 3 shows the phase assemblage for two glasses at different thermal treatment steps. Based on the DSC analysis, both glasses were first heated at 750°C for 2 h for nucleation and then at 1050°C for 4 h for crystal growth. No crystalline phases were detected in TiO₂-free glass (composition #1) at the nucleation step (**Figure 3A**), while β -quartz ss was determined in composition #5 added with 5 mol% TiO₂ (**Figure 3C**), in good agreement with the DSC results. The concentration of β -quartz ss increased with increasing holding time at 750°C for composition #5 (**Figure 3C**). A fully crystallized body was obtained in both glass compositions after the crystal growth stage (1050°C for 4 h). For composition #1, the conversion from β -quartz ss to β -spodumene ss did not complete until after 2 h hold at 1050°C (**Figure 3B**), while in TiO₂-containing composition #5, the conversion completed after 0.5 h (**Figure 3D**). The major phase was β -spodumene ss for the two compositions, while a small amount of tieilite (Al₂O₃·TiO₂) was detected in composition #5. It is worth noting that a high number of cracks were formed in composition #1 due to the lack of volume crystallization, while a crack-free part was achieved in composition #5.

Microstructure

Transmission electron microscopy images in **Figure 4** show the microstructural changes of composition #5 during the nucleation

hold at 750°C. For the green glass, no clear feature was observed even at high magnification (**Figure 4A**). After heat treatment at 750°C for 1 h, droplet-like phase was observed in the sample (**Figure 4B**). The size of the droplets was in the range of 5–10 nm. At a low magnification, β -quartz ss phase (50–80 nm) was observed to form in the glass matrix (**Figure 4C**), which agrees with the XRD results. A higher density of β -quartz grains was visible after holding at 750°C for 4 h (**Figure 4D**). The size of the crystal grew slightly falling in the range of 50–100 nm.

A highly crystallized body composed of large grains, and small droplet-like crystals was observed after final heat treatment at 1050°C for 4 h (**Figure 5A**). Combined with XRD results (**Figure 3D**), the large grains were determined to be β -spodumene ss and small droplets tieilite. The size of β -spodumene grains was in the range of 0.3–1.0 μ m while tieilite 30–50 nm (**Figure 5B**). Elemental mapping confirmed that the droplets were rich in Al and Ti (**Figures 5C,D**).

Viscosity Evolution

Figure 6 shows the viscosity evolution for the two selected glasses as a function of ceramming cycle. For composition #1 without nucleation agent, the viscosity decreased monotonically with increasing temperatures, consistent with most glass compositions. The measurement was stopped at 875°C due to its

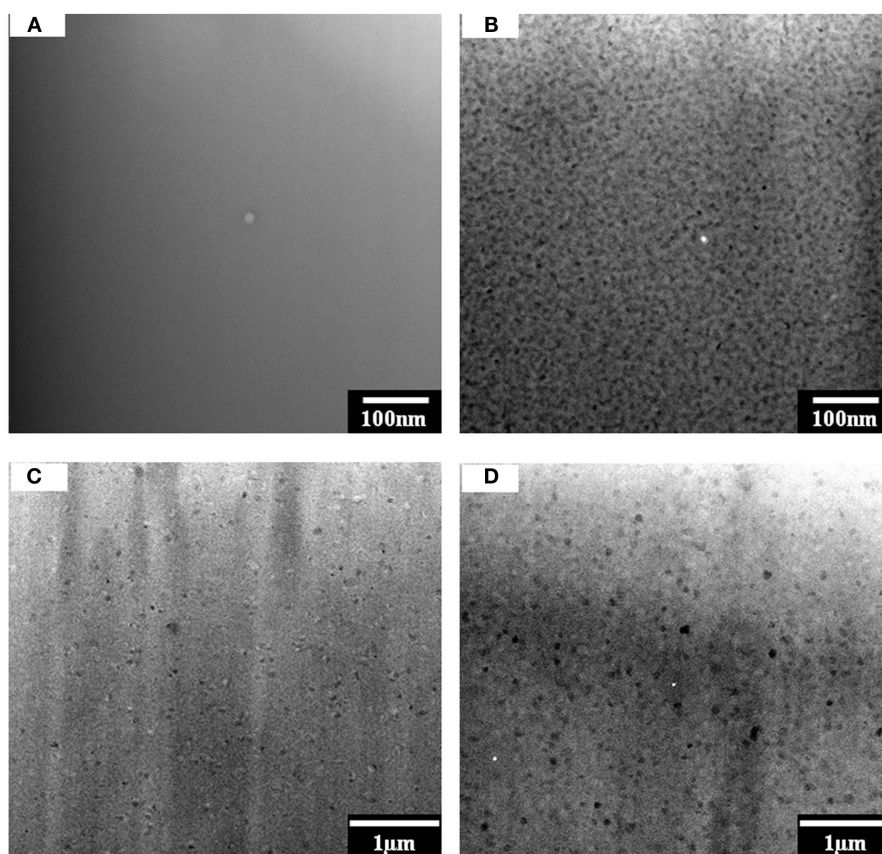


FIGURE 4 | TEM of nucleated glass composition #5: (A) green glass; (B) after holding at 750°C for 1.0 h showing phase separation; (C) low magnification showing the formation of β -quartz ss after at 750°C for 1.0 h; (D) more β -quartz ss after holding at 750°C for 4.0 h.

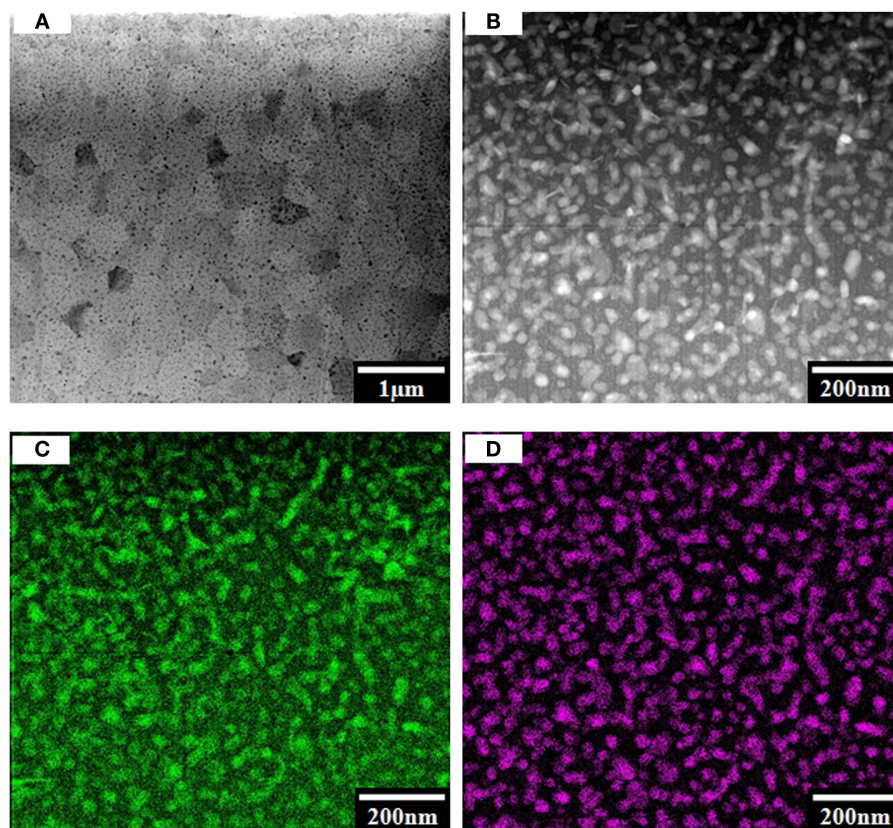


FIGURE 5 | TEM images showing microstructure and elemental mapping of composition #5 after holding at 1050°C for 4.0 h: (A) overview of microstructure; (B) high-magnification image showing the fine crystals; (C) Al map of (B); (D) Ti map of (B).

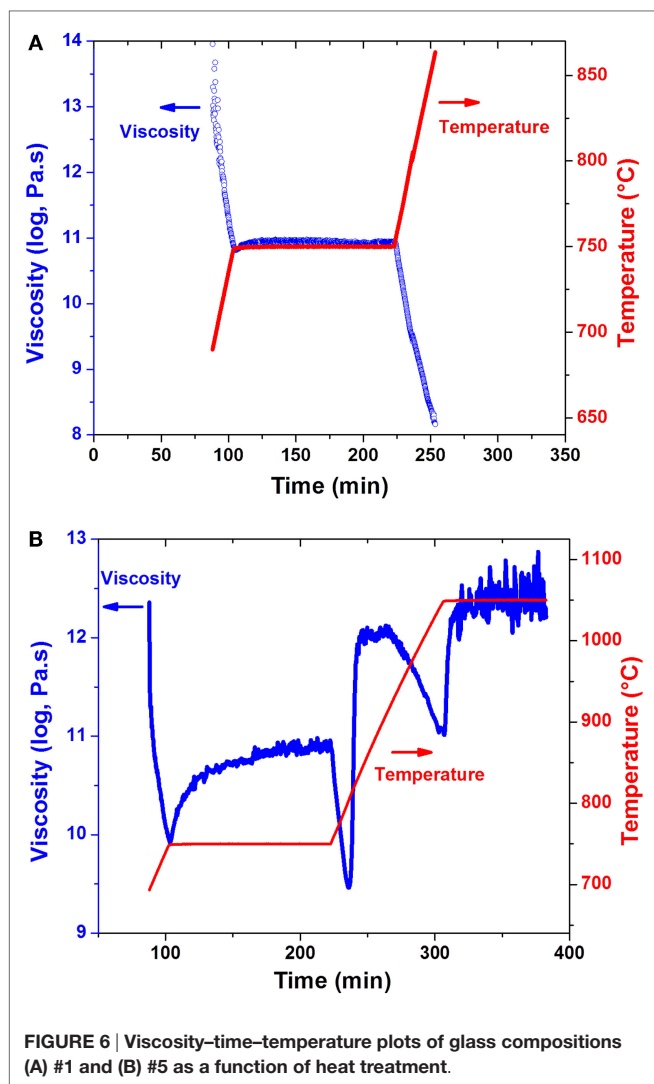
low viscosity, close to 10^8 Pa s, which was below the measurement limit for the BBV method. The viscosity remained almost unchanged during the holding at 750°C, corresponding well with the HTXRD study which shows little to no structural change in this glass (**Figure 3A**). At the end of ceramming cycle, the glass cracked into pieces due to the lack of effective bulk nucleation.

In contrast, the change of viscosity for the TiO_2 -containing glass (composition #5) as a function of ceramming temperature was much more complicated than the monotonic decrease of viscosity in TiO_2 -free glass (**Figure 6B**). The viscosity plot could be divided into three stages. At stage I, an increase of one order of magnitude in viscosity was observed during the hold at 750°C, suggesting either phase separation or nucleation at this stage. At stage II, an abrupt decrease of viscosity with increasing temperature was observed after the initial nucleation hold until 824°C, at which temperature a sharp increase in viscosity was noticed. The temperature for the jump in viscosity was exactly the onset temperature for the largest exothermal peak in DSC (**Figure 2**), which was confirmed by XRD to be the formation of β -quartz (**Figure 3C**). At this stage, the major phase in composition #5 was β -quartz ss with very little amount of glassy phase, suggesting a high viscosity during ceramming. Once the reaction completed, the viscosity of composition #5 started to decrease with increasing temperature due to the lack of new

crystalline phase formation and the relatively stable structure. At stage III, β -quartz ss was converted to β -spodumene ss and no further structural change during the holding at 1050°C, as evidenced by the small variation in viscosity and the unchanged phase assemblage in HTXRD (**Figure 3D**). Overall, the viscosity of the TiO_2 -containing glass was kept above $10^{9.5}$ Pa s during the whole ceramming cycle, which contributed to a near-net-shape ceramming of composition #5 without cracking or visible deformation.

DISCUSSION

Numerous investigations have been conducted to understand the crystallization process in $\text{Li}_2\text{O}-\text{Al}_2\text{O}_3-\text{SiO}_2$ glass-ceramic family due to their increased commercial applications. Nucleation agents, either single or a combination of several, including TiO_2 , ZrO_2 , P_2O_5 , and Ta_2O_5 have been used to produce a bulk nucleation owing to a liquid-liquid phase separation (Barbieri et al., 1997b; Guedes et al., 2001; Wurth et al., 2009; Ananthanarayanan et al., 2010; Li et al., 2010; Nemati et al., 2010; Höche et al., 2011; Höche et al., 2012; Montedo et al., 2012; Chavoutier et al., 2014; Kleebusch et al., 2016; Soares and Zanotto, 2016). Although minor in concentration, nucleation agents are critical to the final microstructure and properties of glass-ceramics. This work



studies the crystallization, and microstructural and viscosity evolutions in $\text{Li}_2\text{O}-\text{Al}_2\text{O}_3-\text{SiO}_2$ glass. It is found that TiO_2 impacts the properties of both green glass and glass-ceramic. In green glass, a higher concentration of TiO_2 results in a high tendency for devitrification and a less thermal stability (Figures 1 and 2). Therefore, the level of TiO_2 must be controlled within a proper range to obtain a stable glass without devitrification for a glass-ceramic composition.

Both the phase assemblage and microstructure of lithium aluminosilicate glass-ceramics are influenced by the presence of TiO_2 . When a proper amount of TiO_2 was added to the $\text{Li}_2\text{O}-\text{Al}_2\text{O}_3-\text{SiO}_2$ glass, phase separation was developed at the nucleation stage, which led to the formation of β -quartz ss (Figures 3 and 4). This is consistent with previous reports that the addition of TiO_2 produced a TiO_2 -rich phase and serves as a nucleation phase for the formation of β -quartz ss (Doherty et al., 1967; Barbieri et al., 1997b,c; Nordmann and Cheng, 1997; Bhattacharyya et al., 2009). In contrast, the TiO_2 -free glass remained amorphous at this nucleation stage (Figure 3).

The viscosity of the system exhibits a strong dependence on the phase assemblage and structure of each composition. The monotonic decrease of viscosity as a function of ceramming cycle for TiO_2 -free composition #1 agrees well with the HTXRD and DSC analysis, both of which show no evidence of new phase formation within the tested temperature range. In contrast, three distinct stages were observed in the viscosity of TiO_2 -containing composition #5 (Figure 6), corresponding well with the thermal events determined by DSC (Figure 2), phase assemblage evolution by HTXRD (Figure 3), and microstructural change by TEM (Figures 4 and 5). At stage I, the increasing viscosity at the nucleation hold was mainly attributed to β -quartz ss formation; at stage II, the abrupt increase in viscosity was a direct consequence of the formation of high concentration of β -quartz ss phase; and at stage III, the conversion β -quartz to β -spodumene ss was completed, which produced a fully crystallized glass-ceramic with little glassy phase and a high-viscosity cerammed body. The increase of viscosity due to crystallization was also observed in a lithium aluminosilicate glass containing ZrO_2 and TiO_2 as nucleation agents. A higher T_g was reported in the nucleated glass than in the precursor glass due to the presence of β -quartz phase (Wurth et al., 2009). The formation of an alumina-rich layer surrounding a ZrTiO_4 -rich core was reported to account for the increase of viscosity (Raghuwanshi et al., 2014). However, no direct analysis of the viscosity evolution in this system has been conducted. The increase in glass viscosity due to the nucleation in TiO_2 -containing lithium aluminosilicate glass has been investigated in a previous study using a fiber elongation method, although the measurement was done on a post-treated sample not an *in situ* measurement during ceramming (Kim et al., 2004). The viscosity of the nucleated composite was decided by the concentration of the crystalline phase and the residual glass composition. The relationship between viscosity and the presence of the crystalline phase was described using the following equation (Kim et al., 2004):

$$\frac{\eta_{\text{app}}}{\eta_g} = (1 - \alpha)^{-3} \quad (1)$$

where η_{app} is the apparent viscosity of the crystallized glass, η_g the viscosity of the precursor glass, and α the volume fraction of crystalline phase. Based on Eq. 1, a higher concentration of β -quartz ss phase led to a high viscosity in the crystallized glass, which was in agreement with the TEM observation and viscosity measurement (Figures 4 and 6). Additionally, with the formation of β -quartz ss ($\text{Li}_2\text{O} \cdot \text{Al}_2\text{O}_3 \cdot 4\text{SiO}_2$), a highly siliceous residual glass was developed, which increased the viscosity of the system. The finding in our *in situ* viscosity measurement at the nucleation step was consistent with the previous reports. Our *in situ* measurement throughout the full ceramming cycle established the viscosity–temperature–time relationship for the first time.

CONCLUSION

An investigation on the evolutions of crystallization, microstructure, and viscosity in lithium aluminosilicate glass was conducted in this work. The addition of a nucleation agent

(TiO₂) was found to have a marked impact on the properties in both the glass and glass-ceramics. At the nucleation stage, phase separation and formation of β -quartz ss phase were observed, resulting in an increase of one order of magnitude in viscosity in TiO₂-containing glass. In contrast, the viscosity in TiO₂-free glass showed a monotonic decrease in viscosity when cerammed using the same cycle. Further viscosity variation due to crystallization and crystal growth was also observed in TiO₂-containing glass. The glass viscosity demonstrated a strong dependence on the phase assemblage and structural changes during ceramming

as supported by HTXRD, DSC, and TEM analysis. Last but not the least, the addition of TiO₂ helped achieve a near-net shape ceramming due to the high glass viscosity throughout the whole thermal treatment, which was critical for the manufacturing of products with complicated three-dimensional shapes.

AUTHOR CONTRIBUTIONS

All authors conducted experiments and contributed to the writing of the draft.

REFERENCES

- Ananthanarayanan, A., Kothiyal, G. P., Montagne, L., and Revel, B. (2010). MAS-NMR studies of lithium aluminum silicate (LAS) glasses and glass-ceramics having different Li₂O/Al₂O₃ ratio. *J. Solid State Chem.* 183, 120–127. doi:10.1016/j.jssc.2009.10.006
- ASTM International. (2013). “Standard test method for annealing point and strain point of glass by beam bending,” in *ASTM C598-93* (West Conshohocken, PA).
- Barbieri, L., Leonelli, C., Manfredini, T., Siligardi, C., and Corradi, A. B. (1997a). Nucleation and crystallization of a lithium aluminosilicate glass. *J. Am. Ceram. Soc.* 80, 3077–3083. doi:10.1111/j.1151-2916.1997.tb03235.x
- Barbieri, L., Corradi, A. B., Leonelli, C., Siligardi, C., Manfredini, T., and Pellacani, G. C. (1997b). Effect of TiO₂ addition on the properties of complex aluminosilicate glasses and glass-ceramics. *Mater. Res. Bull.* 32, 637–648. doi:10.1016/S0025-5408(97)00029-9
- Barbieri, L., Leonelli, C., Manfredini, T., Siligardi, C., Corradi, A. B., Mustarelli, P., et al. (1997c). Nucleation and crystallization of a lithium aluminosilicate glass. *J. Am. Ceram. Soc.* 80, 3077–3083. doi:10.1111/j.1151-2916.1997.tb03235.x
- Beall, G. H., and Doman, R. C. (1987). “Glass-ceramics,” in *Encyclopedia of Physical Science and Technology*, ed. R. A. Meyer. (New York: Academic Press), Vol. 6, 294–307.
- Beall, G. H., and Pinckney, L. R. (1999). Nanophase glass-ceramics. *J. Am. Ceram. Soc.* 82, 5–16. doi:10.1111/j.1151-2916.1999.tb01716.x
- Bhattacharyya, S., Höche, T., Jinschek, J. R., Avramov, I., Wurth, R., Müller, M., et al. (2009). Direct evidence of Al-rich layers around nanosized ZrTiO₄ in glass: putting the role of nucleation agents in perspective. *Cryst. Growth Des.* 10, 379–385. doi:10.1021/cg9009898
- Bocker, C., Rüssel, C., and Avramov, I. (2013). Transparent nano crystalline glass-ceramics by interface controlled crystallization. *Int. J. Appl. Glass Sci.* 4, 174–181. doi:10.1111/ijag.12033
- Chavoutier, M., Caurant, D., Majerus, O., Boulesteix, R., Loiseau, P., Jousseau, C., et al. (2014). Effect of TiO₂ content on the crystallization and the color of (ZrO₂, TiO₂)-doped Li₂O–Al₂O₃–SiO₂ glasses. *J. Non-Cryst. Solids* 384, 15–24. doi:10.1016/j.jnoncrysol.2013.03.034
- Doherty, P., Lee, D., and Davis, R. (1967). Direct observation of the crystallization of Li₂O–Al₂O₃–SiO₂ glasses containing TiO₂. *J. Am. Ceram. Soc.* 50, 77–81. doi:10.1111/j.1151-2916.1967.tb15043.x
- Dressler, M., Rüdinger, B., and Deubener, J. (2011a). An in situ high-temperature X-ray diffraction study of early-stage crystallization in lithium aluminosilicate glass-ceramics. *J. Am. Ceram. Soc.* 94, 1421–1426. doi:10.1111/j.1551-2916.2010.04252.x
- Dressler, M., Rüdinger, B., and Deubener, J. (2011b). An in situ high-temperature X-ray diffraction study of early-stage crystallization in lithium aluminosilicate glass-ceramics. *J. Am. Ceram. Soc.* 94, 1421–1426. doi:10.1111/j.1551-2916.2010.04252.x
- Fernandes, H. R., Tulyaganov, D. U., Goel, I. K., and Ferreira, J. M. F. (2008). Crystallization process and some properties of Li₂O–SiO₂ glass-ceramics doped with Al₂O₃ and K₂O. *J. Am. Ceram. Soc.* 91, 3698–3703. doi:10.1111/j.1551-2916.2008.02724.x
- Guedes, M., Ferro, A. C., and Ferreira, J. M. F. (2001). Nucleation and crystal growth in commercial LAS compositions. *J. Eur. Ceram. Soc.* 21, 1187–1194. doi:10.1016/S0955-2219(00)00333-2
- Henderson, D. (1979). Experimental analysis of non-isothermal transformations involving nucleation and growth. *J. Therm. Anal.* 15, 325–331. doi:10.1007/BF01903656
- Höche, T., Mäder, M., Bhattacharyya, S., Henderson, G. S., Gemming, T., Wurth, R., et al. (2011). ZrTiO₄ crystallisation in nanosized liquid–liquid phase-separation droplets in glass – a quantitative XANES study. *CrystEngComm* 13, 2550–2556. doi:10.1039/c0ce00716a
- Holand, W., Apel, E., van 't Hoen, C., and Rheinberger, V. (2006). Studies of crystal phase formations in high-strength lithium disilicate glass-ceramics. *J. Non-Cryst. Solids* 352, 4041–4050. doi:10.1016/j.jnoncrysol.2006.06.039
- Holand, W., and Beall, G. (2002). *Glass-Ceramic Technology*. Hoboken, NJ: John Wiley & Sons, Inc.
- Holand, W., and Beall, G. (2011). *Glass-Ceramic Technology*, 2nd Edn. Hoboken, NJ: John Wiley & Sons, Inc.
- Höche, T., Patzig, C., Gemming, T., Wurth, R., Rüssel, C., and Avramov, I. (2012). Temporal evolution of diffusion barriers surrounding ZrTiO₄ nuclei in lithia aluminosilicate glass-ceramics. *Cryst. Growth Des.* 12, 1556–1563. doi:10.1021/cg2016148
- Kim, K. D., Lee, S. H., and Ahn, H. K. (2004). Observation of nucleation effect on crystallization in lithium aluminosilicate glass by viscosity measurement. *J. Non-Cryst. Solids* 336, 195–201. doi:10.1016/j.jnoncrysol.2004.01.001
- Kleebusch, E., Patzig, C., Höche, T., and Rüssel, C. (2016). Effect of the concentrations of nucleating agents ZrO₂ and TiO₂ on the crystallization of Li₂O–Al₂O₃–SiO₂ glass: an X-ray diffraction and TEM investigation. *J. Sci. Mater.* 51, 10127–10138. doi:10.1007/s10853-016-0241-9
- Li, Y., Liang, K., Xu, B., and Cao, J. (2010). Crystallization mechanism and microstructure evolution of Li₂O–Al₂O₃–SiO₂ glass-ceramics with Ta₂O₅ as nucleating agent. *J. Therm. Anal. Calorim.* 101, 941–948. doi:10.1007/s10973-009-0598-y
- Lilensten, L., Fu, Q., Wheaton, B. R., Credle, A. J., Stewart, R. L., and Kohli, J. T. (2014). Kinetic study on lithium-aluminosilicate (LAS) glass-ceramics containing MgO and ZnO. *Ceram. Int.* 40, 11657–11661. doi:10.1016/j.ceramint.2014.03.171
- Matusita, K., and Sakka, S. (1980). Kinetic study on crystallization of glass by differential thermal analysis-criterion on application of Kissinger plot. *J. Non-Cryst. Solids* 38–39, 741–746. doi:10.1016/0022-3093(80)90525-6
- Misture, S. T. (2003). Large-volume atmosphere-controlled high-temperature X-ray diffraction furnace. *Meas. Sci. Technol.* 14, 1091. doi:10.1088/0957-0233/14/7/326
- Montedo, O. R. K., Hotza, D., de Oliveira, A. P. N., Meszaros, R., Travitzky, N., and Greil, P. (2012). Crystallisation kinetics of β -spodumene-based glass ceramic. *Adv. Mater. Sci. Eng.* 2012, 8. doi:10.1155/2012/525428
- Nemati, A., Goharian, P., Shabani, M., and Afshar, A. (2010). Effects of nucleation agent particle size on properties, crystallisation and microstructure of glass-ceramics in TiO₂–ZrO₂–Li₂O–CaO–Al₂O₃–SiO₂ system. *Adv. Appl. Ceram.* 109, 318–323. doi:10.1179/174367609X422063
- Nordmann, A., and Cheng, Y.-B. (1997). Crystallization behaviour and microstructural evolution of a Li₂O–Al₂O₃–SiO₂ glass derived from spodumene mineral. *J. Sci. Mater.* 32, 83–89. doi:10.1023/A:1018519030791
- Ostertag, W., Fischer, G. R., and Williams, J. P. (1968). Thermal expansion of synthetic β -spodumene and β -spodumene–silica solid solutions. *J. Am. Ceram. Soc.* 51, 651–654. doi:10.1111/j.1151-2916.1968.tb12638.x

- Raghuwanshi, V. S., Rüssel, C., and Hoell, A. (2014). Crystallization of ZrTiO₄ nanocrystals in lithium-alumino-silicate glass ceramics: anomalous small-angle X-ray scattering investigation. *Cryst. Growth Des.* 14, 2838–2845. doi:10.1021/cg5001232
- Ray, C. S., and Day, D. E. (1990). Determining the nucleation rate curve for lithium disilicate glass by differential thermal-analysis. *J. Am. Ceram. Soc.* 73, 439–442. doi:10.1111/j.1151-2916.1990.tb06532.x
- Stookey, S. D. (1960a). *Method of Making Ceramics and Product Thereof*. US Patent Vol. 2920971. Corning Glass Works, USA.
- Stookey, S. D. (1960b). *Method of Making a Semicrystalline Ceramic Body*. US Patent Vol. 2933857.
- Sinton, C. W., Crawford, A., Mixture, S., Seeger, J., Wondraczek, L., and Deubener, J. (2008). High temperature reactions between soda-lime-silica glass and lithium aluminosilicate glass-ceramics. *Glass Technol. Eur. J. Glass Sci. Technol. A* 49, 133–138.
- Soares, V. O., and Zanotto, E. D. (2016). Effect of P₂O₅ on the nonisothermal sinter-crystallization process of a lithium aluminum silicate glass. *Int. J. Appl. Ceram. Technol.* 13, 948–955. doi:10.1111/ijac.12540
- Wang, M.-C., Li, W.-L., Cheng, C.-W., Chang, K.-M., Chen, Y.-F., and Hsi, C.-S. (2010). The phase transformation and crystallization kinetics of (1-x)Li₂O-xNa₂O-Al₂O₃-4SiO₂ glasses. *Materials Chemistry and Physics* 123, 203–209. doi:10.1016/j.matchemphys.2010.03.083
- Wurth, R., Munoz, F., Müller, M., and Rüssel, C. (2009). Crystal growth in a multicomponent lithia aluminosilicate glass. *Mater. Chem. Phys.* 116, 433–437. doi:10.1016/j.matchemphys.2009.04.010
- Zanotto, E. D. (2010). A bright future for glass-ceramics. *Am. Ceram. Soc. Bull.* 89, 19–27.

Conflict of Interest Statement: The authors declare that the research was conducted in the absence of any commercial or financial relationships that could be construed as a potential conflict of interest.

Copyright © 2016 Fu, Wheaton, Geisinger, Credle and Wang. This is an open-access article distributed under the terms of the Creative Commons Attribution License (CC BY). The use, distribution or reproduction in other forums is permitted, provided the original author(s) or licensor are credited and that the original publication in this journal is cited, in accordance with accepted academic practice. No use, distribution or reproduction is permitted which does not comply with these terms.



Ion-Exchange in Glass-Ceramics

George H. Beall¹, Monique Comte², Matthew J. Dejneka¹, Paulo Marques²,
Philippe Pradeau^{2*} and Charlene Smith¹

¹Corning Incorporated Science and Technology Division, Corning, NY, USA, ²Corning S.A.S, Avon, France

OPEN ACCESS

Edited by:

Joachim Deubener,
Clausthal University
of Technology, Germany

Reviewed by:

Francisco Muñoz,
Spanish National
Research Council, Spain
Chao Liu,
Wuhan University
of Technology, China

*Correspondence:

Philippe Pradeau
pradeaup@corning.com

Specialty section:

This article was submitted
to Glass Science,
a section of the journal
Frontiers in Materials

Received: 14 June 2016

Accepted: 03 August 2016

Published: 23 August 2016

Citation:

Beall GH, Comte M, Dejneka MJ,
Marques P, Pradeau P and Smith C
(2016) Ion-Exchange in
Glass-Ceramics.
Front. Mater. 3:41.
doi: 10.3389/fmats.2016.00041

In the past few years, ion-exchange (IOX) in glasses has found a renewed interest with a lot of new development and research in industrial and academic labs and the commercialization of materials with outstanding mechanical properties. These glasses are now widely used in many electronic devices, including hand-held displays and tablets. The exchange is generally conducted in a bath of molten salt below the transition temperature of the glass. The exchange at the surface of an alkali ion by a bigger one brings compressive stress at the surface. The mechanical properties are dependent on the stress level at the surface and the depth of penetration of the bigger ion. As compared to glasses, glass-ceramics have the interest to display a wide range of aspects (transparent to opaque) and different mechanical properties (especially higher modulus and toughness). There has been little research on IOX in glass-ceramics. In these materials, the mechanisms are much more complex than in glasses because of their polyphasic nature: IOX generally takes place mostly in one phase (crystalline phase or residual glass). The mechanism can be similar to what is observed in glasses with the replacement of an ion by another in the structure. But in some cases this IOX leads to microstructural modifications (for example, amorphization or phase change). This article reviews these IOX mechanisms using several transparent and opaque aluminosilicate glass-ceramics as examples. The effect of the IOX in the various glass-ceramics will be described, with particular emphasis on flexural strength.

Keywords: ion-exchange glass-ceramics, mechanical properties, b-quartz solid solution, b-spodumene solid solution, nepheline, microstructures, X-ray diffraction

INTRODUCTION

In the past few years, ion-exchange (IOX) in glasses has found a renewed interest with a lot of new development and research in industrial and academic labs and the commercialization of materials with outstanding mechanical properties (Varshneya, 2010; Aaldenberg et al., 2016). These glasses are now widely used in many electronic devices, including hand-held displays and tablets (Glaesemann et al., 2012). They find also applications in the architectural and automotive markets.

One can imagine new applications using glass-ceramics instead of glasses as a much wider range of aspect can be obtained. Glass-ceramics display various opacity and color: from opaque to transparent and for opaque materials, including white to black and a range of colors. Glass-ceramics can present also improved mechanical properties as compared to glasses with especially higher toughness and modulus.

Ion-exchange is generally conducted in a bath of molten salt. The exchange from the surface of an alkali ion in the glass or glass-ceramic by a bigger one from the bath leads to compressive stress at the surface and because of the concentration distribution to a stress profile through the

sample. The mechanical properties are dependent on the stress level at the surface (CS) and the depth of penetration of the bigger ion (Gy, 2008).

If the IOX in glasses has been the subject of many studies, there has been little research on the IOX in glass-ceramics. In these materials, the mechanisms are much more complex than in glasses because of their polycrystalline nature: IOX generally takes place mostly in one phase (crystalline phase or residual glass). In some cases, the mechanism is similar to what is observed in glasses with the replacement of an ion by another in the structure; while in other cases, this IOX leads to microstructural modifications (for example, amorphization or phase change of a crystalline phase).

These different mechanisms have been observed at Corning studying IOX in different transparent and opaque aluminosilicate glass-ceramics. This research is going to be presented here with a special emphasis on the impact of IOX on microstructure and mechanical properties, especially flexural strength. The different systems and corresponding IOX mechanisms are summarized in **Table 1**.

Several papers demonstrate a significant increase of the modulus of rupture of glass-ceramics after IOX. Most of them do not detail the IOX mechanisms.

For example, in 1967, Beall et al. (1967) have shown that the modulus of rupture of β -quartz glass-ceramic can be multiplied by a factor of 5 replacing Li^+ by K^+ or Mg^{2+} by 2Li^+ . More recently, Takeuchi et al. (1997) have studied IOX in ferrules made of β -spodumene glass-ceramic and shown that replacement of Li^+ by Na^+ leads to a bending-strength of about 500 MPa, which is similar to that of an alumina ferrule and that a bending-strength of 310 MPa is maintained after scratching. Berthier da Cunha et al. (2007) have shown that IOX in a $\text{Na}_{4+2x}\text{Ca}_{4-x}\text{Si}_6\text{O}_{18}$ ($0 < x < 1$) glass-ceramic is associated with a significant increase of hardness and indentation fracture toughness. A modest but significant increase of strength associated with an increase of

the Weibull modulus has also been observed in lithium disilicate glass-ceramics (Fischer et al., 2008).

Tagantsev (1999) has been the first to describe an interesting mechanism in the case of IOX in a lithium metasilicate glass-ceramic: the replacement of lithium ions by sodium ions is associated with an amorphization of the glass-ceramic in the layer undergoing IOX.

Such an amorphization has also been observed by Laczka et al. in glass-ceramics containing both lithium disilicate and lithium aluminosilicate phases. The IOX induced amorphization was found to occur in both crystalline phases (Laczka et al., 2015).

Another phenomenon has been evidenced in nepheline glass-ceramics (Duke et al., 1967; Ponsot et al., 2014): the IOX (K^+ for Na^+) leads to formation of kalsilite at the surface that leads to a very significant increase of the modulus of rupture.

MATERIALS AND METHODS

The glasses with the compositions indicated in **Table 2** have been melted in platinum crucibles at temperature in the 1600–1650°C range. Batches in the range of 1000–2500 g were used. After melting and fining, the glasses were poured and annealed.

Pieces were cut for the crystallization treatment. The thermal treatments used are reported in **Table 2**. The crystalline phases were determined by X-ray diffraction (XRD).

Then the samples were ion-exchanged in molten baths. The compositions of the baths as well as the temperature and length of the treatments are summarized on **Table 2**.

X-ray diffraction was used to determine the effect of IOX on microstructure. A Bragg–Brentano $\theta/2\theta$ configuration with a $\text{Cu K}\alpha_1$ radiation was used. Patterns were measured on samples surface before and after IOX. Rietveld analysis was performed (Rodriguez-Carvajal, 1993). The X-Ray penetration depth is roughly 100 μm in this configuration. For ion-exchanged samples a gradient of crystallization is observed on this thickness and, consequently, the obtained data (e.g., the average size of the crystals or the cell parameters) are mean values.

Grazing Incidence Angle Diffraction (GIAD) was also performed in one case to quantify the microstructure evolution after ionic exchange as a function of thickness.

Grazing Incidence Angle Diffraction measurements at several fixed incident angles α were performed. The fixed incident angles are 1.5, 7.5, and 15° corresponding, respectively, to depths of ~2, 10, and 20 μm . Then each depth pattern was quantified by Rietveld refinement.

The mechanical performance of the glass-ceramics was measured by a ring on ring test. This test evaluates the biaxial flexure strength. In some cases, measurements have also been made after abrasion. Abrasion was performed with silicon carbide (grain size 70 μm) during 5 s at a pressure of 0.10 MPa (except if something else is specified). This last test was used to quantify retained mechanical performance after having imposed a given flaw population. The size of the samples is indicated on **Table 2**. Ten to 30 optically polished samples were used for each test.

TABLE 1 | Different strengthening mechanism obtained with IOX in glass-ceramics (g.c.).


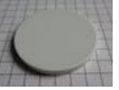

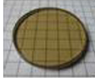
Mechanism	Examples presented here	Aspect of the glass-ceramic
Typical IOX (larger ion for smaller)	In the residual glass	Black fusion formable g.c. Black, opaque  700°C-4hr
	In the crystals	Spodumene g.c. White, opaque 
	Mg-rich β -quartz s.s. g.c.	Transparent  Crystallization and Ch Stuffed β -Quar O. H. BEALL, B. R. KAR Technical Staff Division, Corning
Surface amorphization	Li-rich β -quartz s.s. g.c.	Transparent 
Phase change	Nepheline g.c.	White, opaque

TABLE 2 | Compositions (mol%) of the glass-ceramics and experimental conditions.

Main crystalline phase	MgO–TiO ₂ –Fe ₂ O ₃ with ϵ -Fe ₂ O ₃ structure		Spodumene solid solution	Li-rich β -quartz solid solution	Mg-rich β -quartz solid solution	Nepheline
Composition	GC1	GC2				
SiO ₂	63.82	63.94	69	72.8	71	55
Al ₂ O ₃	13.89	13.6	13	12.6	13	20
B ₂ O ₃	5.1	5.18				
Li ₂ O			8	8.2	4	
Na ₂ O	13.76	13.66		2.6	0.5	
K ₂ O						13
MgO	1.74	1.75			9	5
MgO + ZnO			4			
TiO ₂	0.98	0.99	3.6	2.1		
ZrO ₂				0.9	2.5	7
Fe ₂ O ₃	0.56	0.71				
Other			2.4	0.8		
Crystallization heat treatment:						
– Nucleation (°C – h)		630 – 2	780 – 2	Ramp from 650 to 820 – 0.66	820 – 4	850 – 2
– Growth (°C – h)		700 to 750 – 4	975 – 4	900 – 0.25	875 – 4	1050 – 2
Typical IOX conditions (1):						
– Bath	KNO ₃	KNO ₃	NaNO ₃	KCl/K ₂ SO ₄ ^a	Li ₂ SO ₄ /K ₂ SO ₄ ^a	KNO ₃
– Temperature (°C)	420	430	Around 400	700–725	710–800	450
– Time (h)	6.5	8	2–4	4–8	4–16	2–48
Typical IOX conditions (2):						
– Bath						KCl/K ₂ SO ₄ ^a
– Temperature (°C)						700
– Time (h)						0.5–16
Sample size for ring on ring test		50-mm square, 0.8-mm thick		32-mm diameter, 2.1-mm thick		50-mm square, 0.8-mm thick

^aIOX bath compositions: KCl 54 wt%/K₂SO₄ 48 wt% and Li₂SO₄ 90 wt%/K₂SO₄ 10 wt%.

The reported results are the load to failure distribution because in most cases the strength of the ion-exchanged samples was so high that bending displacement was large enough to make the membrane stresses non-negligible. Therefore, conventional failure stress calculations would overestimate the material stress at failure. The Weibull shape and scale parameters corresponding to failure load are also reported. The scale parameter corresponds to 63.2% of failure probability.

RESULTS

Ion-Exchange in the Residual Glass

The example given here has been obtained developing a glass-ceramic suitable as backs of portable electronic devices (Dejneka et al., 2014).

As compared to metals, this glass-ceramic has the advantage to be transparent to microwave and radio frequency radiation. As compared to glasses, it allows to obtain a black aspect and to be opaque enough to hide the interior of the devices. Other requirements were a high mechanical resistance and, to limit cost, the need to have a precursor glass that can be formed by methods, such as fusion draw. This last requirement allows obtaining thin sheets with pristine surfaces (therefore, no further polishing is needed to obtain products).

However, this last requirement is not met by most of the glass-ceramics as they present generally relatively low viscosity

at the liquidus (typically lower than 2 kPa s). If such a liquidus is suitable to form articles by pressing or rolling, it prevents the use of forming methods, such as fusion draw for which at least 20 kPa s are required.

To obtain a product meeting all these requirements, sodium aluminosilicate glasses displaying high viscosity at the liquidus were used (Table 2). With such glasses, it is known that exchange of sodium ions by potassium is easily obtained and can lead to outstanding mechanical strength. These glasses have been doped with about 1% TiO₂ and Fe₂O₃. After thermal treatment, crystallization of MgO–TiO₂–Fe₂O₃ with a ϵ -Fe₂O₃ structure takes place. The mean size of the crystals is smaller than about 20 nm (Figure 1). This glass-ceramic has several advantages:

- It displays a black color not easy to achieve in a glass; this color is due to Fe²⁺-Ti⁴⁺ charge transfer absorption in the crystals.
- As their levels are low, TiO₂ and Fe₂O₃ do not change the viscosity at the liquidus and the precursor glass stays fusion formable.
- As the level of crystallinity is low, the composition of the residual glass is close to the composition of the base glass and is favorable to an IOX leading to mechanical properties close to those of the undoped glass.

Figure 2 displays the results of the mechanical test performed on two of these materials in comparison with a Corning® Gorilla®

Glass (CGG). In the three cases, IOX increases very significantly the load to failure: from scale parameters of 380–460 N to values higher than 2300 N.

The slopes of the failure probability line are also significantly steeper: the Weibull shape factors that are in the 2.9–4.6 range

before IOX increase to values in the 15–19 range after IOX. The two glass-ceramics have properties at least as good as CGG.

Ion-Exchange Leading to Surface Amorphization: Li-Rich β -Quartz Solid Solution Glass-Ceramics

Glass-ceramics based on crystallization of β -quartz solid solution have been discovered in the 60s. The general chemical formula of the β -quartz solid solution is $\text{Li}_{2-2(x+y)}\text{Mg}_x\text{Zn}_y\text{O} \cdot \text{Al}_2\text{O}_3 \cdot n\text{SiO}_2$ (with $n = 2-10$) where Al^{3+} ions replace Si^{4+} in tetrahedral sites and local electrical neutrality is ensured by the incorporation of small ions, such as Li^+ , Mg^{2+} or Zn^{2+} , into the channels of the structure. Nucleation is ensured by the addition to the batch of TiO_2 and/or ZrO_2 (a few mol%).

It is possible in this system to obtain highly crystalline transparent material by controlling the size of the crystallites (smaller than about 50 nm). An example of microstructure as observed by SEM is given in Figure 3.

The success of these glass-ceramics relies on the ability of some of these compositions (containing mainly lithium as compensator ion) to obtain materials that combine transparency, zero or very low thermal expansion coefficient, and ability to withstand temperatures of at least 700°C during several thousand hours without deformation or substantial modifications of the properties. They have found a wide range of applications ranging from telescope mirrors to ferrules for optical connectors or to

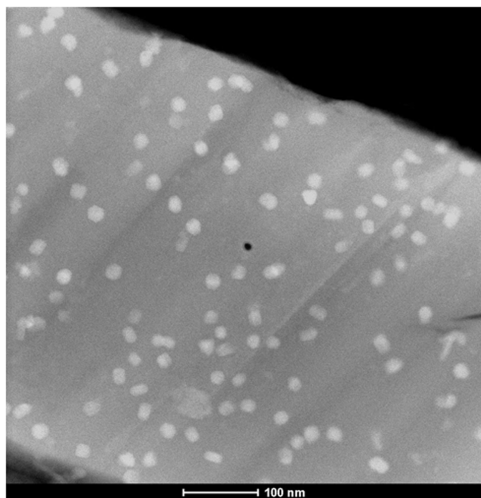


FIGURE 1 | TEM micrograph of the low crystallinity $\text{MgO-TiO}_2\text{-Fe}_2\text{O}_3$ glass-ceramic. (Composition GC2 – Table 1– cerammed at 750°C for 4 h).

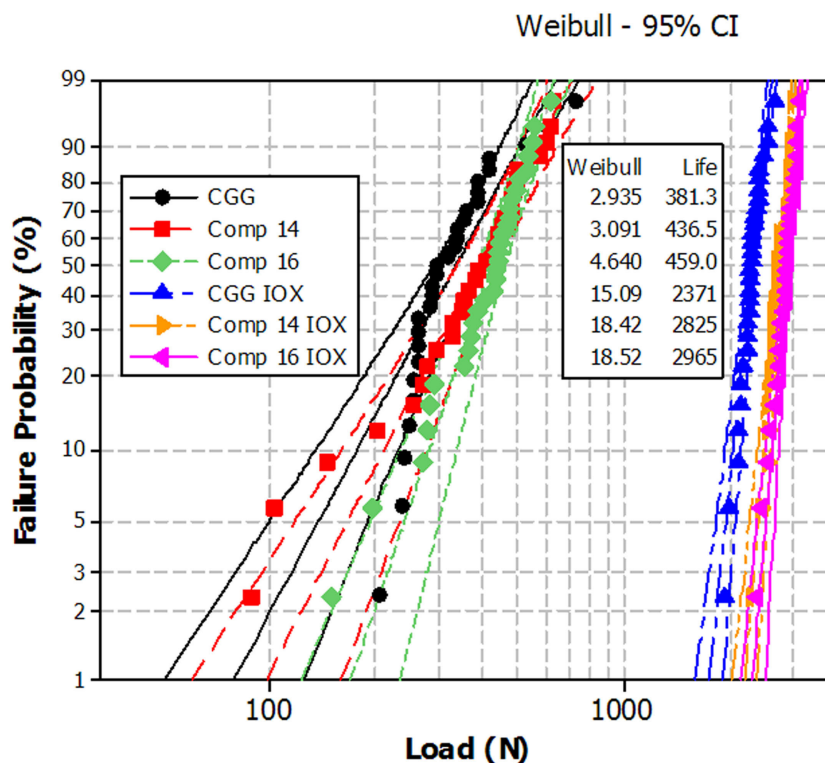


FIGURE 2 | Ring on ring biaxial flexure load to failure of low crystallinity $\text{MgO-TiO}_2\text{-Fe}_2\text{O}_3$ glass-ceramics (cerammed at 700°C for 4 h compared to CGG before and after ion-exchange). The dashed lines indicate the 95% confidence intervals. For the three ion-exchanged materials, compression is present on a layer around 40- μm thick.

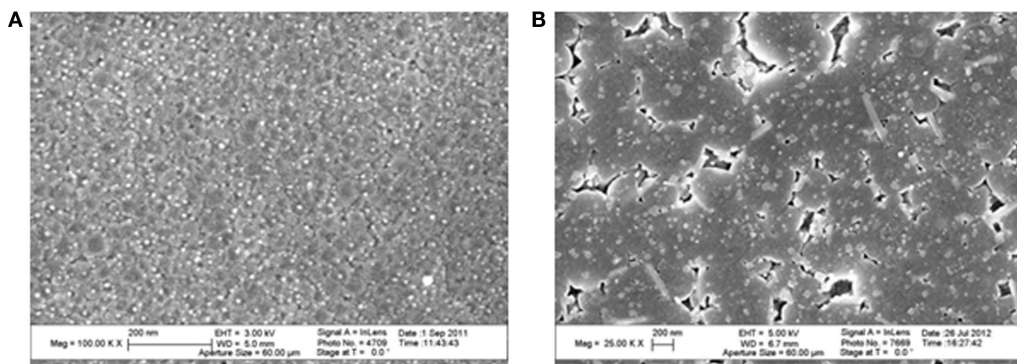


FIGURE 3 | Microstructures of glass-ceramics observed by SEM. They have been revealed by chemical etching. Source: Anne Crochet (Corning SAS). **(A)** Li-rich β -quartz solid solution glass-ceramic β -quartz crystals appear in gray and have a size around 30 nm. TiZrO_4 crystals appear in white and have a size of a few nanometers. **(B)** β -spodumene solid solution glass-ceramic. The pores correspond to the residual glass that has been etched. The bigger blocks are spodumene crystals, the small white dots with a size around 30 nm are spinel and the elongated crystals are rutile.

consumer products, such as cooktops, cookware, or fire-resistant windows.

As already observed (Beall et al., 1967), it has not been possible to obtain an increase of mechanical strength replacing lithium ions by sodium but exchange of lithium by potassium is efficient: in this case IOX has been performed during 4–16 h in the 700–725°C range in a $\text{KCl}/\text{K}_2\text{SO}_4$ bath. The measurement of the potassium profile shows that the depth of penetration of this ion is in the 20–60 μm range according to the time and temperature of exchange. **Figure 4** displays such profiles after IOXs of, respectively, 4 and 8 h at 700°C. The depth of diffusion of potassium is around 20 μm after 4 h and 35 μm after 8 h. This exchange is associated with a significant increase of mechanical strength: Weibull scale parameter of 4092 and 1953 N have been obtained after, respectively, 4 and 8 h, as compared to 820 N for the non-ion-exchanged glass-ceramic. However, it is observed that increasing the IOX time from 4 to 8 h reduces very significantly the mechanical strength dividing the scale parameter by 2.

Surface XRD (BB and GIAD) performed before and after an IOX of 4 h at 700°C evidence a strong microstructure modification (**Figure 5**): before IOX, the main crystalline phase is β -quartz solid solution with minor amount of the TiZrO_4 nucleating phase. After IOX, the crystalline phases are the same but an increase of the amorphous content is observed on the patterns (**Figure 5**). Rietveld analysis shows that the average size of the β -quartz solid solution crystals has significantly decreased (roughly divided by two). These observations strongly suggest that the IOX is associated with a surface amorphization. The GIAD measurements confirm these observations: after IOX, a strong decrease of the amount of the β -quartz phase is observed, this decrease being more important closer to the surface.

Ion-Exchange in the Crystalline Phase

Ion-Exchange in Mg-Rich β -Quartz Solid Solution Glass-Ceramics

We focus now on β -quartz solid solution glass-ceramics containing mainly magnesium to charge balance aluminum and with

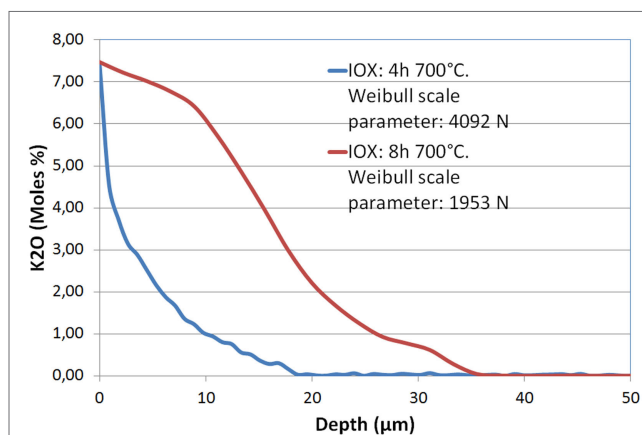


FIGURE 4 | Diffusion profile of K_2O in a Li-rich β -quartz solid solution glass-ceramic after an ion-exchange of 4 and 8 h at 700°C in a $\text{KCl}/\text{K}_2\text{SO}_4$ bath. The Weibull scale parameters reported in the legend show that the longer IOX is associated with a significant strength decrease.

composition given in **Table 2**. The glass-ceramic is transparent (**Table 1**). Because of the use of ZrO_2 alone as nucleating agent, it displays a very high transmission without the residual yellow color generally brought by the addition of TiO_2 (**Table 2**). IOX was performed in a $\text{Li}_2\text{SO}_4/\text{K}_2\text{SO}_4$ bath at temperatures in the range of 710–800°C, during 4–16 h. K_2SO_4 is added to lower the melting temperature. In these conditions, diffusion of lithium ions takes place to a depth of 40–200 μm .

After an IOX of 4 h at 710°C, surface XRD (BB) reveals an increase of the cell parameters of the β -quartz solid solution, suggesting that 2Li^+ ions replace Mg^{2+} in the structure (**Figure 6**).

Ion-exchange is associated with a very significant increase of the flexural strength as indicated in **Figures 7** and **8**. **Figure 7** gives the results of the mechanical test performed on glass-ceramics before and after an IOX of 16 h at 725°C and in this last case before and after abrasion. It is observed that abrasion decreases only very little the load to failure.

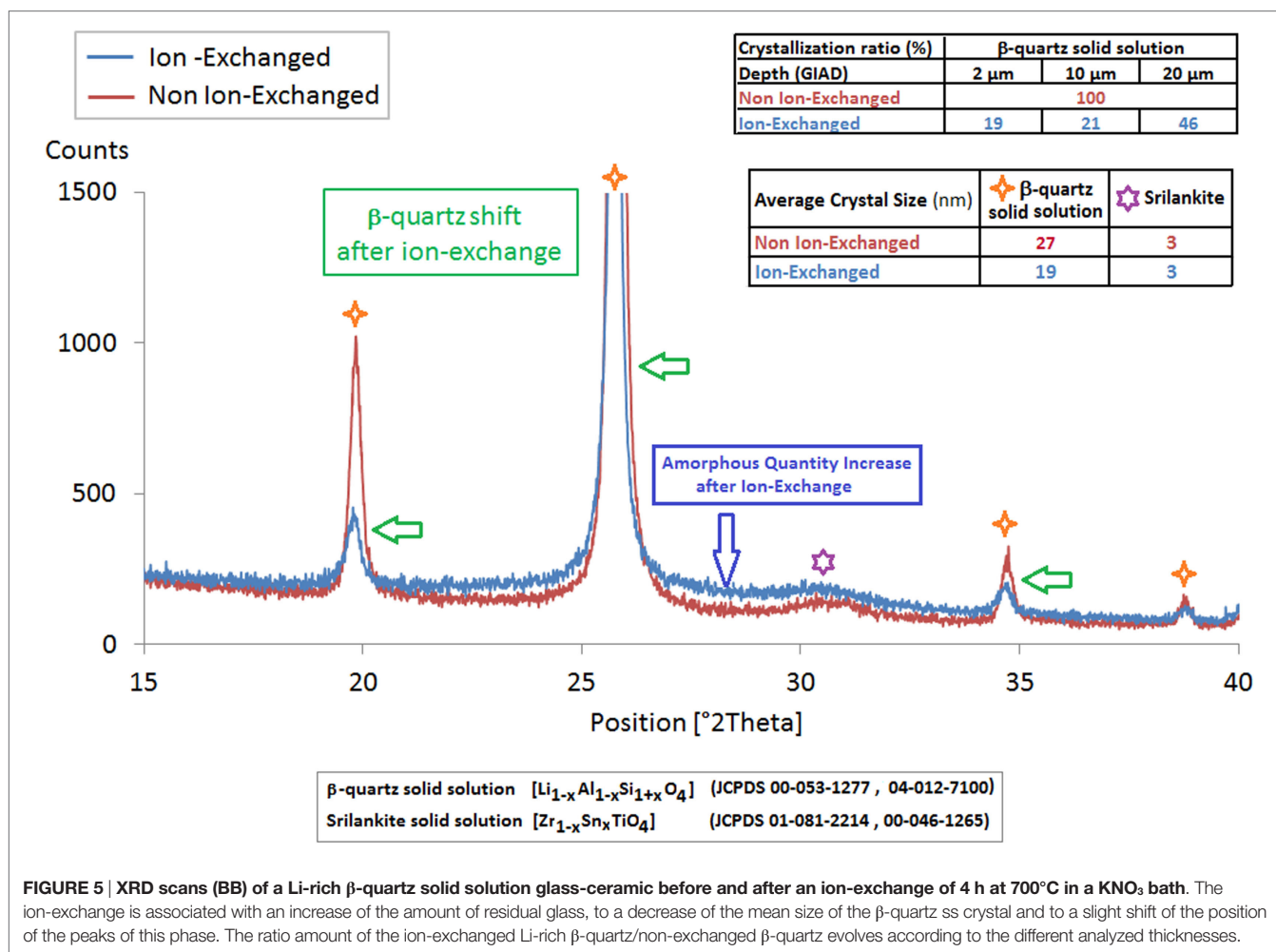


FIGURE 5 | XRD scans (BB) of a Li-rich β-quartz solid solution glass-ceramic before and after an ion-exchange of 4 h at 700°C in a KNO₃ bath. The ion-exchange is associated with an increase of the amount of residual glass, to a decrease of the mean size of the β-quartz ss crystal and to a slight shift of the position of the peaks of this phase. The ratio amount of the ion-exchanged Li-rich β-quartz/non-exchanged β-quartz evolves according to the different analyzed thicknesses.

Figure 8 gives the Weibull scale factor and the thickness of the surface layer in compression (DOL) for different IOX treatments. The mechanical strength attains a maximum at 725°C, then decreases for higher temperature of the bath.

This decrease seems associated with considerable potassium diffusion in the glass-ceramic above 750°C. This potassium diffusion inhibits the diffusion of magnesium. Diffusion profiles of magnesium and potassium after IOXs of respectively 4 h at 750 and 775°C illustrate this effect (**Figure 9**).

Ion-Exchange in Spodumene Glass-Ceramic

Spodumene glass-ceramics have been known for a very long time. They have been used and are still used to produce cookware materials and cooktops thanks to their low thermal expansion [coefficient of thermal expansion (CTE) around $10\text{--}20 \times 10^{-6} \text{K}^{-1}$ – $25\text{--}700^\circ\text{C}$].

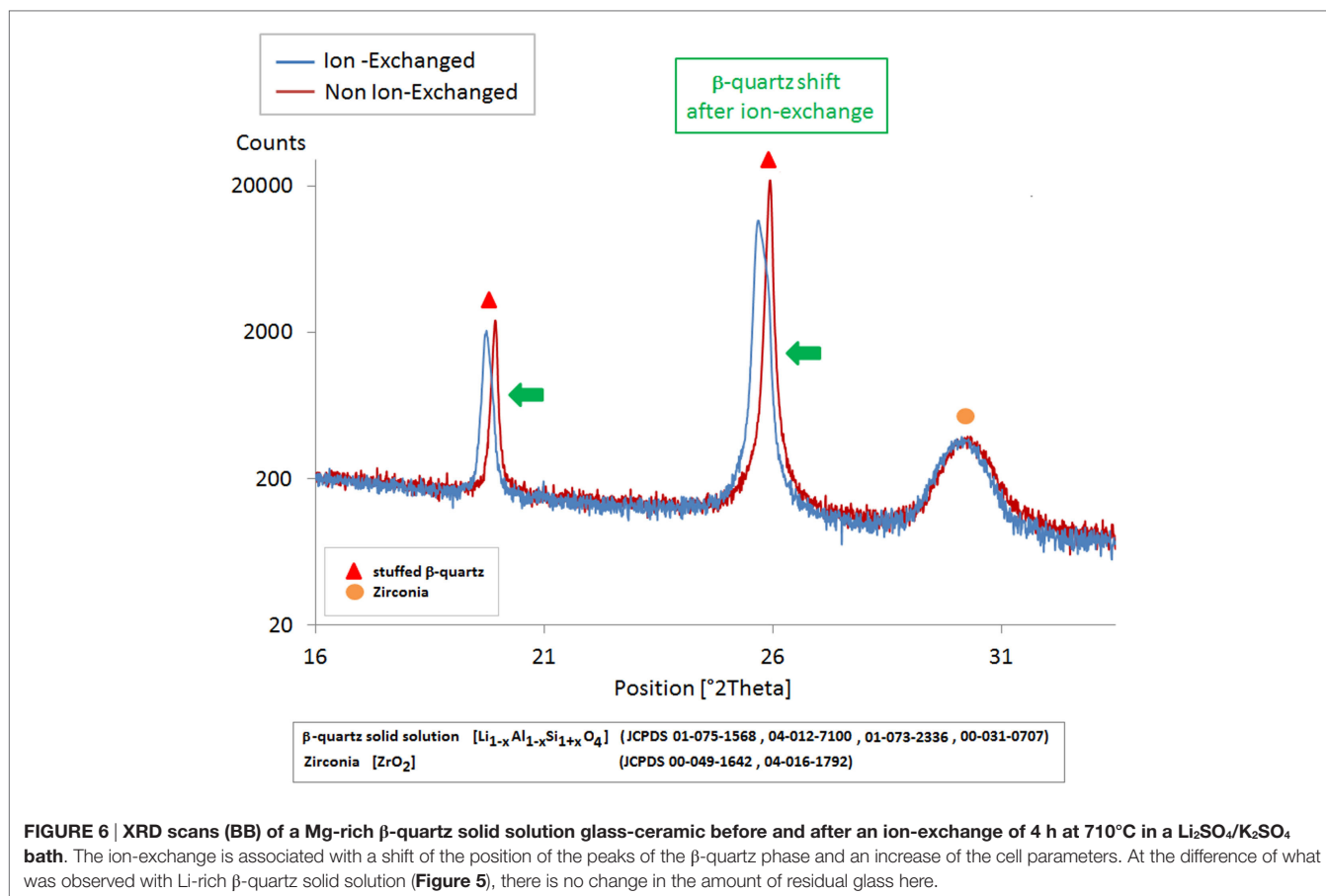
The crystalline phase is a solid solution with formula $\text{Li}_2\text{O} \cdot \text{Al}_2\text{O}_3 \cdot n\text{SiO}_2$ with $n = 2\text{--}8$. The material studied here has been nucleated through the addition of a few wt.% of TiO_2 . **Figure 3B** displays a SEM micrograph of this material. The spodumene crystals have a mean size of about 1 μm. Small amounts of rutile and spinels are also visible. The amount of residual glass is estimated to be around 10%wt.

Ion-exchange in a sodium nitrate bath leads to incorporation of sodium into the glass-ceramic. After exchanging for a few hours around 400°C in a sodium nitrate bath, the sodium ions diffuse up to a depth of around 100 μm as observed by microprobe technique (**Figure 10**). It is believed that sodium replaces lithium that cannot be analyzed by this technique. The concentration of the other elements is constant through the thickness. This IOX is proposed to take place in the crystals. A proof of that is given by the comparison of XRD patterns obtained, respectively, before and after IOX and that shows a very significant increase of the β-spodumene cell parameters, which is in good agreement with the replacement of Li by sodium in the crystals (**Figure 11**).

The result of the ring on ring test is indicated on **Figure 12**. The Weibull scale parameters are, respectively, 1341 and 780 N before and after abrasion.

Ion-Exchange Leading to a Crystalline Phase Modification

Nepheline is a stuffed derivative of tridymite with formula $(\text{Na},\text{K})\text{AlSiO}_4$. A white opaque glass-ceramic containing nepheline as main crystalline phase can be obtained using TiO_2 as nucleating



agent. Starting from a glass rich in sodium, it has been observed that sodium can be exchanged with potassium or in a potassium nitrate bath at 450°C or in a KNO_3/KCl bath at 700°C.

The diffusion of potassium and sodium obtained after 0.5 h at 700°C is represented on **Figure 10**: a diffusion of potassium on about 100 μm is observed. However, there is a strong accumulation of potassium in a 10-μm thick layer near the surface. In this layer, XRD (GIAD) has shown that nepheline $[\text{Na}_{7.11}(\text{Al}_{7.2}\text{Si}_{8.8}\text{O}_{32})]$ (JCPDS 01-079-0991) has transformed to kalsilite $[\text{KAlSiO}_4]$ (JCPDS 00-011-0579) (**Figure 13**).

The formation of kalsilite results in a very high load to failure (**Figure 12**) higher than for the ion-exchanged β-spodumene glass-ceramic described in 3.3.2. However, after abrasion results are inverted: the nepheline glass-ceramic displays a lower strength than the β-spodumene one.

DISCUSSION

The black fusion formable glass-ceramics in which IOX takes place in the residual glass combine the interesting properties of both the crystals and the residual glass: the crystals give to the material its black opaque aspect but are in small enough amount to keep a high viscosity at the liquidus compatible with forming by fusion draw and not to prevent the IOX process that takes place in the residual glass. The residual glass has a composition close to

CGG and leads to mechanical properties at least similar to those of the ion-exchanged CGG.

In the case of IOX involving ions in a crystalline phase, more diverse and complex mechanisms are observed:

β-spodumene glass-ceramics are easy to strengthen by IOX: the sodium for lithium exchange takes place at relatively low temperature (around 400°C) and short times (a few hours). Significant diffusion (around 100 μm) is easily achieved. The surface compression and the improvement of the mechanical strength are due to the volume increase of the crystals.

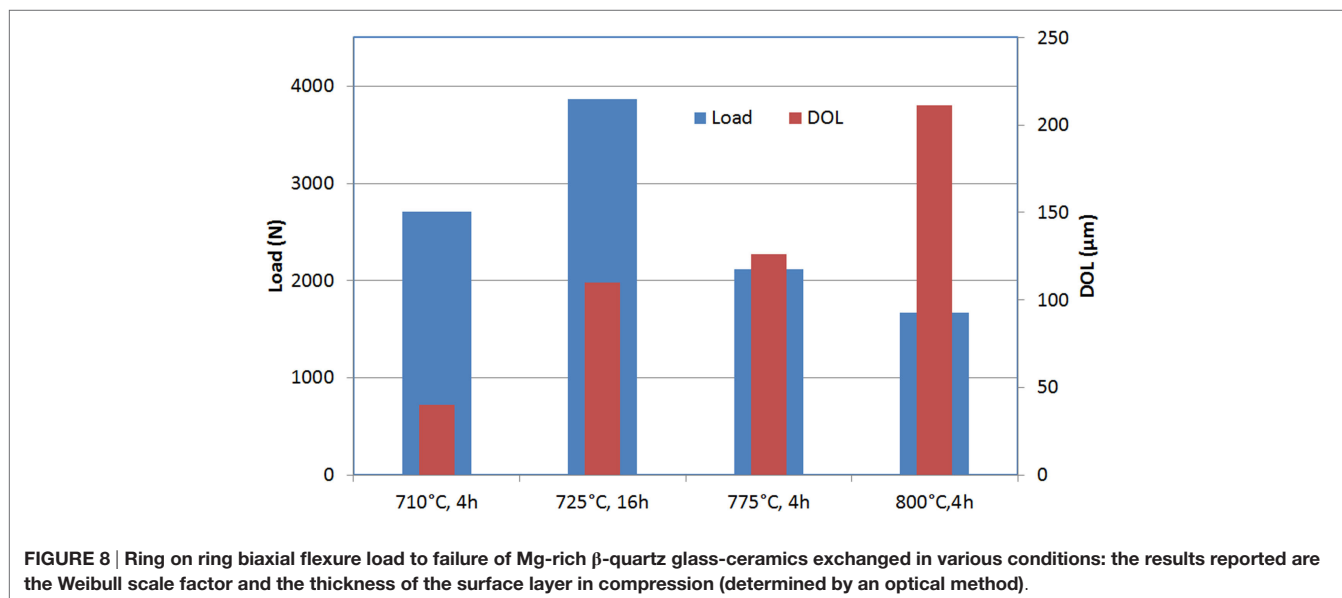
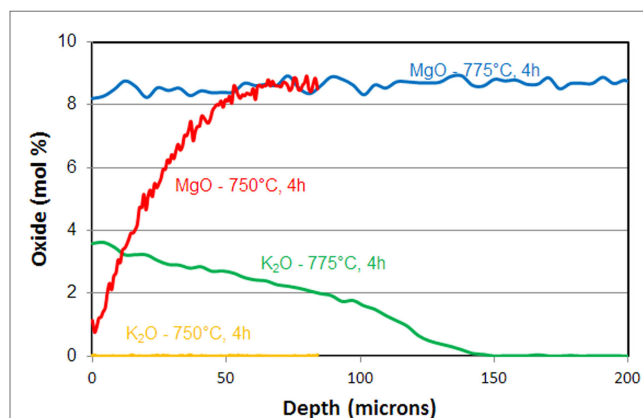
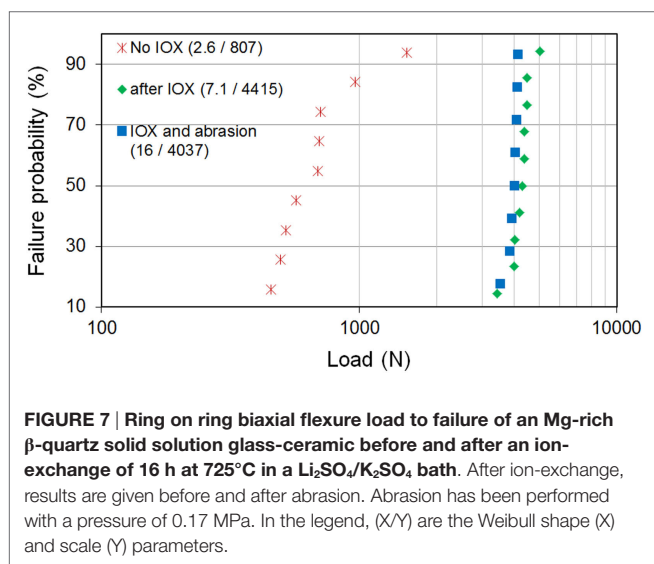
Ion-exchanges are much more difficult to achieve with β-quartz solid solution:

- Replacement of lithium by another alkali in the crystal structure does not appear possible. Exchange of lithium by potassium takes place but at high temperatures (700–725°C) and as potassium cannot be incorporated to the structure, it is associated with a destruction of the crystals. As described earlier, such a phenomenon has already been observed in lithium metasilicate glass-ceramics exchanging sodium for lithium (Tagantsev, 1999) and in glass-ceramics containing both lithium disilicate and lithium aluminosilicate phases (Laczka et al., 2015). The amorphization leads to a volume increase (the glass being less dense than the crystals), which results in compressive stresses. However, amorphization is

also associated with an increase of the coefficient of thermal expansion (CTE) and stress relaxation, which limit strengthening. This competition between compressive stress from the volume change and the higher CTE in the amorphous phase is probably what explains the modest increase of mechanical strength after 8 h of IOX at 725°C despite significant potassium diffusion (Figure 4).

- The exchange of magnesium by lithium takes place in the β -quartz crystals. It should be noted that, as in the previous case, high temperatures are needed to obtain this exchange. The strengthening mechanism is coming from two effects already described in the literature (Beall et al., 1967): the increase of the volume of the crystals (Figure 6) but also the formation of a surface layer with, in contrast to the previous case, a lower CTE than the bulk: the Li-rich β -quartz solid

solution crystals display lower CTE than the Mg-rich crystals (thermal expansions of magnesium containing glass-ceramics in the SiO_2 – MgAl_2O_4 join range from 30 to $45 \times 10^{-7} \text{ K}^{-1}$ at 50 – 70 w% SiO_2 while the thermal expansion of the lithium bearing glass-ceramic in the SiO_2 – LiAlSiO_4 join is slightly negative, about $-5 \times 10^{-7} \text{ K}^{-1}$). The combination of these two mechanisms leads to high mechanical performances. The very small effect of abrasion on the load to failure is worth to be noted. Beside that these glass-ceramics display very different physical properties as compared to CGG: namely a much lower CTE ($22 \times 10^{-7} \text{ K}^{-1}$ – 25 – 300°C – versus 85) and higher Young modulus (98 versus 65 GPa) Vickers hardness (900 versus 556) and toughness ($0.84 \text{ MPa}\cdot\text{m}^{1/2}$ versus 0.67 – measured by chevron notch). Another difference as compared to glass is that because of the very high IOX temperatures



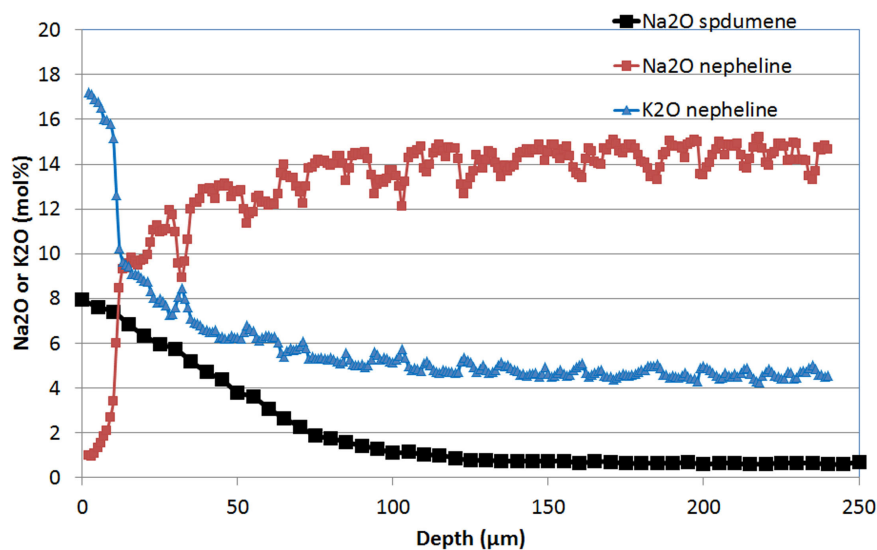


FIGURE 10 | Diffusion profile as measured by microprobe (EPMA) of Na₂O in a β -spodumene glass-ceramic after an ion-exchange of 2 h at 430°C in a sodium nitrate bath and of Na₂O and K₂O in a nepheline glass-ceramic after an ion-exchange of 0.5 h at 700°C in a KCl/K₂SO₄ bath. The concentrations of the other measured elements are constant through the thickness (Li₂O has not been measured).

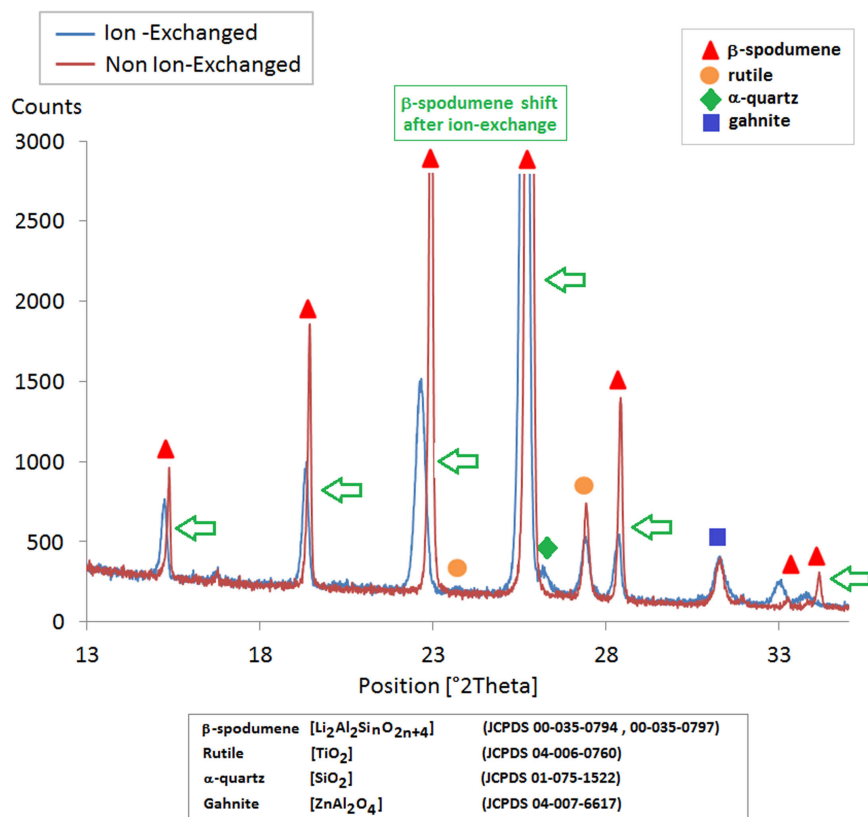


FIGURE 11 | XRD scans of a β -spodumene glass-ceramic before and after ion-exchange. The peaks related to rutile and gahnite do not shift with ion-exchange, while the other peaks that belong to β -spodumene shift during ion-exchange toward lower 2θ values showing an increase of the cell parameters and of the volume of the crystals.

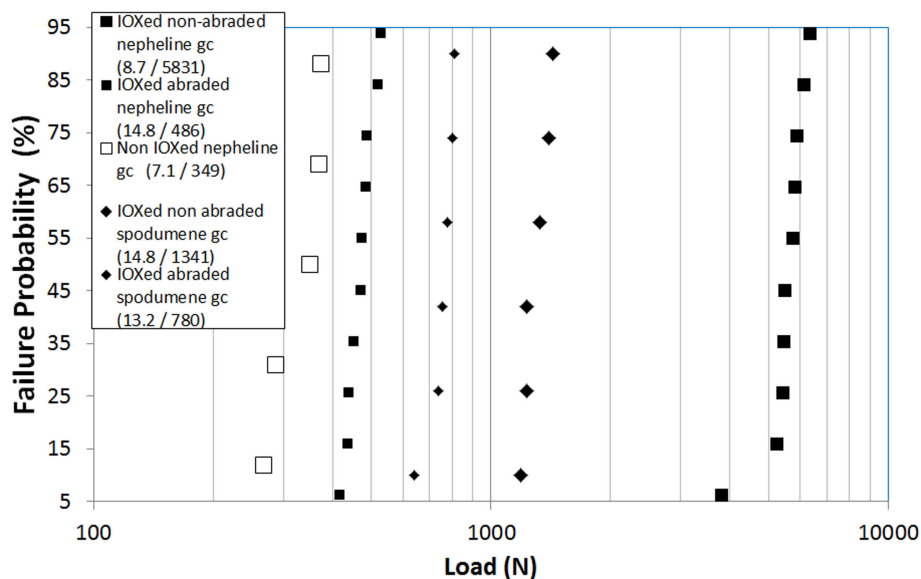


FIGURE 12 | Ring on ring biaxial flexure load to failure of a β -spodumene glass-ceramic after ion-exchange and of a nepheline glass-ceramic before and after ion-exchange. In both cases, after ion-exchange, results are given before and after abrasion. In the legend, (X/Y) are the Weibull shape (X) and scale (Y) parameters. The nepheline glass-ceramic has been exchanged for 6 h at 450°C.

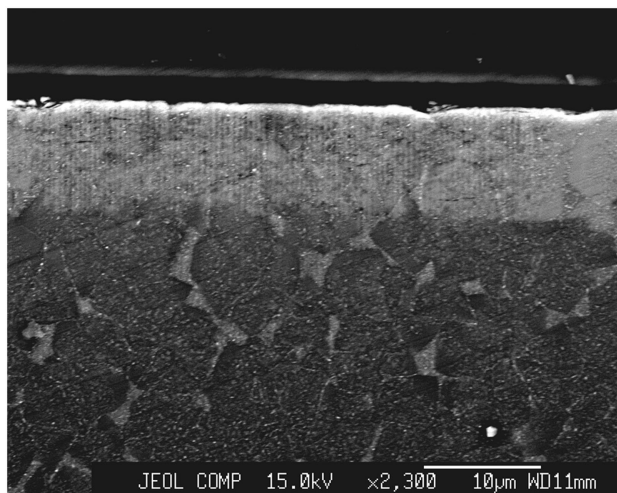


FIGURE 13 | Microstructure of the ion-exchanged zone of a nepheline glass-ceramic observed by SEM (backscattering). The potassium rich zones appear whiter. The 10- μ m whiter layer near the surface (top) is crystallized in kalsilite. Under that layer glassy pockets are observed between the nepheline crystals. They are enriched in potassium as compared to the crystals. Ion-exchange conditions: 0.5 h at 700°C in a KCl/K₂SO₄ bath.

relaxation is not observed when these glass-ceramics are used at temperature below \sim 500°C. All these specific properties could open to these materials applications that are not possible with ion-exchanged glasses.

The case of nepheline glass-ceramic appears unique: when the level of potassium in the crystals is sufficiently high, the crystal structure transforms to kalsilite. This transformation is associated

with a volume increase of about 10% and results in very high load to failure. However, this transformation occurs only near the surface where the potassium concentration is the highest. Below exchange is thought to take place in the nepheline structure with a lower volume increase.

In the example presented here, it has been observed that abrasion decreases very significantly the biaxial flexure strength. It is probably because the introduced flaws have a length close to the thickness of the kalsilite layer.

CONCLUSION

Through examples taken in various aluminosilicate systems, a review of the different IOX mechanisms in glass-ceramics and of the resulting mechanical properties has been presented. Some of these mechanisms (amorphization, crystalline phase change) are not observed with glasses. This illustrates the wide range of possibilities that offer glass-ceramics as compared to conventional glasses.

AUTHOR CONTRIBUTIONS

GB, Nepheline-b spodumene and b quartz glass-ceramics. MC, b spodumene and b-quartz. MD, low crystallinity glass-ceramic. PM, b quartz glass-ceramics. PP, X-ray Diffraction Expert and Corresponding Author. CS, b spodumene and glass-ceramics.

ACKNOWLEDGMENTS

Anne Crochet, Ben Hanson, Yassine Kilali, and Khaled Layouni for, respectively, SEM characterization, microprobe analysis, measurements of mechanical properties and discussion.

REFERENCES

- Aaldenberg, E. M., Lezzi, P. J., Seaman, J. H., Blanchet, T. A., and Tomozawa, M. (2016). Ion-exchanged lithium aluminosilicate glass: strength and dynamic fatigue. *J. Am. Ceram. Soc.* 99, 2645–2654. doi:10.1111/jace.14294
- Beall, G. H., Karstetter, B. R., and Rittler, H. L. (1967). Crystallization and chemical strengthening of stuffed β -quartz glass-ceramics. *J. Am. Ceram. Soc.* 5, 181–190. doi:10.1111/j.1151-2916.1967.tb15077.x
- Berthier da Cunha, T., Wu, J. P., Peitl, O., Fokin, V. M., Zanutto, E. D., Iannucci, L., et al. (2007). Mechanical properties and impact resistance of a new transparent glass-ceramic. *Adv. Eng. Mater.* 9, 191–195. doi:10.1002/adem.200600237
- Dejneka, M., Dutta, I., and Smith, C. (2014). Chemically strengthened low crystallinity black glass-ceramics with high liquidus viscosities. *Int. J. Appl. Glass Sci.* 5-2, 146–160. doi:10.1111/ijag.12076
- Duke, D. A., MacDowell, J. F., and Karstetter, B. R. (1967). Crystallization and chemical strengthening of nepheline glass-ceramics. *J. Am. Ceram. Soc.* 50, 67–74. doi:10.1111/j.1151-2916.1967.tb15041.x
- Fischer, H., De Souza, R. A., Wätjen, A. M., Richter, S., Edelhoff, D., Mayer, J., et al. (2008). Chemical strengthening of a dental lithium disilicate glass-ceramic material. *J. Biomed. Mater. Res. A* 87, 582–587. doi:10.1002/jbm.a.31798
- Gy, R. (2008). Ion exchange for glass strengthening. *Mater. Sci. Eng. B* 149, 159–165. doi:10.1016/j.mseb.2007.11.029
- Glaesemann, G. S., Gross, T. M., Bayne, J. F., and Price, J. J. (2012). “Fractography in the development of ion-exchange cover glass,” in *Fractography of Glasses and Ceramics VI: Ceramic Transactions*, eds J. R. Varner and M. Wightman (Hoboken, NJ: John Wiley & Sons, Inc.), 85–93. doi:10.1002/9781118433010.ch5
- Laczka, K., Cholewa-Kowalska, K., Środa, M., Rysz, J., Marzec, M. M., and Laczka, M. (2015). Glass-ceramics of LAS ($\text{Li}_2\text{O}-\text{Al}_2\text{O}_3-\text{SiO}_2$) system enhanced by ion-exchange in KNO_3 salt bath. *J. Non Cryst. Solids* 428, 90–97. doi:10.1016/j.jnoncrysol.2015.08.003
- Ponsot, I., Dal Mas, G., Bernardo, E., Dal Maschio, R., and Sglavo, V. M. (2014). Double strengthening by ion exchange of sintered nepheline glass-ceramics: a new simplified method. *J. Ceram. Process. Res.* 15(6), 411–417.
- Rodriguez-Carvajal, J. (1993). Recent advances in magnetic structure determination by neutron powder diffraction. *Phys. B* 192, 55–69. doi:10.1016/0921-4526(93)90108-I
- Tagantsev, D. K. (1999). Decrystallization of glass-ceramics under ion exchange diffusion. *J. Eur. Ceram. Soc.* 19, 1555–1558. doi:10.1016/S0955-2219(98)00475-0
- Takeuchi, Y., Mitachi, S., and Nagase, R. (1997). High strength glass-ceramic ferrule for SC-type single mode optical fiber connector. *IEEE Photonics Tech. Lett.* 9, 1502–1504. doi:10.1109/68.634722
- Varshneya, A. (2010). Chemical strengthening of glass: lessons learned and yet to be learned. *Int. J. Appl. Glass Sci.* 1, 131–142. doi:10.1111/j.2041-1294.2010.00010.x

Conflict of Interest Statement: The authors declare that the research was conducted in the absence of any commercial or financial relationships that could be construed as a potential conflict of interest.

Copyright © 2016 Beall, Comte, Dejneka, Marques, Pradeau and Smith. This is an open-access article distributed under the terms of the Creative Commons Attribution License (CC BY). The use, distribution or reproduction in other forums is permitted, provided the original author(s) or licensor are credited and that the original publication in this journal is cited, in accordance with accepted academic practice. No use, distribution or reproduction is permitted which does not comply with these terms.



Transparent Oxyfluoride Nano-Glass Ceramics Doped with Pr^{3+} and $\text{Pr}^{3+}\text{--Yb}^{3+}$ for NIR Emission

Giulio Gorni¹, Alessandro Cosci^{2,3}, Stefano Pelli^{2,3}, Laura Pascual⁴, Alicia Durán¹ and M. J. Pascual^{1*}

¹Instituto de Cerámica y Vidrio, Consejo Superior de Investigaciones Científicas (CSIC), Madrid, Spain, ²Microdevices for Photonics Laboratory (MIP-LAB), Istituto di Fisica Applicata "Nello Carrara", Consiglio Nazionale delle Ricerche (CNR), Sesto Fiorentino, Italy, ³Museo Storico della Fisica e Centro Studi e Ricerche Enrico Fermi, Roma, Italy, ⁴Instituto de Catálisis y Petroleoquímica, Consejo Superior de Investigaciones Científicas (CSIC), Madrid, Spain

OPEN ACCESS

Edited by:

Joachim Deubener,
Clausthal University of Technology,
Germany

Reviewed by:

Paul M. Voyles,
University of Wisconsin-Madison,
USA
Chao Liu,
Wuhan University of Technology,
China

*Correspondence:

Maria Jesús Pascual
mpascual@icv.csic.es

Specialty section:

This article was submitted to
Glass Science,
a section of the journal
Frontiers in Materials

Received: 27 May 2016

Accepted: 14 December 2016

Published: 03 January 2017

Citation:

Gorni G, Cosci A, Pelli S, Pascual L,
Durán A and Pascual MJ (2017)
Transparent Oxyfluoride Nano-Glass
Ceramics Doped with Pr^{3+} and
 $\text{Pr}^{3+}\text{--Yb}^{3+}$ for NIR Emission.
Front. Mater. 3:58.
doi: 10.3389/fmats.2016.00058

$\text{Pr}^{3+}\text{--Yb}^{3+}$ co-doped oxyfluoride glasses and glass-ceramics (GCs) containing LaF_3 nano-crystals have been prepared to obtain NIR emission of Yb^{3+} ions upon Pr^{3+} excitation in the blue region of the visible spectrum. Two different compositions have been tested: 0.1–0.5 $\text{Pr}\text{--Yb}$ and 0.5–1 $\text{Pr}\text{--Yb}$, in addition to Pr^{3+} singly doped samples. The crystallization mechanism of the nano-GCs was studied by differential thermal analysis revealing that it occurs from a constant number of nuclei, the crystal growth being limited by diffusion. High-resolution transmission microscopy demonstrated that phase separation acts as precursor for LaF_3 crystallization and a detailed analysis of the chemical composition (EDXS) revealed the enrichment in RE^{3+} ions inside the initial phase separated droplets, from which the LaF_3 crystals are formed. The RE^{3+} ions incorporation inside LaF_3 crystals was also proved by photoluminescence measurements showing Stark splitting of the RE^{3+} ions energy levels in the glass-ceramic samples. Lifetime measurements showed the existence of a better energy transfer process between Pr^{3+} and Yb^{3+} ions in the GCs compared to the as made glass. The highest value of energy transfer efficiency is 59% and the highest theoretical quantum efficiency is 159%, obtained for GCs 0.1–0.5 $\text{Pr}\text{--Yb}$ treated at 620°C for 40 h.

Keywords: transparent, glass-ceramics, rare-earths, crystallization, down-conversion, solar energy

INTRODUCTION

Solar green energy is one of the emerging fields where rare earth (RE) ions are intensively used to improve silicon solar cells (SSCs) efficiency. In fact, the most important routes to reduce costs and promote the use of solar energy are: decrease refining and crystallization cost of silicon (the most widely used semiconductor), to use less silicon (thinner cells), developing thin films solar cells of less expensive materials (organic, polymeric) and/or improving SSCs efficiency.

Currently, many efforts are focused in the modification of the photovoltaic (PV) cells to make them more efficient. The main problem to improve PV energy conversion efficiency is associated with the spectral mismatch between the energy distribution of photons in the incident solar spectrum and the band-gap of silicon (Huang et al., 2013). Therefore, in the last years, solar down-converter materials doped with RE ions, able to convert the blue part of the solar spectrum to the range 980–1050 nm,

where silicon presents the best response, are becoming increasingly important (Trupe et al., 2002; Richards, 2006; van der Ende et al., 2009).

According to Abrams et al. (2011), a theoretical improvement of SSCs could be as high as 7% for an ideal lossless system; however, improvements (even though smaller than 7%) could be reached with a properly engineered solar converter layer.

Among the converter materials, glasses and glass-ceramics (GCs) for PV application are increasingly important thanks to their relatively easy production and engineering and their capability of hosting a great variety of RE ions in different concentrations.

Oxyfluoride nano-GCs containing luminescent RE ions have been extensively studied for their good mechanical and optical properties. Oxyfluoride nano-GCs are very attractive host materials, because they combine the very low phonon energy of fluoride nano-crystals environment, especially LaF_3 ($<450\text{ cm}^{-1}$). They are able to host Ln^{3+} ions giving rise to high quantum efficiencies, with the high chemical and mechanical stability of a silicate glass matrix (de Pablos-Martín et al., 2012).

This paper describes the structural and optical properties of LaF_3 containing GCs doped with Pr^{3+} and $\text{Pr}^{3+}-\text{Yb}^{3+}$ of composition $55\text{SiO}_2-20\text{Al}_2\text{O}_3-15\text{Na}_2\text{O}-10\text{LaF}_3$ (mol%) produced by melting-quenching (MQ). The properties of the un-doped glass system have been extensively studied elsewhere (Bhattacharyya et al., 2009; Hemono et al., 2009; de Pablos-Martín et al., 2011).

There are many published examples of different glass systems and crystalline phases studied for solar application with $\text{Pr}^{3+}-\text{Yb}^{3+}$. Indeed, we have chosen doping concentrations also relying on literature.

Chen et al. (2008) studied $\beta\text{-YF}_3$ containing GCs doped with 0.1 Pr^{3+} and 0.1–1.5 Yb^{3+} (mol %), obtaining the highest Yb^{3+} emission for 1.0 Yb^{3+} while for 1.5 Yb^{3+} a quenching effect was observed. The corresponding energy transfer efficiency (ETE) and quantum efficiency (QE) were 90 and 190%, respectively.

Lakshminarayana and Qiu (2009) studied $\text{Pr}-\text{Yb}$ down-conversion (DC) in oxyfluoride germanate glasses made by MQ and doped with 0.5 Pr^{3+} and 2–30 Yb^{3+} (mol %). The highest DC signal at 980 nm was measured for the 0.5 $\text{Pr}^{3+}-4\text{ Yb}^{3+}$ but the 0.5 $\text{Pr}^{3+}-2\text{ Yb}^{3+}$ produced almost as good results. Pr^{3+} lifetimes at 608 nm were 9.5 and 4.9 μs and the ETE 35 and 66% for 2 and 4 Yb^{3+} , respectively.

Chen et al. (2012) and Zhou et al. (2012) characterized oxyfluoride GCs containing CaF_2 nanocrystals. Chen et al. (2012) prepared materials with composition $45\text{SiO}_2-25\text{Al}_2\text{O}_3-10\text{Na}_2\text{O}-20\text{CaF}_2-0.1\text{PrF}_3-\gamma\text{YbF}_3$ ($\gamma = 0.1-1.0$) (mol%). The NIR emission suffered quenching for 1 Yb^{3+} and the most intense signal was obtained for 0.5 Yb^{3+} . The decay curve of $\text{Pr}^{3+}:^3\text{P}_0-^3\text{H}_6$ at 610 nm was measured and the lifetime for 0.5 Yb^{3+} was 78 μs , and the ETE and QE were 53 and 153%, respectively. Zhou et al. (2012) studied the compositions $60\text{SiO}_2-20\text{Al}_2\text{O}_3-20\text{CaF}_2:0.4\text{Pr}^{3+}/x\text{Yb}^{3+}$ ($x = 0, 1, 2$, and 4) (mol%). For Yb^{3+} concentrations higher than 1 mol% a quenching of Yb^{3+} emission at 980 nm was measured and for 1 Yb^{3+} the QE was 158%. The authors also tested a c-Si solar cell covered by the doped samples and measured a decrease compared with that covered by a host glass. Their conclusion was that a more efficient solar cell could be obtained by a proper ion doping concentration, an optimized sample thickness and the

introduction of an antireflection film on the interface air-glass interface as well as the introduction of a waveguide structure on the DC layer to reduce emission losses.

Katayama studied the DC process of $\text{Pr}-\text{Yb}$ in oxyfluoride glasses (Katayama and Tanabe, 2010a,b) and in SrF_2 GCs [Katayama and Tanabe, 2010a,b (p. 2); Katayama and Tanabe, 2013] with variable Yb^{3+} concentration: 0.1 $\text{Pr}^{3+}-x\text{Yb}^{3+}$ ($x = 0-2.9$) obtaining the best DC emission for the highest Yb^{3+} concentration. The ETE from the $\text{Pr}^{3+}:^3\text{P}_0$ to $\text{Yb}^{3+}:^2\text{F}_{5/2}$ increases from 42% for the glass to 75% for GCs, and the main ET process is a two-step process with Yb^{3+} and Pr^{3+} emission at 980 and 1300 nm, respectively. Pr^{3+} emission at 1300 nm was more quenched, due to phonons, than in SrF_2 -containing GCs.

Gao and Wondraczek (2013) obtained DC in boro-aluminosilicate glasses and LaBO_3 GCs doped with 1 $\text{Pr}^{3+}-x\text{Yb}^{3+}$ ($x = 0.1-5$). The best DC signal at 980 nm was obtained for 0.5 Yb^{3+} , the signal being quenched for higher concentrations, and the maximum value of the QE, obtained for 5 Yb^{3+} , was 183%.

Among all the studied materials there are a few examples regarding LaF_3 -containing GCs doped with RE for DC produced by MQ, from which we point out the work of Xu et al. (2011) dealing with oxyfluoride GCs doped with $\text{Pr}^{3+}-\text{Yb}^{3+}$ of composition $40\text{SiO}_2-30\text{Al}_2\text{O}_3-18\text{Na}_2\text{O}-12\text{LaF}_3$ (mol%). However, in the work of Xu, the most relevant conclusions are as follows: (1) Pr^{3+} ions are preferentially incorporated inside LaF_3 crystals, as shown by the increase of Pr^{3+} emission at 600 nm in GCs compared to glass and (2) on the contrary Yb^{3+} ions are not hosted inside LaF_3 ; therefore, the precipitation of LaF_3 crystals cannot improve the ET between Pr^{3+} and Yb^{3+} .

Another study of LaF_3 crystals for DC emission is due to Deng et al. (2011) who studied crystalline powders of LaF_3 doped with $\text{Pr}^{3+}-\text{Yb}^{3+}$ prepared by co-precipitation method using La^{3+} , Pr^{3+} , and Yb^{3+} as nitrates and NH_4HF_2 as fluorine source. For a fixed Pr^{3+} concentration of 0.5 mol% several Yb^{3+} concentrations were tested. With the increase of Yb^{3+} concentration the visible emission from Pr^{3+} weakens monotonically, while the NIR emission of Yb^{3+} intensifies. However, a decrease of the Yb^{3+} emission occurs for concentrations higher than 3%.

Xiang et al. (2014) studied $\text{Pr}^{3+}-\text{Yb}^{3+}$ doped $\beta\text{-NaLuF}_4$ hexagonal nanoplates with a size of $250\text{ nm} \times 110\text{ nm}$, synthesized by a solvo-thermal process. The ET from Pr^{3+} ions to Yb^{3+} ions occurs only by a two-step ET process when the Yb^{3+} concentration is very low; however, increasing the Yb^{3+} concentration, a cooperative ET process occurs for Yb^{3+} concentration as high as 20 mol%.

Furthermore, there are many publications about spectroscopic characterization of RE ions doped materials for DC, but very few papers exist where a correlation between optical properties and material processing is made.

In this paper, glasses and GCs of composition $55\text{SiO}_2-20\text{Al}_2\text{O}_3-15\text{Na}_2\text{O}-10\text{LaF}_3$ (mol%) doped with 0.1 Pr^{3+} , 0.5 Pr^{3+} , 0.1–0.5 $\text{Pr}^{3+}-\text{Yb}^{3+}$, and 0.5–1 $\text{Pr}^{3+}-\text{Yb}^{3+}$ have been prepared. The structural properties of the materials have been studied by differential thermal analysis (DTA), X-ray diffraction (XRD), TEM and the optical properties by UV-VIS Absorption, photoluminescence (PL), and lifetime decay. The differences of the DC properties of the samples are described and the relationship of material processing with the optical properties is given.

MATERIALS AND METHODS

Glass Melting and Crystallization

Oxyfluoride glasses with composition $55\text{SiO}_2\text{--}20\text{Al}_2\text{O}_3\text{--}15\text{Na}_2\text{O--}10\text{LaF}_3$ (mol%) ($55\text{Si--}10\text{La}$) have been prepared by melting reagent grade SiO_2 sand (Saint-Gobain, Aviles, Spain, 99.6%), Al_2O_3 (Panreac), Na_2CO_3 (Sigma-Aldrich, >99.5%), LaF_3 (Alfa Aesar, 99.99%). Pr^{3+} and Yb^{3+} were added as fluorides (Alfa Aesar, 99.99%) in 0.1–0.5 and 0.5–1 concentrations (mol%). Samples doped with only Pr^{3+} were also prepared for comparison of the optical properties. A more complete description of glass preparation was given in (de Pablos-Martín et al., 2011).

Al_2O_3 was previously annealed at 800°C for 12 h. Batch materials were weighed to obtain 100 g of glass, mixed for 1 h to ensure a good homogenization, put in a covered Pt crucible and annealed for 2 h at 1200°C . The Pt crucible was then placed in an elevator furnace for 1.5 h at 1650°C , the molten glasses were quenched in air onto a brass mold, fused again for 30 min to improve homogeneity and quenched onto a cold (-10°C) brass mold. The glasses were annealed at 600°C for 30 min for stress relaxation.

Glass-ceramics were obtained by heat treatment at 620°C for 1, 3, 5, 20, 40, and 80 h and at 660 and 680°C for 20 h. In all the cases, a heating rate of $10^\circ\text{C}/\text{min}$ was used followed by quenching in air.

Heat treatments were performed on bulk specimens (size 1–1.25 mm).

DTA and Crystallization Mechanism

Non-isothermal crystallization kinetics was studied by DTA/TG (SDT Q600—TA Instruments). Measurements have been performed on 20–30 mg of glass with particles size between 1 and 1.25 mm to reproduce bulk conditions. DTA scans were carried out with heating rates in the range $10\text{--}60^\circ\text{C}/\text{min}$.

The glass transition temperature T_g , crystallization activation energy E_a , and Avrami parameters (n , m) were calculated from DTA measurements.

The Avrami parameter n allows assessing the crystallization process and was obtained employing the Ozawa equation (Ozawa, 1970):

$$\left(\frac{d[\ln[-\ln(1-x)]]}{d(\ln q)} \right)_T = -n, \quad (1)$$

where x is the partial area of the crystallization peak calculated for a fixed temperature T and q is the heating rate. By using the Kissinger equation (Kissinger, 1956) the crystallization activation energy E_a was obtained by

$$\ln \left(\frac{q}{T_p^2} \right) = -\frac{E_a}{RT_p} + C, \quad (2)$$

where T_p , R , and C are the crystallization peak temperature, the gas constant and a constant, respectively. Finally, the m parameter, representing the growth dimensionality, was obtained by the Matusita equation (Matusita and Sakka, 1980):

$$\ln \left(\frac{q^n}{T_p^2} \right) = -\frac{mE_a}{RT_p} + C'. \quad (3)$$

X-Ray Diffraction

The heat-treated samples were milled and sieved ($< 63 \mu\text{m}$) and characterized by XRD with a Bruker D8 Advance diffractometer. Diffractograms were acquired in the range $10 \leq 2\theta \leq 70^\circ$ with a step size of 0.02° and 1 s acquisition for each step. Crystals size, D , was estimated using the Scherrer equation (Eq. 4), where λ is the wavelength (1.54056 \AA — $\text{CuK}\alpha_1$), B_m the full width at half maximum of the LaF_3 peak (111) and θ its diffraction angle. The factor 0.94 corresponds to spherical crystals. Pseudo-Voigt function has been used to fit diffraction peak parameters. The instrumental broadening B_i has been also taken into account using NaF powder properly milled and sieved ($< 63 \mu\text{m}$):

$$D = \frac{0.94\lambda}{\cos\theta \sqrt{B_m^2 - B_i^2}}. \quad (4)$$

Crystalline growth can be described by the following equation:

$$r = Ut^p, \quad (5)$$

where r is the crystal radius, U the crystal growth rate, t the time, and p a growth exponent. The logarithmic form of Eq. 5 is commonly used:

$$\log(r) = \log(U) + p \log(t). \quad (6)$$

High-Resolution Transmission Microscopy (HRTEM)

TEM samples of glasses and GCs were prepared by cutting slices, plane parallel grinding, dimpling to a residual thickness of $10\text{--}15 \mu\text{m}$, and ion-beam thinning using Ar^+ ions. The angle of incidence was set to 8° , the beam energy to 5 kV, current to 5 mA, and milling time to $10\text{--}14 \text{ h}$. HRTEM including scanning transmission microscopy-high angle annular dark field and energy dispersive X-ray spectroscopy (EDXS) were performed with a JEOL 2100 field emission gun transmission electron microscope operating at 200 kV and providing a point resolution of 0.19 nm. The microscope was equipped with an energy dispersive X-ray spectrometer (EDXS—INCA x-sight, Oxford Instruments). EDXS analysis was performed in STEM mode, with a probe size of ca. 1 nm. In order to determine the particle distribution, we first assumed the particles to be spheres. No high contrast was obtained when working in the Scherzer focus, the shape of the particles was not well defined and difficult to measure. Thus, slightly under-focused TEM images were used to solve this problem. HAADF-STEM images were obtained where the particle shape was more distinguishable, and it is possible to measure the average diameter of the particles. By this method, only well-defined particles were measured which still resulted in a statistically well-representative data collection.

Optical Properties

Bulk specimens were cut from the annealed glass and heat treated to obtain glass-ceramic materials. 0.1 Pr and 0.1–0.5 Pr–Yb glasses were treated at 620°C for 20 h and 40 h, and at 660°C for 20 h. 0.5 Pr and 0.5–1 Pr–Yb glasses were treated at 620°C for 40 h and 660°C for 20 h. All the samples have been

polished and optically characterized by UV–VIS absorption and PL spectroscopy.

UV–VIS spectra (Lambda 950—Perkin Elmer) were acquired between 300–2200 nm.

A photomultiplier tube (PMT) R6872 for UV–VIS and a Peltier cooled PbS for NIR detection were used as detectors.

A lock-in (5210-Princeton Research Instrument) configuration with an InGaN led at 435 nm (Roithner) as source for Pr^{3+} excitation and a fiber laser at 976 nm to excite Yb^{3+} ions was used to obtain PL spectra. A $2 \times 2 \text{ mm}^2$ spot was produced with a lens focusing system and the samples were excited on the side edge to reduce re-absorption processes. Emission spectra were collected by an iHR-320 (Jobin-Yvon) spectrometer equipped with two gratings: 1200 g/mm blazed at 500 nm, and 600 g/mm blazed at 1000 nm. The detection system was calibrated using an incandescence lamp with known emission spectrum. A S-20 PMT and an InGaAs PD were used for UV–VIS and IR detection, respectively. Finally, all PL spectra were properly corrected for the instrument response.

Lifetime decay curves, upon excitation at 435 nm, were acquired with a fast oscilloscope (Tektronix), and the source was modulated electronically by a controller (ITC4000-Thorlabs).

For no single exponential decay, lifetimes were calculated using the following formula:

$$\tau_{\text{avg}} = \frac{\int_0^\infty t I(t) dt}{\int_0^\infty I(t) dt} \quad (7)$$

The ETE and the QE were calculated using the following equations:

$$\text{ETE} = 1 - \frac{\tau_{\text{Pr/Yb}}}{\tau_{\text{Pr}}} \quad (8)$$

$$\text{QE} = \eta_{\text{Pr}}(1 - \text{ETE}) + 2\eta_{\text{Yb}}\text{ETE} \quad (9)$$

where τ_{Pr} and $\tau_{\text{Pr/Yb}}$ are the Pr^{3+} lifetime, corresponding to the same excited state level, in doped and co-doped samples, while η_{Pr} and η_{Yb} are the Pr^{3+} and Yb^{3+} QEs.

RESULTS AND DISCUSSION

DTA and Crystallization Mechanism

Differential thermal analysis curves and the variation of glass transition temperature (T_g), crystallization starting temperature (T_x), and crystallization peak temperature (T_p), with the heating rate are given in **Figures 1A,B** for the samples doped with 0.1–0.5 Pr–Yb.

It was not possible to estimate T_g , T_x , T_p from DTA curves performed at heating rate of $10^\circ\text{C}/\text{min}$ due to very small endothermic peak (T_g) and exothermic peak (T_x , T_p) corresponding to LaF_3 crystallization. For 0.5–1 Pr–Yb doped glass the first values were obtained from a heating rate of $30^\circ\text{C}/\text{min}$.

The stability parameter, defined as $\Delta T = T_p - T_g$, is 114°C for both co-doped glasses for a heating rate of $10^\circ\text{C}/\text{min}$ (calculated by extrapolation from the fits). The variation of T_x and T_p with the heating rate is faster than that of T_g , as confirmed by the slope parameter α in the equation $T = \alpha q$, summarized in **Table 1**. The calculated T_g for a heating rate of $10^\circ\text{C}/\text{min}$ are 570°C for 0.1–0.5 Pr–Yb and 585°C for 0.5–1 Pr–Yb. Higher T_x and T_p

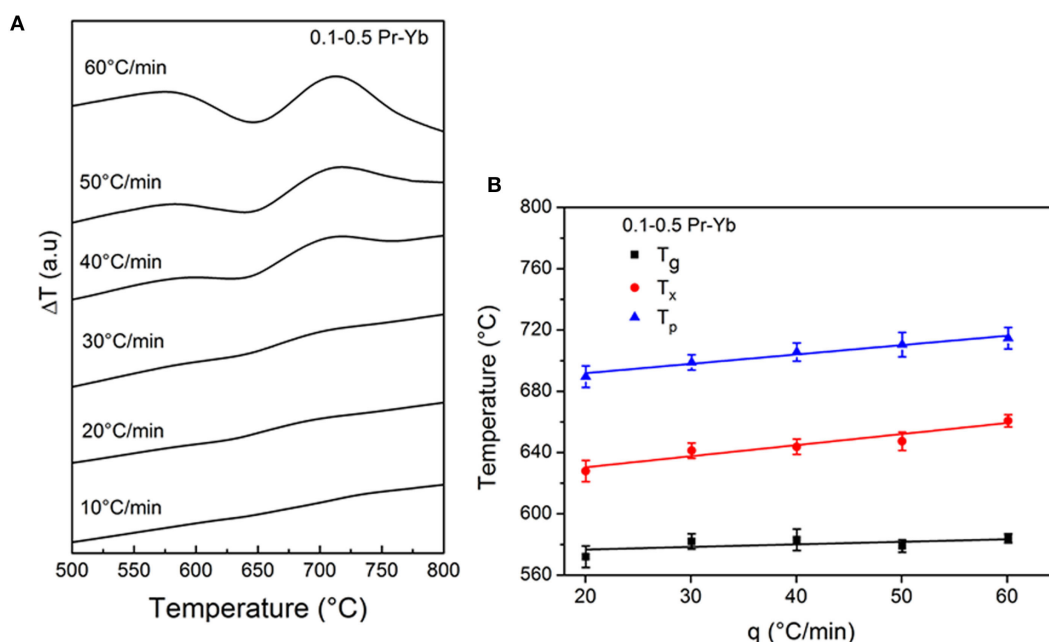


FIGURE 1 | (A) Differential thermal analysis curves for 0.1–0.5 Pr–Yb glass performed at heating rates 10–60 $^\circ\text{C}/\text{min}$. **(B)** Variation of the glass transition temperature (square), crystallization starting temperature (circle), and LaF_3 crystallization peak temperature (triangle) with the heating rate.

values indicate a delay of the crystallization onset for materials with higher concentration of dopants.

By using Eq. 2, crystallization activation energies were calculated and their values are (329 ± 16) kJ/mol and (342 ± 18) kJ/mol for 0.1–0.5 Pr–Yb and 0.5–1 Pr–Yb, respectively. These results are similar to those obtained for the un-doped (de Pablos-Martín et al., 2011) and Tm^{3+} doped glass (de Pablos-Martín et al., 2013), Avrami n parameter was calculated, using Eq. 1, from the slope of each line; a n mean value was obtained from the slope of the five lines represented in **Figures 2A,B** for 0.1–0.5 Pr–Yb and 0.5–1 Pr–Yb, respectively. By substituting the calculated crystallization activation energy into the Matusita equation (Eq. 3) and plotting the left side of Eq. 3 as a function of E_a/RT_p , the m parameter has been obtained from the slope of the lines represented in **Figures 2C,D**.

For 0.1–0.5 Pr–Yb, $n = 1.23 \pm 0.08$ and $m = 1.2 \pm 0.1$, while for 0.5–1 Pr–Yb $n = 0.86 \pm 0.08$ and $m = 0.84 \pm 0.08$. The

TABLE 1 | Coefficients α (min) from the lines $T = \alpha, q$ for the glass transition temperature (T_g), crystallization starting temperature (T_s), and crystallization peak temperature (T_p).

Glass	α_g	α_s	α_p
55Si–10La 0.1–0.5 Pr–Yb	0.17 ± 0.02	0.7 ± 0.1	0.61 ± 0.06
55Si–10La 0.5–1 Pr–Yb	0.46 ± 0.07	0.7 ± 0.1	0.54 ± 0.06

two values of (n, m) for each composition are the same within uncertainties. The higher value obtained for the 0.1–0.5 Pr–Yb glass could be interpreted considering that the crystallization process is faster than for the 0.5–1 Pr–Yb glass. These parameters can be approximated to the nearest integer or semi-odd integer resulting in $n = 1$ and $m = 1$ for both materials. This means that the use of Kissinger equation is valid for the calculation of the crystallization activation energy and corresponds to a volumetric crystallization with crystal growth controlled by diffusion (Donald, 2004). The same (n, m) parameters were also obtained for the un-doped glass and for Tm^{3+} doped glass (de Pablos-Martín et al., 2013), confirming that dopants do not affect the crystallization mechanism but may affect the crystallization kinetics and influence LaF_3 crystals size.

X-Ray Diffraction

X-ray diffraction measurements for GCs 0.1–0.5 Pr–Yb treated at 620°C for 1, 3, 5, 20, 40, and 80 h are given in **Figure 3A**, while diffractograms for heat treatment at 620, 660, and 680°C for 20 h are compared in **Figure 3B**. Very similar diffractograms have been obtained for GCs 0.5–1 Pr–Yb and are not represented.

In all the cases, LaF_3 was the only appearing crystalline phase confirmed by the reference (JCPDS 32-0483). All the distinguishable peaks of the diffraction pattern were labeled by Miller indexes. Crystals size was estimated using the generalized

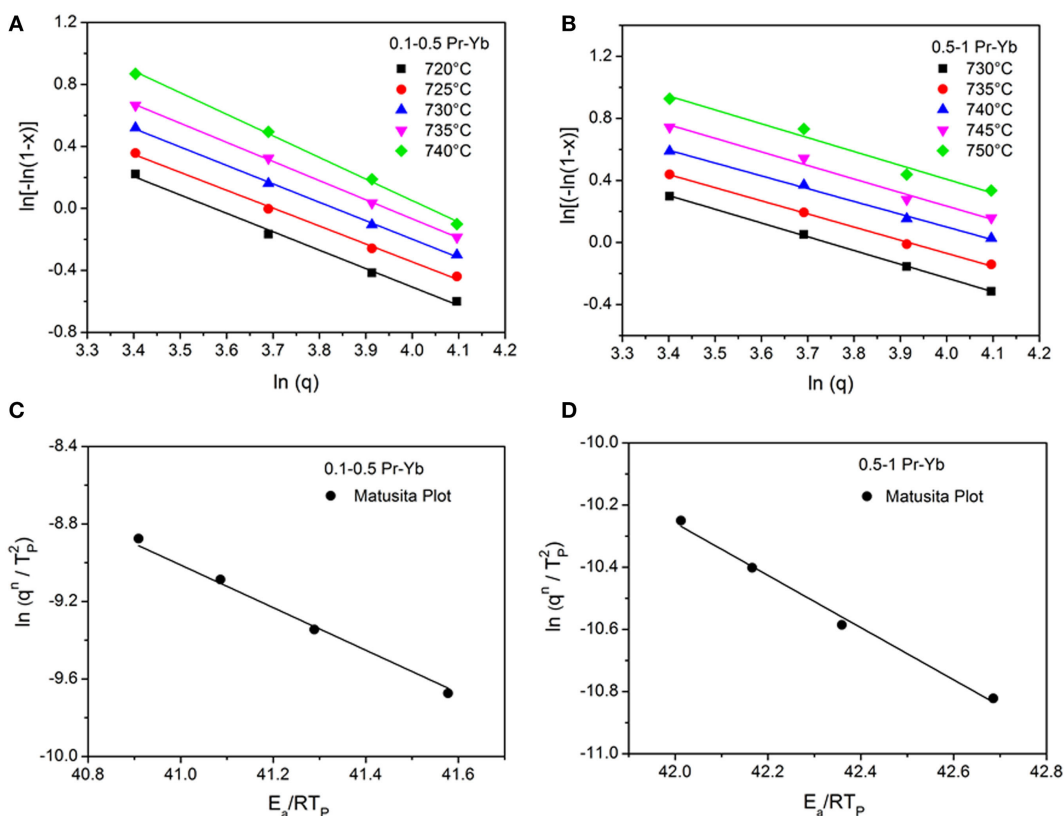


FIGURE 2 | Ozawa plot for **(A)** 0.1–0.5 Pr–Yb and **(B)** 0.5–1 Pr–Yb doped glass. **(C)** Matusita plot for 0.1–0.5 Pr–Yb and **(D)** 0.5–1 Pr–Yb doped glass.

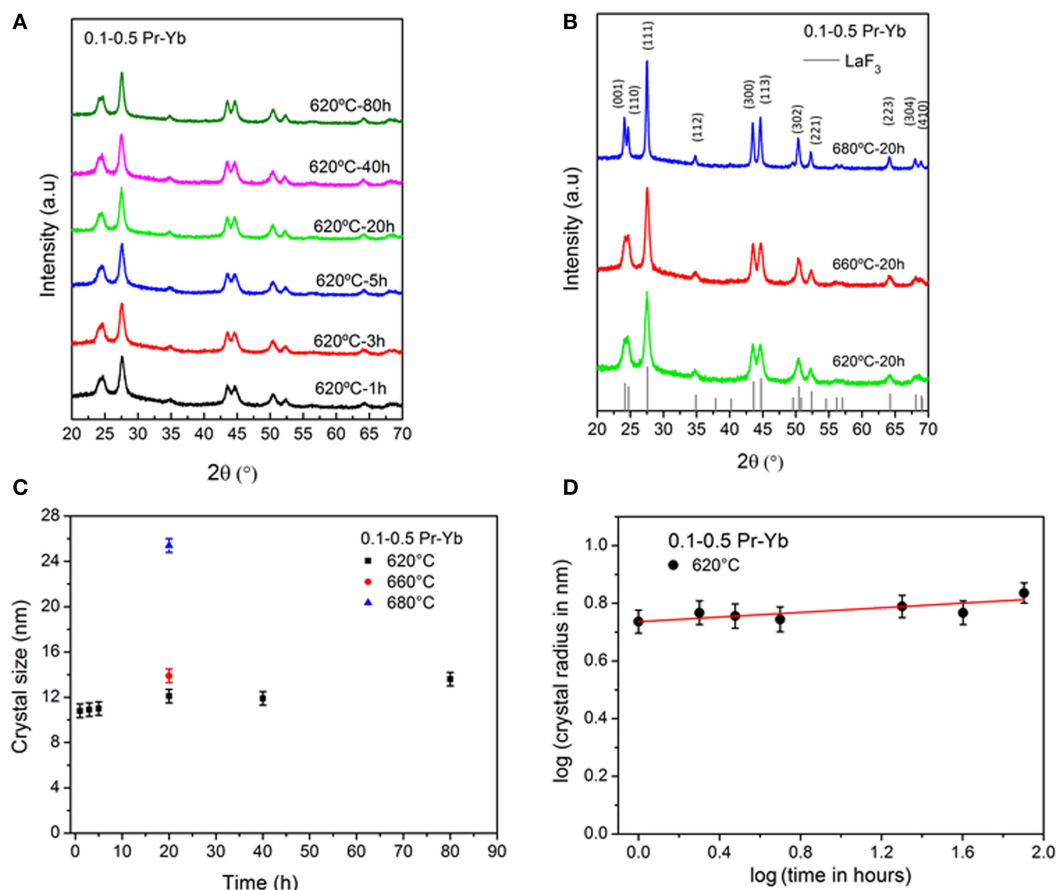


FIGURE 3 | Diffraction patterns for glass-ceramics (GCs) 0.1–0.5 Pr–Yb treated at **(A)** 620°C for 1, 3, 5, 20, 40, and 80 h and at **(B)** 620, 660, and 680°C for 20 h. All diffraction patterns have been labeled by their Miller indices and the LaF_3 reference peaks are shown in the bottom. **(C)** Crystal size variation with the treatment time or temperature for GC 0.1–0.5 Pr–Yb treated at 620°C (square) during 1, 3, 5, 20, 40, 80 h, 660°C (circle) and 680°C (triangle) for 20 h. **(D)** Crystal growth p exponent for GCs treated at 620°C during 1, 3, 5, 20, 40, and 80 h.

Scherrer equation (Eq. 4), to take into account the instrumental broadening, applied to LaF_3 (111) peak ($2\theta \approx 27.5^\circ$).

Crystal growth exponent p has been estimated by Eq. 6. **Figure 3C** shows crystal size variation with treatment time, and **Figure 3D** shows the crystal growth exponent p for GCs 0.1–0.5 Pr–Yb.

For GCs, 0.1–0.5 Pr–Yb crystals size at 620°C, shown in **Figure 3C**, is almost constant ≈ 12 nm for different treatment times, while treating the samples at different temperatures for the same time of 20 h, crystals size shows important changes. The increase of crystals size at higher temperature is indicated by the more intense diffraction peaks and by the narrowing of the peaks. At 660°C, crystals size is ≈ 14 nm and at 680°C ≈ 26 nm. As a consequence, for the heat treatment at 680°C, 20 h, the material partially lost its transparency due to quite bigger crystals. In fact, even though crystals are still quite small, the phase separation droplets containing several crystals inside have quite bigger sizes (as it will be shown in next section—Section “TEM”), ranging from an average value of 37 nm at 620°C up to ≈ 100 nm at 680°C.

The GC starts to lose transparency at temperatures higher than 660°C. Moreover, temperatures higher than the glass softening temperature, $\approx 670^\circ\text{C}$, are not useful for practical purpose.

Glass-ceramics 0.5–1 Pr–Yb treated at 620°C, 1 h are almost amorphous and crystal size stabilizes to a constant value, around 11 nm, for treatments longer than 3 h. The onset of crystallization is delayed compared to GCs doped with 0.1–0.5 Pr–Yb, and this is associated with the higher activation energy (342 kJ/mol vs 329 kJ/mol). This is related to the nucleating effect of fluorides which promotes the production of smaller nuclei compared to what happens with lower fluoride content, according to which smaller nuclei should be favored. In fact, it is known that fluorine content in oxyfluoride glasses acts as a nucleating agent and suppresses crystal growth by increasing nuclei quantity (Chen et al., 2007; Bhattacharyya et al., 2009).

Pr^{3+} singly doped samples showed very similar behavior and only LaF_3 crystals precipitate in the glass matrix, and the crystals size is similar to the one obtained for the co-doped samples.

The calculation of p exponents was carried out using Eq. 6, starting from plots of crystals size for GCs treated at 620°C for 20 h. Data are plotted in **Figure 3D** for GCs 0.1–0.5 Pr–Yb. The crystal growth exponent at 620°C is $p = 0.040 \pm 0.005$, while for GCs 0.5–1 Pr–Yb the p exponent is $p = 0.03 \pm 0.01$. The very small dependence of crystal growth on the time of heat treatment together with small values for crystal growth exponent p , indicates the presence of an inhibition phenomenon explained in detail in Bhattacharyya et al. (2009) and de Pablos-Martín et al. (2011, 2012). These previous studies showed that La and Si-enriched phase separation droplets are precipitated already during the preparation of the initial glass. Upon conversion of the glass into a nano-GCs by appropriate annealing, LaF₃ nano-crystals are formed within these droplets. Similar results have been obtained in this work as shown in Section “TEM.”

TEM

Figure 4A shows a TEM image of the 0.1–0.5 Pr–Yb glass. The starting glass presents phase separation with a narrow size distribution of the droplets between 15–40 nm and an average

droplets size of 28 nm (**Figure 4B**). The majority of the droplets do not present any structure inside. However, in very few droplets, small crystalline domains of 5–7 nm in size have been also detected, but this incipient crystallinity in the base glass is not detectable by XRD. The chemical composition along 80 nm scanning line (**Figure 4C**) was measured by EDXS and represented in **Figure 4D**. The droplets are enriched in F, La, Pr and Yb, a clear evidence of RE incorporation inside the droplets. Furthermore, excess of Si and Al are relocated toward the periphery of the droplets, and the formation of a barrier enriched in glass formers prevent further crystal growth, during the crystallization process, due to the increase of viscosity.

Figure 5A shows an image of the GC 0.1–0.5 620°C, 20 h and bigger droplets, with average size ≈ 33 nm, were detected as compared to the untreated glass (**Figure 5B**). A feature of this glass system is the crystals formation inside the initial phase separation droplets, already enriched in crystals components in the as made glass. The size of the crystals inside each droplet is clearly observed in **Figure 5C**, and their size distribution is represented in **Figure 5D**. An average crystals size of 10 nm was obtained for this heat treatment, in agreement with the value obtained by XRD

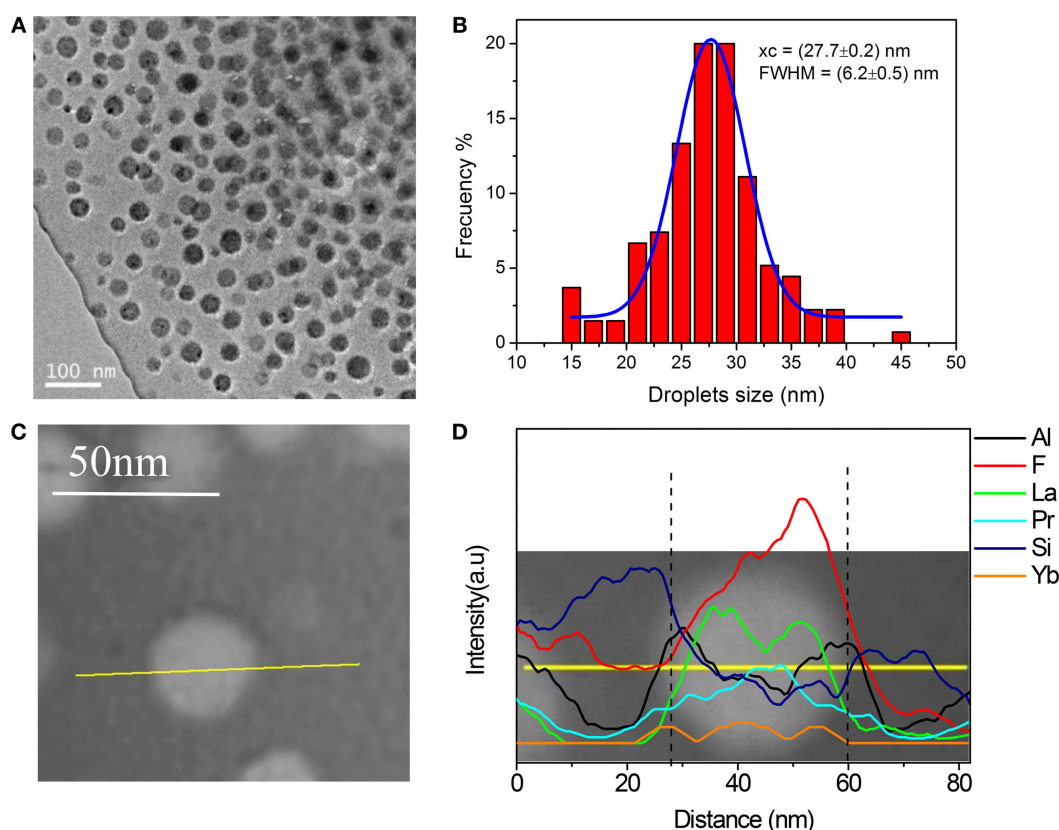


FIGURE 4 | (A) TEM image of the 0.1–0.5 Pr–Yb glass showing phase separation droplets. **(B)** Droplet size distribution. **(C)** STEM image of the glass sample where the yellow line is the scanning line along which EDXS analysis was performed **(D)**.

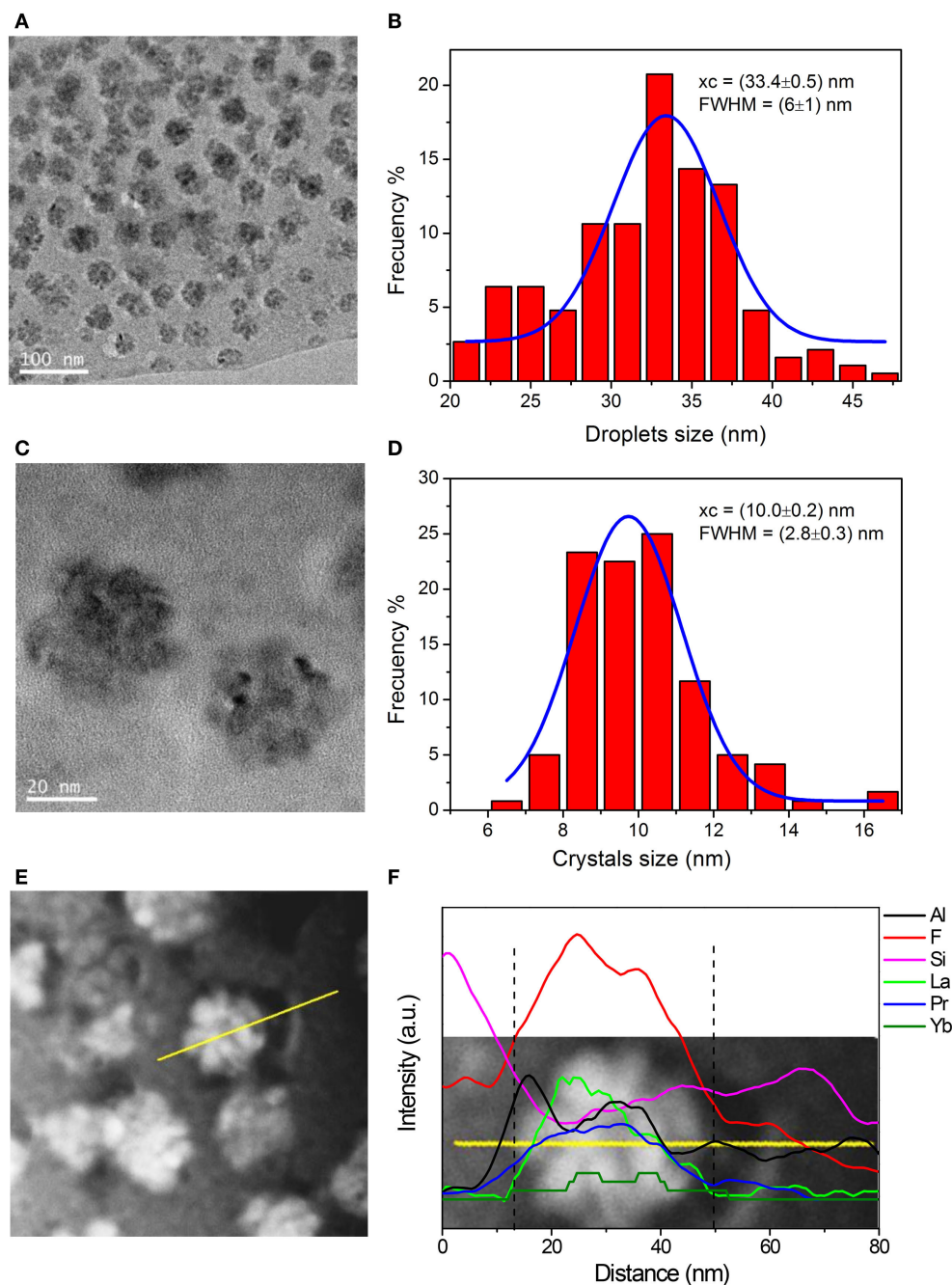


FIGURE 5 | (A) TEM image of the glass-ceramic 0.1–0.5 Pr–Yb 620°C, 20 h and corresponding droplet size distribution **(B)**. **(C)** TEM image of two droplets and crystals size distribution inside the droplet **(D)**. **(E)** STEM image of the sample and EDXS analysis along the yellow line containing one droplet **(F)**.

measurements. **Figures 5E,F** show EDXS analysis of one single droplet. Al and Si are mostly confined in the interphase and tend to be smaller in correspondence of the maximum F, La, Pr, and Yb concentration, i.e., inside the droplet. Clear presence of RE ions inside the phase separation droplets and crystals is observed for glass and GCs. The detection of Yb is quite difficult, but its presence in the crystals is observed.

Optical Properties

UV–VIS optical density for Pr^{3+} - and Pr^{3+} – Yb^{3+} -doped glasses and GCs are represented in **Figure 6**.

Glasses have lower absorbance compared to GCs that suffer Rayleigh scattering caused by density fluctuations due to the presence of nano-crystals inside the glass matrix. The strong UV absorption (Urbach tail) below 350 nm is due to electronic

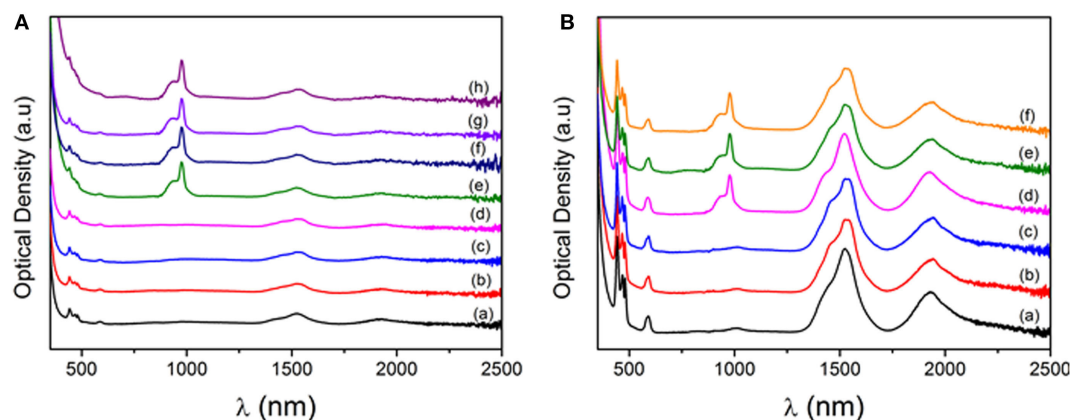


FIGURE 6 | (A) Optical density for Glass 0.1 Pr (a), glass-ceramic (GC) 0.1 Pr 620°C, 20 h (b), GC 0.1 Pr 620°C, 40 h (c), GC 0.1 Pr 660°C, 20 h (d), Glass 0.1–0.5 Pr–Yb (e), GC 0.1–0.5 Pr–Yb 620°C, 20 h (f), GC 0.1–0.5 Pr–Yb 620°C, 40 h, and GC 0.1–0.5 Pr–Yb 660°C, 20 h (h). **(B)** Optical density for Glass 0.5 Pr (a), GC 0.5 Pr 620°C, 40 h (b), 0.5 Pr GC 660°C, 20 h (c), glass 0.5–1 Pr–Yb (d), GC 0.5–1 Pr–Yb 620°C, 40 h (e), and GC 0.5–1 Pr–Yb 660°C, 20 h (f).

transitions between the ligand (oxygen mainly) and the glass network former ion (silicon). In all materials the transitions between the 4f and 4f states corresponding to Pr^{3+} and Yb^{3+} ions are clearly visible. From the left, the following Pr^{3+} transitions can be assigned: $^3\text{H}_0\text{--}^3\text{P}_{2,1,0}$ at 442, 466, and 480 nm, $^3\text{H}_4\text{--}^1\text{D}_2$ at 590 nm, $^3\text{H}_4\text{--}^3\text{F}_4$ at 1460 nm, $^3\text{H}_4\text{--}^3\text{F}_3$ at 1590, and $^3\text{H}_4\text{--}^3\text{F}_2$ at 1930 nm. The Yb^{3+} transition $^2\text{F}_{7/2}\text{--}^2\text{F}_{5/2}$ is also observed at 980 nm. For 0.5 Pr and 0.5–1 Pr–Yb GCs (**Figure 6B**), a small underlying structure is observed for Pr^{3+} absorption to the $^3\text{F}_3$ level, reflecting the different local field felt by Pr^{3+} ions compared to glasses, a proof of Pr^{3+} incorporation inside LaF_3 crystals that causes a narrowing of the band and the Stark components can be appreciated. However, clearer evidence of RE^{3+} ions inside LaF_3 crystals appears in the PL spectra.

PL spectra for Pr^{3+} doped and $\text{Pr}^{3+}\text{--Yb}^{3+}$ co-doped glasses and GCs are given in **Figure 7**. Excitation has been provided by an InGaN LED centered at 435 nm and Pr^{3+} ions have been excited to the $^3\text{P}_2$ level. By non-radiative decay, the $^3\text{P}_0$ level is populated and Pr^{3+} radiative emissions from this level to the three excited states $^3\text{H}_{4,5,6}$ and $^3\text{F}_{2,3,4}$ are clearly visible in the range 450–750 nm.

For samples singly doped with Pr^{3+} , the emission at 1.05 μm corresponding to the transition from $^1\text{D}_2\text{--}^3\text{F}_{3,4}$ levels is observed and the emission at 600 nm corresponding to the $^1\text{D}_2\text{--}^3\text{H}_4$ transition, in both doped and co-doped samples, overlaps with the $^3\text{P}_0\text{--}^3\text{H}_6$ emission band. The population of $^1\text{D}_2$ level is due to multi-phonon relaxation from the $^3\text{P}_0$ level, and this contribution is stronger in glass than in GCs, meaning the incorporation of Pr^{3+} ions inside LaF_3 crystals, where phonons are much smaller.

However, in co-doped samples, the $^3\text{P}_0$ level is also quenched by the presence of Yb^{3+} ions, producing a DC signal in the range 950–1150 nm, as a consequence of an ET process. The Pr^{3+} transition $^1\text{G}_4\text{--}^3\text{H}_5$ at 1.3 μm is not observed in any samples, glass or GCs. Moreover, the $^3\text{P}_0\text{--}^1\text{G}_4$ transition at 950 is not observed either.

For all samples, a more evident distinction in the Pr^{3+} emission between glass and GCs is observed. Again, co-doped glasses present the lowest Yb^{3+} DC signal at 976 nm while the Pr^{3+} transition $^3\text{P}_0\text{--}^3\text{H}_6$ gets smaller passing from glass to GCs. Glass does not show sharp Stark splitting while a clear splitting of the $^3\text{H}_{5,6}$ and $^3\text{F}_4$ is visible in the GCs, a convincing proof that Pr^{3+} ions are incorporated into LaF_3 crystals. However, Yb^{3+} ions should be incorporated in LaF_3 crystals as well. In fact, a difference in the local environment between Pr^{3+} and Yb^{3+} does not seem favorable for ET processes. Additionally, DC emission gets stronger in GCs.

Xu et al. (2011) studied a 0.5–0.5 Pr–Yb doped oxyfluoride GCs containing LaF_3 crystals and found that the visible emission increases more than NIR emission passing from glass to GCs. Moreover, NIR emission of Yb^{3+} ions did not increase monotonously with the heat treatment temperature or time. These results are in contradiction with ours. They concluded that Yb^{3+} ions are not favored to be incorporated inside LaF_3 crystals, while we observed incorporation. TEM images (**Figure 5**), and particularly the elemental analysis with 1 nm resolution, showed an enrichment of Yb^{3+} inside the droplets, while no significant Yb^{3+} concentration was detected in the glass matrix.

While for 0.1–0.5 Pr–Yb doped samples the effect of the increase of temperature seems comparable to the increase of heat treatment time, for 0.5–1 Pr–Yb doped materials the increase of temperature produces the most evident improvement of Yb^{3+} DC emission at 976 nm. This may be explained considering that a doping with 0.1–0.5 Pr–Yb produces a lower nuclei density, but bigger crystals are still possible by rising the annealing temperature (**Figure 3C**). In particular, bigger crystals can host more RE^{3+} ions and a heat treatment at 620°C, 40 h thus produces an improvement of DC signal.

For 0.5–1 Pr–Yb, due to the quite higher fluoride content into the initial melt, the as made glass has a higher nuclei density thanks to the nucleating action of fluorine. The smaller initial

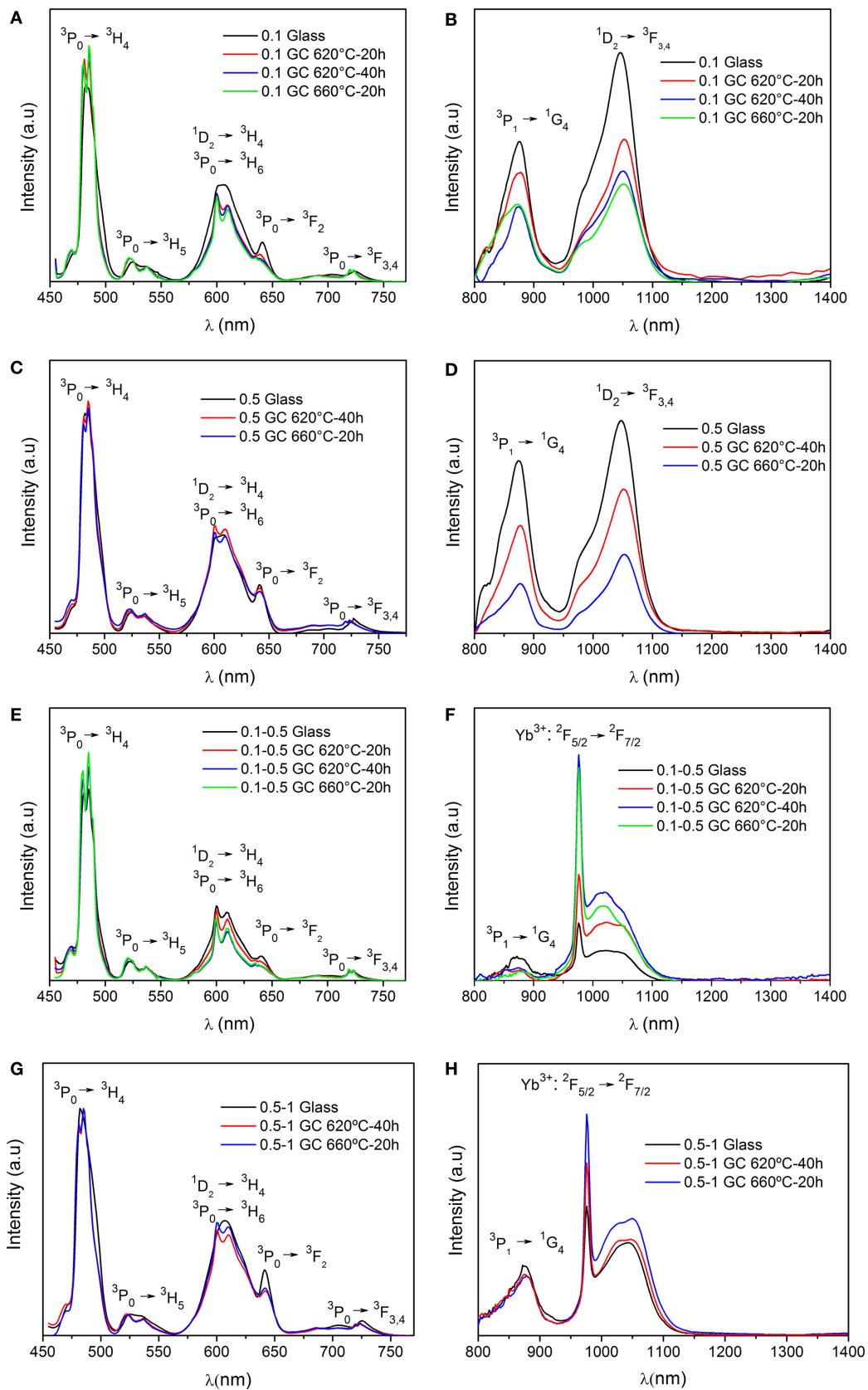


FIGURE 7 | PL emission spectra for (A,B) 0.1 Pr, (C,D) 0.5 Pr, (E,F) 0.1–0.5 Pr–Yb, (G,H) 0.5–1 Pr–Yb doped samples. Excitation is at 435 nm.

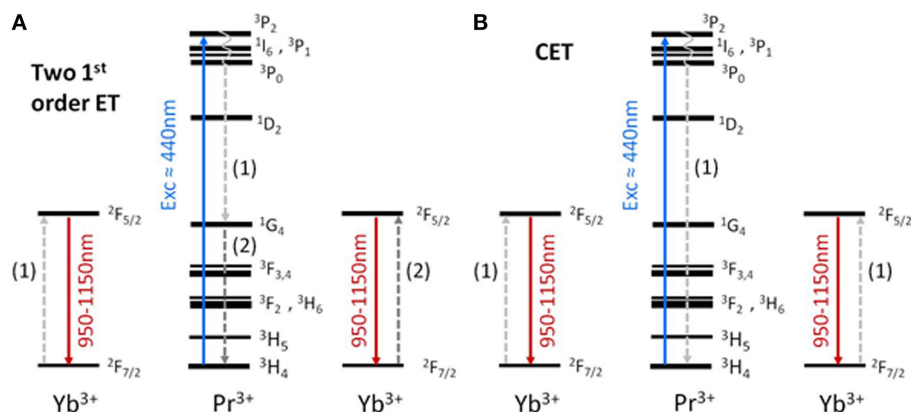


FIGURE 8 | (A) Two first order energy transfer (ET) processes, the first being a cross relaxation. **(B)** Cooperative energy transfer between one Pr^{3+} and two Yb^{3+} ions.

nuclei make it more difficult to produce bigger crystals, due to the reduction of the effective cross-section to capture other crystal forming ions and to the presence of a diffusion barrier of higher viscosity around LaF_3 crystals that is formed earlier and which is expected to be thicker. In addition, in a glass doped with more RE^{3+} ions, viscosity increases compared to un-doped glass (or to a less doped glass), at the temperatures of nano-glass ceramic formation ($T_g + 20\text{--}80^\circ\text{C}$) (de Pablos-Martín et al., 2013). As a consequence, RE^{3+} ions diffusion inside crystals can require longer times, and therefore, the best improvement is obtained by rising the temperature until a decrease of viscosity starts to allow more RE^{3+} ions diffusion inside the LaF_3 crystals but avoiding the growth of nanocrystals above 20 nm.

As suggested by van Wijngaarden et al. (2010), the cross relaxation scheme, **Figure 8A**, is the most common scheme for Pr–Yb DC. The two step ET process firstly allows Yb^{3+} ions excitation to the $^2\text{F}_{5/2}$, and then Pr^{3+} ions from the $^1\text{G}_4$ level transfer energy to Yb^{3+} ions.

Xiang et al. (2014) found that, increasing Yb^{3+} concentration to 10 mol%, cooperative energy transfer (CET) process, **Figure 8B**, becomes increasingly important and for very high concentration as 20 mol% CET process is the main ET process.

In this study, the absence of the emission at $1.3\ \mu\text{m}$ ($^1\text{G}_4\text{--}^3\text{H}_5$) from Pr^{3+} ions indicates that $^1\text{G}_4$ level is not populated or that this level is highly quenched in glass as well as in GCs. Considering that even for glass samples doped with only 0.1 mol% of Pr^{3+} this emission is not observed, we are tempted to affirm that this transition hardly occurs in our samples. Furthermore, the $^3\text{P}_0\text{--}^1\text{G}_4$ transition at 950 nm is not observed in any sample and this is in agreement with the absence of population of the $^1\text{G}_4$ level and finally, it could be a proof of the fact that the CET from the Pr^{3+} $^3\text{P}_0$ can be relevant for co-doped samples. Hence, it is possible to conclude that the ET between Pr^{3+} to Yb^{3+} ($^2\text{F}_{7/2}\text{--}^2\text{F}_{5/2}$) is improved in GCs respect to glass and CET could be quite relevant.

As suggested by Gao and Wondraczek (2013), the ET from the $^1\text{G}_4$ level of Pr^{3+} to the $^2\text{F}_{5/2}$ level of Yb^{3+} is rather unlikely because the $^1\text{G}_4$ level is almost $200\ \text{cm}^{-1}$ lower than the Yb^{3+} $^2\text{F}_{5/2}$ level and an opposite back ET, from the Yb^{3+} $^2\text{F}_{5/2}$ to the Pr^{3+} $^1\text{G}_4$

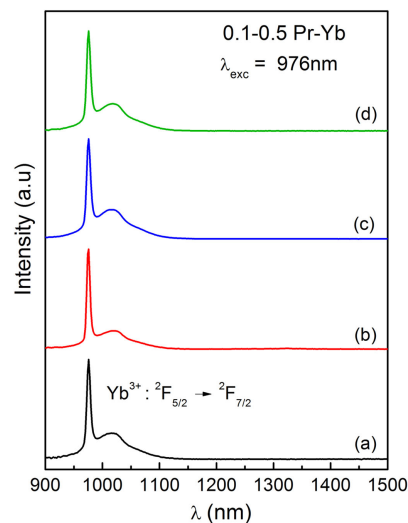


FIGURE 9 | PL spectra upon Yb^{3+} direct excitation at 976 nm for the glass (a), glass-ceramics (GC) 620°C, 20 h (b), GC 620°C, 40 h (c), and GC 660°C, 20 h (d) for the 0.1–0.5 Pr–Yb composition.

level, should be favored. Considering that the ET from $^1\text{G}_4$ of Pr^{3+} to the $^2\text{F}_{5/2}$ of Yb^{3+} is not observed in our measurements, the back ET from Yb^{3+} to Pr^{3+} ions was also studied by direct excitation of Yb^{3+} ions with a laser fiber at 976 nm. The corresponding PL measurements for GCs 0.1–0.5 Pr–Yb GC are given in **Figure 9**. The same results have been obtained for the GCs 0.5–1 Pr–Yb.

As clearly observed, no Pr^{3+} emission is present for direct excitation of Yb^{3+} at 976 nm, meaning the absence of a back ET mechanism. Therefore, the first order ET from $^1\text{G}_4$ of Pr^{3+} to $^2\text{F}_{5/2}$ of Yb^{3+} is quite unlikely.

Figure 10 shows Pr^{3+} lifetime at 610 nm ($^3\text{P}_0\text{--}^3\text{H}_6$) for 0.1–0.5 Pr–Yb and 0.5–1 Pr–Yb co-doped samples, respectively. Lifetimes have been calculated by best fit and in all cases a bi-exponential fit has been necessary. Fast decays correspond to ET between neighbor ions while longer lifetimes give indication

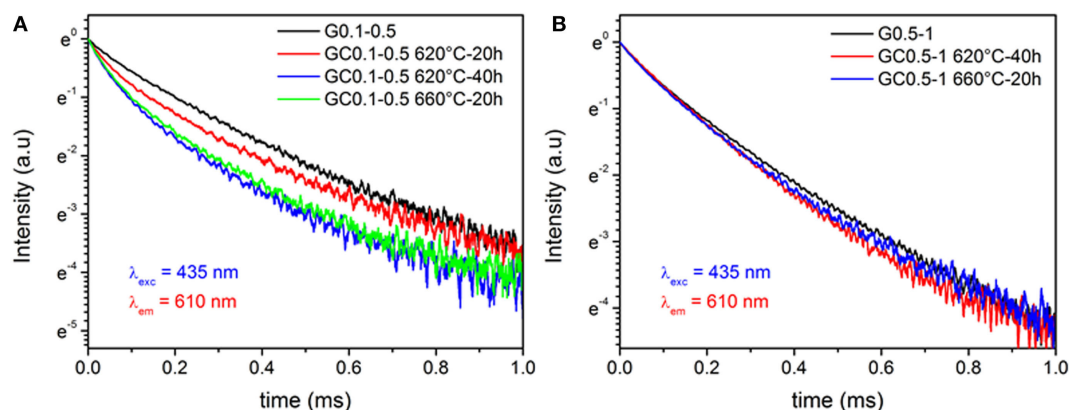


FIGURE 10 | $\text{Pr}^{3+}:\text{}^3\text{P}_0\text{--}\text{}^3\text{H}_6$ transition lifetime at 610 nm upon 435 nm excitation, for (A) 0.1–0.5 Pr–Yb and (B) 0.5–1 Pr–Yb co-doped samples.

TABLE 2 | Pr^{3+} lifetime at 610 nm for co-doped and Pr^{3+} singly doped (in parenthesis) glasses and glass-ceramics (GCs) with the corresponding energy transfer efficiency (ETE) and quantum efficiency (QE).

Sample	Lifetime (μs)	ETE (%)	QE (%)
G 0.1–0.5	240 (269)	11	111
GC 0.1–0.5 620°C, 20 h	147 (271)	46	146
GC 0.1–0.5 620°C, 40 h	123 (297)	59	159
GC 0.1–0.5 660°C, 20 h	127 (290)	56	156
G 0.5–1	214 (235)	9	109
GC 0.5–1 620°C, 40 h	165 (298)	44	144
GC 0.5–1 660°C, 20 h	150 (277)	46	146

about radiative emission lifetime, although there can be also not negligible contributions from ET over long distances (Katayama and Tanabe, 2013). Lifetime uncertainty is $\approx 5\%$. Pr^{3+} emission in GCs has a more evident non-exponential profile. Pr^{3+} decays in co-doped samples is faster than glass, and this is a further proof of a more efficient ET mechanism between Pr^{3+} and Yb^{3+} ions. For Pr^{3+} singly doped samples, lifetime increases passing from glass to GCs and their values are summarized in **Table 2**.

ETE and QE of all co-doped samples have been calculated using Eqs 8 and 9. An estimation of the highest theoretical QE was obtained setting η_{Pr} and η_{Yb} in Eq. 9 equal to 1. The values are summarized in **Table 2**. ETE is quite smaller for glass than for GCs and for 0.1–0.5 Pr–Yb composition it is 11% for glass and almost 60% for GC 620°C, 40 h and the highest QE is 159%. For 0.5–1 Pr–Yb, the highest ETE value, obtained for GC 660°C, 20 h, is 46% and the highest QE is 146%. Therefore, the best results in terms of ETE and QE are obtained for the 0.1–0.5 Pr–Yb GC 620°C, 40 h, and this could be explained considering the higher ratio between Pr^{3+} and Yb^{3+} ions that should favor a more uniform Yb^{3+} distribution around Pr^{3+} increasing the probability of DC emission.

Figure 11 shows Yb^{3+} emission at 976 nm for both co-doped compositions. Near single exponential decay are observed for GCs samples, while non-radiative relaxation channels are more important for glasses. GCs lifetimes increase as compared to glasses and this is a further proof of Yb^{3+} ions inside LaF_3 crystals. All Yb^{3+} lifetimes are summarized in **Table 3**.

CONCLUSION

Nano oxyfluoride GCs doped with 0.1 and 0.5 Pr and co-doped with 0.1–0.5 Pr–Yb and 0.5–1 Pr–Yb have been prepared with LaF_3 as only crystal phase. In all the cases, glasses and GCs treated at 620 and 660°C are perfectly transparent, due to the small crystal size (12–14 nm).

Crystallization kinetics showed that the crystal growth of LaF_3 starts from a constant number of nuclei already present in the as made glass and the process is controlled by diffusion. In particular, by increasing dopants concentration, the nuclei density increases but nuclei size gets smaller. Likewise, the increase of T_g and T_x for higher dopants concentrations causes a delay in the crystallization onset and limits RE^{3+} ions diffusion due to higher viscosity.

Down-conversion emission of Yb^{3+} was observed in the range 950–1,150 nm upon Pr^{3+} excitation at 440 nm, and CET from the $^3\text{P}_0$ level of Pr^{3+} could play relevant role in the ET process from Pr^{3+} to Yb^{3+} .

Pr^{3+} and Yb^{3+} ions get incorporated inside LaF_3 crystals in GCs samples. This fact is strongly supported by the more evident Stark splitting of Pr^{3+} emission spectra passing from glass to GCs, by the Pr^{3+} lifetime decrease in GCs suggesting that a better ET occurs and by Yb^{3+} lifetime increase in GCs indicating a decrease of non-radiative processes compared to glasses.

Glass-ceramics samples show better DC emission in the range 950–1150 nm compared to glasses and by a proper heat treatment it is possible to find the best combination to enhance Yb^{3+} DC and suppress unwanted Pr^{3+} emission. The highest ETE and QE were 59 and 159%, respectively, for GC 0.1–0.5 Pr–Yb 620°C, 40 h.

The results here described encourage continuing with further analysis of these materials as DC materials. In particular, different RE^{3+} ions concentration combinations should be tested. The DC emission by Yb^{3+} ions show the possibility of using this glass system in Photonics, even though further studies, regarding RE^{3+} ions concentrations, materials thickness, etc., should be performed to optimize the best DC signal and the application of these materials.

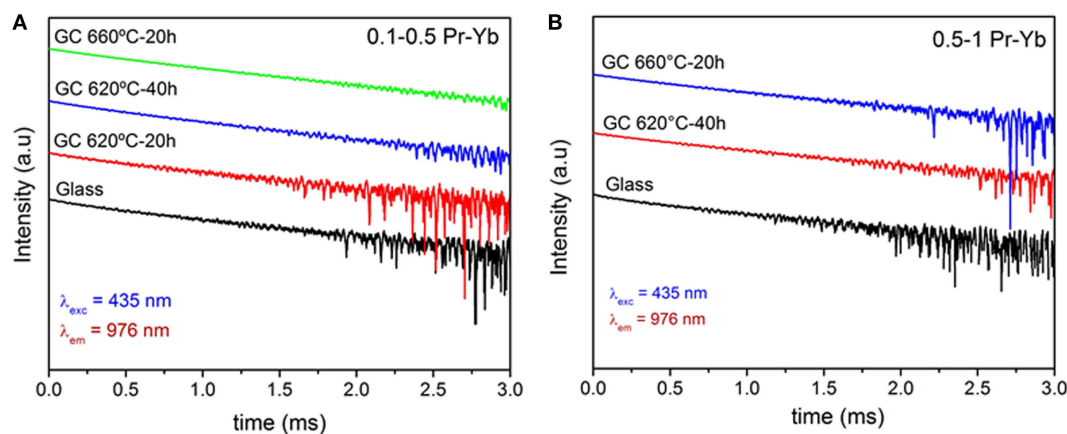


FIGURE 11 | $\text{Yb}^{3+}:\text{F}_{5/2}-\text{F}_{7/2}$ transition lifetime at 976 nm upon 435 nm excitation, for (A) 0.1–0.5 Pr–Yb and (B) 0.5–1 Pr–Yb co-doped samples.

TABLE 3 | $\text{Yb}^{3+}:\text{F}_{5/2}-\text{F}_{7/2}$ lifetime for all co-doped samples.

Sample	Lifetime (μs)
G 0.1–0.5	640
GC 0.1–0.5 620°C, 20 h	750
GC 0.1–0.5 620°C, 40 h	758
GC 0.1–0.5 660°C, 20 h	756
G 0.5–1	630
GC 0.5–1 620°C, 40 h	700
GC 0.5–1 660°C, 20 h	705

AUTHOR CONTRIBUTIONS

GG prepared the materials and studied their structural properties. He also measured lifetimes with SP. He contributed to the discussion of results and writing of the paper. AC contributed to the PL measurements. SP contributed to the management of the experiment and to the PL and lifetime measurements. LP performed HR-TEM characterization and analysis. AD and MP

REFERENCES

- Abrams, Z. R., Niv, A., and Zhang, X. (2011). Solar energy enhancement using down-converting particles: a rigorous approach. *J. Appl. Phys.* 109, 114905–114909. doi:10.1063/1.3592297
- Bhattacharyya, S., Höche, T., Hemono, N., Pascual, M. J., and van Aken, P. A. (2009). Nano-crystallization in $\text{LaF}_3\text{-Na}_2\text{O-Al}_2\text{O}_3\text{-SiO}_2$ glass. *J. Cryst. Growth* 311, 4350–4355. doi:10.1016/j.jcrysgro.2009.07.027
- Chen, D., Wang, Y., Yu, Y., Huang, P., and Weng, F. (2008). Near-infrared quantum cutting in transparent nanostructured glass-ceramics. *Opt. Lett.* 33, 1884–1886. doi:10.1364/OL.33.001884
- Chen, D., Wang, Y., Yu, Y., and Ma, E. (2007). Influence of Yb^{3+} content on microstructure and fluorescence of oxyfluoride glass-ceramics containing LaF_3 nano-crystals. *Mater. Chem. Phys.* 101, 464–469. doi:10.1016/j.matchemphys.2006.08.005
- Chen, Q. J., Zhang, W. J., Huang, X. Y., Dong, G. P., Peng, M. Y., and Zhang, Q. Y. (2012). Efficient down- and up-conversion of $\text{Pr}^{3+}\text{-Yb}^{3+}$ co-doped transparent oxyfluoride glass-ceramics. *J. Alloys Compd.* 513, 139–144. doi:10.1016/j.jallcom.2011.10.007
- de Pablos-Martín, A., Durán, A., and Pascual, M. J. (2012). Nanocrystallisation in oxyfluoride systems: mechanisms of crystallisation and photonic properties. *Int. Mater. Rev.* 57, 165–186. doi:10.1179/1743280411Y.0000000004

contributed to the structure and planning of the work, management of the experiments, work supervision and discussion, and writing of the paper.

ACKNOWLEDGMENTS

The authors would like to thank Juan Vargas (technician at ICV-CSIC) for samples preparation.

FUNDING

Financial support of the Spanish National Project MAT2013-48246-C2-1-P. GG wishes to acknowledge a grant given by the Tuscany region “Progetto Giovani Si” (Italy). AC wishes to acknowledge the financial support of the Ministero dell’Istruzione, dell’Università e della Ricerca (MIUR) through the Centro Fermi project “Premiale 2012 – Fisica e strumentazione per la salute dell’uomo.”

- de Pablos-Martín, A., Hemono, N., Mather, G. C., Bhattacharyya, S., Höche, T., Bornhöft, H., et al. (2011). Crystallization kinetics of LaF_3 nanocrystals in an oxyfluoride glass. *J. Am. Ceram. Soc.* 94, 2420–2428. doi:10.1111/j.1551-2916.2011.04547.x
- de Pablos-Martín, A., Ristic, D., Bhattacharyya, S., Höche, T., Mather, G. C., Ramirez, M. O., et al. (2013). Effects of Tm^{3+} additions on the crystallization of LaF_3 nanocrystals in oxyfluoride glasses: optical characterization and up-conversion. *J. Am. Ceram. Soc.* 96, 447–457. doi:10.1111/jace.12120
- Deng, K., Wei, X., Wang, X., Chen, Y., and Yin, M. (2011). Near-infrared quantum cutting via resonant energy transfer from Pr^{3+} to Yb^{3+} in LaF_3 . *Appl. Phys. B* 102, 555–558. doi:10.1007/s00340-011-4413-7
- Donald, I. W. (2004). Crystallisation kinetics of a lithium zinc silicate glass studied by DTA and DSC. *J. Non Cryst. Solid* 345–346, 120–126. doi:10.1016/j.jnoncrsol.2004.08.007
- Gao, G., and Wondraczek, L. (2013). Near-infrared down-conversion in $\text{Pr}^{3+}/\text{Yb}^{3+}$ co-doped boro-aluminosilicate glasses and LaBO_3 glass ceramics. *Opt. Mater. Express* 3, 633–644. doi:10.1364/OME.3.000633
- Hemono, N., Pierre, G., Muñoz, F., de Pablos-Martín, A., Pascual, M. J., and Durán, A. (2009). Processing of transparent glass-ceramics by nano-crystallisation of LaF_3 . *J. Eur. Ceram. Soc.* 29, 2915–2920. doi:10.1016/j.jeurceramsoc.2009.05.013

- Huang, X., Han, S., Huang, W., and Liu, X. (2013). Enhancing solar cell efficiency: the search for luminescent materials as spectral converters. *Chem. Soc. Rev.* 42, 173–201. doi:10.1039/c2cs35288e
- Katayama, Y., and Tanabe, S. (2010a). Near infrared down-conversion in Pr^{3+} - Yb^{3+} codoped oxyfluoride glass ceramics. *Opt. Mater.* 33, 176–179. doi:10.1016/j.optmat.2010.07.016
- Katayama, Y., and Tanabe, S. (2010b). Spectroscopy and 1 μm luminescence by visible quantum cutting in Pr^{3+} - Yb^{3+} codoped glass. *Materials* 3, 2405–2411. doi:10.3390/ma3042405
- Katayama, Y., and Tanabe, S. (2013). Mechanism of quantum cutting in Pr^{3+} - Yb^{3+} codoped oxyfluoride glass ceramics. *J. Lumin.* 134, 825–829. doi:10.1016/j.jlumin.2012.06.042
- Kissinger, H. E. (1956). Variation of peak temperature with heating rate in differential thermal analysis. *J. Res. Nat. Bur. Stand.* 57, 217–221. doi:10.6028/jres.057.026
- Lakshminarayana, G., and Qiu, J. (2009). Near-infrared quantum cutting in $\text{RE}^{3+}/\text{Yb}^{3+}$ ($\text{RE} = \text{Pr}$, Tb , and Tm): GeO_2 - B_2O_3 - ZnO - LaF_3 glasses via down-conversion. *J. Alloys Compd.* 481, 582–589. doi:10.1016/j.jallcom.2009.03.034
- Matusita, K., and Sakka, S. (1980). Kinetic study on crystallization of glass by differential thermal analysis – criterion on application of Kissinger plot. *J. Non Cryst. Solid* 38, 741–746. doi:10.1016/0022-3093(80)90525-6
- Ozawa, T. (1970). Kinetic analysis of derivative curves in thermal analysis. *J. Therm. Anal.* 2, 301–324. doi:10.1007/BF01911411
- Richards, B. S. (2006). Luminescent layers for enhanced silicon solar cell performance: down-conversion. *Sol. Energy Mater. Sol. Cells* 90, 1189–1207. doi:10.1016/j.solmat.2005.07.001
- Trupe, T., Green, M. A., and Wurfel, P. (2002). Improving solar cell efficiencies by down-conversion of high energy photons. *J. Appl. Phys.* 92, 1668–1674. doi:10.1063/1.1505677
- van der Ende, B. M., Aarts, L., and Meijerink, A. (2009). Near-infrared quantum cutting for photovoltaics. *Adv. Mater.* 21, 3073–3077. doi:10.1002/adma.200802220
- van Wijngaarden, J. T., Scheidelaar, S., Vlugt, T. J. H., Reid, M. F., and Meijerink, A. (2010). Energy transfer mechanism for down-conversion in the (Pr^{3+} , Yb^{3+}) Couple. *Phys. Rev. B* 81, 155112–155116. doi:10.1103/PhysRevB.81.155112
- Xiang, G., Zhang, J., Hao, Z., Zhang, X., Pan, G., Luo, Y., et al. (2014). The energy transfer mechanism in Pr^{3+} and Yb^{3+} codoped β - NaLuF_4 nanocrystals. *Phys. Chem. Chem. Phys.* 16, 9289–9293. doi:10.1039/C4CP01184H
- Xu, Y., Zhang, X., Dai, S., Fan, B., Ma, H., Adam, J.-L., et al. (2011). Efficient near-infrared down-conversion in Pr^{3+} - Yb^{3+} codoped glasses and glass ceramics containing LaF_3 nanocrystals. *J. Phys. Chem. C* 115, 13056–13062. doi:10.1021/jp201503v
- Zhou, J., Tenga, Y., Ye, S., Linc, G., and Qiu, J. (2012). A discussion on spectral modification from visible to near-infrared based on energy transfer for silicon solar cells. *Opt. Mater.* 34, 901–905. doi:10.1016/j.optmat.2011.12.002

Conflict of Interest Statement: The authors declare that the research was conducted in the absence of any commercial or financial relationships that could be construed as a potential conflict of interest.

Copyright © 2017 Gorni, Cosci, Pelli, Pascual, Durán and Pascual. This is an open-access article distributed under the terms of the Creative Commons Attribution License (CC BY). The use, distribution or reproduction in other forums is permitted, provided the original author(s) or licensor are credited and that the original publication in this journal is cited, in accordance with accepted academic practice. No use, distribution or reproduction is permitted which does not comply with these terms.



Nucleation and Crystal Growth in Laser-Patterned Lines in Glasses

Takayuki Komatsu* and Tsuyoshi Honma

Department of Materials Science and Technology, Nagaoka University of Technology, Nagaoka, Japan

Laser-induced crystallization is a new method for the design and control of the crystallization of glasses and opens a new door in the study of nucleation and crystal growth in glasses. Nonlinear optical Sm-doped β -BaB₂O₄ (β -BBO) crystal lines were patterned by continuous-wave Yb:YVO₄ fiber laser (wavelength 1080 nm) in 8Sm₂O₃-42BaO-50B₂O₃ glass as an example, and nucleation and crystal growth behaviors in the laser-patterned bending and crossing lines were examined. It was confirmed that the growth of *c*-axis oriented β -BBO crystals follows along the laser scanning direction even if laser scanning direction changes. The model of *self-organized homo-epitaxial crystal growth* was demonstrated for the orientation of β -BBO crystals at the crossing point of two lines, in which the first crystal line at the crossing point acts as nucleation site for the second crystal line. This study proposes a new crystal growth technology.

Keywords: laser patterning, nucleation, crystal growth, homo-epitaxial, nonlinear optical crystal

OPEN ACCESS

Edited by:

Wolfram Höland,
Ivoclar Vivadent AG, Liechtenstein

Reviewed by:

Ana Candida Martins Rodrigues,
Universidade Federal de São Carlos,
Brazil

Akihiko Sakamoto,
OLED Material Solutions, Japan

*Correspondence:

Takayuki Komatsu
komatsu@mst.nagaokaut.ac.jp

Specialty section:

This article was submitted
to Glass Science,
a section of the journal
Frontiers in Materials

Received: 15 May 2016

Accepted: 01 July 2016

Published: 14 July 2016

Citation:

Komatsu T and Honma T (2016)
Nucleation and Crystal Growth in
Laser-Patterned Lines in Glasses.
Front. Mater. 3:32.
doi: 10.3389/fmats.2016.00032

INTRODUCTION

For a deep understanding of the crystallization of glasses and for development of new functional glass-ceramics, the design and control of nucleation and crystal growth are extremely important. One of the most affecting points to this issue is glass composition, because the nucleation behavior and the kind of crystals formed in a given glass depend largely on the chemical composition of the glass. Heat treatment condition such as temperature, time, and atmosphere is also important for the control of nucleation and crystal growth rates in glasses. Usually, glass-ceramics are synthesized through heat treatment of glasses in an electric furnace, and various functional glass-ceramics being available for practical applications have been developed (Beall and Pinckney, 1999; Sakamoto and Yamamoto, 2010; Höland and Beall, 2012).

Spatially selected patterning of crystals in glasses by laser irradiation, i.e., laser-induced crystallization, is also extremely attractive, which is a new method for the design and control of the crystallization of glasses and also opens a new door in the study of nucleation and crystal growth in glasses (Komatsu et al., 2007; Komatsu and Honma, 2013; Inoue et al., 2015; Komatsu, 2015). In the laser-induced crystallization, a steep temperature gradient is created in the laser-irradiated local region, and such a steep temperature gradient is moved along laser scanning direction, consequently providing the patterning of crystals with high orientation. In the laser-induced crystallization, therefore, it is possible to design spatially nucleation site and control crystal growth direction. So far, various crystals with high orientation such as ferroelectric LiNbO₃ (Honma and Komatsu, 2010; Komatsu et al., 2011), multi-ferroic β' -RE₂(MoO₄)₃ (RE, rare earth) (Tsukada et al., 2009; Suzuki et al., 2014), nonlinear optical Li₂Si₂O₅ (Honma et al., 2008a,b), LaBGeO₅ (Stone et al., 2010), SbSI (Gupta et al., 2011), and oxyfluoride BaAlBO₃F₂ (Shinozaki et al., 2012) have been patterned in glasses.

Recently, nonlinear optical oxyfluoride BaAlBO₃F₂ crystal lines were patterned in BaF₂-Al₂O₃-B₂O₃ glasses, and the model of “*self-organized homo-epitaxial crystal growth*” has been proposed for the crystal orientation at the crossing point of two laser-patterned lines (Shinozaki et al., 2015).

This finding gives new potential for future application in the crystallization of glasses. It is of importance to confirm the self-organized homo-epitaxial crystal growth in other glasses, and to demonstrate this growth as a common phenomenon in the laser-induced crystallization. In this work, crossing lines of nonlinear optical β -BaB₂O₄ (β -BBO) crystal were patterned by laser irradiation in Sm₂O₃-BaO-B₂O₃ glasses, and nucleation and crystal growth behaviors at the crossing point were examined from polarized optical microscope (POM) observations. So far, the patterning of highly oriented crystal lines (not crossing lines) of β -BBO in some glasses has been realized (Honma et al., 2003; Suzuki et al., 2012, 2013; Ogawa et al., 2013; Nishii et al., 2015), and thus, β -BBO crystal would be a good example for the study of nucleation and crystal growth in the laser-induced crystallization in glasses.

EXPERIMENTAL SECTION

A glass with the composition of 8Sm₂O₃-42BaO-50B₂O₃ (mol%) was prepared by melt quenching. Commercial powders of reagent grade Sm₂O₃, BaCO₃, and H₃BO₃ were melted in a platinum crucible at 1200°C for 40 min in an electric furnace. The melts were poured onto an iron plate and pressed to a thickness of ~ 1.5 mm by another iron plate. Glass transition (T_g) and crystallization peak temperatures (T_p) were determined by using differential thermal analysis (DTA) at a heating rate of 10 K/min. The quenched glasses were annealed at T_g for 30 min to release internal stresses (e.g., Ogawa et al., 2013).

Glasses were mechanically polished to a mirror finish with CeO₂ powders. Glasses were irradiated by continuous-wave Yb:YVO₄ fiber laser (beam shape: single mode and ± 1 nm bandwidth) with a wavelength of $\lambda = 1080$ nm using objective lens (magnification: 50 times, numerical aperture: NA = 0.8). The laser beam was unpolarized, and the diameter of laser spot was 2–3 μ m. Plate-shaped glasses with a thickness of ~ 1 mm were put on the stage and mechanically moved during laser irradiation to pattern crossing crystal lines.

Raman scattering and micro-photoluminescence (PL) spectra at room temperature for laser-patterned lines were measured with a laser microscope (Tokyo Instruments Co., Nanofinder) operated at Ar⁺ laser ($\lambda = 488$ nm). Second harmonic generations (SHGs) were measured using a Q-switched Nd: yttrium aluminum garnet (YAG) laser with $\lambda = 1064$ nm, in which linearly polarized incident light was used and second harmonic (SH) light ($\lambda = 532$ nm) was detected. Conventional POM observations for laser-irradiated parts were carried out using an apparatus of Olympus-BX51, in which the crossed polarizer and analyzer were used together with a sensitive color plate. Light being used is white light. Furthermore, samples placed at the stage were rotated, and the change in interference color was observed.

RESULTS AND DISCUSSION

The glass of 8Sm₂O₃-42BaO-50B₂O₃ has the values of $T_g = 566^\circ\text{C}$ and $T_p = 681^\circ\text{C}$. Sm³⁺ ions in the glass have the optical absorption coefficient (α : at room temperature) of $\alpha = 10.1\text{ cm}^{-1}$ at $\lambda = 1080$ nm (Yb:YVO₄ fiber laser) (Ogawa et al., 2013).

Considering the data on the quality of β -BBO crystals patterned by laser irradiation in our research group (e.g., Ogawa et al., 2013), the condition of laser power $P = 0.8$ W and laser scanning speed of $S = 4\text{ }\mu\text{m/s}$ was used for the patterning of β -BBO crystals in the glass. In this study, first the crystal growth behavior of β -BBO crystals in straight, bending, and spiral lines is discussed briefly, and then, the nucleation and crystal growth behaviors of β -BBO crystals at the crossing point of two lines are described. This step would be valuable for the discussion on the self-organized homo-epitaxial crystal growth in the crossing lines of the glass. The data on POM observations on straight, bending, and spiral lines have been already reported in the previous paper (Ogawa et al., 2013), but the quantitative data on the azimuthal dependence of SHG signals for these lines was measured in this study.

Crystal Growth and Orientation in Straight, Bending, and Spiral lines

The discrete straight and bending (bending angle: 45°) lines with β -BBO crystals (the width of lines: 5 μ m) were patterned by laser irradiation with $P = 0.8$ W and $S = 4\text{ }\mu\text{m/s}$ at the surface of 8Sm₂O₃-42BaO-50B₂O₃ glass. It is possible to form β -BBO crystalline dots initially at a given place by laser irradiation without moving but cracks are frequently induced around crystalline dots after stopping or moving of laser irradiation. Therefore, in this study, β -BBO crystal particles synthesized by the crystallization of the glass in an electric furnace were used as the initial nucleation site. That is, laser was first irradiated (focused) onto a β -BBO crystal particle placed at the glass surface and then scanned with the scanning speed of $S = 4\text{ }\mu\text{m/s}$.

The azimuthal dependence of SHG signals for the straight and bending lines consisting of β -BBO crystals is shown in **Figure 1**. The formation of β -BBO crystals in these lines has been confirmed in the previous paper (e.g., Ogawa et al., 2013). The POM photographs for these lines are included in **Figure 1**. The

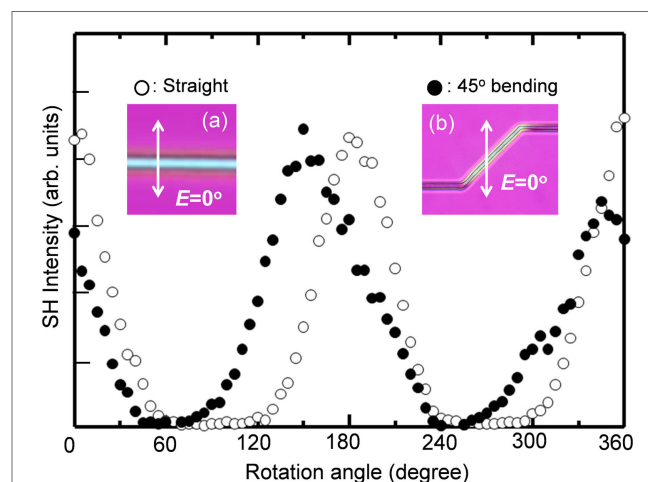


FIGURE 1 | Azimuthal dependence of SHG signals for the straight and bending (bending angle: 45°) lines consisting of β -BBO crystals in the glass. (A,B) are conventional POM photographs for these lines.

maximum SH intensities for the straight line are observed at the rotation angles of $\sim 0^\circ$ and $\sim 180^\circ$, and the minimum SH intensities are located at 90° and 270° . In β -BBO, the presence of $[\text{B}_3\text{O}_6]^{3-}$ anionic hexagonal groupings slightly distorted with a threefold axis is the origin of the large second-order nonlinear optical coefficient ($d_{22} \sim 2 \text{ pm/V}$). The effective second-order nonlinear optical coefficient, d_{eff} , is given by the equation of $d_{\text{eff}} = d_{22}\cos^2\theta$. It was confirmed that the SH intensity for the straight line shown in **Figure 1** changes as a function of $\cos^2\theta$, indicating that β -BBO crystals in the straight line are highly oriented and grow with the c -axis orientation along the laser scanning direction (e.g., Honma et al., 2003; Ogawa et al., 2013). The c -axis orientation of β -BBO crystals has been already proposed in the previous papers (e.g., Honma et al., 2003; Ogawa et al., 2013).

On the other hand, as can be seen in **Figure 1**, the maximum SH intensities for the bending line are observed at the rotation angles of $\sim 150^\circ$ and $\sim 345^\circ$, and the minimum SH intensities are located at $\sim 50^\circ$ and 255° . In particular, when compared with the straight line, it is found that the rotation angle providing the maximum SH intensity in the bending line shifts toward the lower angle with the magnitude of $\sim 30^\circ$. Furthermore, it should be pointed out that the profile of SH intensities against the rotation angle in the bending line is broad when compared with the straight line. It is regarded that the bending line with the bending angle of 45° consists of two components of straight line part and bending line part against the linearly polarized incident laser for SHG measurements, i.e., the components of two rotation angles of θ and $\theta + 45^\circ$. In other words, the SH intensity for the bending line would be expressed as a sum of two contributions (functions) of $\cos^2\theta$ and $\cos^2(\theta + 45^\circ)$. This would be the reason for the shift of the peak position of the maximum SH intensity and the broadness of the profile of SH intensity in the bending line compared with the straight line. Indeed, the profile of SH intensity for the bending line was well fitted with a function of $f(\theta) = \cos^2\theta + \cos^2(\theta + 45^\circ)$. The results shown in **Figure 1** also indicate that the c -axis orientation of β -BBO crystals is kept even in the bending line.

The azimuthal dependence of SHG signals for the spiral line consisting of β -BBO crystals is shown in **Figure 2**. The POM photographs for this lines and the SH wave images (the intensities of green light with $\lambda = 532 \text{ nm}$) observed are included in **Figure 2**. SHGs are detected at all rotation angles, and any specific (critical) angles providing maximum or minimum SH intensities are not observed. In β -BBO crystals, strong SHGs are observed when the direction of the electric field in the linearly polarized incident lasers (E) is parallel to the direction of the polarization in $[\text{B}_3\text{O}_6]^{3-}$ units (P_0), i.e., $E//P_0$. In the spiral line with the c -axis orientation of β -BBO crystals, the configuration of $E//P_0$ is always achieved at any angles, and as a result, it is expected that similar SH intensities are detected in all rotation angles as shown in **Figure 2**. The results shown in **Figure 2** also demonstrate that the c -axis orientation of β -BBO crystals is kept even in the spiral line.

From the c -axis orientation of β -BBO crystal lines demonstrated in **Figures 1** and **2**, it is considered that the preferential crystal growth direction is the c -axis. β -BBO with a crystal structure of R3c has the lattice parameters of $a = b = 1.2547 \text{ nm}$ and $c = 1.2736 \text{ nm}$ (Eimerl et al., 1987), indicating that the

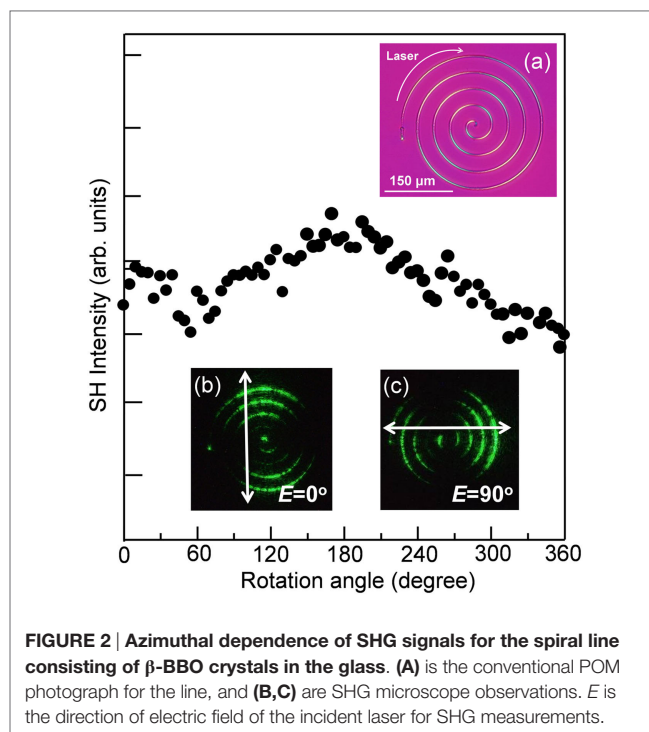


FIGURE 2 | Azimuthal dependence of SHG signals for the spiral line consisting of β -BBO crystals in the glass. **(A)** is the conventional POM photograph for the line, and **(B,C)** are SHG microscope observations. E is the direction of electric field of the incident laser for SHG measurements.

difference in the lattice parameters is very small. As well known, however, β -BBO has a large anisotropic structure, in which planar $[\text{B}_3\text{O}_6]^{3-}$ units stack along the c -axis direction, and Ba^{2+} ions are located between stacked $[\text{B}_3\text{O}_6]^{3-}$ units. The thermal expansion coefficient (α) of β -BBO is $\alpha = 4 \times 10^{-6}/\text{K}$ for the a -axis and $\alpha = 36 \times 10^{-6}/\text{K}$ for the c -axis, indicating that the chemical bond strength between Ba^{2+} and planar $[\text{B}_3\text{O}_6]^{3-}$ units is weaker than that between $[\text{B}_3\text{O}_6]^{3-}$ units. In other words, it is expected that the modification in the bonding distance between Ba^{2+} and planar $[\text{B}_3\text{O}_6]^{3-}$ units is more flexible. These structural features of β -BBO would induce the c -axis orientation even for the bending and spiral lines as shown in **Figures 1** and **2**. That is, it would be possible to change or rotate gradually the c -axis direction at the bending or curved points.

The nucleation and crystal growth rates of β -BBO crystals in $8\text{Sm}_2\text{O}_3$ -42 BaO -50 B_2O_3 glass have not been reported so far. It is well known that a glass with the composition of 40 BaO -20 TiO_2 -40 SiO_2 displays the highest internal nucleation (I) rare for fersite $\text{Ba}_2\text{TiSi}_2\text{O}_8$ crystals so far measured in inorganic glasses (Cabral et al., 2003), i.e., $I \sim 10^{17}/\text{m}^3\text{s}$. This nucleation rare of $I \sim 10^{17}/\text{m}^3\text{s}$ equals to $I \sim 0.1/\mu\text{m}^3\text{s}$. The maximum steady-state nucleation rates (I_{max}) for 51 silicate glasses with different compositions have been summarized as a function of reduced glass transition temperature (T_{gr}) ($T_{\text{gr}} = T_g/T_m$, T_m is the melting temperature) (Fokin et al., 2003). The silicate glasses summarized have mainly the values of $I_{\text{max}} = 10^9$ – $10^{13}/\text{m}^3\text{s}$, corresponding to the values of $I_{\text{max}} = 10^{-9}$ – $10^{-5}/\mu\text{m}^3\text{s}$. The value of $I_{\text{max}} \sim 10/\text{mm}^3\text{s}$, corresponding to $10^{-8}/\mu\text{m}^3\text{s}$, has been reported for lithium disilicate (Li_2O -2 SiO_2) glass (Deubener, 2000). In the laser-induced crystallization, only spatially limited region, i.e., the region of 10–20 μm , is heated locally, and furthermore, the keeping period

for high temperature in a given laser-irradiated position is short due to the laser scanning with speeds of $S = 1\text{--}10\text{ }\mu\text{m/s}$ and also to the heat dissipation to the surrounding glassy part (not laser-irradiated part). These features of small heating region and short keeping time at a fixed region would result in the small probability of nucleation during laser scanning. Indeed, highly (*c*-axis) oriented $\text{Li}_2\text{Si}_2\text{O}_5$ crystal lines have been patterned in $\text{Li}_2\text{O}\cdot 2\text{SiO}_2$ glass without causing any new nucleation during laser scanning (Honma et al., 2008a,b). The results shown in **Figures 1 and 2** propose that at least, at the laser irradiation condition of $P = 0.8\text{ W}$ and $S = 4\text{ }\mu\text{m/s}$, only the crystal growth of β -BBO is taking place during the laser scanning in $8\text{Sm}_2\text{O}_3\text{-}42\text{BaO-}50\text{B}_2\text{O}_3$ glass without causing any nucleation, and this would be one of the key points for the laser patterning of β -BBO crystals with high orientation. It should be pointed out that highly oriented $\text{Ba}_2\text{TiSi}_2\text{O}_8$ crystal lines have been patterned by laser irradiation in $40\text{BaO-}20\text{TiO}_2\text{-}40\text{SiO}_2$ glass, although $\text{Ba}_2\text{TiSi}_2\text{O}_8$ nanocrystals are formed by heat treatment in an electric furnace (Enomoto et al., 2007; Honma et al., 2008a,b; Maruyama et al., 2008). Similar behaviors have been observed in the laser patterning and nano-scaled crystallization of the formation of nonlinear optical $\text{BaAlBO}_3\text{F}_2$ crystals in $50\text{BaF}_2\text{-}25\text{Al}_2\text{O}_3\text{-}25\text{B}_2\text{O}_3$ glass (Shinozaki et al., 2012). In the crystallization of CaF_2 in $\text{CaF}_2\text{-Al}_2\text{O}_3\text{-SiO}_2$ -based oxyfluoride glasses, however, it has been reported that lines consisting of CaF_2 nanocrystals have been patterned by laser irradiation as similar to the case in heat treatment in an electric furnace (Kanno et al., 2009; Shinozaki et al., 2013). That is, lines consisting of the assembly of CaF_2 nanocrystals have been patterned, but the patterning of highly oriented CaF_2 single crystal lines have not been reported so far. The nucleation and crystal growth behaviors in the laser-induced crystallization, therefore, depend not only on laser irradiation condition but also on glass composition.

The laser-induced crystallization technique proposed and applied in our group is based perfectly on the thermal effect (heating) as similar to the crystallization in an electric furnace. Therefore, basically, the crystalline phase formed in the laser-induced crystallization in a given glass is the same as that formed in the crystallization in an electric furnace. In this sense, it should be emphasized that even in the laser-induced crystallization, the design of the system and composition of base glasses is still a key point for the patterning of crystals with high qualities. That is, even in the laser-induced crystallization, the design and control of the morphology of crystals depend largely on the chemical composition of a given glass.

Nucleation and Homo-Epitaxial Crystal Growth in Crossing Lines

As indicated in the above section, through the use of optimal laser power and scanning speed, it is possible to depress nucleation during laser scanning and to induce homogeneous crystal growth providing the patterning of highly oriented β -BBO crystal lines in $8\text{Sm}_2\text{O}_3\text{-}42\text{BaO-}50\text{B}_2\text{O}_3$ glass. Here, the nucleation and crystal growth behaviors of β -BBO crystals in the laser-induced crystallization are discussed more in detail by patterning crossing lines. A schematic illustration for crossing line experiments is shown

in **Figure 3**. First, a discrete straight line consisting of highly oriented β -BBO crystals was patterned by laser irradiation with $P = 0.8\text{ W}$ and $S = 4\text{ }\mu\text{m/s}$ in $8\text{Sm}_2\text{O}_3\text{-}42\text{BaO-}50\text{B}_2\text{O}_3$ glass, in which a β -BBO crystal particle synthesized by the crystallization of the glass in an electric furnace was used as an initial nucleation site. Then, the second laser irradiation with $P = 0.8\text{ W}$ and $S = 1\text{--}4\text{ }\mu\text{m/s}$ was carried out against the first line with the crossing angle of 90° (perpendicularly). In the second line patterning, any β -BBO crystal particles were not used, and thus, the laser irradiation does not induce any crystallization before crossing against the first line but just only the change in the glass structure (refractive index change).

The POM photograph for the crossing lines is shown in **Figure 4**. In the POM observations, the crossed polarizer and analyzer were used, and the appearance of bright and homogeneous interference color indicates the formation of nonlinear optical crystals. On the other hand, structurally isotropic glassy materials do not give any interference color. It is, therefore, concluded from the POM photograph in **Figure 4** that, in the second lines with

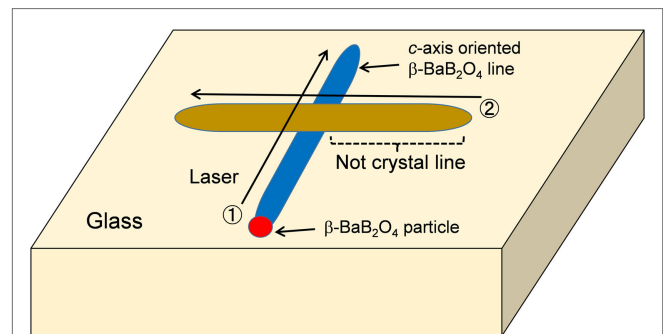


FIGURE 3 | Schematic experimental procedure for the patterning of crossing crystal lines. First, the crystal line ① was patterned, and then, the second laser irradiations ② were carried out for the first line with the crossing angle of 90° .

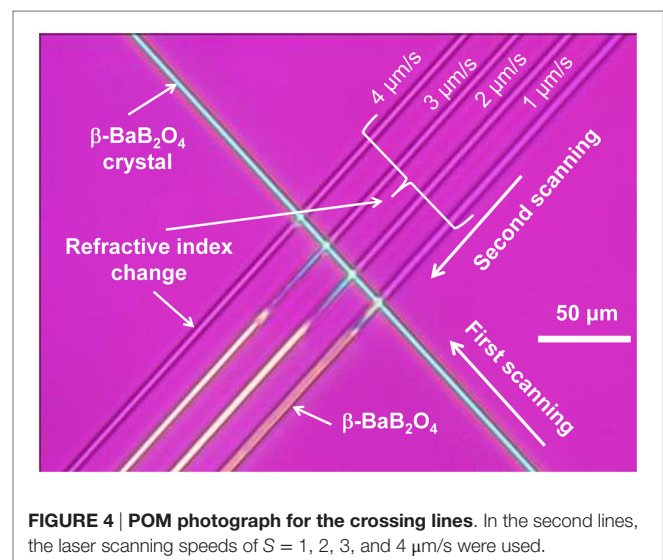


FIGURE 4 | POM photograph for the crossing lines. In the second lines, the laser scanning speeds of $S = 1, 2, 3,$ and $4\text{ }\mu\text{m/s}$ were used.

the laser scanning speeds of $S = 1, 2$, and $3 \mu\text{m/s}$, the formation of crystals is induced after crossing against the first crystal line, although any crystals were not formed before crossing. In the second line with $S = 4 \mu\text{m/s}$, any crystallization was not induced even after crossing. These results indicate that nucleation and crystal growth behaviors at the crossing region depend on the scanning speed of the second line patterning. That is, the scanning with low speed is more effective for the nucleation and crystal growth at the crossing region.

The micro-Raman scattering spectrum at room temperature for the crystalline part in the second line ($P = 0.8 \text{ W}$, $S = 1 \mu\text{m/s}$) after crossing is shown in **Figure 5**. The Raman bands are assigned to β -BBO crystal (Suzuki et al., 2012), indicating that nonlinear optical crystals (i.e., β -BBO) formed in the second line after crossing is the same as that in the first line consisting of β -BBO. As can be seen in **Figure 5**, the intensities of Raman bands in the second line (b) are much larger than those in the first line (a). The first line consisting of β -BBO crystals was patterned with the condition of $P = 0.8 \text{ W}$ and $S = 4 \mu\text{m/s}$. On the other hand, the second line was patterned with $P = 0.8 \text{ W}$ and $S = 1 \mu\text{m/s}$. As shown in **Figure 4**, the formation behavior of β -BBO crystals after crossing depends on the laser scanning speed. The Raman scattering spectra shown in **Figure 5**, i.e., the difference in the Raman band intensity between the first line (a) and the second line (b), therefore, suggest that the amount of β -BBO crystals increases with the decrease in the laser scanning speed from 4 to $1 \mu\text{m/s}$, and also, their quality might be improved in the condition of low laser scanning speed. Considering crystal growth kinetics in glass, low laser scanning speed, i.e., keeping high temperature for long period, would be favorable for crystal growth. Of course, however, optimal laser irradiation condition (optimal laser power and scanning speed) is required for the patterning of homogeneous crystal lines (Honma et al., 2005; Inoue et al., 2015).

The micro PL spectrum at room temperature for the second line after crossing is shown in **Figure 6**. Four luminescence

peaks are observed at ~ 565 , ~ 600 , ~ 645 , and $\sim 705 \text{ nm}$. These are typical emissions of Sm^{3+} assigned to ${}^4\text{G}_{5/2} \rightarrow {}^6\text{H}_j$, i.e., ${}^4\text{G}_{5/2} \rightarrow {}^6\text{H}_{5/2}$ at 565 nm , ${}^4\text{G}_{5/2} \rightarrow {}^6\text{H}_{7/2}$ at 600 nm , ${}^4\text{G}_{5/2} \rightarrow {}^6\text{H}_{9/2}$ at 645 nm , and ${}^4\text{G}_{5/2} \rightarrow {}^6\text{H}_{11/2}$ at 705 nm . Since there is no peaks at around 683 nm (${}^5\text{D}_0 \rightarrow {}^7\text{F}_0$), 725 nm (${}^5\text{D}_0 \rightarrow {}^7\text{F}_2$), and 760 nm (${}^5\text{D}_0 \rightarrow {}^7\text{F}_3$) attributing to Sm^{2+} , samarium ions exist at trivalent Sm^{3+} in the second line after crossing. That is, there is no change in the valence of Sm ions during laser irradiation. The first and second lines show strong PL intensities compared with the glassy part (not laser-irradiated part), suggesting that some Sm^{3+} ions are incorporated into β -BBO crystals. It is, therefore, considered that Sm^{3+} -doped β -BaB₂O₄ crystals are formed in the lines patterned by laser irradiation. It is noted that the intensities of PL spectra in the second line (b) ($S = 1 \mu\text{m/s}$) are much larger than those in the first line (a) ($S = 4 \mu\text{m/s}$), as similar to Raman scattering spectra (**Figure 5**). The PL spectra shown in **Figure 6**, therefore, suggest that the amount of Sm^{3+} -doped β -BBO crystals formed in the second line after crossing is larger than that in the first line. The incorporation of Sm^{3+} into β -BaB₂O₄ crystals has been also proposed even in the discrete straight line (Honma et al., 2004).

As indicated in **Figures 1** and **4**, β -BBO crystals with the c -axis orientation are patterned in the first crystal line. Furthermore, it is found that the nucleation and crystal growth of β -BBO crystals occur effectively at the crossing region of two lines. In order to look at the crystallization behavior at the crossing region more in detail, the POM photograph focusing the crossing region in the second line patterned with $S = 2 \mu\text{m/s}$ is again shown in **Figure 7**. It is found that the second line just after crossing has a light color, being the same as that in the first line consisting of the c -axis oriented β -BBO crystals. The same color means the same retardation, i.e., the same crystal orientation of nonlinear optical crystals. It is, therefore, considered that the orientation of β -BBO crystals in the second line after crossing is the same as that in the first line. It is seen that the homogeneous light blue color in the second line changes to other color in the part beyond the

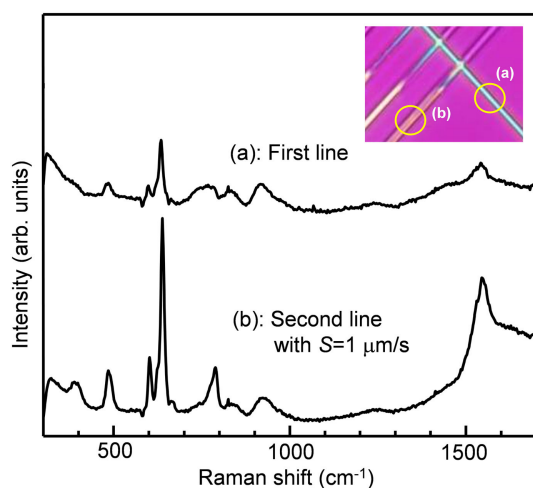


FIGURE 5 | Micro-Raman scattering spectra at room temperature for the first (A) and second (B) lines patterned by laser irradiation.

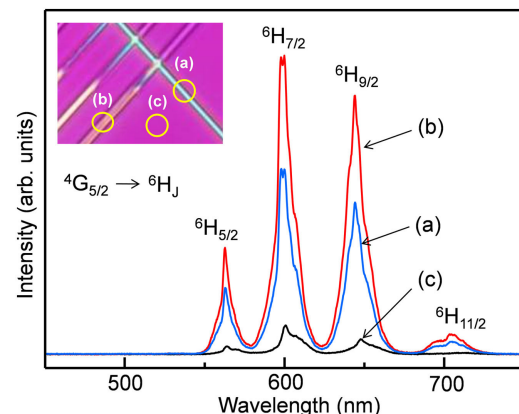


FIGURE 6 | Micro-photoluminescence (PL) spectra at room temperature for the first (A) and second (B) lines patterned by laser irradiation. The PL spectrum for the glassy part (C) (not laser-irradiated part) is also shown.

distance of about 20 μm from the crossing point. This means that the orientation of β -BBO crystals in this part changes gradually. Considering the crystal growth mechanism in the crossing line experiments, it is suggested that the side plane of the first β -BBO crystal line acts as the nucleation site for the crystallization in the second line.

The difference in the lattice parameters ($a = b = 1.2547$ nm and $c = 1.2736$ nm) in β -BBO is very small, indicating that the lattice mismatch between the c -plane and a ($=b$)-plane is very small. However, β -BBO has a large anisotropic structure, in particular, the stacking of planar $[\text{B}_3\text{O}_6]^{3-}$ units along the c -axis direction, indicating a large difference in the atomic arrangement in the a -plane and c -plane, i.e., a large structural mismatch. It is, therefore, considered that the growth of the c -plane at the a -plane would be difficult structurally. This would be the reason that the a -plane of β -BBO crystals is created in the second line after crossing, as schematically shown in **Figure 7**. The relationship in the crystal growth direction at the crossing point between the first and second lines is expressed as the combination of the a -plane/ the a -plane of the same crystalline phase of β -BBO, and this crystal growth is regarded as “a homo-epitaxial crystal growth” in the crossing lines of nonlinear optical β -BBO crystals patterned by laser irradiation. The preferential crystal growth direction of β -BBO patterned by laser is the c -axis. Therefore, during the crystal growth in the second line, β -BBO tends to have the c -axis orientation. It would be difficult energetically to change the crystal growth direction from the a -axis to the c -axis in an instance at a given position, but the gradual change would be expected. Consequently, the transition zone for the c -axis orientation, i.e., from the a -axis orientation to the c -axis orientation, would be created. Finally, even in the second line, β -BBO crystals with the c -axis orientation would be patterned, as schematically shown in **Figure 8**. The phenomenon on the nucleation and crystal growth of β -BBO crystals in the second line after crossing is illustrated schematically in **Figure 9**. A similar behavior of homo-epitaxial crystal growth in the crossing lines patterned by laser irradiation has been reported in the patterning of nonlinear optical $\text{BaAlBO}_3\text{F}_2$ crystals (Shinozaki et al., 2015). That is, the present study is the second example for the homo-epitaxial crystal growth

in the crystallization of glasses, and the homo-epitaxial crystal growth is regarded as a common feature in the laser-induced crystallization in glasses.

It should be pointed out that the behavior of hetero-epitaxial crystal growth in the crystallization of glasses has been found in $\text{Li}_2\text{O}-\text{Al}_2\text{O}_3-\text{SiO}_2$ glasses containing P_2O_5 nucleation agent, in which the hetero-epitaxial growth of lithium metasilicate Li_2SiO_3 and lithium disilicate $\text{Li}_2\text{Si}_2\text{O}_5$ on Li_3PO_4 crystals is found in heat treatment in an electric furnace (Headley and Loehman, 1984). There are many glasses that show the formation of two different kinds of crystalline phases in the crystallization. In such glasses, hetero-epitaxial crystal growth might be expected largely through the control of heat treatment. However, it should be pointed out that the design and control of the nucleation site and the crystal growth direction in the crystallization in an electric furnace would be difficult. On the other hand, in the laser-induced crystallization, which enables the heating position, direction, and period, the nucleation site and crystal growth direction might be designed and controlled more effectively. In particular, crossing line experiments are proposed to be a good technique for the

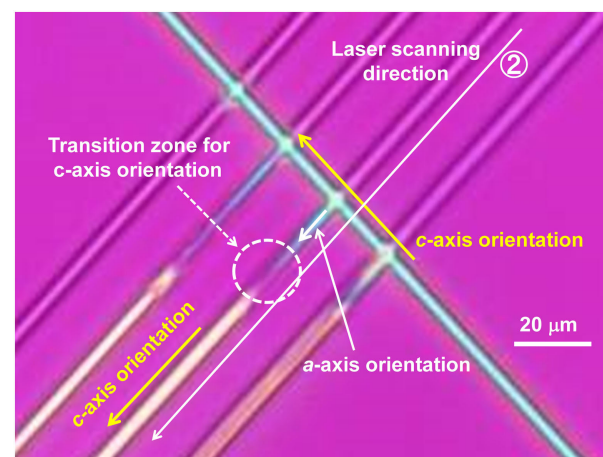


FIGURE 8 | POM photograph focusing the crossing points of the first and second lines.

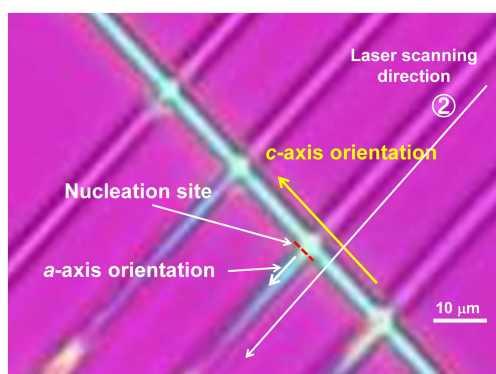


FIGURE 7 | POM photograph focusing the crossing points of the first and second lines.

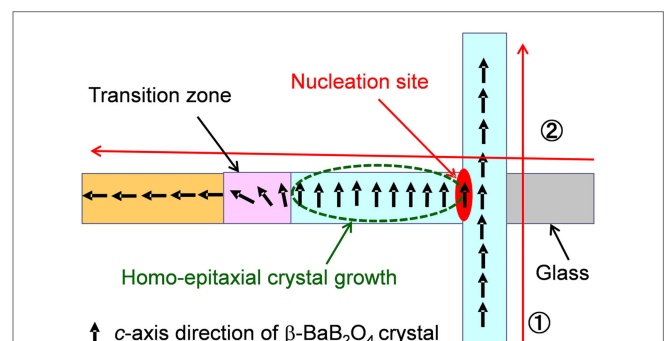


FIGURE 9 | Schematic illustration for the nucleation and crystal growth in the second line after crossing.

study of nucleation and crystal growth in glasses as demonstrated in the present study.

CONCLUSION

Nonlinear optical β -BaB₂O₄ (β -BBO) crystal lines were patterned by continuous-wave Yb:YVO₄ fiber laser (wavelength 1080 nm) in 8Sm₂O₃-42BaO-50B₂O₃ glass, and the nucleation and crystal growth behaviors in the laser-patterned crossing lines were examined from POM observations. The model of self-organized homo-epitaxial crystal growth was demonstrated for the orientation of β -BBO crystals at the crossing point of two lines, in which the first crystal line at the crossing point acts as nucleation site for the second crystal line. The nucleation site and crystal growth direction are controlled effectively in the laser-induced crystallization.

REFERENCES

- Beall, G. H., and Pinckney, L. R. (1999). Nano glass-ceramics. *J. Am. Ceram. Soc.* 82, 5–16. doi:10.1111/j.1151-2916.1999.tb01716.x
- Cabral, A. A., Fokin, V. M., Zannotto, E. D., and Chinaglia, C. R. (2003). Nanocrystallization of fersnoite glass. I. Nucleation and growth kinetics. *J. Non-Cryst. Solids* 330, 174–186. doi:10.1016/j.jnoncrysol.2003.08.046
- Deubener, J. (2000). Compositional onset of homogeneous nucleation in (Li,Na) disilicate glasses. *J. Non-Cryst. Solids* 274, 195–201. doi:10.1016/S0022-3093(00)00188-5
- Eimerl, D., Davis, L., Velsko, S., Graham, E. K., and Zalkin, A. (1987). Optical, mechanical, and thermal properties of barium borate. *J. Appl. Phys.* 62, 1968–1983. doi:10.1063/1.339536
- Enomoto, I., Benino, Y., Fujiwara, T., and Komatsu, T. (2007). Chemically etched sharpened tip of transparent crystallized glass fibers with nonlinear optical Ba₂TiSi₂O₈ nanocrystals. *J. Ceram. Soc. Japan* 115, 374–378. doi:10.2109/jcersj.115.374
- Fokin, V. M., Zannotto, E. D., and Schmelzer, J. W. P. (2003). Homogeneous nucleation versus glass transition temperature of silicate glasses. *J. Non-Cryst. Solids* 321, 52–65. doi:10.1016/S0022-3093(03)00089-9
- Gupta, P., Stone, A., Woodward, N., Dierolf, V., and Jain, H. (2011). Laser fabrication of semiconducting ferroelectric single crystal SbSI features on chalcogenide glass. *Opt. Mater. Express* 1, 652–657. doi:10.1364/OME.1.000652
- Headley, T. J., and Loehman, R. E. (1984). Crystallization of a glass-ceramic by epitaxial growth. *J. Am. Ceram. Soc.* 67, 620–625. doi:10.1111/j.1151-2916.1984.tb19606.x
- Honma, T., Benino, Y., Fujiwara, T., and Komatsu, T. (2003). Technique for writing of nonlinear optical single-crystal lines in glass. *Appl. Phys. Lett.* 83, 2796–2798. doi:10.1063/1.1615833
- Honma, T., Benino, Y., Fujiwara, T., Komatsu, T., and Sato, R. (2005). Crystalline phase and YAG laser-induced crystallization in Sm₂O₃-Bi₂O₃-B₂O₃ glasses. *J. Am. Ceram. Soc.* 88, 989–992. doi:10.1111/j.1551-2916.2005.00166.x
- Honma, T., Benino, Y., Fujiwara, T., Sato, R., and Komatsu, T. (2004). Micro-Raman and photoluminescence spectra of Sm³⁺-doped β -BaB₂O₄ crystal lines written by YAG laser irradiation in glass. *J. Phys. Chem. Solids* 65, 1705–1710. doi:10.1016/j.jpcs.2004.04.010
- Honma, T., and Komatsu, T. (2010). Patterning of two-dimensional planar lithium niobate architectures on glass surface by laser scanning. *Opt. Express* 18, 8019–8024. doi:10.1364/OE.18.008019
- Honma, T., Komatsu, T., and Benino, Y. (2008a). Patterning of c-axis-oriented Ba₂TiX₂O₈ (X=Si, Ge) crystal lines in glass by laser irradiation and their second-order optical nonlinearities. *J. Mater. Res.* 23, 885–888. doi:10.1557/jmr.2008.0135
- Honma, T., Nguyen, P. T., and Komatsu, T. (2008b). Crystal growth behavior in CuO-doped lithium disilicate glasses by continuous-wave fiber laser irradiation. *J. Ceram. Soc. Jpn.* 116, 1314–1318. doi:10.2109/jcersj.116.1314
- Höland, W., and Beall, G. H. (2012). *Glass-Ceramic Technology*, 2nd Edn. Hoboken, NJ: The American Ceramic Society, John Wiley & Sons.

AUTHOR CONTRIBUTIONS

TK proposed the idea of this study and guided the experiments. TK and TH analyzed the experimental data and prepared the manuscript through the discussion.

ACKNOWLEDGMENTS

We thank Mr. Kazuki Ogawa for his experiments in the laser-induced crystallization and Dr. Kenji Shinozaki for discussion. This work was supported from the Grant-in-Aid for Scientific Research from the Ministry of Education, Science, Sports, Culture and Technology, Japan (No. 23246114, No. 15K13804) and by Program for High Reliable Materials Design and Manufacturing in Nagaoka University of Technology.

- Inoue, T., Gao, X., Shinozaki, K., Honma, T., and Komatsu, T. (2015). Laser patterning of non-linear optical Bi₂ZnB₂O₇ crystal lines in glass. *Front. Mater.* 2:42. doi:10.3389/fmats.2015.00042
- Kanno, M., Honma, T., and Komatsu, T. (2009). Two-dimensional mapping of Er³⁺ photoluminescence in CaF₂ crystal lines patterned by lasers in oxyfluoride glass. *J. Am. Ceram. Soc.* 92, 825–829. doi:10.1111/j.1551-2916.2009.03010.x
- Komatsu, T. (2015). Design and control of crystallization in oxide glasses. *J. Non-Cryst. Solids* 428, 156–175. doi:10.1016/j.jnoncrysol.2015.08.017
- Komatsu, T., and Honma, T. (2013). Laser patterning and characterization of optical active crystals in glasses. *J. Asian Ceram. Soc.* 1, 9–16. doi:10.1016/j.jascr.2013.02.006
- Komatsu, T., Ihara, R., Honma, T., Benino, Y., Sato, R., Kim, H. G., et al. (2007). Patterning of nonlinear optical crystals in glass by laser-induced crystallization. *J. Am. Ceram. Soc.* 90, 699–705. doi:10.1111/j.1551-2916.2006.01441.x
- Komatsu, T., Koshiba, K., and Honma, T. (2011). Preferential growth orientation of laser-patterned LiNbO₃ crystals in lithium niobium silicate glass. *J. Solid State Chem.* 184, 411–418. doi:10.1016/j.jssc.2010.12.016
- Maruyama, N., Honma, T., and Komatsu, T. (2008). Electronic polarizability and Judd-Ofelt parameters of Nd³⁺ and Er³⁺ ions in transparent crystallized glasses with nonlinear optical Ba₂TiSi₂O₈ nanocrystals. *J. Chem. Phys.* 128, 184706. doi:10.1063/1.2908231
- Nishii, A., Shinozaki, K., Honma, T., and Komatsu, T. (2015). Morphology and orientation of β -BaB₂O₄ crystals patterned by laser in the inside of samarium barium borate glass. *J. Solid State Chem.* 221, 145–151. doi:10.1016/j.jssc.2014.09.031
- Ogawa, K., Honma, T., and Komatsu, T. (2013). Birefringence imaging and orientation of laser patterned β -BaB₂O₄ crystals with bending and curved shapes in glass. *J. Solid State Chem.* 207, 6–12. doi:10.1016/j.jssc.2013.08.021
- Sakamoto, A., and Yamamoto, S. (2010). Glass-ceramics: engineering principles and applications. *Int. J. Appl. Glass Sci.* 1, 237–247. doi:10.1111/j.2041-1294.2010.00027.x
- Shinozaki, K., Abe, S., Honma, T., and Komatsu, T. (2015). Self-organized homo-epitaxial growth in nonlinear optical BaAlBO₃F₂ crystal crossing lines patterned by laser in glass. *Opt. Mater.* 49, 182–189. doi:10.1016/j.optmat.2015.09.016
- Shinozaki, K., Honma, T., and Komatsu, T. (2012). New oxyfluoride glass with high fluorine content and laser patterning of nonlinear optical BaAlBO₃F₂ single crystal line. *J. Appl. Phys.* 112, 093506. doi:10.1063/1.4764326
- Shinozaki, K., Noji, A., Honma, T., and Komatsu, T. (2013). Morphology and photoluminescence properties of Er³⁺-doped CaF₂ nanocrystals patterned by laser irradiation in oxyfluoride glasses. *J. Fluorine Chem.* 145, 81–87. doi:10.1016/j.jfluchem.2012.10.007
- Stone, A., Sakakura, M., Shimotsuma, Y., Stone, G., Gupta, P., Miura, K., et al. (2010). Formation of ferroelectric single-crystal architectures in LaBGeO₅ glass by femtosecond vs. continuous-wave lasers. *J. Non-Cryst. Solids* 356, 3059–3065. doi:10.1016/j.jnoncrysol.2010.03.048
- Suzuki, F., Honma, T., and Komatsu, T. (2013). Direct laser patterning of β -BaB₂O₄ crystals with high orientation in the inside of glass fiber. *J. Am. Ceram. Soc.* 96, 1339–1341. doi:10.1111/jace.12275

- Suzuki, F., Honma, T., and Komatsu, T. (2014). Unique crystal growth with crystal axis rotation in multi-ferroic β' -(Sm,Gd)₂(MoO₄)₃ narrow lines patterned by lasers in glass. *J. Phys. Chem. Solids* 75, 954–958. doi:10.1016/j.jpcs.2014.04.007
- Suzuki, F., Ogawa, K., Honma, T., and Komatsu, T. (2012). Laser patterning and preferential orientation of two-dimensional planar β -BaB₂O₄ crystals on the glass surface. *J. Solid State Chem.* 185, 130–135. doi:10.1016/j.jssc.2011.11.005
- Tsukada, Y., Honma, T., and Komatsu, T. (2009). Self-organized periodic domain structure for second harmonic generation in ferroelastic β' -(Sm,Gd)₂(MoO₄)₃ crystalline on glass surfaces. *Appl. Phys. Lett.* 94, 059901. doi:10.1063/1.3076080

Conflict of Interest Statement: The authors declare that the research was conducted in the absence of any commercial or financial relationships that could be construed as a potential conflict of interest.

Copyright © 2016 Komatsu and Honma. This is an open-access article distributed under the terms of the Creative Commons Attribution License (CC BY). The use, distribution or reproduction in other forums is permitted, provided the original author(s) or licensor are credited and that the original publication in this journal is cited, in accordance with accepted academic practice. No use, distribution or reproduction is permitted which does not comply with these terms.



Apatite Glass-Ceramics: A Review

Tomas Duminis*, Saroash Shahid and Robert Graham Hill

Unit of Dental Physical Sciences of the Centre for Oral Growth and Development, Institute of Dentistry, Barts and the London School of Medicine and Dentistry, Queen Mary University of London, London, UK

This article is a review of the published literature on apatite glass-ceramics (GCs). Topics covered include crystallization mechanisms of the various families of apatite GCs and an update on research and development on apatite GCs for applications in orthopedics, dentistry, optoelectronics, and nuclear waste management. Most apatite GCs crystallize through a homogenous nucleation and crystallization mechanism, which is aided by a prior liquid-liquid phase separation. Careful control of the base glass composition and heat-treatment conditions, which determine the nature and morphology of the crystal phases in the GC can produce GC materials with exceptional thermal, mechanical, optical, and biological properties. The GCs reviewed for orthopedic applications exhibit suitable mechanical properties and can chemically bond to bone and stimulate its regeneration. The most commercially successful apatite GCs are those developed for dental veneering. These materials exhibit excellent translucency and clinical esthetics and mimic the natural tooth mineral. Due to the ease of solid solution of the apatite lattice, rare earth doped apatite GCs are discussed for potential applications in optoelectronics and nuclear waste management. One of the drawbacks of the commercial apatite GCs used in orthopedics is the lack of resorbability; therefore, the review provides a direction for future research in the field.

Keywords: apatite, glass, glass-ceramic, biomaterial, fluorapatite, chlorapatite, nucleation and crystallization, orthopedic

OPEN ACCESS

Edited by:

Joachim Deubener,
Clausthal University of Technology,
Germany

Reviewed by:

Ana Candida Martins Rodrigues,
Federal University of São Carlos,
Brazil

Maziar Montazerian,
Federal University of São Carlos,
Brazil

*Correspondence:

Tomas Duminis
t.duminis@qmul.ac.uk

Specialty section:

This article was submitted to
Glass Science,
a section of the journal
Frontiers in Materials

Received: 18 June 2016

Accepted: 15 December 2016

Published: 09 January 2017

Citation:

Duminis T, Shahid S and Hill RG
(2017) Apatite Glass-Ceramics:
A Review.
Front. Mater. 3:59.
doi: 10.3389/fmats.2016.00059

INTRODUCTION

Apatite is named after the Greek word “*apát*” meaning deceit because, in appearance, apatite is often mistaken for a number other minerals. Apatite has a chemical formula $\text{Ca}_5(\text{PO}_4)_3(\text{F, Cl, OH})$. Due to an adaptive framework structure of apatite (White et al., 2005), its lattice can readily accommodate a number of ionic substitutions. Naturally occurring apatites are found in igneous, metamorphic, and sedimentary earth rocks and relatively recently, versions of fluor- and hydroxyapatite (HAp) were found on the surface of the Moon (McCubbin et al., 2010). Additionally, meteorites from the planet Mars, for example, Chassigny, which fell in provincial France in 1815, brought melt inclusions of Martian fluor- and chlorapatites (McCubbin and Nekvasil, 2008). Apatite is also the major inorganic component naturally found in the hard tissues of vertebrates; therefore, it has a profound biological and clinical significance.

Biological apatites have a chemical formula of $\text{Ca}_5(\text{PO}_4)_3(\text{OH})$, with some degree of CO_3^{2-} substitution for PO_4^{3-} , F^- for OH^- , and Na^+ or Mg^{2+} for Ca^{2+} ions. Synthetic HAp has been used in various forms of health care, such as for bone replacement, dental cements, and dental porcelains. However, sintered porous or even dense HAp bone implants often fail due to poor mechanical properties that are inferior to the mechanical properties of the human bone (Table 1). Moreover, sintered blocks of

TABLE 1 | Mechanical properties of the glass-ceramics for orthopedic applications.

Material	Phase	Density (g/cm ³)	Thermal expansion coefficient (×10 ⁻⁶ K ⁻¹)	Compressive strength (MPa)	Flexural strength (MPa)	Young's modulus (GPa)	Fracture toughness (MPa √m ²)	Reference
Cortical bone	Hydroxyapatite (HAp) + organic matrix	1.9	27.5 ± 3.9	133–295	35–283	7–20	5–7	An and Draughn (2000)
HA	HAp	3.16	10	120–150	60–120	35–120	0.8–1.2	Ranu (1987) Orlovskii et al. (2002)
A–W	Fluor/oxyapatite and wollastonite	3.07	8–10	1,080	215	118	2	Kokubo (2008)
Bioverit I	Apatite and fluorphlogopite	2.8	8–12	500	140–180	70–88	1.2–2.1	Höland and Beall (2012)
Bioverit II	Apatite and fluorphlogopite	2.5	8–12	450	90–140	70	1.2–1.8	Höland and Beall (2012)
Bioverit III	Fluorapatite (FAP) and aluminum phosphate	2.7–2.9	14–18	–	60–90	45	0.6	Höland and Beall (2012)
A–M	FAP and mullite	2.7–3.3	8–10	–	90–330	70–90	1.0–3.3	Ducheyne et al. (2011)

HAp require machining to shape to match the complex contours of the defect using expensive diamond tipped tools. A porous and bioactive 3D material may be highly desirable for bone regeneration because a porous material will allow osteoblasts to proliferate and integrate inside the 3D structure and enable vascularization of the newly formed bone, provided the porosity of the material is adequate. However, with the introduction of porosity into any bone substitute material or implant, mechanical properties are compromised as discussed by Karageorgiou and Kaplan (2005), rendering many of the porous bone substitute materials inappropriate for load-bearing applications.

Since the early 1970s, a number of melt-derived glass-ceramics have been developed that crystallize to apatite phases on controlled heat treatment. A glass-ceramic material can be cast into complex shapes by the “lost wax” casting route, which is usually a simple and cost-effective process. For illustration purposes, the reader is presented with an apatite–mullite glass-ceramic chess piece (**Figure 1**) produced by casting molten glass to shape by the “lost wax” method, which shows the complexity of shapes and surface detail that can be attained by this route. Machinable glass-ceramics (GCs), such as mica GCs discussed in this review can also be processed by computer-aided design/computer aided manufacturing (CAD/CAM).

Apatite-containing GCs are highly biocompatible and can induce bone formation *in vivo* (Ducheyne et al., 2011). Therefore, apatite-based GCs are highly attractive for medical and dental applications. A bioactive material is defined as a material that exhibits a biological response at the interface once in contact with a biological tissue. A bioactive material may induce a biological response through its surface topography or by a controlled release of therapeutic ions. A number of bioactive apatite-containing glass-ceramics have been developed for orthopedic applications, and these can be categorized based on the type of secondary crystal phases present in the GC; apatite–wollastonite (A–W), commercially known as Cerabone®; apatite–fluoromica (A–FM),

**FIGURE 1 | Apatite–mullite chess piece cast to shape by the lost wax method.**

commercially known as Bioverit®, and apatite–mullite (A–M). Several apatite-containing GCs have also been developed for restorative dentistry applications for the fabrication of dental inlays, crowns, bridges, and veneers. These are namely apatite–leucite (A–L), commercially known as IPS d.SIGN®, and with apatite as the only phase, for example IPS e.max ZirPress® and IPS e.max Ceram®.

Apatite is a good host crystal phase for rare earth elements and exhibits low phonon energies (particularly FAP); therefore, apatite-containing glass-ceramics have also been investigated for potential applications in optoelectronics. Apatite phases are also

particularly attractive in nuclear waste immobilization, such as for the immobilization of Cl and Sr isotopes, where these radioactive elements can be readily incorporated into the apatite lattice.

A review on the history and trends of the bioactive glass-ceramics, including those that do not contain apatite phases has been recently published (Montazerian and Zanotto, 2016). The scope of this article is to review the fundamentals of the structure–property relationship and crystallization mechanisms of the various apatite glass-ceramics used in health care as well as those for potential applications in optoelectronics and nuclear waste management.

PRIOR LIQUID–LIQUID PHASE SEPARATION (LLPS)—PRECURSOR TO NUCLEATION AND CRYSTAL GROWTH

Liquid–liquid phase separation, also known as amorphous phase separation (APS), can occur in undercooled liquids either at or below the glass *liquidus* temperature. If LLPS occurs above the glass *liquidus* temperature, then such phase separation is termed stable immiscibility. On the other hand, if LLPS occurs below the *liquidus* state, such LLPS is termed metastable immiscibility. Undercooled liquids can undergo phase separation through spinodal decomposition or *via* nucleation and growth processes (binodal decomposition) (Figure 2).

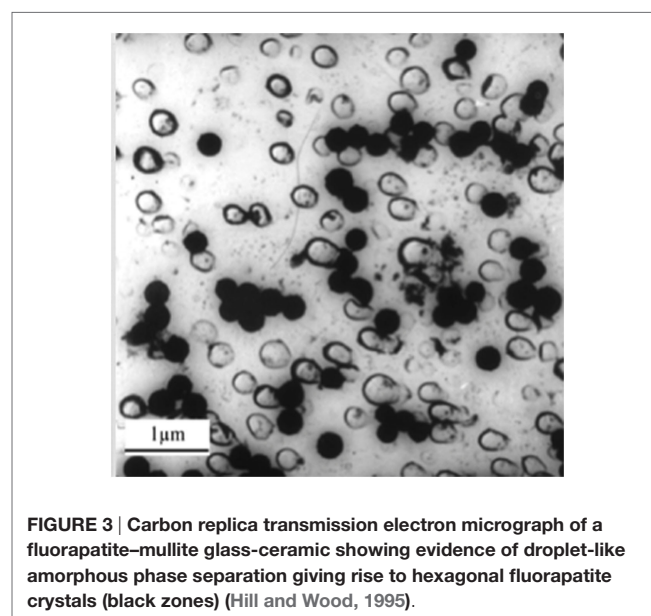
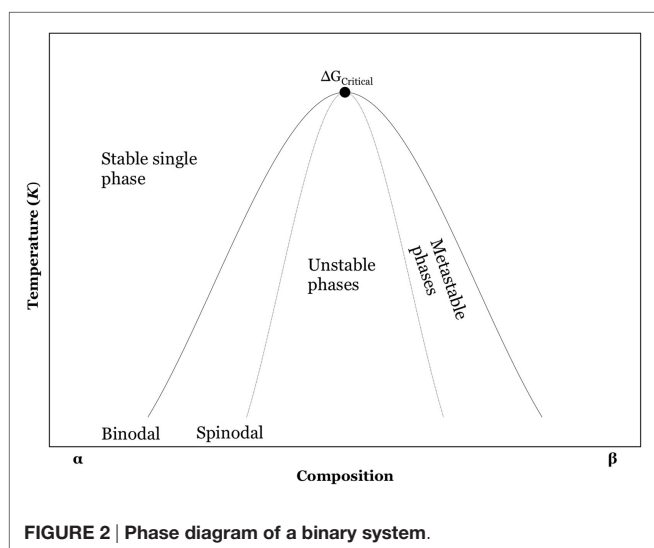
Spinodal decomposition is a diffusion driven mechanism with no activation energy barrier. A system that undergoes spinodal decomposition is always unstable. In contrast, phase separation by nucleation and growth (in the binodal region) has a large free energy barrier and it is a metastable process involving an activation energy. Small angle neutron scattering (SANS) techniques can be used to study LLPS in both spinodally and binodally decomposed glasses. SANS scattering at lower q values correspond to larger phases, which can be attributed to a phase separation under the binodal region of the phase diagram, whereas neutrons scattered at higher q values correspond to a finer scale phase separation,

which may be attributed to spinodally decomposed structures (Hill et al., 2007). Spinodal decomposition, unlike nucleation, generally results in sharp scattering maximum often referred to as a “spinodal ring” particularly during the early stages of phase separation. Spinodal decomposition is difficult to observe by microscopy techniques because of the diffuse interfaces between the phases. In contrast, nucleated amorphous phases can be readily observed by microscopy. Transmission electron microscopy (TEM) analysis shows (Hill and Wood, 1995) that LLPS *via* nucleation and growth results in sharp boundaries between the phases as observed in Figure 3.

Most of the glass-ceramics discussed in this review undergo a bulk nucleation and crystallization, which has been attributed to prior LLPS. Crystal nucleation may be aided by the composition of one of the phases being closer to the crystal phase than the parent glass composition. Figure 3 shows a droplet-like phase that is rich in calcium and phosphorus that crystallizes to fluorapatite (FAP) (Hill and Wood, 1995). However, the A–W GC exhibits surface crystallization of both phases without the occurrence of prior LLPS (Kokubo et al., 1982).

There are two main ideas of how prior LLPS can influence the subsequent crystallization. Vogel and Gerth (1962) proposed that the effect of prior LLPS on glass crystallization is due to the existence of interfaces in a phase-separated glass, which provide internal surfaces for heterogeneous nucleation. However, Cahn (1969) and James (1981) suggested that if the composition of the LLPS phase is close to the composition of the subsequent crystal phase, the activation energy is lowered and subsequent homogeneous crystallization is favored.

There are few studies on the importance of LLPS in regard to glass-ceramics, and it is worth briefly reviewing these studies. Ramsden and James (1984a,b) found that quenched BaO–SiO₂ glasses in which LLPS developed simultaneously with the nucleation of the crystals, the crystal nucleation rate increased with isothermal heat-treatment time. Ramsden and James (1984b)



reported that the same system without prior LLPS did not show any increases in crystal nucleation rates. Thus, Ramsden and James (1984a,b) and later Zanotto et al. (1986) concluded that the predominant effect on crystal nucleation arises from the compositional changes brought about by phase separation. Although it has been shown that LLPS has a profound role in the formation of simple glass-ceramics, its effect in complex multicomponent systems, such as those with strong nucleants should not be generalized.

Tomoizawa (1972) reported that lithium silicate glasses showed considerably increased crystal nucleation rates when the glass had undergone LLPS and proposed that the LLPS droplets consist of silica-depleted diffusion zones at their interfaces, therefore giving rise to sites for heterogeneous nucleation.

The mechanism by which LLPS enhances subsequent crystallization depends on the composition of the glass and the composition of the crystalline phase. Apatite GC systems developed by Hill et al. (2004) bulk nucleate *via* prior amorphous separation, but can also crystallize through a surface mechanism. In simple glasses such as the lithium silicate glasses, LLPS enhances nucleation rate, by reducing the activation energy for nucleation. Although LLPS can enhance subsequent crystallization of a glass, based on the classical nucleation theory, the LLPS droplet diameter (D) should be larger than the critical radius (r^*) for crystal nucleation in order for nucleation to take place within the droplet phase. Therefore, fine scale LLPS can potentially suppress nucleation and subsequent crystallization.

In a study by Clifford et al. (2001a), it was found that base glasses in the A–M systems with a molar Ca to P ratio of 1.67 (glasses with an apatite stoichiometry) crystallize through an internal or bulk mechanism, and that base glasses with Ca to P ratios higher or lower than 1.67 crystallize through a surface mechanism. Interestingly, Clifford et al. (2001a) note that compositions with a molar Ca to P ratio above or below 1.67 can crystallize in bulk following an annealing hold for 1 h just above the glass transition temperature. Clifford et al. (2001a) study provides evidence that LLPS in the apatite–mullite system can be produced below the *liquidus* by nucleation and growth.

Rafferty et al. (2000b, 2003) used high temperature dynamic mechanical thermal analysis (DMTA) to show the presence of two mechanical loss peaks ($\tan \delta$) and two reductions in the storage modulus (E') corresponding to two glass transition temperatures (Figure 4) for many of the A–M glass compositions providing evidence of an LLPS. On crystallization of FAp, only one glass transition temperature (T_g) was observed indicating that one of the two amorphous phases had crystallized to FAp.

Crystals or LLPS droplets in an undercooled liquid can undergo Ostwald ripening (OR) during a heat treatment. During an OR process, crystals or LLPS droplets can grow and produce larger LLPS droplets or crystals. Thermodynamically, OR is a favorable process because larger particles exhibit lower surface energy in contrast to smaller particles. Apatite crystal growth through OR process is observed in apatite glass-ceramics, such as reported by Höland et al. (2015). One of the key characteristics of an OR process is the reduction in the number of droplets/crystals and an increase in volume as a function of time, pressure or temperature.

Fluorapatite is part of the hexagonal group of crystals; therefore, it exhibits a kinetically favored growth in the crystallographic *c*-direction, which is seen in Höland et al. (2015)'s findings, whereby crystal length as a function of time due to OR process was more pronounced as opposed to crystal expansion at crystallographic *a*-direction. OR process can be used to produce a highly homogenous and mechanically superior microstructure of a GC.

BIOMEDICAL APPLICATIONS OF APATITE GLASS-CERAMICS

Orthopedics

Fluor/Oxyapatite–Wollastonite Glass-Ceramics

Kokubo et al. (1982) developed apatite–wollastonite (A–W) (β -CaSiO₃) system based on SiO₂–P₂O₅–CaO–MgO–CaF₂, also known by its commercial name Cerabone®. The β -wollastonite phase in the A–W system enhances mechanical performance of the glass-ceramic (Table 1). Kokubo et al. (1987) reported on the A–W GC ability to resist failure by fatigue. It was estimated that the life-time of an A–W GC, under a constant loading of 65 MPa in simulated body fluid is 10 years, compared to a sintered HAp, which under the same loading can sustain the loading before fracture for only 1 min. Both, apatite and β -wollastonite phases in the A–W system crystallize through a surface mechanism (Kokubo et al., 1982). As such, the A–W GC cannot be cast to shape by the “lost wax” technique and is processed through powder sintering route.

It was often claimed that the apatite phase in the A–W systems is FAp; however, Clifford and Hill (1996) noted that the A–W glasses are very deficient in fluorine content with regard to the FAp stoichiometry. Clifford and Hill (1996) further suggested that the apatite formed in A–W systems is therefore more likely to be a mixture of fluor- and oxyapatite. Based on the pioneering electron spin resonance (ESP) studies on fluor/oxyapatites, it has been long known that O²⁻ can occupy F⁻ sites (Segall et al., 1962; Piper et al., 1965). Nonetheless, at present, the availability of high-resolution solid-state characterization techniques such as ¹⁷O MAS-NMR coupled with dynamic nuclear polarization (DNP) and high field ¹⁹F MAS-NMR could provide fast and accurate elucidation of oxygen and fluorine environments in the A–W GC; however, such work is yet to be published.

Calver et al. (2004) reported that modified Kokubo et al. (1982) A–W glass with higher metal fluoride content (AW3, Table 2) resulted in a completely changed apatite crystallization behavior. Calver et al. (2004) found that a base glass with the highest CaF₂ content favored volume FAp nucleation and crystallization. Calver et al. (2004) also found that A–W systems showed reduced T_g and FAp crystallization exotherms with increasing calcium fluoride content. Therefore, low calcium fluoride content in the original A–W system is actually suppressing crystallization of FAp. Filho et al. (1996) suggest that fully crystallized GCs, which are otherwise bioactive, will not exhibit any further bioactivity through the release of ions, such as Ca²⁺ and HPO₄²⁻, once such ions take up higher energy coordination states in the apatite lattice. Therefore, from a bioactivity point of view, it may not always be

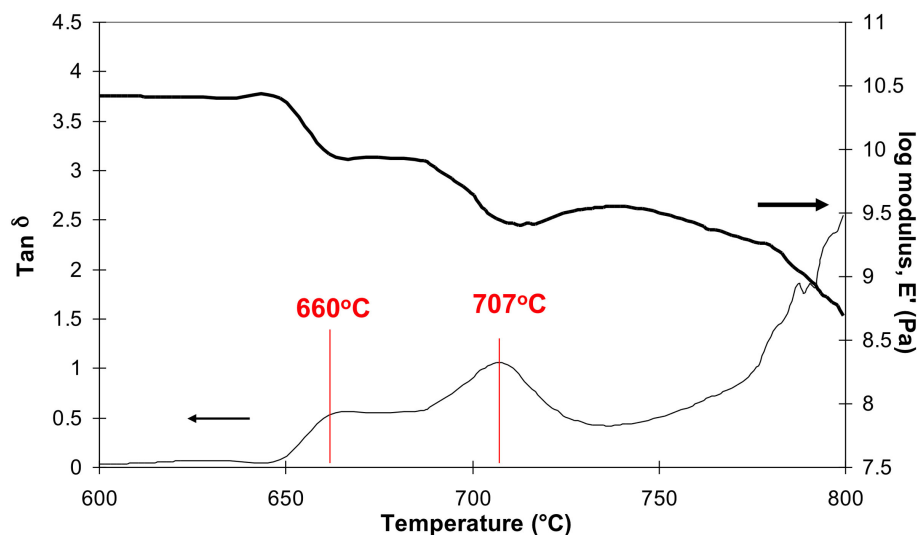


FIGURE 4 | Dynamic mechanical testing analysis (DMTA) of an A-M glass-ceramic showing two glass transitions, one at 660°C and second at 707°C and two decreases in modulus after Rafferty et al. (2000b) collected at a 5°C/min heating rate in a single frequency mode at 1 Hz.

TABLE 2 | A-W base glass compositions in mol% (Calver et al., 2004).

	SiO ₂	P ₂ O ₅	MgO	CaO	CaF ₂
AW1	35.46	7.15	7.11	50.28	0
AW2	35.46	7.15	7.11	49.88	0.4
AW3	35.46	7.15	7.11	45.51	4.77

desirable to consume therapeutic ions for the formation of apatite within the glass matrix, as opposed to the release of such ions and subsequent formation of apatite on the surfaces of the material, that potentially lead to the formation of a strong and chemically stable implant–bone interface. Furthermore, the molar Ca to P ratio in a stoichiometric apatite crystal is 10 to 6 (1.67); therefore, GC systems containing a stoichiometric Ca to P ratio, or in other words, glass formulations with smaller compositional differences between the glass and the crystal phase preferentially crystallize in bulk, which is unfortunately not the case in the A–W system. On the other hand, the A–W system is inherently aluminum free; thus, risks associated with aluminum neurotoxicity, summarized by Kumar and Gill (2009) and reported by Reusche et al. (2001), are completely absent.

It could be argued as to why the original A–W system developed by Kokubo et al. (1982) contains magnesium and a non-stoichiometric Ca:P:F ratio that could otherwise aid bulk nucleation and crystallization of apatite phases. There is a considerable and long-standing proof, for example, as found by X-ray diffraction analyses of precipitated apatites by LeGeros et al. (1980), which demonstrates that the presence of Mg²⁺ ions in an aqueous solution cause a strain on the apatite structure causing it to collapse and, therefore, suppress its growth. In view of the biological apatite found in bone as opposed to tooth, Mg²⁺ ions alongside osteocalcin and proteoglycan proteins play a significant role in the development of a nanoscale apatite (Blumenthal et al., 1975),

providing the bone tissue with a fine microstructure and the excellent properties that come with it. Therefore, on that basis, it could be argued that the A–W system is highly biomimetic in view of the elemental composition of the human bone.

In vivo animal studies on the implanted A–W glass-ceramic provide evidence for excellent osseointegration around the A–W implant and a chemical calcium phosphate-based interface (Kitsugi et al., 1989, 1990) between the implant and bone, with high bending and compressive strengths of 157 and 1060 MPa, respectively (Nakamura et al., 1985). Kokubo et al. (1990) found that A–W GC immersed in tris(hydroxymethyl)aminomethane (TRIS) buffer did not show bioactivity through the formation of apatite and these findings were contradictory to animal studies conducted previously, where the A–W GC was found to form a strong chemical interface with the living bone. Therefore, Kokubo et al. (1990) developed a simulated body fluid (SBF), an alternative immersion medium for *in vitro* assessment of bioactivity of the A–W GC. Kokubo et al. (1990) argued that TRIS buffer does not mimic the actual body environment because it is completely deficient in ions, such as Ca²⁺ and HPO₄^{2−} naturally found in the bodily fluids and, therefore, argued that the lack of apatite formation in TRIS buffer, as opposed to high bioactivity of the A–W GC in SBF, also supports the view that the apatite phase on the surfaces of the A–W GC forms by a chemical reaction between the A–W GC and the ions present in the body fluid. In view of this, it can be further postulated that apatite crystals within the A–W GC act as nuclei on which ions, such as Ca²⁺ and PO₄^{3−} in the solution nucleate and feed apatite formation until the eventual fusion between the apatite crystals in the A–W and the apatite in the living bone, whereby a chemical interface is formed.

Kokubo et al. (1992) reported that if aluminum is included in the A–W parent glass composition and then subsequently crystallized, the A–W GC does not show any bioactivity in SBF

as opposed to the same A–W material without aluminum. The addition of aluminum results in a more chemically stable residual glass phase, which reduces the release of Ca^{2+} and PO_4^{3-} ions, thereby affecting apatite formation (Strnad, 1992). Later, Blades et al. (1998) conducted *in vivo* animal study on aluminum-containing glass ionomer cements (GICs) as potential bone cements, where as low as 1 ppm of aluminum released was found to inhibit mineralization of the newly formed osteoid in rabbit bone. It is important to distinguish that the role of aluminum in Blades et al. (1998) study may be attributed to aluminum toxicity to bone-forming cells (Rodriguez et al., 1990) and direct inhibition of crystal growth as opposed to reduced bioactivity involving structural parameters of the residual glass phase, as proposed in Strnad (1992) study.

Good oseointegration through the formation of apatite on the implant surfaces (Neo et al., 1993) combined with good mechanical properties (Kokubo et al., 1985, 1986) perhaps explains why the A–W glass-ceramic has found promising applications in bone and vertebra replacement (Kokubo, 2008) and it is reported that over 50,000 successful bone implants have been made using the A–W glass-ceramic system (Zanotto, 2010). However, from a manufacturing point of view, a bulk crystallizing A–W material, such as proposed by Calver et al. (2004), could provide a more cost-effective material. *In vitro* and *in vivo* bioactivity of the modified A–W system developed by Calver et al. (2004) still needs to be established. The original A–W GC is currently manufactured by Nippon Electric Glass Co., Ltd. (Japan) (Montazerian and Zanotto, 2016).

Fluorapatite–Mica Glass-Ceramics

Grossman (1972) of Corning Glass Works, developed the first machinable mica glass-ceramic system, later marketed by Dentsply International under the name Dicor®. Dicor® was seen as a very significant development since the new GC material could be easily machined to shape without a critical failure. Machinability of the mica glass-ceramics is attributed to the eminent cleavage of the mica-type crystals as a result of anisotropic crystal growth. This facilitates crack propagation in the direction of cutting without causing a critical failure of the material.

Although mica glass-ceramics initially did not contain any apatite phases, Vogel et al. (1986) developed two GC systems (Table 3) with FAp and tri/tetrasilic Mg₃(AlSi₃O₁₀F₂)Na/K/Mg₃(Si₄O₁₀F₂)Na/K mica phases and an additional silica-free GC with apatite and aluminum phosphate phases.

Commercially available Bioverit I® and Bioverit II® systems crystallize to FAp and mica phases in bulk. Bioverit II® GC crystallizes to a smaller fraction of FAp, which can be explained by the very low P₂O₅ content in the composition (Table 3). Both systems have undergone prior APS into two droplet phases and a glassy matrix phase (Höland and Beall, 2012). One droplet phase is rich in apatite elements whereas the second droplet phase is closer to the mica composition. This may explain why both phases, apatite and mica, crystallize in bulk. Bioverit III is a silica-free phosphate glass that crystallizes to FAp and an aluminum phosphate (AlPO₄) (Höland and Beall, 2012); Bioverit III material exhibits lower mechanical properties (Höland and Beall, 2012); therefore, it has not been so extensively studied.

TABLE 3 | Examples of Bioverit® base glass composition in mol% (Höland and Vogel, 2013).

	Bioverit I	Bioverit II
SiO ₂	29.44	44.12
Al ₂ O ₃	9.04	17.47
P ₂ O ₅	4.66	0.08
CaO	14.89	0.21
MgO	21.29	17.44
Na ₂ O	2.15	4.23
K ₂ O	3.57	3.10
TiO ₂	–	–
F	14.96	13.17
Cl	–	0.17

Bioverit II contains a higher fraction of mica crystals. Therefore, Bioverit II GC exhibits better machinability but at the expense of lower mechanical properties than Bioverit I (Table 1). Based on ¹⁹F MAS-NMR experiments of mica ceramics, it was demonstrated that the fluoride ion in mica systems exists mainly in Mg(n)-F type environments, with a chemical shift at about –174 ppm for Mg(3)-F (Fechtelkord et al., 2003). As of 2016, A–FM GCs, Bioverit I and II are currently manufactured by VITRON Spezialwerkstoffe GmbH (Germany).

Fluorapatite–Mullite Glass–Ceramics

Mullite is a rare naturally occurring aluminosilicate mineral. Mullite-reinforced matrices exhibit enhanced mechanical properties. FAp phases can act as nucleation and crystal growth sites for new apatite phases between the implant and living bone. Both crystal phases in the fluorapatite–mullite system show elongated needle-like microstructure and exceptional mechanical properties, particularly flexural strength and fracture toughness of up to 330 MPa and 3.3 MPa $\sqrt{\text{m}^2}$, respectively (Table 1). The A–M GC exhibits spherulitic crystallization, which enhances fracture toughness properties of the material (Stanton et al., 2010). The system nucleates in bulk; therefore, it is readily castable by the “lost wax” route.

The first melt-derived castable FAp (Ca₅(PO₄)₃F)—mullite (Al₆Si₂O₁₃) glass-ceramics were developed by Hill et al. (1991) and were based on the SiO₂–Al₂O₃–P₂O₅–CaO–CaF₂ system. Additionally, Samuneva et al. (1998) were also able to produce an A–M glass-ceramic by a sol–gel route, rather than a melt-quench route.

Hill et al. (1991) noted that base glasses with relatively low CaF₂ content (A–C, Table 4) surface crystallized to apatite and mullite phases upon heat treatment, whereas base glasses with metal fluoride content (D and E, Table 4) bulk crystallized to anorthite with only a small fraction of FAp. The work by Hill et al. (1991) and also subsequent work by Hill and Wood (1995); Clifford and Hill (1996); Hill et al. (2000); Rafferty et al. (2000a); Clifford et al. (2001a,b), and later by Stanton and Hill (2005) suggests that metal fluoride as well as phosphorus content in fluoro-phospho-aluminate systems will likely influence prior LLPS and will therefore determine whether the glass crystallizes *via* the homogenous bulk route (aided by the LLPS composition) or the heterogeneous surface route.

Stanton and Hill (2005) postulated that once crystallization of FAp crystal has begun, the surrounding glass becomes depleted in F, Ca, and P and moves closer to the mullite composition, whereupon, it crystallizes to mullite by the homogenous mechanism. Stamboulis et al. (2004) explained crystallization of FAp and mullite phases in the A–M system in even greater detail by analyzing heat-treated A–M samples with magic angle spinning-nuclear magnetic resonance (MAS-NMR) spectroscopy. Spectra from ^{27}Al MAS-NMR in **Figure 5** (left) show how aluminum resonance is relatively unchanged until the GC reaches second crystallization temperature (T_{p2}) whereupon it crystallizes to mullite. It can be observed from **Figure 5** (left) that a broad peak seen at around 50 ppm, assigned to Al(IV), remains unchanged even after FAp crystallization (T_{p1}). During second phase crystallization, an additional peak, at around 12 ppm, which is assigned to an Al(VI) in mullite is observed. Stamboulis et al. (2004) further explain that, during first and second crystallization processes, charge balancing cations for maintaining aluminum in a fourfold coordination state, Al(IV) are consumed during FAp formation; therefore, at higher temperatures, the lack of charge balancing cations to keep aluminum in a IV coordination state forces aluminum to take up higher coordination states, in this case, Al(VI). ^{19}F MAS-NMR spectra as shown in **Figure 5** (right) show how the fluorine environment changes with increasing heat-treatment temperature. The lowermost ^{19}F spectrum of the untreated LG120 glass in **Figure 5** (right) demonstrates two broad peaks at -90 and -150 ppm that can be attributed to the amorphous fluorine environments in the untreated glass, F–M(n) and Al–F–M(n)

(Zeng and Stebbins, 2000). However, at T_{p1} , a sharp peak at around -103 ppm develops at the expense of F–Ca(n) peak, which is assigned to fluorine in a F–Ca(3) environment in FAp. At higher temperatures, such as T_{p2} , fluorine from Al–F–M(n) peak is also fully consumed and Stamboulis et al. (2004) further proposed that F–M(n) such as F–Ca(n) species preferentially charge balance the non-bridging oxygens in the phosphorus locality. It can be additionally postulated that such preference to balance the non-bridging oxygens in the phosphorus locality reduces kinetic energy barrier to FAp nucleation and crystal growth, since the local environment of Ca, P, and F in the glass is similar to that present in FAp.

Relatively recently, Stamboulis et al. (2006), Hill et al. (2007), and O'Donnell et al. (2010) conducted real-time SANS and neutron diffraction (ND) experiments on the A–M systems developed in the early 1990s. They postulated that amorphous glasses that form the A–M system may have undergone phase separation by spinodal decomposition during the casting process on a scale of 25–27 nm (Hill et al., 2007). Similarly, the same cast A–M system isothermally heat treated at 740°C and 750°C initially showed neutron scattering at higher q , which then moved to lower q with increasing temperatures where the scale of the LLPS corresponded to about 35 nm. This provides evidence that undercooled liquids can undergo LLPS by nucleation and growth, whereupon the chemical system can overcome the thermodynamic and kinetic energy barriers to nucleation and subsequent amorphous phase growth. It is suggested by Hill et al. (2007) that the A–M cast glass is initially phase-separated by spinodal decomposition, whereby rapid cooling creates a barrier to nucleation and growth. However, it may be argued that scattering at lower q in the as-cast glasses may be attributed to a finer LLPS by nucleation and growth. SANS experiments by Hill and coworkers provide evidence that finer scale phase separation in the apatite–mullite system increases in size as a function of temperature, which can be either attributed to the fact that the cast A–M system is initially spinodally decomposed and then undergoes LLPS by

TABLE 4 | A–M base glass compositions in mol% (Hill et al., 1991).

	SiO_2	Al_2O_3	P_2O_5	CaO	CaF_2
A	37.50	25.00	12.50	25.00	0.00
B	35.29	23.53	11.76	23.53	5.88
C	33.33	22.22	11.11	22.22	11.11
D	31.58	21.05	10.53	21.05	15.79
E	30.00	20.00	10.00	20.00	20.00

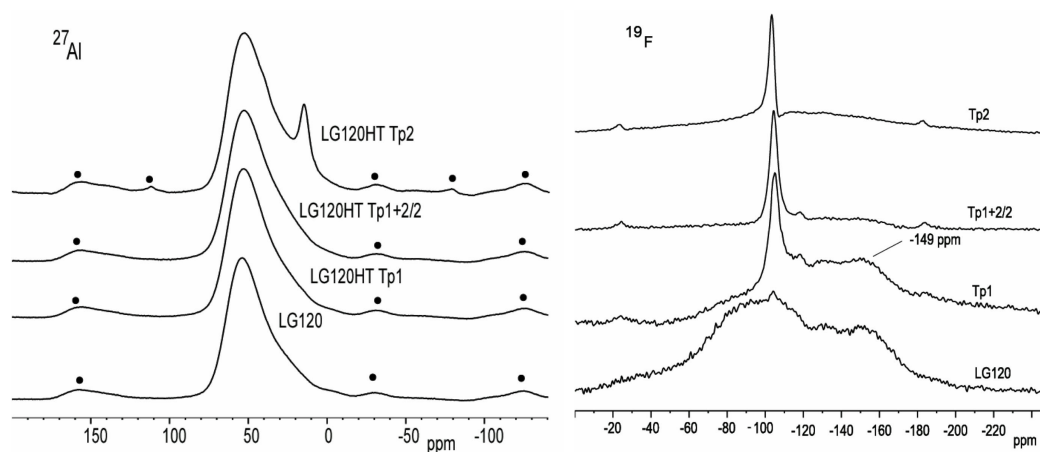


FIGURE 5 | ^{27}Al (left) and ^{19}F (right) MAS-NMR spectra of LG120 heat treated at different temperatures (Stamboulis et al., 2004).

nucleation and growth or more likely LLPS growth by an OR mechanism.

Further studies of an A–M glass-ceramic analyzed by heat treating an amorphous precursor glass up to 1,200°C with *in situ* TOF-ND (O'Donnell et al., 2010) explain the crystallization behavior of the A–M system in more detail. O'Donnell et al. (2010) reported that FAp and mullite crystallized on heating until 1,130°C followed by the partial dissolution of both phases at higher temperatures. It was also found that on the subsequent cooling of the A–M system, recrystallization occurred and additional new phases were produced, namely berlinite (AlPO₄) and cristobalite (SiO₂), which formed at around 1,025°C in addition to the FAp and mullite. This indicates that the subsequent cooling of the GC can produce additional crystal phases, which may be undesirable but can be avoided by introducing higher cooling rates to create an energy barrier to nucleation and growth of the undesirable crystal phases.

Stanton and Hill (2005) found that apatite phases in the A–M system grow as dendrites and spherulites. Generally, the microstructure of a GC is strongly influenced by the conditions of the heat-treatment of the parent glass, this namely includes duration, temperature, and cooling rate and whether or not the base glass compositions is doped with additional nucleants, for example, such as reported with niobium-doped FAp GCs by Denry et al. (2012). Mechanical properties, particularly fracture toughness of the A–M GC developed by Hill and coworkers, surpass mechanical properties of the alternative glass-ceramic systems discussed in this review.

In vivo animal studies conducted by Freeman et al. (2003) show that a fully crystallized A–M glass-ceramic osseointegrates with bone as shown in **Figure 6B**; however, its amorphous precursor base glass implant does not osseointegrate, which is evident from the fibrous tissue around the glass implant as shown in **Figure 6A** and the lack of implant/bone interfaces. Goodridge et al. (2007) report on both, *in vitro* and *in vivo* properties of the porous A–M glass ceramic system produced through selective laser sintering (SLS) method, using cast A–M and commercial A–W glass-ceramics as positive controls. In the 4 weeks study, Goodridge et al. (2007) reports that no sign of inflammation or adverse tissue reaction was observed around all the implants. Analyses of the implant–bone interfaces by scanning electron microscopy (SEM) showed evidence for bone ingrowth into the both porous materials, the A–M system produced through SLS method and the A–W sintered glass-ceramic. Although Goodridge et al. (2007) report that the laser sintered apatite–mullite system developed by Hill et al. (1991) does not form apatite in SBF, previous studies indicate that SBF studies are not adequate in the assessment of bioactivity of aluminum-containing GCs (Strnad, 1992).

Stanton et al. (2009) assessed the interfacial chemistry between the A–M system and a titanium alloy, for potential applications of the A–M system for orthopedic implant coatings. Stanton et al. (2009) enameled the A–M glass-ceramic to titanium by heat treatment and thereafter analyzed the interfacial reaction zone between the A–M glass-ceramic and the titanium alloy by high-angle annular dark field TEM (HAADF-TEM). Stanton et al. (2009) found that titanium diffused into the intermediate layer of the glass-ceramic and postulated that complex titanium silicides

and titanium phosphides were formed based on the elemental analysis of the interfacial zones by energy dispersive X-rays (EDX), which produced characteristic photons for Ti, Si, and P elements, but not O elements. This study provides evidence that the A–M system can chemically adhere to titanium. This can be useful in overcoming the problem of coating detachment observed with micromechanical surface retention of plasma sprayed HAp coatings (Filiaggi et al., 1991). The A–M glass-ceramic coating may enhance osseointegration at the bone–implant interface and provide long-term stability of the A–M coated implants.

Wood and Hill (1991) produced cements from the A–M glass-ceramic ionomer-type systems with varying degrees of crystallinity for potential application as bone cements. Wood and Hill (1991) found that the degree of crystallinity of the A–M glass-ceramic can influence the properties of the cements, such as working and setting times of the cement pastes and the mechanical properties of the set cements.

Strontium-Substituted FAp Glass-Ceramics

Hill et al. (2004) developed strontium-substituted FAp glass-ceramics for potential orthopedic applications, in the system SiO₂–Al₂O₃–P₂O₅–CaO/SrO–CaF₂/SrF₂ (**Table 5**). Since strontium has a higher atomic number than calcium, strontium-substituted materials exhibit higher radiopacity, which enables the clinician to distinguish between the implant and bone on a radiograph.

Hill et al. (2004) observed that substituting strontium for calcium has little effect on the parent glass structure. However, the crystallization behavior of the glasses as a function of strontium content was markedly altered. Base glasses without any strontium exhibited complete bulk crystallization with the first crystallization temperature being independent of the particle size, whereas

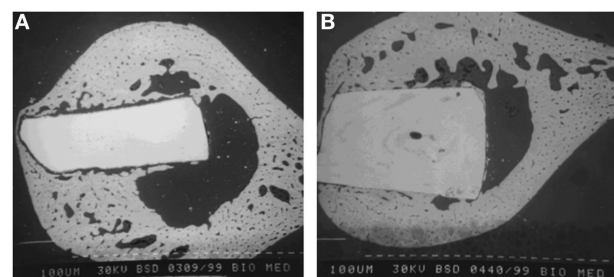


FIGURE 6 | Backscattered scanning electron micrographs of implanted LG120 base glass (A) and implanted LG120 glass-ceramic following subsequent crystallization to fluorapatite and mullite phases (B) (Freeman et al., 2003).

TABLE 5 | Strontium-substituted fluorapatite base glass compositions in mol% (Hill et al., 2004).

Glass code	SiO ₂	Al ₂ O ₃	P ₂ O ₅	CaO	CaF ₂	SrO	SrF ₂
LG26	32.14	21.43	10.71	21.43	14.29	0.00	0.00
LG119	32.14	21.43	10.71	10.71	14.29	10.71	0.00
LG125	32.14	21.43	10.71	0.00	14.29	21.43	0.00
LG26Sr	32.14	21.43	10.71	0.00	0.00	21.43	14.29

glasses with strontium and no calcium exhibited predominantly surface nucleation. Glasses with equimolar proportions of calcium and strontium crystallized through bulk and surface. Hill et al. (2004) demonstrate that increasing strontium substitution hinders bulk crystallization of apatite, which is reflected in an increase in crystallization temperature, and promotion of surface nucleation of apatite at the expense of bulk nucleation, as evidenced by particle size dependence on the crystallization temperature of the FAp phases. Hill et al. (2004) also observed that equimolar strontium–calcium composition resulted in a glass with a reduced second exotherm associated with mullite crystallization. This can be attributed to an increased mobility of the glass network and a lower glass transition temperature, which produces a more dominant heterogeneous crystallization effect. Such a reduction in crystallization temperature would suggest a new crystalline phase, and not simply a reduction in crystallization temperature Hill et al. (2004).

In another study, Hill et al. (2006) elucidated Ca and Sr sites in mixed FAp through ^{19}F MAS-NMR. Results showed the F to be present as F–Ca(3) in the all calcium glass and as F–Sr(3) in the all strontium glass. In the mixed glasses, fluorine was present as mixed sites: F–Ca(3), F–Ca(2)Sr, F–CaSr(2), and F–Sr(3). Ca had a higher tendency to occupy the F–M(3) sites than Sr, which may reflect the higher charge to size ratio of Ca^{2+} relative to Sr^{2+} and its greater affinity for F^- ions.

An *in vivo* animal study by Sabareeswaran et al. (2013) on a glass-ceramic that surface crystallized to a strontium FAp phase and a Sr-celsian phase (feldspar) as identified by XRD was found to be highly osteoconductive and biocompatible. X-ray microtomography (XMT) analyses of the synthetic–organic interfaces showed highly mineralized newly formed bone adjacent to the synthetic implant surface.

It is known that, at low concentrations, strontium can promote mineralization of bone (Verberckmoes et al., 2003). It is also known that strontium-containing bio-glasses show increased osteoblast proliferation and alkaline phosphatase activity (Gentleman et al., 2010). Therefore, it would be desirable to establish ion release (particularly Sr^{2+}) profile for the strontium FAp GC systems developed by Hill et al. (2004).

FAp and Chlorapatite Glass-Ceramics

Recently, Chen et al. (2014a,b) developed novel alkali-free FAp and chlorapatite (ClAp) glass-ceramics from bioactive glasses. Chen et al. (2014a) produced a series of bioactive glasses of varying metal fluoride content and found that bioactive glasses with high fluoride content crystallized to FAp and crystalline CaF_2 and SrF_2 on quenching. This demonstrates that metal fluoride content can determine crystallization window (T_x) between the glass transition (T_g) and the crystallization onset (T_{onset}). It is desirable to obtain initially amorphous base glass so that the crystallization of, say a FAp phase, can be controlled. Chen et al. (2014a) also found that the amorphous base glass powder without any fluoride content crystallized to a wollastonite phase through a surface mechanism. Additionally, all fluoride-containing glasses bulk crystallized to FAp *via* a homogenous nucleation mechanism.

Chen et al. (2014c) were able to develop novel bioactive chlorapatite, ClAp glass-ceramics in the system of

$\text{SiO}_2\text{--P}_2\text{O}_5\text{--CaO--CaCl}_2$. It is known that ClAp completely converts to HAp in the presence of water (Elliott and Young, 1967), hence making ClAp glass-ceramics attractive for both, medical, and dental applications. Chen et al. (2014c) emphasize that ClAp is less stable than FAp. This is attributed to the chloride ion being larger than hydroxyl or fluoride ion. The fluoride ion is small enough to fit in the center of the Ca(II) triangle in the FAp lattice, whereas larger ions such as hydroxyl and chloride do not fit in the center of the Ca(II) triangle but are rather displaced above the plane of the Ca(II) triangle. The chloride ion is larger than hydroxyl ion, and therefore, it is displaced further away from the Ca(II) triangle. This intrinsic apatite lattice instability brought about by the chloride ion allows the rapid exchange for a smaller ion, such as a hydroxyl ion. On increasing the fluoride or chloride content in the bioactive glass systems, Chen et al. (2014b,c) found that there was an increasing tendency of the glasses to crystallize. The halogen-free glass surface crystallized to a pseudowollastonite ($\alpha\text{-CaSiO}_3$) and an apatite, presumably an oxyapatite. Pseudowollastonite induces apatite formation in SBF (Siriphannon et al., 2000) and is highly resorbable *in vivo* (De Aza et al., 2000). ClAp phases in the Chen et al. (2014b) crystallized *via* the homogenous route, which from a material processing point of view is highly desirable. FAp is largely insoluble *in vivo* so ClAp GCs offer the potential for producing highly resorbable GC implants. Nonetheless, there is a need for further characterization of these ClAp GCs, including characterization of the *in vivo* activity and the relationships between the composition, heat-treatment, microstructure, and mechanical properties.

Dentistry

FAp–Leucite Glass-Ceramics

Höland et al. (1994) developed FAp-leucite (KAlSi_2O_6) (A–L) glass-ceramics in the $\text{SiO}_2\text{--Al}_2\text{O}_3\text{--Na}_2\text{O--K}_2\text{O--P}_2\text{O}_5\text{--F}$ system, for potential application in restorative dentistry. Research led by Höland led to the development of the commercial A–L glass-ceramic IPS d.SIGN (Ivoclar Vivadent, Liechtenstein). Needle-like apatite phase in the A–L system crystallized through a homogenous crystallization mechanism, which is a likely indication of prior LLPS. Additionally, upon DSC analyses of the A–L system, Höland et al. (2000) observed a unique phenomenon; the A–L system exhibits two endothermic reactions, first at 565°C and second endothermic reaction at 634°C. Previously, the two endothermic reactions were assigned to a phase transformation into two amorphous phases; one glassy, silica-rich phase and a droplet-like phase rich in Ca and P elements. Höland et al. (2000) suggests that the second endothermic reaction at 634°C is a transformation to a crystal phase, namely a sodium–calcium orthophosphate (NaCaPO_4), which was confirmed by XRD analysis. Furthermore, Höland et al. (2000) observed another interesting phenomena; at higher temperatures (640°C), NaCaPO_4 crystals dissolved and recrystallized to a new crystal phase. However, this new crystal phase could not be matched to any known phases when checked against the International Center of Diffraction Data (ICDD) database. Additionally, Höland et al. (2000) found that once the new phase is formed, apatite crystallization proceeds at 700°C. Heat treatment of the A–L system at 700°C for 8 h does not result in a material with needle-like

microstructure; it requires additional heat treatment at 1,050°C for 2 h for the development of needle-like FAp crystals (Höland et al., 2000). This demonstrates that the thermal treatment of the base glass can strongly influence both, the appearance and other properties of the GC material.

Höland et al. (2000) suggest that the morphology of the needle-like apatite is comparable to that of the apatite in natural teeth; therefore, such needle-like FAp morphology imparts the GC restoration with exceptional esthetics. The A–L glass-ceramic exhibits good chemical durability, solubility of the GC being only at 60–70 $\mu\text{g}/\text{cm}^2$. Translucency of the A–L system varies between 5.8 and 10.4%, depending on the mode of processing. The A–L shows thermal expansion of $14.1\text{--}14.8 \times 10^{-6} \text{ K}^{-1}$, which is close to that of titanium; therefore, the A–L glass-ceramic is highly suitable for direct sintering on metal abutments. Since 1998, there have been more than 60 million dental restorations performed using commercial IPS d.SIGN® A–L glass-ceramic (Höland and Rheinberger, 2008), making it the most commercially successful apatite glass-ceramic developed to date.

Strontium-Substituted A–L Glass-Ceramics

Höland et al. (2015) developed radiopaque strontium FAp (Sr–FAp) containing glass-ceramics (Table 6) for dental applications where Sr–FAp phase crystallized through homogenous mechanisms. Höland et al. (2015) were also able to obtain secondary and tertiary crystal phases, in addition to Sr–FAp, including leucite (KAlSi_2O_6), rubidium leucite (RbSi_2O_6), cesium pollucite ($\text{CsAl}_2\text{Si}_2\text{O}_6$), and sodium strontium orthophosphate (NaSrPO_4). However, both leucite phases and pollucite phases showed surface crystallization. Höland et al. (2015) found that some of the base glasses that were rapidly quenched into water (to prevent crystallization) did not avoid crystallization completely. Based on XRD analyses of all parent glasses, Höland et al. (2015) found that all glasses, except reference glass No. 5, were nanocrystalline. XRD analyses of the base glasses No. 1 and No. 2 showed the presence of nanoscale $\text{Sr}_5(\text{PO}_4)_3\text{F}$, whereas base glasses No. 3 and 4 contained nanocrystalline phases of NaSrPO_4 . Höland et al. (2015) also report that only two of the “as-quenched” base glasses were optically clear, namely, No. 1 and 5, as opposed to base glasses No. 2, 3, and 4, which were opalescent in the visible light. Höland et al. (2015) showed that Sr–FAp glass-ceramics are radiopaque; therefore, these dental GCs may become more clinically relevant once commercialized.

NANOSCALE APATITE GLASS-CERAMICS AND OPTOELECTRONICS

Glass-ceramics containing nanoscale phases of crystals are produced by carefully controlling heat treatments of the parent glasses, in which the nucleation rate is enhanced and the crystal growth rate is low. Crystal growth rates can be suppressed by keeping the crystal growth temperature close to T_g . The T_g of the residual glass phase increases as crystallization occurs. Crystallization of fluorine containing phases, such as FAp is particularly attractive here since a reduction in fluorine content in the residual glass phase results in a large increase

TABLE 6 | Strontium fluorapatite base glass compositions in mol% (Höland et al., 2015).

Glass code	1	2	3	4	5
SiO_2	58.7	59.4	60.4	61.1	66
Al_2O_3	9	9.1	9	9.1	8.5
Y_2O_3	3.1	2.2	0.1	0.1	–
La_2O_3	–	–	0.3	–	–
CaO	–	–	–	–	1.8
SrO	5.5	5.5	7.9	5.9	–
ZnO	–	–	–	–	1.3
Na_2O	10.1	10.2	8.4	10	8.9
K_2O	7.5	7.6	2.6	2.7	6.4
P_2O_5	1.8	1.8	1.8	1.7	0.2
F	2.4	2.3	2.6	2.4	3.2
Cs_2O	–	–	4.9	–	–
Rb_2O	–	–	–	4.8	–
ZrO_2	0.5	0.5	0.5	0.6	2.1
TiO_2	0.2	0.2	0.2	0.2	1.2
CeO_2	0.4	0.4	0.4	0.4	0.3
B_2O_3	0.3	0.3	0.4	0.2	0.1
Li_2O	0.5	0.5	0.5	0.8	–
Crystal phase	$\text{Sr}_5(\text{PO}_4)_3\text{F}$, KAlSi_2O_6	$\text{Sr}_5(\text{PO}_4)_3\text{F}$, KAlSi_2O_6 , NaSrPO_4	$\text{Sr}_5(\text{PO}_4)_3\text{F}$, $\text{CsAlSi}_2\text{O}_6$, NaSrPO_4	$\text{Sr}_5(\text{PO}_4)_3\text{F}$, $\text{RbAlSi}_2\text{O}_6$, NaSrPO_4	$\text{Ca}_5(\text{PO}_4)_3\text{F}$

in T_g . Alternatively, nanocrystalline phases in GCs can be obtained by developing parent glasses that phase-separate on a nanoscale, whereby subsequent crystal growth is limited by the boundaries of the LLPS domain, provided the parent glass does not overcome kinetic energy barrier to OR during heat treatment. Regardless of the application of the nano-GCs, the size and microstructure of apatite crystals are very important factors that determine whether a glass-ceramic is opaque or transparent after crystallization. Transparent GCs contain crystals smaller than the wavelength of light. Such nanoscale GCs are used for different applications, ranging from transparent zero thermal expansion coefficient cooking hobs, consumer electronics to laser amplifiers in optoelectronics. Transparency of the GC is highly desirable in these applications because light transmission through a transparent GC is highly efficient due to no or low internal light scattering.

Rare earth elements, such as those in the lanthanide group have special photon absorption and reemission properties. Under near-infrared excitation, rare earth elements can absorb low energy photons and reemit high energy photons (anti-Stokes emission). In contrast, quantum dots or organic dyes, on the other hand, are excited by high-energy photons but reemit low-energy photons (Stokes emission), which exhibit luminescence in the visible spectrum.

Glasses and glass-ceramics doped with rare earth elements exhibit special optical properties. Such glasses and glass-ceramics are used for applications in solid-state lasers, optical amplifiers, and display screens. Glasses doped with rare earth elements usually exhibit broader spectral bands and smaller absorption and reemission characteristics as compared to glass-ceramics, which are more efficient and show higher absorption and re-emission characteristic in addition to narrower spectral bands (Zhang et al., 2012, 2013a,b).

Furthermore, fluoride-containing crystals such as FAp are also known to have low phonon energies and low-dielectric loss, which is an attractive property in optoelectronics. Despite the commercial use of single crystal lasers based on apatites and the fact that apatite lattices are also very attractive for accommodating rare earth ions, there is limited number of publications on nanocrystalline apatite glass-ceramics since the first patent publication by Pinckney and Dejneka (1998).

Tulyaganov (2000) developed FAp ($\text{Ca}_5(\text{PO}_4)_3\text{F}$)–anorthite ($\text{CaAl}_2\text{Si}_2\text{O}_8$)–diopside ($\text{CaMgSi}_2\text{O}_6$) glass-ceramics in the system of SiO_2 – Al_2O_3 – P_2O_5 – CaO – CaF_2 – MgO (Table 7) for potential applications in optical amplifiers. In the above system, FAp crystallization was through a homogenous mechanism, whereas anorthite and diopside phases crystallized *via* a surface mechanism.

Hill et al. (2010) found evidence that FAp crystallization in the GC developed by Tulyaganov (2000) was on a nanoscale and self-limiting. Hill et al. (2010) provide evidence that FAp crystallization is self-limiting because the system exhibits LLPS on a nanoscale, i.e., the size of the phase-separated domain restricts subsequent crystal growth such that it cannot grow easily beyond the bounds of the LLPS. Hill et al. (2010) also argued that if the crystallization of the fluorine-containing crystal phase occurs close to the glass transition temperature and the crystallization process results in a significant increase in the glass transition temperature, the surrounding “glassy” phase will limit further crystal growth because of the increased glass transition temperature. Hill et al. (2010) proposed that metal fluoride content at or below the stoichiometry of the FAp crystal is one of the factors needed to obtain nanoscale phases of FAp in the GC studied. These results are explained in terms of an approach, which views glasses as being inorganic polymers where the presence of fluorine disrupts the glass network, and thereby reduces the energy barrier to homogeneous nucleation and crystallization of the FAp phases. Notably, Hill et al. (2010) also found some evidence that Mg can occupy Ca(II) sites of the FAp lattice, which was previously unknown in GCs. It is widely known that Mg^{2+} cations limit apatite crystal growth by blocking surface sites on the FAp crystal.

Doped single crystal FAp have been considered for potential applications in lasers (Ohlmann et al., 1968; Deloach et al., 1993, 1994). However, their poor thermomechanical properties

(Hopkins et al., 1971; Payne et al., 1994) can result in beam distortion due to thermal distortion that produces refractive index variations within the crystal. Furthermore, production of single crystals of FAp is not only expensive but unlike a glass-ceramic route cannot be processed into fibers and complex shapes. Polycrystalline apatites generally result in an opaque material, which is undesirable for optoelectronics unless the crystals are nanoscale and less than the wavelength of light. Consequently, nanocrystalline FAp GCs are of particular interest.

Zhang et al. (2012, 2013a,b) developed Nd and Eu-doped visually transparent FAp glass-ceramics (Table 8) for potential applications in optical amplifiers. Nd and Eu ions are f-block elements and can exhibit high degree of up-conversion in appropriate crystal lattices; therefore, they are highly attractive dopants in rare earth accommodating lattices, such as the apatite. Zhang et al. (2012, 2013a,b) systems crystallize to FAp and mullite; therefore, careful control of the heat treatment is crucial to avoid the crystallization of the mullite phase.

The ZH1 Nd doped glass (Table 8), as compared to its undoped version, showed a markedly reduced FAp crystallization temperature, in contrast, ZH3, strontium version of the same parent glass (Table 8) did not show a reduction in crystallization temperature but rather a less pronounced area under the exotherm assigned to FAp. Furthermore, although Zhang et al. (2013b) systems contain strong nucleants, such as P_2O_5 , comparing DSC traces of doped and undoped ZH3 versions, less pronounced FAp exotherms observed with Nd doped GC may be attributed to enhanced heterogeneous nucleation mechanism, as opposed to reduced overall crystallization; however, such explanation would have to be confirmed by analyzing particle size dependence on the crystallization temperature. Notably, Zhang et al. (2012) system (ZH1, Table 8) could remain optically clear after 24-h heat treatment at 790°C. This indicates that Zhang et al. (2012) system has undergone LLPS on a nanoscale, which therefore restricts FAp growth beyond the LLPS domain. Additionally, the kinetic barrier to OR during heat treatment is, therefore, not overcome in Zhang et al. (2012, 2013a,b) systems, which prevents crystal growth into the light scattering dimensions.

Furthermore, SrFAp (Zhang et al., 2013b), as opposed to CaFAp (Zhang et al., 2012), GC was found to have a markedly reduced visible spectrum transmittance, which authors attributed to a lower volume fraction of SrFAp crystals ($12 \pm 2\%$) as opposed to volume fraction of CaFAp ($19 \pm 6\%$) in the alternative calcium-containing GC system. Additionally, Zhang et al. (2012) found that Nd-doped calcium FAp GC showed better absorption and emission properties as compared to a strontium FAp GC (Zhang et al., 2013b) and argued that better absorption and emission

TABLE 7 | Fluorapatite–anorthite–diopside base glass composition in mol%.

SiO_2	Al_2O_3	P_2O_5	CaO	CaF_2	MgO
34.7	11.1	5.4	37.2	1.8	9.7

TABLE 8 | Compositions of Nd and Eu doped base glasses in mol% (Zhang et al. (2012, 2013a,b)).

	SiO_2	Al_2O_3	P_2O_5	CaCO_3	SrCO_3	CaF_2	SrF_2	La_2O_3	LiCO_3	B_2O_3	ZrO_2	Nd_2O_3	Eu_2O_3
$\text{Ca}_5(\text{PO}_4)_3\text{F}:\text{Nd}^{3+}$ (ZH1)	29.4	18	12	20	0	18	0	0.3	0.5	0.3	0.5	1	0
$\text{Ca}_5(\text{PO}_4)_3\text{F}:\text{Eu}^{3+}$ (ZH2)	29.4	18	12	20	0	18	0	0.3	0.5	0.3	0.5	0	1
$\text{Sr}_5(\text{PO}_4)_3\text{F}:\text{Nd}^{3+}$ (ZH3)	29.4	18	12	0	20	0	18	0.3	0.5	0.3	0.5	1	0

properties of a calcium FAp GC may be attributed to a higher fraction of Nd ions being incorporated into the former crystal lattice. Therefore, Nd-doped calcium FAp GCs likely have an advantage over Nd-doped strontium FAp GCs.

Nonetheless, Zhang et al. (2012, 2013a,b) were able to closely match the refractive index between the glass matrix and the crystal phases for smooth photon transitions across the medium. Additionally, the crystals in the GCs are smaller than the excitation and emission wavelengths and, therefore, such crystals are outside of the light scattering dimensions that in turn produce an energy-efficient material for luminescence applications.

NUCLEAR WASTE IMMOBILIZATION

Currently, high-level radioactive waste (HLW) from nuclear fission products are fused at high temperatures ($\sim 1,250^{\circ}\text{C}$) with a borosilicate glass and subsequently stored in repositories. However, due to long half-life of α -emitting radioactive elements, these HLW can potentially only be stored for up to 300 years in these glass matrices. GC, on the other hand, can provide a useful alternative for nuclear waste immobilization because they will provide two barriers of containment: one being the host crystal phase(s) and second the amorphous glass matrix. Additionally, a devitrified material is more resistant to water due to a higher network connectivity of the residual glassy phase.

Weber et al. (1979) and Weber (1993) analyzed Cm-doped silicates with the apatite structure but found them to be poor nuclear waste hosts as they completely transformed into an amorphous state. This resulted in a volume expansion and microfracturing of the material.

It is quite important to point out that phosphate apatite, as opposed to other apatitic phases show better resistance to amorphization (due to nuclear decay) and better chemical stability. Soulet et al. (2001) demonstrated that phosphosilicate FAp ceramics exhibit increasing resistance to amorphization when SiO_4 is substituted by PO_4 . Fang et al. (2014) also found that phosphate apatites exhibit superior chemical stability (under acetic acid challenge) when the atomic proportion of phosphorus replaced by silicon and sulfur did not exceed one-third.

At the Atomic Weapons Establishment (UK), Donald et al. (2007) developed novel calcium phosphate-based halogen-containing calcium apatite ceramics for a universal actinide- and halide-containing waste immobilization. In the preliminary study, Donald et al. (2007) produced four types of experimental halide-containing nuclear waste streams, in addition to a series of mainly sodium aluminum phosphate (NaAlP) glasses for subsequent encapsulation of the waste-hosting calcium phosphate ceramics. However, it is important to underline that apatite ceramics developed by Donald et al. (2007) require additional encapsulation in a durable glass matrix. Therefore, it may be argued that systems developed by Donald et al. (2007) are not traditional GCs; however, research led by Donald et al. (2007) is

still ongoing. From a manufacturing point of view, developing a “traditional” apatite GC could possibly provide a more economical alternative. Nonetheless, apatite-containing glass-ceramics are potentially excellent candidates as nuclear waste hosts, which evident from studies on the apatite ceramic materials. Therefore, there is a great but challenging potential for new developments in this field.

CONCLUSION

The review provides an overview of the apatite glass-ceramics, their crystallization behavior, their remarkable properties, and commercial applications in the fields of medicine and dentistry, optoelectronics, and potential nuclear waste management.

The A–W glass-ceramic discussed in the review shows excellent osseointegration and exhibits clinically suitable mechanical properties, including fracture toughness and flexural strength. However, the failure of this system to bulk nucleate and a lack of bioresorbability open up new challenging fronts for research and development to overcome these drawbacks. Data on the newly developed chlorapatite GCs suggest that these materials may provide the desired resorbability and osseointegration; however, further work is required in terms of their *in vivo* activity and structure–property relationship, including the microstructure and mechanical properties.

To date, the most commercially successful apatite glass-ceramics are those developed for dental veneering. These dental GCs exhibit low solubility, excellent translucency, and clinical esthetics, and are biomimetic in nature.

Current information in the literature suggests that apatite is potentially a good host phase for radioactive waste entrapment. Apatite glass-ceramics would be highly attractive for this application; however, a lack of publications in this area suggests that further studies are required.

The authors would like to conclude that apatite lattice inherently exhibits ease of solid solution whereby various ionic substitutions can take place. As such, its solid-state chemistry is of great interest in both, the fundamental as well as the applied research. Understanding derived from research in apatite-containing glass-ceramics continues to intrigue and convey new concepts in structural solid-state chemistry and the applied sciences discussed in this review with undoubtedly a great future potential.

AUTHOR CONTRIBUTIONS

TD produced the manuscript. SS and RH contributed to the critical revision and direction of the manuscript.

FUNDING

The authors would like to thank Cera Dynamics Limited, part of the James Kent Group and the Institute of Dentistry (Queen Mary University of London) for jointly funding TD.

REFERENCES

- An, Y. H., and Draughn, R. A. (2000). *Mechanical Testing of Bone and the Bone-Implant Interface*. Boca Raton: CRC Press.
- Blades, M., Moore, D., Revell, P., and Hill, R. (1998). *In vivo* skeletal response and biomechanical assessment of two novel polyalkenoate cements following femoral implantation in the female New Zealand White rabbit. *J. Mater. Sci. Mater. Med.* 9, 701–706. doi:10.1023/A:1008990516159
- Blumenthal, N. C., Betts, F., and Posner, A. S. (1975). Effect of carbonate and biological macromolecules on formation and properties of hydroxyapatite. *Calcif. Tissue Res.* 18, 81–90. doi:10.1007/BF02546228
- Cahn, J. W. (1969). The metastable liquidus and its effect on crystallization of glass. *J. Am. Ceram. Soc.* 52, 4. doi:10.1111/j.1151-2916.1969.tb11194.x
- Calver, A., Hill, R. G., and Stamboulis, A. (2004). Influence of fluorine content on the crystallization behavior of apatite-wollastonite glass-ceramics. *J. Sci. Mater.* 39, 2601–2603. doi:10.1023/B:JMSC.0000020038.79675.0f
- Chen, X., Brauer, D. S., Wilson, R. M., Hill, R. G., and Karpukhina, N. (2014a). Bioactivity of sodium free fluoride containing glasses and glass-ceramics. *Materials* 7, 5470–5487. doi:10.3390/ma7085470
- Chen, X., Brauer, D. S., Wilson, R. M., Hill, R. G., and Karpukhina, N. (2014b). Novel alkali free bioactive fluorapatite glass ceramics. *J. Non Cryst. Solids* 402, 172–177. doi:10.1016/j.jnoncrysol.2014.05.025
- Chen, X., Hill, R., and Karpukhina, N. (2014c). Chlorapatite glass-ceramics. *Int. J. Appl. Glass Sci.* 5, 207–216. doi:10.1111/ijag.12082
- Clifford, A., and Hill, R. (1996). Apatite-mullite glass-ceramics. *J. Non Cryst. Solids* 196, 346–351. doi:10.1016/0022-3093(95)00611-7
- Clifford, A., Hill, R., Towler, M., and Wood, D. (2001a). The crystallisation of glasses from the ternary $\text{CaF}_2\text{-CaAl}_2\text{Si}_2\text{O}_8\text{-P}_2\text{O}_5$ system. *J. Sci. Mater.* 36, 3955–3961. doi:10.1023/A:1017974306184
- Clifford, A., Hill, R., Rafferty, A., Mooney, P., Wood, D., Samunova, B., et al. (2001b). The influence of calcium to phosphate ratio on the nucleation and crystallization of apatite glass-ceramics. *J. Mater. Sci. Mater. Med.* 12, 461–469. doi:10.1023/A:1011213406951
- De Aza, P. N., Luklinska, Z. B., Martinez, A., Anseau, M. R., Guitian, F., and De Aza, S. (2000). Morphological and structural study of pseudowollastonite implants in bone. *J. Microsc.* 197(Pt 1), 60–67. doi:10.1046/j.1365-2818.2000.00647.x
- Deloach, L., Payne, S., Chase, L., Smith, L., Kway, W., and Krupke, W. (1993). Evaluation of absorption and emission properties of Yb-3 + doped crystals for laser applications. *IEEE J. Quant. Electron.* 29, 1179–1191. doi:10.1109/3.214504
- Deloach, L., Payne, S., Smith, L., Kway, W., and Krupke, W. (1994). Laser and spectroscopic properties of Sr-5(PO₄)(3F-Yb. *J. Opt. Soc. Am. B* 11, 269–276. doi:10.1364/JOSAB.11.000269
- Denry, I., Holloway, J., and Gupta, P. (2012). Effect of crystallization heat treatment on the microstructure of niobium-doped fluorapatite glass-ceramics. *J. Biomed. Mater. Res. B Appl. Biomater.* 100B, 1198–1205. doi:10.1002/jbm.b.32684
- Donald, I., Metcalfe, B., Fong, S., Gerrard, L., Strachan, D., and Scheele, R. (2007). A glass-encapsulated calcium phosphate wasteform for the immobilization of actinide-, fluoride-, and chloride-containing radioactive wastes from the pyrochemical reprocessing of plutonium metal. *J. Nucl. Mater.* 361, 78–93. doi:10.1016/j.jnucmat.2006.11.011
- Ducheyne, P., Healy, K. E., Grainger, D. W., Huttmacher, D. W., and Kirkpatrick, C. J. (2011). *Comprehensive Biomaterials*. Oxford: Elsevier.
- Elliott, J. C., and Young, R. A. (1967). Conversion of single crystals of chlorapatite into single crystals of hydroxyapatite. *Nature* 214, 904–906.
- Fang, Y., Ritter, C., and White, T. (2014). Crystal chemical characteristics of elledite-type apatite: implications for toxic metal immobilization. *Dalton Trans.* 43, 16031–16043. doi:10.1039/C4DT02088J
- Fechtelkord, M., Behrens, H., Holtz, F., Fyfe, C., Groat, L., and Raudsepp, M. (2003). Influence of F content on the composition of Al-rich synthetic phlogopite: Part 1. New information on structure and phase-formation from Si-29, H-1, and F-19 MAS NMR spectroscopies. *Am. Mineral.* 88, 47–53. doi:10.2138/am-2003-0106
- Filho, O. P., Latorre, G. P., and Hench, L. L. (1996). Effect of crystallization on apatite-layer formation of bioactive glass 45S₅. *J. Biomed. Mater. Res.* 30, 509–514. doi:10.1002/(SICI)1097-4636(199604)30:4<509::AID-JBM9>3.0.CO;2-T
- Filiaggi, M. J., Coombs, M. A., and Pilliar, R. M. (1991). Characterization of the interface in the plasma-sprayed HA coating/Ti-6Al-4V implant system. *J. Biomed. Mater. Res.* 25, 1211–1229. doi:10.1002/jbm.820251004
- Freeman, C. O. I., Brook, M., Johnson, A., Hatton, P. V., Hill, R. G., and Stanton, K. T. (2003). Crystallization modifies osteoconductivity in an apatite-mullite glass-ceramic. *J. Mater. Sci. Mater. Med.* 14, 985–990. doi:10.1023/A:1026306901058
- Gentleman, E., Fredholm, Y. C., Jell, G., Lotfibakhshaei, N., O'Donnell, M. D., Hill, R. G., et al. (2010). The effects of strontium-substituted bioactive glasses on osteoblasts and osteoclasts *in vitro*. *Biomaterials* 31, 3949–3956. doi:10.1016/j.biomaterials.2010.01.121
- Goodridge, R. D., Wood, D. J., Ohtsuki, C., and Dalgarno, K. W. (2007). Biological evaluation of an apatite-mullite glass-ceramic produced via selective laser sintering. *Acta Biomater.* 3, 221–231. doi:10.1016/j.actbio.2006.10.005
- Grossman, D. G. (1972). Machinable glass-ceramics based on tetrasilicic mica. *J. Am. Ceram. Soc.* 55, 446–449. doi:10.1111/j.1151-2916.1972.tb11337.x
- Hill, R., Calver, A., Skinner, S., Stamboulis, A., Law, R., Nakamura, T., et al. (2006). A MAS-NMR and combined Rietveld study of mixed calcium/strontium fluorapatite glass-ceramics. *Bioceramics* 18(Pts 1 and 2), 309–311:305–308. doi:10.4028/www.scientific.net/KEM.309-311.305
- Hill, R., Calver, A., Stamboulis, A., and Bubb, N. (2007). Real-time nucleation and crystallization studies of a fluorapatite glass-ceramics using small-angle neutron scattering and neutron diffraction. *J. Am. Ceram. Soc.* 90, 763–768. doi:10.1111/j.1551-2916.2006.01474.x
- Hill, R., Patel, M., and Wood, D. J. (1991). “Preliminary studies on castable apatite-mullite glass-ceramics,” in *4th International Symposium on Ceramics in Medicine* (London: Butterworth Heineman Ltd.).
- Hill, R., Rafferty, A., Mooney, P., and Wood, D. (2000). The influence of glass composition on nucleation crystallisation microstructure and properties of apatite-mullite glass-ceramics. *Glass Sci. Technol.* 73(1 Suppl. C), 146–153.
- Hill, R., and Wood, D. (1995). Apatite-mullite glass-ceramics. *J. Mater. Sci. Mater. Med.* 6, 311–318.
- Hill, R. G., O'Donnell, M. D., Law, R. V., Karpukhina, N., Cochrane, B., and Tulyaganov, D. U. (2010). The early stages of nucleation and crystallisation of an apatite glass-ceramic: evidence for nano-scale crystallisation. *J. Non Cryst. Solids* 356, 2935–2941. doi:10.1016/j.jnoncrysol.2010.05.102
- Hill, R. G., Stamboulis, A., Law, R. V., Clifford, A., Towler, M. R., and Crowley, C. (2004). The influence of strontium substitution in fluorapatite glasses and glass-ceramics. *J. Non Cryst. Solids* 336, 223–229. doi:10.1016/j.jnoncrysol.2004.02.005
- Höland, W., and Beall, G. H. (2012). *Glass-Ceramic Technology*. Hoboken, NJ: Westerville, OH: Wiley; The American Ceramic Society.
- Höland, W., Frank, M., Schweiger, M., and Rheinberger, V. (1994). Development of translucent glass-ceramics for dental application. *Glastech. Ber. Glass Sci. Technol.* 67, 117–122.
- Höland, W., and Rheinberger, V. (2008). “Dental glass-ceramics,” in *Bioceramics and Their Clinical Applications*, ed. T. Kokubo (Cambridge, England: Woodhead Publishing Limited), 561.
- Höland, W., Rheinberger, V., Wegner, S., and Frank, M. (2000). Needle-like apatite-leucite glass-ceramic as a base material for the veneering of metal restorations in dentistry. *J. Mater. Sci. Mater. Med.* 11, 11–17. doi:10.1023/A:1008977416834
- Höland, W., Schweiger, M., Dittmer, M., and Ritzberger, C. (2015). Radiopaque strontium fluoroapatite glass-ceramics. *Front. Bioeng. Biotechnol.* 3:149. doi:10.3389/fbioe.2015.00149
- Höland, W., and Vogel, W. (2013). “Machinable and phosphate glass-ceramics,” in *Introduction to Bioceramics*, ed. L. L. Hench (London: Imperial College Press), 215–228.
- Hopkins, R. H., Damon, D. H., Piotrowski, P., Walker, M. S., and Uphoff, J. H. (1971). Thermal properties of synthetic fluorapatite crystals. *J. Appl. Phys.* 42, 272–275. doi:10.1063/1.1659583
- James, P. (1981). Nucleation in glass forming systems – a review. *J. Am. Ceram. Soc.* 60, 352–352.
- Karageorgiou, V., and Kaplan, D. (2005). Porosity of 3D biomaterial scaffolds and osteogenesis. *Biomaterials* 26, 5474–5491. doi:10.1016/j.biomaterials.2005.02.002
- Kitsugi, T., Yamamuro, T., and Kokubo, T. (1989). Bonding behavior of a glass-ceramic containing apatite and wollastonite in segmental replacement of the rabbit tibia under load-bearing conditions. *J. Bone Joint Surg. Am.* 71A, 264–272. doi:10.2106/00004623-198971020-00014
- Kitsugi, T., Yamamuro, T., and Kokubo, T. (1990). Analysis of A.W glass-ceramic surface by micro-beam X-ray-diffraction. *J. Biomed. Mater. Res.* 24, 259–273. doi:10.1002/jbm.820240211

- Kokubo, T. (2008). "Bioactive glass-ceramics," in *Bioceramics and Their Clinical Applications*, ed. T. Kokubo (Cambridge, England: Woodhead Publishing Limited), 288–289.
- Kokubo, T., Ito, S., Sakka, S., and Yamamuro, T. (1986). Formation of a high-strength bioactive glass ceramic in the system MgO–CaO–SiO₂–P₂O₅. *J. Sci. Mater.* 21, 536–540. doi:10.1007/BF01145520
- Kokubo, T., Ito, S., Shigematsu, M., Sakka, S., and Yamamuro, T. (1985). Mechanical-properties of a new type of apatite-containing glass ceramic for prosthetic application. *J. Sci. Mater.* 20, 2001–2004. doi:10.1007/BF01112282
- Kokubo, T., Ito, S., Shigematsu, M., Sanka, S., and Yamamuro, T. (1987). Fatigue and life-time of bioactive glass-ceramic A-W containing apatite and wollastonite. *J. Sci. Mater.* 22, 4067–4070. doi:10.1007/BF01133359
- Kokubo, T., Kushitani, H., Ohtsuki, C., Sakka, S., and Yamamuro, T. (1992). Chemical-reaction of bioactive glass and glass-ceramics with a simulated body-fluid. *J. Mater. Sci. Mater. Med.* 3, 79–83. doi:10.1007/BF00705272
- Kokubo, T., Kushitani, H., Sakka, S., Kitsugi, T., and Yamamuro, T. (1990). Solutions able to reproduce *in vivo* surface-structure changes in bioactive glass-ceramic A-W. *J. Biomed. Mater. Res.* 24, 721–734. doi:10.1002/jbm.820240607
- Kokubo, T., Shigematsu, M., Nagashima, Y., Tashiro, M., Nakamura, T., Yamamuro, T., et al. (1982). Apatite- and wollastonite-containing glass-ceramics for prosthetic application. *Bull. Inst. Chem. Res. Kyoto Univ.* 60, 260–268.
- Kumar, V., and Gill, K. (2009). Aluminium neurotoxicity: neurobehavioural and oxidative aspects. *Arch. Toxicol.* 83, 965–978. doi:10.1007/s00204-009-0455-6
- LeGeros, R. Z., Taheri, M. H., Quiroiglo, G. B., and LeGeros, J. P. (1980). "Formation and stability of apatites: effects of some cationic substituents," in *2nd International Congress on Phosphorus Compounds* (Boston, MA: IMPHOS (Paris)), 89–103.
- McCubbin, F., and Nekvasil, H. (2008). Maskelynite-hosted apatite in the Chassigny meteorite: Insights into late-stage magmatic volatile evolution in martian magmas. *Am. Mineral.* 93, 676–684. doi:10.2138/am.2008.2558
- McCubbin, F., Steele, A., Hauri, E., Nekvasil, H., Yamashita, S., and Hemley, R. (2010). Nominally hydrous magmatism on the Moon. *Proc. Natl. Acad. Sci. U. S. A.* 107, 11223–11228. doi:10.1073/pnas.1006677107
- Montazerian, M., and Zanotto, E. D. (2016). History and trends of bioactive glass-ceramics. *J. Biomed. Mater. Res. A* 104, 1231–1249. doi:10.1002/jbm.a.35639
- Nakamura, T., Yamamuro, T., Higashi, S., Kokubo, T., and Ito, S. (1985). A new glass-ceramic for bone replacement: evaluation of its bonding to bone tissue. *J. Biomed. Mater. Res.* 19, 685–698. doi:10.1002/jbm.820190608
- Neo, M., Nakamura, T., Ohtsuki, C., Kokubo, T., and Yamamuro, T. (1993). Apatite formation on three kinds of bioactive material at an early stage *in vivo*: a comparative study by transmission electron microscopy. *J. Biomed. Mater. Res.* 27, 999–1006. doi:10.1002/jbm.820270805
- O'Donnell, M., Karpukhina, N., Calver, A., Law, R., Bubb, N., Stamboulis, A., et al. (2010). Real time neutron diffraction and solid state NMR of high strength apatite-mullite glass ceramic. *J. Non Cryst. Solids* 356, 2693–2698. doi:10.1016/j.jnoncrysol.2010.08.038
- Ohlmann, R. C., Steinbruegge, K. B., and Mazelsky, R. (1968). Spectroscopic and laser characteristics of neodymium-doped calcium fluorophosphate. *Appl. Opt.* 7, 905–914. doi:10.1364/AO.7.000905
- Orlovskii, V., Komlev, V., and Barinov, S. (2002). Hydroxyapatite and hydroxyapatite-based ceramics. *Inorg. Mater.* 38, 973–984. doi:10.1023/A:1014029514176
- Payne, S., Smith, L., Deloach, L., Kway, W., Tassano, J., and Krupke, W. (1994). Laser, optical, and thermomechanical properties of Yb-doped fluorapatite. *IEEE J. Quant. Electron.* 30, 170–179. doi:10.1109/3.272077
- Pinckney, L. R., and Dejneka, M. J. (1998). *Transparent Apatite Glass-Ceramics*. WIPO, WO 1998043922 A1.
- Piper, W. W., Kravitz, L. C., and Swank, R. K. (1965). Axially symmetric paramagnetic color centers in fluorapatite. *Phys. Rev.* 138, A1802–A1814. doi:10.1103/PhysRev.138.A1802
- Rafferty, A., Clifford, A., Hill, R., Wood, D., Samuneva, B., and Dimitrova-Lukacs, M. (2000a). Influence of fluorine content in apatite-mullite glass-ceramics. *J. Am. Ceram. Soc.* 83, 2833–2838. doi:10.1111/j.1151-2916.2000.tb01640.x
- Rafferty, A., Hill, R., and Wood, D. (2000b). Amorphous phase separation of ionomer glasses. *J. Sci. Mater.* 35, 3863–3869. doi:10.1023/A:1004885531712
- Rafferty, A., Hill, R., and Wood, D. (2003). An investigation into the amorphous phase separation characteristics of an ionomer glass series and a sodium-boro-silicate glass system. *J. Sci. Mater.* 38, 2311–2319. doi:10.1023/A:1026240525763
- Ramsden, A., and James, P. (1984a). The effects of amorphous phase-separation on crystal nucleation kinetics in BaO–SiO₂ glasses. 1. General survey. *J. Sci. Mater.* 19, 1406–1419. doi:10.1007/BF01026965
- Ramsden, A., and James, P. (1984b). The effects of amorphous phase-separation on crystal nucleation kinetics in BaO–SiO₂ glasses. 2. Isothermal heat-treatments at 700-degrees c. *J. Sci. Mater.* 19, 2894–2908. doi:10.1007/BF01026965
- Ranu, H. S. (1987). The thermal properties of human cortical bone: an *in vitro* study. *Eng. Med.* 16, 175–176. doi:10.1243/EMED_JOUR_1987_016_036_02
- Reusche, E., Pilz, P., Oberascher, G., Lindner, B., Egensperger, R., Gloeckner, K., et al. (2001). Subacute fatal aluminum encephalopathy after reconstructive otoneurosurgery: a case report. *Hum. Pathol.* 32, 1136–1140. doi:10.1053/hupa.2001.28251
- Rodriguez, M., Felsenfeld, A. J., and Llach, F. (1990). Aluminum administration in the rat separately affects the osteoblast and bone mineralization. *J. Bone Miner. Res.* 5, 59–67. doi:10.1002/jbmr.5650050110
- Sabareeswaran, A., Basu, B., Shenoy, S. J., Jaffer, Z., Saha, N., and Stamboulis, A. (2013). Early osseointegration of a strontium containing glass ceramic in a rabbit model. *Biomaterials* 34, 9278–9286. doi:10.1016/j.biomaterials.2013.08.070
- Samuneva, B., Dimitrov, V., Kalimanova, S., Gattef, E., and Hill, R. (1998). Crystallization of gels in the apatite-mullite system. *J. Solgel Sci. Technol.* 13, 951–956. doi:10.1023/A:1008695812143
- Segall, B., Ludwig, G. W., Woodbury, H. H., and Johnson, P. D. (1962). Electron spin resonance of a centre in calcium fluorophosphate. *Phys. Rev.* 128, 76–79. doi:10.1103/PhysRev.128.76
- Siriphanon, P., Kameshima, Y., Yasumori, A., Okada, K., and Hayashi, S. (2000). Influence of preparation conditions on the microstructure and bioactivity of alpha-CaSiO₃ ceramics: formation of hydroxyapatite in simulated body fluid. *J. Biomed. Mater. Res.* 52, 30–39. doi:10.1002/1097-4636(200010)52:1<30::AID-JBM5>3.0.CO;2-Z
- Soulet, S., Carpena, J., Chaumont, J., Kaitasov, O., Ruault, M., and Krupa, J. (2001). Simulation of the alpha-annealing effect in apatitic structures by He-ion irradiation: influence of the silicate/phosphate ratio and of the OH(-)/F(-) substitution. *Nucl. Instrum. Methods Phys. Res. B* 184, 383–390. doi:10.1016/S0168-583X(01)00764-9
- Stamboulis, A., Hill, R., Calver, A., Bubb, N., Manuel, P., Nakamura, T., et al. (2006). Real time neutron diffraction studies of apatite glass ceramics. *Bioceramics* 18(Pts 1 and 2), 309–311:309–312. doi:10.4028/www.scientific.net/KEM.309-311.309
- Stamboulis, A., Hill, R., Law, R., Matsuya, S., Barbosa, M., Monteiro, F., et al. (2004). A MAS NMR study of the crystallisation process of apatite-mullite glass-ceramics. *Bioceramics* 16, 254–252. doi:10.4028/www.scientific.net/KEM.254-256.99
- Stanton, K., O'Flynn, K., Nakahara, S., Vanhumbecck, J., Delucca, J., and Hooghan, B. (2009). Study of the interfacial reactions between a bioactive apatite-mullite glass-ceramic coating and titanium substrates using high angle annular dark field transmission electron microscopy. *J. Mater. Sci. Mater. Med.* 20, 851–857. doi:10.1007/s10856-008-3650-8
- Stanton, K. T., and Hill, R. G. (2005). Crystallisation in apatite-mullite glass-ceramics as a function of fluorine content C3 – proceedings of the 14th international conference on crystal growth and the 12th international conference on vapor growth and epitaxy. *J. Cryst. Growth* 275, e2061–e2068. doi:10.1016/j.jcrysgro.2004.11.266
- Stanton, K. T., O'Flynn, K. P., Kiernan, S., Menuge, J., and Hill, R. (2010). Spherulitic crystallization of apatite-mullite glass-ceramics: mechanisms of formation and implications for fracture properties. *J. Non-Cryst. Solids* 356, 1802–1813. doi:10.1016/j.jnoncrysol.2010.07.006
- Strnad, Z. (1992). Role of the glass phase in bioactive glass-ceramics. *Biomaterials* 13, 317–321. doi:10.1016/0142-9612(92)90056-T
- Tomozawa, M. (1972). Liquid-phase separation and crystal nucleation in Li₂O–SiO₂ glasses. *Phys. Chem. Glasses* 13, 161.
- Tulyaganov, D. U. (2000). Phase equilibrium in the fluorapatite-anorthite-diopside system. *J. Am. Ceram. Soc.* 83, 3141–3146. doi:10.1111/j.1151-2916.2000.tb01695.x
- Verberckmoes, S., De Broe, M., and D'Haese, P. (2003). Dose-dependent effects of strontium on osteoblast function and mineralization. *Kidney Int.* 64, 534–543. doi:10.1046/j.1523-1755.2003.00123.x

- Vogel, W., and Gerth, K. (1962). "Catalyzed crystallization in glass," in *63rd Anniversary of the American Ceramic Society Symposium on Nucleation and Crystallization of Glasses and Melts*, ed. M. K. Reser (Toronto, Canada: American Ceramic Society), 11–22.
- Vogel, W., Holand, W., Naumann, K., and Gummel, J. (1986). Development of machineable bioactive glass-ceramics for medical uses. *J. Non-Cryst. Solids* 80, 34–51.
- Weber, W. (1993). Alpha-decay-induced amorphization in complex silicate structures. *J. Am. Ceram. Soc.* 76, 1729–1738. doi:10.1111/j.1151-2916.1993.tb06641.x
- Weber, W. J., Turcotte, R. P., Bunnell, L. R., Roberts, F. P., and Westsik, J. H. Jr. (1979). "Radiation Effects in Vitreous and Devitrified Simulated Waste Glass," in *Ceramics in Nuclear Waste Management*, eds T. D. Chikalla and J. E. Mendel (Virginia: National Technical Information Service, Springfield), 294–299.
- White, T., Ferraris, C., Kim, J., Madhavi, S., Ferraris, G., and Merlino, S. (2005). Apatite – an adaptive framework structure. *Micro Mesoporous Mineral Phases* 57, 307–401. doi:10.2138/rmg.2005.57.10
- Wood, D., and Hill, R. (1991). Glass ceramic approach to controlling the properties of a glass-ionomer bone cement. *Biomaterials* 12, 164–170. doi:10.1016/0142-9612(91)90195-G
- Zanotto, E. (2010). A bright future for glass-ceramics. *Am. Ceram. Soc. Bull.* 89, 19–27.
- Zanotto, E., James, P., and Craievich, A. (1986). The effects of amorphous phase-separation on crystal nucleation kinetics in BaO-SiO₂ glasses. 3. Isothermal treatments at 718°C to 760°C – small-angle X-ray-scattering results. *J. Sci. Mater.* 21, 3050–3064. doi:10.1007/BF00553336
- Zeng, Q., and Stebbins, J. (2000). Fluoride sites in aluminosilicate glasses: high-resolution F-19 NMR results. *Am. Mineral.* 85, 863–867. doi:10.2138/am-2000-5-630
- Zhang, S., Huang, J., Chen, Y., Gong, X., Lin, Y., Luo, Z., et al. (2012). Preparation and spectral properties of Nd³⁺ -doped transparent glass ceramic containing Ca-5(PO₄)(3)F nanocrystals. *J. Non Cryst. Solids* 358, 2835–2840. doi:10.1016/j.jnoncrysol.2012.07.005
- Zhang, S., Huang, J., Chen, Y., Gong, X., Lin, Y., Luo, Z., et al. (2013a). Site-selective excitation and emission of Eu³⁺ -doped transparent glass ceramic containing Ca-5(PO₄)(3)F nanocrystals. *Opt. Mater. Express* 3, 868–874. doi:10.1364/OME.3.000868
- Zhang, S., Huang, J., Chen, Y., Gong, X., Lin, Y., Luo, Z., et al. (2013b). Spectroscopic properties of Nd³⁺ -doped transparent glass ceramic containing Sr-5(PO₄)(3)F nanocrystals. *J. Non Cryst. Solids* 366, 35–41. doi:10.1016/j.jnoncrysol.2013.01.048

Conflict of Interest Statement: The authors declare that the research was conducted in the absence of any commercial or financial relationships that could be construed as a potential conflict of interest.

Copyright © 2017 Duminis, Shahid and Hill. This is an open-access article distributed under the terms of the Creative Commons Attribution License (CC BY). The use, distribution or reproduction in other forums is permitted, provided the original author(s) or licensor are credited and that the original publication in this journal is cited, in accordance with accepted academic practice. No use, distribution or reproduction is permitted which does not comply with these terms.

Advantages of publishing in Frontiers



OPEN ACCESS

Articles are free to read,
for greatest visibility



COLLABORATIVE PEER-REVIEW

Designed to be rigorous
– yet also collaborative,
fair and constructive



FAST PUBLICATION

Average 85 days from
submission to publication
(across all journals)



COPYRIGHT TO AUTHORS

No limit to article
distribution and re-use



TRANSPARENT

Editors and reviewers
acknowledged by name
on published articles



SUPPORT

By our Swiss-based
editorial team



IMPACT METRICS

Advanced metrics
track your article's impact



GLOBAL SPREAD

5'100'000+ monthly
article views
and downloads



LOOP RESEARCH NETWORK

Our network
increases readership
for your article

Frontiers

EPFL Innovation Park, Building I • 1015 Lausanne • Switzerland
Tel +41 21 510 17 00 • Fax +41 21 510 17 01 • info@frontiersin.org
www.frontiersin.org

Find us on

